DISSERTATIONES
CHIMICAE
UNIVERSITATIS
TARTUENSIS
248

ROHIT KUMAR

ZIF-8-derived M-N-C electrocatalysts for oxygen reduction reaction in AEMFC and MFC devices

DISSERTATIONES CHIMICAE UNIVERSITAS TARTUENSIS
248

DISSERTATIONES CHIMICAE UNIVERSITAS TARTUENSIS
248

ROHIT KUMAR

ZIF-8-derived M-N-C electrocatalysts for oxygen reduction reaction in AEMFC and MFC devices

UNIVERSITY OF TARTU
Press
1632

Institute of Chemistry, Faculty of Science and Technology, University of Tartu, Estonia

The dissertation is accepted for the commencement of the degree of Doctor of Philosophy in Chemistry on 9th June 2026, by the Council of the Institute of Chemistry, Faculty of Science and Technology, University of Tartu, Estonia.

Supervisors: Professor Kaido Tammeveski
Institute of Chemistry, University of Tartu, Estonia

Dr. Marek Mooste
Institute of Chemistry, University of Tartu, Estonia

Dr. Ivar Zekker
Institute of Chemistry, University of Tartu, Estonia

Opponent: Professor Barbara Mecheri
Department of Chemical Science and Technologies,
University of Rome Tor Vergata, Italy

Commencement: September 3, 2026 at 14:15 in Ravila 14A-1020, Tartu (Chemicum) and Microsoft Teams (online)

ISSN 1406-0299 (print) ISSN 2806-2159 (pdf)
ISBN 978-9908-57-251-2 (print) ISBN 978-9908-57-252-9 (pdf)

University of Tartu Press
www.tyk.ee

TABLE OF CONTENTS

1. LIST OF ORIGINAL PUBLICATIONS

The current thesis is based on the following six publications, symbolised as Roman numerals (I–VI) in the text.

I. **R. Kumar**, M. Mooste, Z. Ahmed, S. Akula, I. Zekker, M. Marandi, M. Käärik, J. Leis, A. Kikas, A. Treshchalov, M. Otsus, J. Aruväli, V. Kisand, A. Tamm, K. Tammeveski, Highly active ZIF-8@CNT composite catalysts as cathode materials for anion exchange membrane fuel cells, *Industrial Chemistry & Materials* 1 (2023) 526–541.

II. **R. Kumar**, M. Mooste, Z. Ahmed, I. Zekker, M. Marandi, M. Käärik, J. Leis, A. Kikas, A. Treshchalov, M. Otsus, J. Aruväli, V. Kisand, A. Tamm, K. Tammeveski, Catalyzing oxygen reduction by morphologically engineered ZIF-derived carbon composite catalysts in dual-chamber microbial fuel cells, *Journal of Environmental Chemical Engineering* 12 (2024) 112242.

III. **R. Kumar**, M. Mooste, I. Zekker, M. Käärik, J. Leis, A. Kikas, A. Treshchalov, J. Kozlova, M. Otsus, J. Aruväli, V. Kisand, K. Kukli, K. Tammeveski, Tailoring highly efficient ZIF-derived Fe_xCe_y@N–C composite catalysts for oxygen reduction reaction in H-shape microbial fuel cells, *International Journal of Hydrogen Energy* 98 (2025) 793–806.

IV. **R. Kumar**, M. Mooste, I. Zekker, J. Kozlova, M. Otsus, M. Käärik, J. Aruväli, A. Kikas, A. Treshchalov, J. Leis, V. Kisand, K. Kukli, K. Tammeveski, Hybrid Fe/Fe_4N and Fe-N_x decorated Fe-N-C material for efficient oxygen reduction reaction electrocatalysis in microbial fuel cells, *Journal of Alloys and Compounds* 1060 (2026) 187251.

V. **R. Kumar**, M. Mooste, I. Zekker, J. Kozlova, M. Käärik, M. Otsus, A. Treshchalov, J. Aruväli, J. Leis, A. Kikas, V. Kisand, K. Kukli, K. Tammeveski, Mn-N-C material with high-density and accessible Mn-N_x sites emerging as an efficient oxygen reduction reaction electrocatalyst for AEMFCs, *Journal of Power Sources* 667 (2026) 239191.

VI. **R. Kumar**, M. Mooste, I. Zekker, J. Kozlova, M. Käärik, M. Kõiv, A. Treshchalov, J. Aruväli, J. Leis, A. Kikas, V. Kisand, K. Kukli, J.H. Zagal, K. Tammeveski, Bimetal phthalocyanines on pre-treated ZIF-8@CNT scaffolds for efficient oxygen reduction reaction in AEMFCs. (Manuscript)

Author's contribution:

Paper I Synthesis of catalyst materials, electrochemical measurements (except fuel cell testing), interpretation of data and was mainly responsible for writing the manuscript.

Paper II Synthesis of catalyst materials, electrochemical measurements, enrichment of electroactive biofilm, microbial fuel cell assembly and testing, analysed the data and was mainly responsible for writing the manuscript.

Paper III Synthesis of catalyst materials, electrochemical measurements, enrichment of electroactive biofilm, microbial fuel cell assembly and testing, analysed the data and was mainly responsible for writing the manuscript.

Paper IV Synthesis of catalyst materials, electrochemical measurements, enrichment of electroactive biofilm, microbial fuel cell assembly and testing, analysed the data and was mainly responsible for writing the manuscript

Paper V Synthesis of catalyst materials, electrochemical measurements, MEA preparation, fuel cell assembly and testing, analysed the data and was mainly responsible for writing the manuscript.

Paper VI Synthesis of catalyst materials, electrochemical measurements, MEA preparation, fuel cell assembly and testing, analysed the data and was mainly responsible for writing the manuscript.

2. ABBREVIATIONS AND SYMBOLS

A	geometric surface area of the electrode
AEM	anion exchange membrane
AEMFC	anion exchange membrane fuel cell
BE	binding energy
BET	Brunauer-Emmett-Teller
BF	bright field
%CE	Coulombic efficiency
CNTs	carbon nanotubes
COD	chemical oxygen demand
CoPc	cobalt(II) phthalocyanine
C_O	concentration of oxygen in the bulk solution
CV	cyclic voltammetry
D_O	diffusion coefficient of oxygen
EAB	electroactive biofilm
E_0	standard potential
$E_{1/2}$	half-wave potential
E_{onset}	onset potential
EDX	energy-dispersive X-ray spectroscopy
EET	extracellular electron transfer
ESVAR	electrode surface area-to-anode volume ratio
FC	fuel cell
FePc	iron(II) phthalocyanine
GC	glassy carbon
GDE	gas diffusion electrode
GDL	gas diffusion layer
HAADF	high angle annular dark field
HFC	hydrogen fuel cell
HOR	hydrogen oxidation reaction
HR-TEM	high-resolution transmission electron microscopy
$\%H_2O_2/\%HO_2^-$	percentage yield of peroxide formation
I_R	ring current
I_D	disk current
J	current density
J_K	kinetic current density
J_L	diffusion-limited current density
J_o	exchange current density
K-L	Koutecky-Levich
k	electrochemical rate constant
LSV	linear sweep voltammetry
MEA	membrane-electrode assembly
MFC	microbial fuel cell
$M\text{-}N_x$	nitrogen-coordinated transition metal sites

M-N-C	transition metal-nitrogen-carbon catalyst
MOF	metal organic framework
MnPc	manganese(II) phthalocyanine
MPc	metal phthalocyanine
MP-AES	microwave plasma atomic emission spectroscopy
MWCNTs	multiwalled carbon nanotubes
n	electron transfer number
N	Pt-ring collection efficiency
NLPM	normal litres per minute
NPMC	non-precious metal catalyst
OCV	open circuit voltage
ORR	oxygen reduction reaction
PBS	phosphate buffered saline
PEFC	polymer electrolyte fuel cell
PEM	proton exchange membrane
PEMFC	proton exchange membrane fuel cell
PGM	platinum-group-metal
P_{max}	maximum power density
PSD	pore size distribution
QSDFT	quenched solid density functional theory
RDE	rotating disk electrode
RHE	reversible hydrogen electrode
RRDE	rotating ring-disk electrode
Sa_{μ}	micropores surface area
Sa_{m}	mesopores surface area
S_{BET}	specific surface area
SCE	saturated calomel electrode
SEM	scanning electron microscopy
SHE	standard hydrogen electrode
STEM	scanning transmission electron microscopy
TPB	triple phase boundary
v	potential scan rate
V_{tot}	total pore volume
V_{μ}	micropore volume
ν	kinematic viscosity of the electrolyte solution
ω	electrode rotation rate
XPS	X-ray photoelectron spectroscopy
XRD	X-ray diffraction
XRF	X-ray fluorescence
ZIF-8	zeolitic imidazolate framework-8

3. INTRODUCTION

Globally, rising energy demand is pushing fossil fuels to the brink of systemic obsolescence. In the European region, output from existing natural oil and gas reservoirs has declined by approximately 15%, driven by extensive overuse and natural field depletion. This rising geopolitical and environmental pressure has forced a strategic pivot toward the rapid commercialisation of renewable energy technologies, particularly within the transportation sector [1]. This shift underscores the urgent need for high-efficiency energy conversion devices, such as hydrogen fuel cells (HFCs), to ensure long-term energy security and decarbonisation [2, 3]. An acute transition towards fuel cell electric vehicles (FCEVs) over the coming years is underway, though it is still at the research and development stage, especially for heavy-duty FCEVs [4–6]. Despite several innovations in HFCs design, their widespread adoption still lags desired momentum. For instance, proton exchange membrane fuel cells (PEMFCs) are currently considered a mature, widely deployed energy conversion device, with recent applications in aviation and particularly in heavy-duty mobility and stationary backup power applications [7–11]. However, they rely heavily on expensive platinum-based catalysts for the oxygen reduction reaction (ORR), which imposes significant sustainability and economic limitations [12]. As a potential alternative, anion-exchange membrane fuel cells (AEMFC) offer a promising avenue due to their cost-effectiveness and compatibility with a broad spectrum of non-precious metal catalysts (NPMC) [13, 14]. Even though AEMFC utilises Pt catalyst at the anode, its subsequent replacement at the cathode with a transition metal-nitrogen-carbon (M-N-C) catalyst leads to a substantial reduction in the overall fuel cell device cost. However, achieving optimal ORR electrocatalytic performance and durability with these M-N-C-cathode AEMFC devices, particularly in the automobile sector, requires further research.

Similarly, microbial fuel cell (MFC) gained significant popularity during the early 2000s for their ability to treat wastewater while simultaneously generating electricity [15–18]. Therefore, this technology provided a sustainable, cost-effective and scalable solution for energy-intensive treatment plants through self-sustaining mini-powerhouse devices. While wastewater treatment remains a prime focus of MFCs, their ability to generate a measurable electrical signal in response to specific biochemical reactions makes them ideal for developing sensors for environmental monitoring, medical diagnostics, and industrial processes [19–22]. Therefore, they hold substantial promises for the high-value market but are still at a nascent stage of commercialisation. However, given the inherent potential of MFCs, Europe accounts for a major share of the global MFC market, supported by stringent environmental regulations and a strong focus on circular economic initiatives to meet the European Green Deal goals [23]. In fact, the pervasive reliance on fossil fuels further reinforces the need for such greener and innovative renewable energy sources [24, 25]. Nevertheless, their longevity and practical implementation are mainly hindered by the high overpotential of the ORR at the

cathode, especially in neutral pH environment [26–29]. Concurrently, reliance on Pt-based catalysts presents a major setback to this technology, mainly due to the high cost of platinum and its susceptibility to poisoning. While over the years, M-N-C emerged as the premier alternative due to its competitive electrocatalytic activity comparable to that of platinum-group-metal (PGM) catalysts, their poor stability and low active-site density remains the critical scientific challenge [30–32]. Therefore, current efforts are focused on tuning their structural/electronic features to effectively address these persistent challenges.

Apparently, the research carried out in this PhD thesis systematically resolved the main bottleneck in AEMFC and MFC technologies, the sluggish ORR kinetics. To achieve this, a series of M-N-C (M = Fe, Co, Ce, Mn) electrocatalysts was prepared by leveraging the potential of ZIF-8@CNT-derived nitrogen-doped carbon (NC) scaffolds. These specific M-N-C catalysts exhibited excellent structural/electronic features, optimal for governing the adsorption/desorption energetics of key oxygen intermediates and could drive ORR via a desired four-electron pathway. The first part of this thesis implements Fe and FeCo-based M-N-C catalysts for catalysing ORR in both alkaline [I] and neutral environments [II]. The second part then pivoted to examine the specific role of cerium (Ce) incorporation in modulating the electronic structure and inducing morphological alterations within the ZIF-8@CNT-based M-N-C catalysts [III]. The resulting FeCe@N-C electrocatalyst offered distinct structural alterations that refined the electronic properties of the carbon structure, and Ce acted as a free-radical scavenger. The fourth part explores the transformation of iron phthalocyanine (FePc) into Fe-N_x rich Fe-N-C catalyst using a novel *in-situ* nitridation strategy that aligns specific Fe nitride phases (Fe_4N) to regulate the electronic structure of NC framework [IV]. Recognising the structural refinements originating from ZIF-8 structural evolution during pyrolysis, the fifth part of the thesis paid special attention to optimising the ZIF-8 and Mn molar ratio [V]. The dynamic structural evolution of ZIF-derived carbons governed the porosity characteristics, density and spatial distribution of Mn-N_x active sites. Lastly, a unique dual-pyrolysis methodology was utilised to promote ORR electrocatalysis over pre-activated ZIF-8@CNT derived NC scaffolds sequentially anchored with bimetallic metal phthalocyanines (MPc) (FeCo, FeMn, CoMn) [VI]. All the prepared catalysts underwent comprehensive physico-chemical characterisation, which revealed critical information about their evolved structural and tailored electronic features after high-temperature pyrolysis.

Finally, these tailored M-N-C materials were implemented as cathode catalysts in AEMFC [I, V, VI] and MFC [II, III, IV] devices. The AEMFC tests demonstrated excellent voltage stability and power performance. Furthermore, under MFC operating conditions, the enhanced ORR kinetics at the cathode accelerated the bio-oxidation of organic substrates, thereby improving wastewater treatment and energy generation efficiencies. Ultimately, this thesis shows a simple yet versatile methodology for designing highly active and efficient ZIF-8@CNT-based M-N-C cathode catalysts for sustainable next-generation energy conversion devices.

4. LITERATURE OVERVIEW

4.1. Polymer electrolyte fuel cells

Hydrogen fuel cells (HFCs) are electrochemical device that convert chemical energy stored in a fuel (H_2) and an oxidant (O_2) into electrical energy, yielding only heat and water as byproducts [33]. Depending on the type of electrolyte, operating temperatures and application, these are classified into (1) polymer electrolyte fuel cells (PEFCs), (2) alkaline fuel cells [34], (3) solid-oxide fuel cells [35], (4) molten carbonate fuel cells [36] and (5) phosphoric acid fuel cells [37–39]. Amongst these, the PEFCs are considered the most ideal candidate due to their safety, higher energy density, quick start-stop time, low operational temperature (50-100 ^{o}C), and especially the zero carbon footprint [40]. In fact, while high-temperature HFC variants, such as solid oxide or molten carbonate fuel cells, offer superior electrical efficiency in stationary settings, they are fundamentally incompatible with the dynamic needs of the automotive sector [41]. This limitation strongly shifts the research focus towards low-temperature PEFCs [42, 43].

PEFCs are categorised into two distinct branches: (1) PEMFC and (2) AEMFC. In PEMFC, the hydrogen oxidation reaction (HOR) occurs at the anode, liberating H^+ and electrons. The electrons pass through the external circuit, while H^+ traverse the proton-conducting membrane to reach the cathode. At the cathode, during the oxygen reduction reaction (ORR), the electrons and H^+ react with O_2 to produce H_2O, thereby completing the electrical circuit. Conversely, in an AEMFC, the ORR in alkaline media produces OH^- ions that diffuse across anion exchange membrane (AEM) towards anode. There, they react with H_2 to yield H_2O and electrons. Therefore, despite sharing similar physical architecture, these two systems follow distinct electrochemical reactions with opposite ion-conducting pathways. Notably, HOR is highly efficient on Pt-based catalysts, yielding a negligible anodic overpotentials even at low catalyst loadings. This directs the core scientific focus on the cathodic ORR process as a principal kinetic bottleneck in PEFCs. The electroreduction of O_2 proceeds via a sequence of multi-electron elementary steps [44]. Ideally, the complete reduction of O_2 molecule to OH^- ions (alkaline) or H_2O (acidic) requires 4 electrons (e^-), however, there is a competitive $2e^-$ pathway leading to peroxide production. Most importantly, the O_2 double bond (O=O) is very stable and requires a dissociation energy of 494 kJ mol^{-1}, rendering a high energetic barrier for ORR [45, 46]. Therefore, the adsorption/desorption kinetics of oxygen intermediates (*OOH, *O, *OH) dictates the overall kinetics of the ORR process [47, 48].

Under acidic conditions (low pH), like in PEMFCs, the ORR can proceed either via a direct $4e^-$ pathway (1) or via $2e^-$ pathway (2):

$$O_2 + 4H^+ + 4e^- \rightarrow 2H_2O \qquad E_0 = 1.229 \text{ V } vs \text{ SHE} \qquad (1)$$

$$O_2 + 2H^+ + 2e^- \rightarrow H_2O_2 \qquad E_0 = 0.695 \text{ V } vs \text{ SHE} \qquad (2)$$

Reaction (2) can be followed by further electroreduction of hydrogen peroxide (3) or disproportionation reaction (4):

$$H_2O_2 + 2H^+ + 2e^- \rightarrow 2H_2O \qquad E_0 = 1.776 \text{ V } vs \text{ SHE} \qquad (3)$$

$$2H_2O_2 \rightarrow 2H_2O + O_2 \qquad (4)$$

In alkaline conditions (high pH), like in AEMFCs, the ORR can either adopt a direct $4e^-$ pathway (5) or can proceed via a $2e^-$ pathway (6):

$$O_2 + 2H_2O + 4e^- \rightarrow 4OH^- \qquad E_0 = 0.401 \text{ V } vs \text{ SHE} \qquad (5)$$

$$O_2 + H_2O + 2e^- \rightarrow HO_2^- + OH^- \qquad E_0 = -0.065 \text{ V } vs \text{ SHE} \qquad (6)$$

followed by further reduction of hydroperoxide anion (7) or disproportionation reaction (8):

$$HO_2^- + H_2O + 2e^- \rightarrow 3OH^- \qquad E_0 = 0.867 \text{ V } vs \text{ SHE} \qquad (7)$$

$$2HO_2^- \rightarrow 2OH^- + O_2 \qquad (8)$$

where E_0 is the standard potential at 25 °C and SHE stands for standard hydrogen electrode.

While PEMFCs have been extensively studied over recent decades and have achieved undeniable commercial success in the transportation and stationary power sectors, their global adoption remains highly constrained by expensive Pt-based cathode catalysts [49]. Moreover, the US Department of Energy (DOE) has established strict technical targets to reduce total Pt usage to 0.1 g kW^{-1} by 2050 [50]. Because PEMFC operates in a highly acidic environment, where Pt demonstrates superior chemical stability than transition-metal electrocatalysts, the operational and manufacturing costs remain an ultimate barrier. Furthermore, significant progress in the NPMC development has sparked hope to replace Pt-based catalysts [51], with M-N-C catalysts exhibiting exceptional electrocatalytic activity for ORR that occasionally outperforms the commercial carbon-supported Pt catalysts (Pt/C) [52–55]. However, their practical reliability in PEMFCs remains compromised due to poor electrochemical stability under harsh acidic environments [56]. Within this highly corrosive, low-pH environment, M-N-C materials are susceptible to demetallation and carbon support corrosion, leading to structural collapse and increased mass-transfer limitations [57]. In contrast, the AEMFC that operates in alkaline media mitigates such corrosion stress on the internal components and thermodynamically favours the stability of the M-N-C structure [14, 58]. Moreover, AEMFCs utilises a wide range of low-cost NPMC materials, which ultimately lowers the overall PEFC production costs [13, 59].

Unlike PEMFCs, where the acidic environment intensifies the formation of destructive hydroxyl radicals *via* Fenton-type reactions, an alkaline environment mitigates this effect, thereby enhancing catalyst and membrane stability [60]. Notably, under alkaline conditions, the adsorbed OH^- ions create electronic and

steric hindrance to the chemisorption of the O_2 molecule. As a result, O_2 is reduced to superoxide (O_2^-) anion using an outer-sphere electron transfer reaction [61, 62]. This characteristic provides surface flexibility, as no specific site-adsorbate binding geometries are required. Therefore, unlike acidic conditions, a broad range of NPMCs becomes viable, allowing the utilisation of diverse transition metals and carbon-based materials. Apart from catalyst chemistry, the polymer membrane plays a crucial role in governing the transport of OH^-/H^+ ions during PEFC operation [59, 63, 64]. For instance, the polymer electrolyte membrane should exhibit certain essential features, i.e., an optimal thickness (to achieve high ionic conductivity), chemical/thermal stability, low gas permeability, and excellent mechanical strength to mitigate undesired gas crossover or mechanical degradation during PEFC operation [64–66]. Notably, the H^+ intrinsically carry higher diffusivity than OH^-, resulting in a greater ionic conductivity in PEMFC compared to AEMFC [67, 68]. However, traditional PEMs (e.g., Nafion™) are made of perfluorinated compounds, which are classified as per- and polyfluoroalkyl substances (PFAS) [69, 70]. PFAS do not break down easily in the environment [71, 72]. For these reasons, AEMs have gained specific attention due to their lower capital costs and the possibility to use hydrocarbon backbones that do not contain PFAS [73]. Nevertheless, their insufficient chemical durability poses serious drawback in reaching the same level of technological maturity as PEM [74, 75]. A single-cell unit of an H_2-O_2 fed AEMFC consists of a membrane electrode assembly (MEA) sandwiched between conductive bipolar plates with reactant gas flow channels (Figure 1). The anode where HOR ($2H_2 + 4OH^- \rightarrow 4H_2O + 4e^-$) occurs and the cathode where ORR (Eq. 5) occurs is separated by AEM to traverse OH^- ions to the anode. The anode and cathode catalyst layers are deposited onto a porous gas-diffusion layer (GDL), which facilitates the transport of reactants and product water across the catalyst layers (Figure 1). Overall, the following reaction takes place in an AEMFC.

$$2H_2 + O_2 \rightarrow 2H_2O \tag{9}$$

The efficiency of PEFC is dependent on the density and accessibility of triple-phase boundaries (TPBs) [76, 77]. These TPBs, formed at the nexus of gaseous reactant (H_2 or O_2), the electronic conductor (catalyst) and the ion-conducting phase (ionomer), facilitate the necessary electrochemical reactions (HOR or ORR) [77, 78]. Theoretically, the equilibrium cell voltage of 1.229 V (Eq. (1)) should remain constant, but practical operation introduces overpotentials in the activation, ohmic, and mass-transport regions, resulting in voltage loss [79]. This behaviour is characterised by the shape of the polarisation curve, where the initial drop at low current density signifies activation overpotential, which is usually attributed to sluggish ORR kinetics, since HOR, even at minimal catalyst loading, is intrinsically very fast [80]. Following this, the ohmic overpotential dominates at intermediate current densities, stemming from H^+/OH^- transfer resistance [81]. Lastly, at higher current densities, where reaction kinetics are non-limiting, performance is hindered by insufficient reactant concentration at the TPB interface,

resulting in mass-transfer losses [82, 83]. Collectively, these phenomena manifest as the voltage and power performance decrease during PEFC operation. Fabricating the catalyst morphology and pore architecture is one possible way to promote TPBs formation, which ultimately improves the PEFC efficiency. Nevertheless, even after years of research, particularly focused on structurally engineering the catalyst layer to achieve excellent active-site dispersion and porosity, AEMFC faces a major setback in real-life operation [84, 85]. The primary reason is the use of O_2 from ambient air at the cathode, which contains CO_2 and other impurities that collectively compromise the AEMFC performance [86]. Even the trace amounts of CO_2 can react with OH^- to form weak nucleophiles, such as carbonates or bicarbonates, that dilutes the electrolyte concentration and severely impacts the ion-exchange capacity of the AEM. Consequently, this degrades the overall AEMFC performance [87–89].

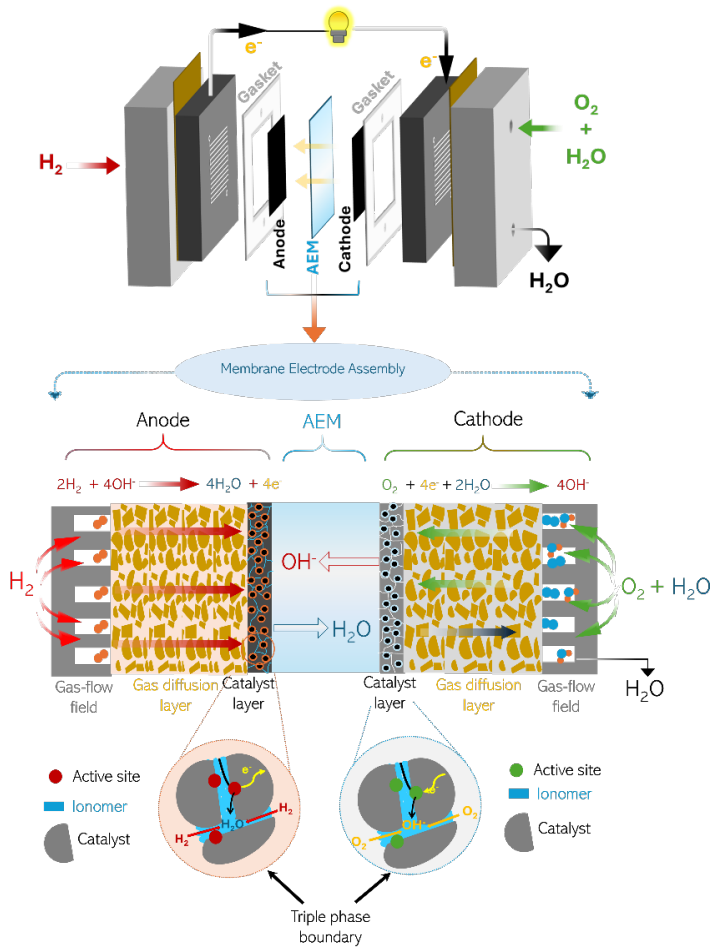

Figure 1. Schematic diagram of a single H_2-O_2 AEMFC cell and zoomed-in membrane electrode assembly structure.

Despite these challenges, the consistent improvements in AEMFC performance complement the systematic scientific progress in AEM fabrication, operational design, and catalyst engineering [90]. The enduring scientific interest in this technology is driven by accelerating breakthroughs in the use of earth-abundant, non-noble-metal catalysts that decouple fuel cell costs from PGMs.

4.2. Microbial fuel cells

Microbial fuel cells (MFC) represent a versatile and rapidly expanding class of bio-electrochemical systems, that works at the intersection of electrochemistry and microbiology (Figure 2) [19, 91, 92]. These bio-catalysed devices carry higher degree of operational complexity compared to other PEFCs due to their delicate biotic-abiotic working interface. Despite this, they have maintained considerable scientific prominence due to their innate environmental benefits and carbon neutrality [15, 18, 93]. Their core conceptual roots for MFC were introduced in 1911 by Prof. Michael Cressé Potter [16]. He provided the first empirical evidence that microorganisms (e.g., E. coli) could break down organic substrates through metabolic pathways and produce electricity, accompanied by a measurable flow of electrons. This paved the way for MFC technology, a device that utilises electrochemically active bacteria (primarily exoelectrogens) to catalyse the oxidation of organic substrates (e.g., acetate) or complex wastewater [93–95]. Acetate as a substrate offers rapid start-up time, high degradability and non-fermentability, making it directly available to exoelectrogens [96–98]. Although, glucose offers a significantly higher electron yield per mole ($24e^-$) compared to acetate ($8e^-$), it undergoes multi-staged complex breakdown. In mixed-culture systems such as wastewater, the fermentative microbes utilise glucose to produce ethanol, lactate or volatile fatty acids. These would consume energy required for biomass synthesis, reducing the Coulombic efficiency (%CE) of the MFC by suppressing electroactive microbial activity [99]. Therefore, acetate is considered a more viable carbon substrate for long-term MFC operation. Furthermore, since anaerobic sludge is commonly used as an inoculum source due to its diverse microbial consortia, acetate plays a pivotal role in selectively enriching the exoelectrogens within the electroactive biofilm. These specific microbial communities, i.e. *Shewanella oneidensis*, *Geobacter sulfurreducens*, can transfer electrons outside their cell membrane to a solid electron acceptor through the extracellular electron transfer (EET) mechanism [100, 101]. In a natural environment, bacteria can use oxygen, nitrate, or sulphate as electron sinks or terminal electron acceptors for respiration [102]. While in an MFC, these bacteria are forced to use the solid electrode (anode) as their only available electron sink [103–105]. These microorganisms adhere to the anode surface, forming an electroactive biofilm (EAB) that promotes EET via direct or mediated electron transfer (Figure 2) [104]. The produced electrons then circulate through an external circuit while H^+ traverse PEM to reach the cathode, where they reduce target species, i.e., O_2, H^+, or metals (M^{n+}) [105]. The O_2 is the preferred terminal

electron acceptor due to its ubiquitous, cost-free availability and high theoretical redox potential [91, 106].

However, the ORR kinetics at neutral pH are extremely sluggish and are widely regarded as the primary bottleneck of MFCs [107, 108]. Unlike acidic and alkaline media, significantly reduced H^+ activity at neutral pH hinders O_2 adsorption and the stabilisation of oxygen intermediates via a proton-coupled electron transfer (PCET) mechanism. Mechanistically, because the bulk concentration of H^+ reaching the cathode is low (10^{-7} M), the cathode-electrolyte interface becomes H^+ depleted zone as operational time increases [109, 110]. However, the situation worsens due to the slow rate of H^+ migration across the membrane, and thus, H_2O serves as the primary H^+ source to complete the ORR process [111, 112]. This alternative pathway increases the energy activation barrier, and as a result, the ORR predominantly proceeds via less efficient $2e^-$ pathway, in which H_2O_2 is the final product rather than H_2O [108]. Moreover, despite a dual-chamber setup, the slower cathode electron consumption rate can reduce the rate of organic substrate consumption and adenosine triphosphate production at the anode, thereby degrading the quality of EAB and deteriorating MFC performance [113, 114]. This situation becomes more severe in a single-chamber MFC setup, where direct contact between the EAB and the cathode critically impedes the ORR [115].

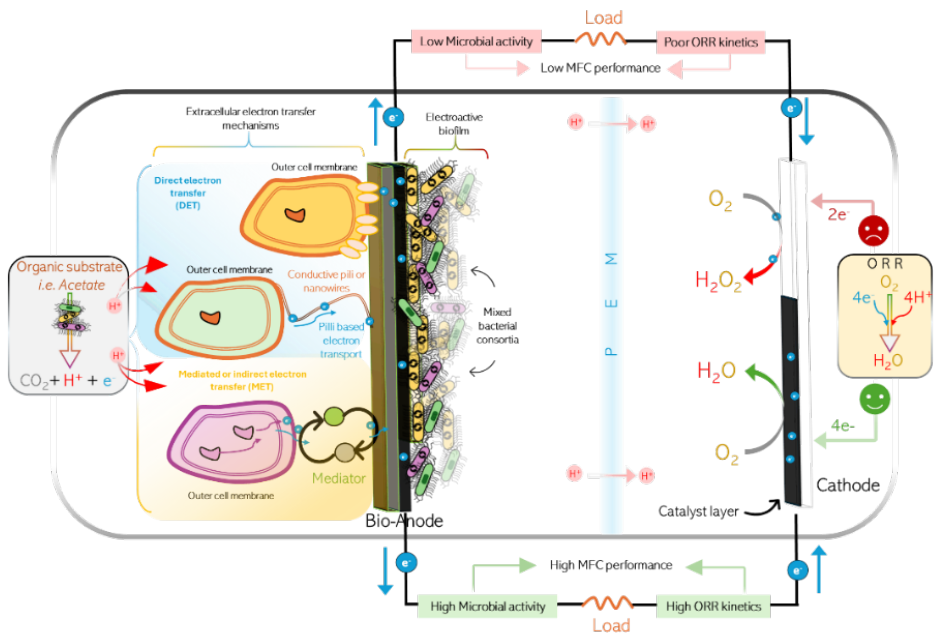

Figure 2. Sketch of a typical dual-chamber MFC device representing the anode chamber (left) where microbes catalyse the degradation of acetate, the cathode (right) where O_2 acts as a terminal electron acceptor and the proton exchange membrane (middle) separating these two compartments. The anode compartment highlights the key electron transfer mechanisms of exoelectrogens.

Therefore, cathode kinetics play a dual role: determining the electrical power output and the biological health of the system. Therefore, a catalyst is often needed to catalyse the ORR via a dominant $4e^-$ pathway [114, 116]. The Pt-based catalysts remain the primary, albeit costly, benchmark constraining the scalability of MFC technology [117]. Alternatively, M-N-C materials possess remarkable potential to replace these expensive Pt-based catalysts [30, 92, 118]. For instance, single-atom (SA) Fe-N-C materials often exhibit impressive electrocatalytic activity but are simultaneously vulnerable to Fenton-type reactions during long-term MFC operations [119, 120]. Recently, bimetallic catalysts, i.e., FeCo-N-C or FeMn-N-C, have attracted increased attention due to their intrinsic dual-metal synergy and greater ability to tune the electronic structure of the carbon substrate [121]. Furthermore, coupling dual-metals alleviates the Fenton reaction and allows the catalyst to follow a predominant $4e^-$ ORR pathway. However, these dual-metal catalysts can still generate a considerable amount of undesired reactive oxygen species (ROS). This oxidative challenge is more pronounced in single-chamber MFC, where ROS (e.g., $^{\bullet}OH$) can migrate towards the anode due to the absence of PEM, unlike in dual-chamber MFC [113, 122]. Once ROS reach the anode surface, they can irreversibly disrupt the EET pathways, compromising the overall EAB functionality [123, 124]. In this context, cerium (Ce)-containing M-N-C catalysts have shown great success, as Ce can act as a free radical (i.e., ROS) scavenger [125, 126]. Nevertheless, ensuring the stability of these materials, especially in neutral solution, remains a critical challenge in long-term MFC operations. Consequently, the success of MFC technology as a viable green energy solution depends on the development of M-N-C cathode catalysts that can offer both the kinetic efficiency of Pt and the required long-term durability [108]. Besides the kinetics of these processes, the system-level performance is also governed by cell architecture (e.g., H-shaped or tubular), inter-electrode distance, substrate concentration, electrode surface area-to-anode volume ratio and PEM biofouling [27, 127, 128]. Therefore, the longevity of these devices requires a thorough examination of these collective technical parameters, along with the implementation of novel M-N-C architecture cathode catalysts.

4.3. Non-precious metal catalysts for ORR

4.3.1. Transition metal derivative-based catalysts

As discussed in previous sections, the ORR plays a central and proficient role in electrochemical energy conversion devices, i.e. AEMFCs and MFCs. Its kinetics not only determine the peak power output but also dictate the long-term operational stability of these devices. In the context of MFCs, a slower cathode acts as a bottleneck for microbial activity at the anode, collectively hindering the MFC from achieving sufficient wastewater treatment efficiency and power output. Furthermore, the heavy reliance on expensive Pt-based catalysts impedes their widespread adoption. In this regard, NPMC materials, such as transition metal-

based oxides, sulphides, chalcogenides, phosphides, carbides, and M-N-C type catalysts, are widely studied and have emerged as the most promising contenders to Pt and other PGM catalysts [52, 53].

Transition metal oxides (TMOs) are low-cost, easy-to-synthesise materials, and have thus captured the spotlight for ORR electrocatalysis [129, 130]. Mostly, TMOs are semiconductors with a wide bandgap (E_g) ranging from 2 to 4 eV [131]. For example, Fe_2O_3 has an E_g of nearly 2.1 eV, whereas the pure metal has an E_g of 0 eV [132]. Therefore, their poor electrical conductivity serves as the primary barrier for high ORR activity [130]. One effective approach to resolve such concerns is to utilise a highly conductive carbon material, such as graphene, carbon nanotubes or to introduce surface defects into these materials. Particularly, introducing oxygen vacancies can finely tune their intrinsic conductivity and energy band structure. For instance, the ORR activity of MnO_2 was enhanced by introducing oxygen defects using a simple heat-treatment [133]. Following this heat treatment, oxygen-vacant β-MnO_2 showed a positive shift in the half-wave potential ($E_{1/2}$) for ORR. Later, in a study by Zhang et al., Mn-defects were created to engineer the electronic structure of Mn_3O_4 synthesised via thermal oxidation of manganese glycerate [134]. This enhanced electrical conductivity and facilitated the adsorption-desorption energetics of oxygen intermediates. Subsequently, several attempts were made to tune the crystal structure of these TMOs, particularly by varying the exposed facets, which yielded subtle improvements in the ORR activity [135]. Another effective strategy is to replace oxygen with a less electronegative element i.e., carbon (C), phosphorus (P) or sulphur (S), which profoundly increasing the covalent bonding character and conductivity of these materials [136]. This effectively reduces the wide-bandgap resistance from which TMOs suffer. Therefore, the shift towards transition metal carbides (TMCs), phosphides (TMPs), and sulphides (TMSs) has proven to be an effective strategy to overcome the shortcomings of oxide-based lattices. The incorporation of C atoms modifies the mechanical strength and electronic conductivity of transition metals. Moreover, the tensile strain induced by C increases the M-M distance, which modifies their *d*-band centre and facilitates the adsorption of O_2 molecules [137]. Meanwhile, TMPs and TMSs utilise a strong ligand effect to modify the d-band centre of the metal sites. The TMSs (i.e. FeS_2, Co_9S_8) represent a novel class of catalysts, where the interactions between metal and sulphur offer enhanced charge-transfer kinetics compared to oxides [138, 139]. However, these materials face a substantial decline in the electrocatalytic performance under extended operational timeframe in both neutral and alkaline electrolytes. In fact, these materials are thermodynamically prone to surface oxidation, possess low electrochemically active surface area and poor conductivity, which makes them unsuitable for practical fuel cell applications.

4.3.2. Transition metal-nitrogen-carbon (M-N-C) catalysts

To circumvent the stability and active site density paradoxes in bulk transition-metal derivatives, research has culminated in the development of transition-

metal- and heteroatom (i.e., N, S, P)- doped carbon (M-N/P/S-C) catalysts [52, 53]. In particular, the fascination with M-N-C material stems from their unique ability to interlink the chemical properties of carbon, which serves as the structural host, nitrogen, which alters the electronic environment and the transition metal (M) that offers additional bonding flexibilities to effectively facilitate the cleavage of O=O bond [54, 55, 140, 141]. While other heteroatoms, such as S and P, are concurrently used as potential dopants, N remained the most preferred choice [142, 143]. This is primarily due to the similar atomic radii of N (~75 pm) and C (~77 pm), which allow their isomorphous substitution with minimal steric strain [144]. Secondly, N has a higher electronegativity than S or P, making it an ideal dopant to induce a charge imbalance and electron deficiency across the C atoms, thereby promoting O_2 chemisorption [144]. Therefore, this specific class of material has witnessed a paradigm shift towards atomic-scale engineered architecture, in which discrete, isolated metal atoms (e.g., Fe, Co, Mn, Cu, Zn) are coordinated and stabilised within the N-doped carbon matrix. These atomically dispersed moieties ensure high active-site utilisation efficiency, offering remarkable ORR activity and electrochemical stability. Their history can be traced back to 1964, when Jasinski outlined MPc as the first M-N_4 macrocycle-based ORR electrocatalyst [145]. The square-planar M-N_4 coordination geometry of MPc served as the primary active site for ORR. Apparently, the low electrical conductivity and poor stability of MPc remained a big challenge. Over the years, advancements based on the synthetic strategy and precursor choice were made to enhance the electrocatalytic activity of these NPMC [146].

Currently, high-temperature pyrolysis is used for obtaining these materials [147]. It involves the conventional doping method, where a carbon source, nitrogen source, and transition metal salt are mixed in a liquid phase (i.e., dissolved in a solvent) or solid phase (i.e. ball-milling or grinding) and then subjected to pyrolysis at 600-1000 °C under an inert (e.g., N_2) atmosphere [147]. At these elevated temperatures, the precursors undergo a series of thermochemical transformations, that includes dehydration, cross-linking/condensation and carbonisation [148]. Eventually, this structural reorganisation impregnates the carbon host with metal and nitrogen dopants, yielding a M-N-C coordination architecture. The impressive ORR performance of these materials is rooted in the nitrogen functionalities of pyridinic-N, pyrrolic-N, graphitic-N and metal-coordinated nitrogen (M-N_x; x = 1-4) sites formed during pyrolysis as portrayed in Figure 3 [54, 141, 149].

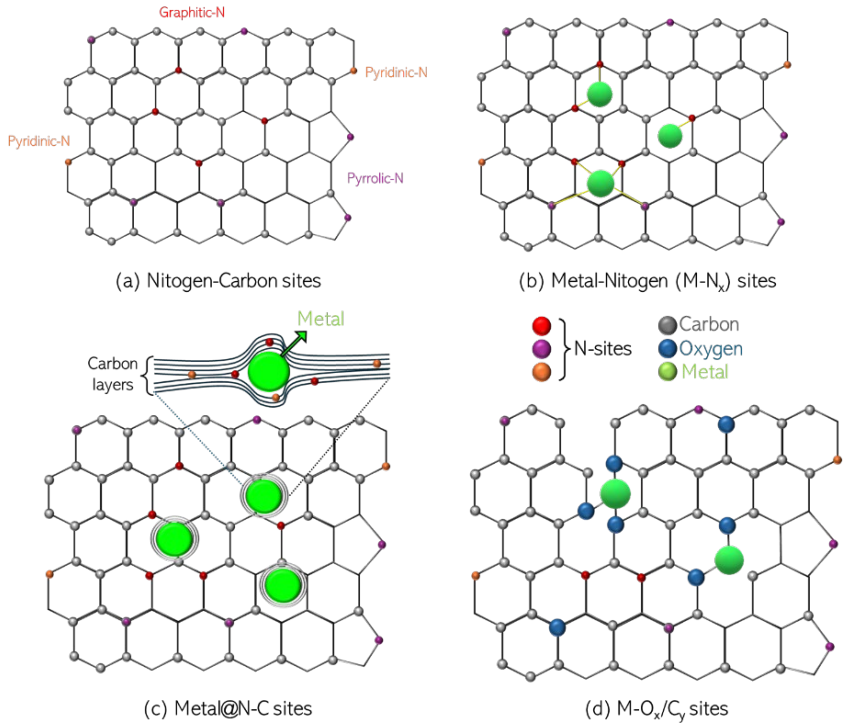

Figure 3. Types of active sites in M-N-C catalysts for the oxygen reduction reaction.

The pyridinic-N resides at the edges or vacancy defects of the graphitic carbon lattice (Figure 3a). The higher electronegativity of N induces a strong inductive effect, withdrawing σ-electron density from the adjacent C atom, making it an electron-deficient Lewis acid site [142, 150, 151]. This charge redistribution favours the chemisorption of the O_2 molecules in an end-on or side-on orientation. Following adsorption, the non-bonding lone electron pair of pyridinic-N acts as a Lewis base that polarises the adjacent water molecules and facilitates the initial PCET to π*-antibonding orbital of O_2. This electron transfer destabilises the O_2 molecule, driving its reduction to *OOH intermediate, which subsequently cleaves the O=O bond [152]. Conversely, the pyrrolic-N occupies one of the C in a five-membered ring and disrupts the hexagonal carbon symmetry [153]. The localised π-electron density develops a partial positive charge on its neighbouring C atom and favours initial O_2 adsorption. Lastly, the graphitic-N is formed by isomorphous substitution of C within the basal plane of the hexagonal lattice [154]. It donates one electron to the π*-conduction band of the carbon lattice, thereby promoting the ORR process. Several scientific investigations claim pyridinic-N to be the main driver of the ORR process, while others pinpoint pyrrolic-N and graphitic-N, leaving the definitive hierarchy of these sites a subject of ongoing debate. Notably, the transition metal within the M-N_x moiety offers superior bonding due to a direct engagement of the metal's d-orbitals and

π*-antibonding orbital of O_2 molecules [155]. Their interaction facilitates the efficient cleavage of O=O bond, promoting a predominant $4e^-$ ORR pathway. Consequently, these atomically dispersed M-N_x moieties are widely recognised as the primary driver of the ORR kinetics [154, 156]. However, the catalytic efficiency of these sites is strictly governed by the metal's valence-shell electrons and its nitrogen-coordination environment, which ultimately dictate interactions with the key oxygen intermediates. For instance, in a square-planar geometry of Fe-N_4, the O_2 molecules approach the Fe centre preferably in an axial, end-on position (Pauling-type), first establishing the coordination between the 5σ-bonding orbital of O_2 and d_{z^2} orbital of Fe [157]. According to Xie et al. [157], the efficiency of this step is dependent on the spin-coupling orientation between Fe and O_2. It was found that the parallel spin-orientation state first proceeds *via* inter d-d ($d_{xz} \rightarrow d_{z^2}$) transition, succeeded by d→2π* electron transfer process. In contrast, the antiparallel spin state undergoes a hybridisation mechanism and does not require the intermediate d-d transition step. This collectively triggers the elongation and cleaving of O=O bond. In the second pivotal step, the optimal adsorption strength of the Fe centre effectively stabilises the $^*OOH$ intermediate, alleviating the energetics of its subsequent reduction to O^* and $^*OH$ products. Also, other transition metals (e.g., Mn, Co) have shown promising ORR activity and are thus becoming popular alongside Fe [158].

Despite Fe-N_4 superior kinetics, its vulnerability to Fenton reaction and propensity to one-electron redox cycle increases the risk of ROS generation [159, 160]. Certainly, this situation is less pronounced in alkaline conditions than in neutral pH environment of MFC, where continuous supply of H^+ might exacerbate this phenomenon. In this regard, Mn with $3d^5 4s^2$ electronic configuration exhibits several advantages that include its abundance in earth's crust, suppressed Fenton reactivity, enhanced electrocatalytic stability and dynamic redox activity shift between multiple oxidation states from +2 to +6 [158]. Evidently, the density functional theory (DFT) calculations have verified that Mn-N_4 coordinating sites exert favourable adsorption free-energy for $^{\cdot}OH$ intermediate, compared to Fe-N_4, where the it acts as the rate-determining step [161]. Because Mn-N_4 sites naturally exists in a high spin-state ($t_{2g}^3\ e_g^2$) configuration, it readily aligns with the triplet high-spin ground state of O_2, lowering the spin-state barrier for initial activation. This crucially balances the adsorption kinetics of oxygen intermediates, leading to a $4e^-$ ORR pathway [161]. Conversely, due to Mn^{2+} half-filled d-orbital, Mn-N_4 tends to form a stable bond with the O-intermediates, compensating turnover frequency (TOF) and intrinsic reaction kinetics compared to Fe-N_4 sites. This scenario is more prominent with Co-N_4 sites, because Co^{2+} with $3d^7 4s^2$ electronic configuration results in sub-optimal binding strengths for oxygen species [162]. In particular, the d_{z^2} orbital that extends perpendicular to Co-N_4 plane is partially or fully occupied depending on its spin state (high/low). When O_2 molecule approaches, its lone pair experiences a strong electronic repulsion from filled d_{z^2} orbital of Co^{2+}, preventing the strong interaction [163]. This presents a kinetic hurdle to activate and break the O=O bond. Consequently, Co-N_4 sites at the edges of the graphitic carbon

host predominantly perform $2e^-$ ORR [164, 165]. However, when these sites are located within the basal plane of carbon substrate, they thermodynamically promote a $4e^-$ ORR pathway [164].

These M-N-C catalysts (M: Fe, Co, Mn) undoubtedly possess high intrinsic activity; however, the spatial distribution of the inherent active sites, as isolated centres, dictates an associative pathway for O_2 electroreduction [166, 167]. Recently, dual-atom catalysts (DACs) have emerged as a remarkable avenue, in which the two adjacent metal sites cooperatively alter the local electronic structure and provide geometric flexibility to decouple the binding energies of oxygen species [168]. Crucially, these dual-atom sites allow the side-on or bridge (Yeager-type) adsorption of O_2 molecules. This specific orientation enables a dissociative ORR pathway, where the O=O bond might get cleaved immediately upon adsorption [169]. For example, Park et al. used advanced in situ adsorption spectroscopy and DFT techniques to understand the adsorption energetics of oxygen intermediates on atomically engineered FeCo-based DAC [170]. They revealed that Fe-N_4 SA sites possess significantly stronger binding affinity to *OH intermediate (ΔG_{*OH} = -0.57 eV) compared to FeCo dual-atom sites (ΔG_{*OH} = -0.03 eV), which modulated this energy to a near-ideal value. This synergy shifted the d-band centre and reduced the population of antibonding states, effectively lowering the dissociation barrier of the $^\cdot$OOH radical. By facilitating direct O=O bond scission *via* a dissociative mechanism, the FeCo DAC exhibited higher TOF (0.055 s^{-1} at 0.85 V) than its single-site analogue (0.024 s^{-1} at 0.85 V) and favoured $4e^-$ reduction. Collectively, the theoretical and experimental findings demonstrate that incorporating Co mitigated the linear-scaling constraints inherent to single-atom catalysts. This perfectly aligns with the findings of Tang et al., who reported that the oxygen-bridged FeCo-N_6-O configuration provided complementary evidence for d-band centre modulation and enhanced charge polarisation [171]. To investigate the effect of Mn sites, Wang et al. prepared an atomically dispersed FeMn-N-C catalyst using 1,10-phenanthroline as both a metal complexing agent and an N source [172]. The resulting FeMn dual-atom sites fine-tuned the binding energies of *OOH/*OH intermediates, thus accelerating the reaction kinetics. Furthermore, the FeMn/NC catalyst showed an impressive $E_{1/2}$ of 0.94 V, outperforming Fe/NC and Mn/NC catalysts by 0.03 and 0.08 V, respectively. Encouraged by these findings, other DAC combinations have been widely explored to broaden the scope and electrocatalytic competency of bimetallic M-N-C materials towards ORR electrocatalysis [168, 173].

Traditionally, increasing the precursor metal concentration was viewed as the most direct route to address the low active-site density problem in M-N-C catalysts. However, at the high pyrolysis temperatures, the metallic species frequently interact with the evolving carbon matrix, inevitably forming stable metal carbides (e.g., Fe_3C) or aggregates of metal nanoparticles [174]. At high temperatures, carbon atoms can diffuse into these metal clusters, which, upon supersaturation, form a protective graphitic carbon layer around them, i.e., core-shell metal@NC sites (Figure 3). Although these sites are typically regarded as catalytically inert, they can function as electronic promoters when located in the vicinity of M-N_x

moieties. By modulating the d-band centre of metal in the M-N_x site, it can optimise the binding energies of reaction intermediates and boost ORR kinetics [54, 175]. However, these metal@NC sites can become detrimental if the carbon layer is poorly graphitised or too thin to allow demetallation under long-term operation [174, 176]. Thus, the current research is aimed at obtaining M-N-C catalysts with accessible high-density of active sites.

In M-N-C catalyst, the nature and type of N-site play a pivotal role, especially in the formation of M-N_x active centres with specific geometries that govern the adsorption and reduction of O_2 molecules. Therefore, a suitable N-precursor is of paramount importance for yielding a high density of preferred active sites (e.g., M-N_x) [55, 175]. Ideally, a nitrogen precursor should have certain key features such as high nitrogen content, high chelating affinity, strong coordination ability by utilising its lone-pair electrons to establish stable coordination bonds and optimal thermal stability [151]. For example, Chen et al. conducted a comprehensive study to identify the catalytic competency of Co-N_4 sites derived from pyrrolic-N and pyridinic-N centres [165]. Their results demonstrated a striking bifurcation in pathway selectivity, with pyrrole-type Co-N_4 sites showing a 5-fold higher H_2O_2 production rate than pyridinic-type Co-N_4 sites. This divergent electrocatalytic behaviour was solely dedicated to the choice of N-precursor (4-dimethylaminopyridine or 2-methylimidazole) deployed to obtain the M-N-C materials. While M-N_4 is the most viable configuration, the use of distinct N-precursors can facilitate the formation of unsaturated (e.g., x = 2, 3) or oversaturated (e.g., x = 5) M-N_x sites, which are all active for ORR.

Typically, small molecules such as urea, melamine and dicyandiamide (DCDA) are common N-precursors due to their low cost and high nitrogen content. These qualities make them an ideal precursor for the design of nitrogen-rich carbon frameworks; however, the pyrolysis temperature dictates their final nitrogen configuration and electrocatalytic efficiency [177]. For instance, at >500 ^{o}C urea transforms to graphitic carbon nitride (g-C_3N_4) [178], while melamine and DCDA yield volatile gases (e.g., NH_3, HCN) before the formation of graphitic carbon lattice [177]. This decomposition results in a significant loss of nitrogen content and structural integrity. Moreover, these precursors lack spatial confinement effects and at elevated temperatures the formation of metal nanoparticles can occur. In this regard, 1,10-phenanthroline offers a superior chelation effect and a high degree of graphitisation upon pyrolysis providing a three-dimensional bidentate ligand to immobilise metal ions [179, 180]. This structural arrangement can kinetically suppress metal migration at high temperature and yields a high density of M-N_4 sites. However, 1,10-phenanthroline tends to form stacked graphitic carbon layers upon pyrolysis, which compromise the surface area and mass-transfer processes [179]. Therefore, the need for N-precursors that combine pre-organised coordination geometry with rigid porosity characteristics has established metal-organic frameworks (MOFs) and metallo-macrocycles as suitable templates for designing high-performance M-N-C catalysts.

4.3.3. Role of carbon structure in M-N-C catalysts

Carbon constitutes the majority of the material by atomic percentage, providing the essential foundation for electrical conductivity, mechanical strength and the porous hierarchy of the overall M-N-C material. Nitrogen precursors such as urea, melamine, DCDA or 1,10-phenanthroline can serve as a primary carbon source, but at elevated temperatures, the release of gaseous fragments results in a significant loss of carbon yield [179, 181]. Therefore, integrating a secondary carbon source, such as carbon nanotubes (CNTs), carbon black (e.g., Vulcan®), graphene, or conductive polymers, is essential to achieve structural robustness and electrical conductivity. Among them, CNTs have attracted attention due to their unique structural properties, which are absent in other carbon allotropes [177, 182]. For example, Vulcan® is characterised by amorphous quasi-spherical particles with high structural disorder, which could increase the ohmic resistance and limit electron conduction [183, 184]. On the other hand, graphene with a planar sp^2 carbon in a hexagonal lattice structure exhibits excellent electrical conductivity [185]. The N-doped graphene consists of edge/basal planes to anchor metal to form M-N_x sites for ORR. However, their performance is severely hampered by π-π restacking, leading to a bundled, stacked sheet morphology that can hinder access to the active sites [185]. In contrast, CNTs provide a 1D wire-like geometry that presents some advantages over Vulcan® and graphene [186], e.g., the curved and cylindrical surface of CNTs prevents restacking, and the nanotubular sp^2 structure offers long-range electron transport channel reducing ohmic resistance problems. Furthermore, multiwalled carbon nanotubes (MWCNTs) exhibit extraordinary mechanical strength and electrochemical durability due to multiple interlinked nanotubes [187]. However, pristine CNTs do not favour O_2 chemisorption due to their symmetrical charge distribution, and doping with heteroatoms and transition metals is needed to provide CNTs with active sites for ORR [186]. Therefore, CNTs emerged as suitable support material to design a M-N-C catalysts with high active site density, high porosity and electrochemical stability [177].

During high-temperature pyrolysis, the complex structural rearrangements coupled with volatilisation of gaseous compounds generate a dense network of pores i.e. micropores (<2 nm), mesopores (2–50 nm), macropores (>50 nm) or a combination of them (hierarchical), which governs the diffusion of reactants to the active sites within this porous network [178, 180]. The micropores play a key role in increasing specific surface area, enabling a high density of exposed active sites [188]. In particular, the atomically dispersed M-N_x moieties within these micropores and their accessibility affects catalytic activity. However, excessive microporosity can hinder O_2 accessibility and electrocatalytic performance [180, 188]. To address this, meso- and macropores are necessary to accelerate reactant diffusion and product removal, resulting in hierarchical pore network providing the optimal diffusion of O_2 to the active sites [140].

In contrast, under fuel cell conditions, these pores must facilitate the formation of TPBs where the electrochemical reactions occur [76]. As illustrated in Figure 4, the carbon nanostructure strictly governs the mass transport of reactants to the active sites (N-C, M-N_x). The macropores provide pathways for gaseous reactants to diffuse across the GDL and reach the catalyst layer. The mesopores facilitate the travel of O_2 and H^+/OH^- within the catalyst layer through ionomer-filled voids [189]. Several studies have highlighted the importance of hierarchical porosity, in which a balance in pore architecture enhances mass transfer [140, 180, 190].

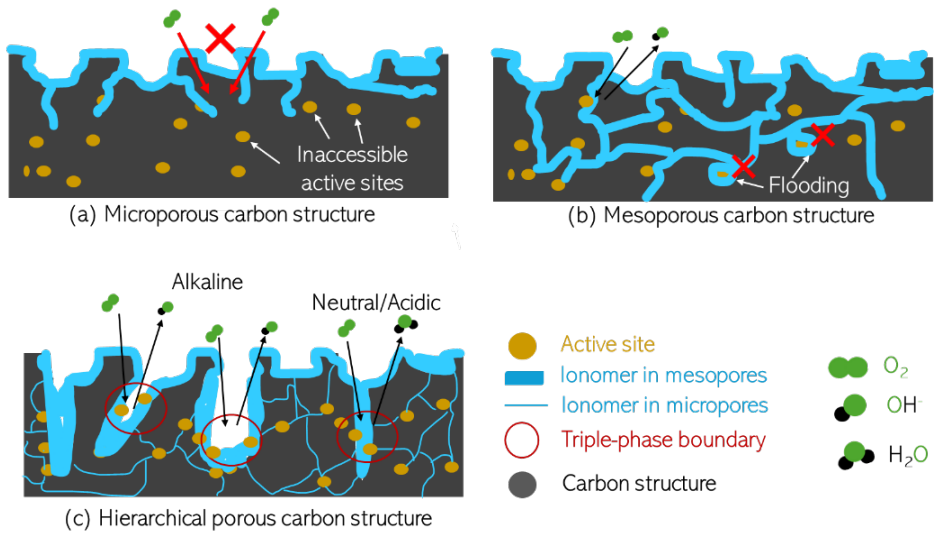

Figure 4. Schematic illustration of active-sites reachability by O_2 molecules in microporous, mesoporous, and a hierarchical porous carbon structure.

This hierarchical arrangement effectively expands the uniform distribution of TPB throughout the catalyst layer, thereby minimising overpotentials during fuel cell operation. Therefore, the ideal carbon material should offer a high specific surface area and hierarchical porosity [54, 189]. While chemical activation is the most effective strategy, resulting in a high specific surface area, the carbon structure primarily consists of micropores, which undoubtedly boost electrocatalytic performance but fail to deliver high energy efficiency in fuel cells [191]. Notably, the templating method provides a sophisticated approach to engineer hierarchical carbon architectures and they are categorised into two groups: soft templating (self-assembly) and hard templating (nanocasting) [192]. The soft templates, i.e., amphiphilic surfactants (CTAB, SDS, etc.) and block copolymers (Pluronic F127, P123, etc.), through direct polymerisation of carbon precursors, provide carbon materials with a controlled porosity [193, 194]. However, they vaporise during high-temperature pyrolysis, making them non-reusable. In contrast, hard templates utilise inorganic scaffolds, such as silica nanoparticles, due to their high thermal stability and robust skeletons that prevent the collapse of the carbon

structure during pyrolysis. Moreover, these templates must be leached out using harmful concentrated acids (e.g., HF), which represents their main limitation due to the environmental impact [195].

Inorganic nanoparticles, such as MgO or ZnO, have attracted significant scientific attention as templates due to their easy removal using mild acids, such as HCl [196, 197]. Nevertheless, the extensive use of hard templates and the tedious removal processes constitute a major shortcoming that can compromise the quality of the resultant carbon [198, 199]. As another alternative, the ionothermal synthesis has emerged as a sustainable methodology to bypass the inherent structural instability associated with soft templates, but this method is expensive and offers limited recyclability [200]. Therefore, these challenges must overcome to design an efficient carbon structure with a balanced porosity and better active-sites anchoring efficiency. In this context, MOFs are classified as an emerging class of hybrid materials with highly ordered, three-dimensional cage-like structures that exhibit high surface area and porous properties. These were first discovered by Prof. Omar M. Yaghi in 1995, and later, their different categories were reported, including MIL-n, ZIF-n, and conductive MOFs (c-MOF) [201].

4.4. ZIF-8 and M-N_4 macrocycles-based M-N-C catalysts

Zeolitic imidazolate frameworks (ZIFs) have emerged as a promising subclass of MOFs, combining the isomorphic zeolite topologies with the coordinative properties of MOFs. They are fabricated by the self-assembly of tetrahedrally coordinated transition-metal ions with organic linkers [202]. In 2006, for the first time, Prof. Omar M. Yaghi synthesised and reported 12 distinct ZIFs prepared by copolymerizing Zn^{2+} and Co^{2+} with imidazole-type linkers [203]. The authors discovered that among the prepared ZIFs, ZIF-8 exhibited exceptional thermal stability and the highest specific surface area of 1947 m^2 g^{-1}. Also, ZIF-8 can adopt various morphologies, such as rhombic dodecahedra and nanoplates [204]. Each unit of rhombic dodecahedral ZIF-8 exhibits a sodalite topology with a large central pore (diameter = 11.6 Å), six-membered ring apertures of 3.4 Å, and six additional four-membered ring apertures with a diameter of 0.8 Å [205]. With its unique structural integrity, ZIF-8 is widely used for catalyst backbone fabrication in different electrocatalysis applications as ZIF-8 can act as both carbon and nitrogen source simultaneously.

During pyrolysis, the imidazole ligands undergo thermal breakdown, releasing sp^2- and sp^3-bonded and N-doped carbon materials accompanied by evaporation of Zn. Moreover, the formation of key N-species, such as pyridinic-N, pyrrolic-N and graphitic-N, provides active centres for efficient ORR electrocatalysis. Therefore, owing to the high surface area and electrical conductivity of pyrolysed ZIF-8, it has garnered special scientific importance for energy-related applications, e.g., PEFCs [206]. In 2019, Xue and colleagues demonstrated its application as an ORR catalyst in a single-chamber MFC device [207]. Over the years, various strategies have been explored to utilise ZIF-8 in the design of M-N-C

materials: (i) using as a precursor and nitrogen source, (ii) one-pot mixing or in-situ doping, (iii) physical mixing or ball-milling, (iv) the host-guest impregnation of metal ions into a pre-formed ZIF-8 framework [208]. In-situ doping is commonly used but often results in poor crystallinity and a low active site density. Moreover, simultaneous mixing of transition metal salts, a zinc source, and imidazole ligands can result in distorted crystal shapes, reduced pore volumes, or even the formation of non-ZIF phases [202, 203]. Therefore, single-step carbonisation of pre-formed ZIF-8 with metal precursor salts has emerged as an easy and reproducible synthetic approach for designing M-N-C materials with high M-N_x site density and long-term durability. The well-defined pores of ZIF-8 enable efficient impregnation of transition-metal ions via structural confinement. Furthermore, during pyrolysis, carbon structures and active sites form concurrently, thereby mitigating the aggregation of metal species and yielding a high concentration of M-N_x active sites. Transition metals such as Fe, Co, and Mn are typically used to impregnate the evolving ZIF-8 structure, yielding monometallic and bimetallic M-N-C architectures. However, the temperature-dependent Zn stabilization plays a crucial role in the resulting density and accessibility of the active sites. In a study by Wang et al., it was revealed that the ZIF-8 parent geometry remains intact up to 500 °C, and above 800 °C, Zn^{2+} converts to Zn^0 and leaves the carbon matrix [209]. Intriguingly, on reaching 900 °C, the Zn-N_4 sites shift towards a square planar geometry, which establishes strong interactions between the Zn's d-orbital and basal carbon plane. These interactions thermally stabilise the Zn within the evolving C framework and restrict its complete elimination. In fact, in the presence of transition metals, Zn elimination is rapid due to the isovalent nature of the metal ions can substitute the Zn sites and form an M-N_x coordination. This cation-substitution mechanism has demonstrated that ZIF-8 can serve as a sacrificial template during pyrolysis. However, performing pyrolysis below 900 °C can result in a poorly graphitised carbon framework with a higher proportion of Zn-N_x sites, whereas over 900 °C the carbon structure is highly graphitised and the significant loss of N and C content leads to a drastic reduction in active site density [209]. These residual Zn-N_x sites can be also considered ORR-active as computational studies have shown that hybridization of $3d_{z^2}$ and 4s orbitals in Zn^{2+} generates new antibonding orbitals, facilitating their interactions with the oxygen intermediates and favours O_2 adsorption [210]. Although the ORR on the Zn-N_x sites is selectively catalysed via a $2e^-$ pathway, which can downshift ORR activity from the $4e^-$ pathway [211, 212]. The acid treatment is considered a potential solution for dissolving these Zn-N_x sites and thus improving the catalyst's electrocatalytic activity towards the $4e^-$ pathway.

MPc have gained significant popularity for the design of M-N-C-architected materials as the well-coordinated M-N_4 sites within the MPc serve as the active centre for ORR electrocatalysis [145, 213–216]. It is worth noting that the central metal plays a crucial role in determining the electrocatalytic properties of the molecules. Apparently, FePc exhibits the highest ORR activity among CoPc and MnPc due to its perfect d-orbital symmetry with O_2 molecule [177, 217]. However, the pristine planar molecular structure of MPc is not conducive to initial O_2

adsorption due to the symmetrical charge distribution around the M-N_4 centre. Therefore, high-temperature pyrolysis was considered a suitable approach to alter the intrinsic electronic properties of these MPc [218–221]. Despite this, their electrocatalytic activity is fundamentally limited by low electrical conductivity and specific surface area. While the addition of CNTs offers a pathway to improve electrical conductivity, it fails to achieve high active site density and atomic dispersion of metal sites. Furthermore, the metal agglomeration at high temperatures exaggerates this issue [222, 223]. The integration of ZIF-8 and MPc presents an interesting platform, where the 3D cage morphology of ZIF-8 facilitates the confinement of MPc molecules, and the progressive Zn volatilisation provides a high specific surface area [224]. This hybrid structure offers high active site density, mitigates metal agglomeration, and, with hierarchical porosity, delivers remarkable ORR activity in both neutral and alkaline environments. This makes the integrated MPc/ZIF-8 catalysts very attractive for fuel cells. Nevertheless, the relative loading of metal precursor and ZIF-8 ultimately determine the final catalyst's structure, directly governing the density and accessibility of active sites [225]. Excessive ZIF-8 loading may lead to mass-transfer issues due to excessive Zn retention and a dense carbon framework [205, 209]. Conversely, insufficient ZIF-8 content can accelerate metal agglomeration due to inadequate nitrogen content. Therefore, a balance between these should be established to achieve a well-defined nanostructure of the M-N-C material. Moreover, without a suitable carbon source, ZIF-8 can self-agglomerate; thus, incorporating MWCNTs resolves this by providing a carbon support that enhances long-range electrical conductivity and mass transfer.

5. AIMS OF THE STUDY

The objective of this PhD thesis was to design non-precious transition metal-based M-N-C catalysts using ZIF-8 and MPc. Specific emphasis was placed on tailoring their electronic/textural features, that facilitates charge-mass transfer processes and accelerates the underlying reaction kinetics. This was achieved by systematically impregnating different transition metals (Fe, Co, Mn) and a rare-earth metal (Ce) to establish a correlation between carbon structure evolution and the incorporation of active sites. Furthermore, the specific contribution of ZIF-8 loading and its integration with MPc was explicitly studied. The following objectives were adopted to fulfil the core focus of the thesis:

1. One-step pyrolysis to develop Fe- and Co-based bimetallic electrocatalysts using ZIF-8@CNT derived NC scaffolds, examining their physicochemical properties and electrocatalytic ORR performance in alkaline and neutral media. Finally, these catalysts were employed at cathodes in MFC and AEMFC devices [I, II]. The influence of Ce incorporation into the Fe-doped ZIF-8@CNT-derived NC matrix on the electronic structure of the resulting catalysts was studied. Furthermore, this objective evaluated the benefits of this tailored structure on the ORR pathway and electrocatalytic performance in both alkaline and neutral electrolytes. The performance of MFC energy generation and wastewater treatment with these Ce incorporated cathode catalysts was examined [III].
2. To design a single-metal Fe-N-C material for MFC application using a novel in-situ nitridation strategy. This objective primarily focused on refining the ORR pathway and enhancing the MFC power generation performance [IV].
3. To develop a single-metal ORR electrocatalyst using a two-step pyrolysis strategy, characterise their physicochemical properties, electrocatalytic performance in alkaline solution, and lastly, the AEMFC performance [V]. This objective mainly focuses on optimising the metal-to-ZIF-8 ratio for fabricating the catalyst materials.
4. To study the effect of integrated MPc and ZIF-8 on the ORR activity, structural features and AEMFC performance of the designed bimetallic electrocatalysts [VI].

6. EXPERIMENTAL

6.1. Synthesis of ZIF-8@CNT composite-based bimetallic catalysts

In the articles [I, II, III, V, VI], ZIF-8 (Basolite® Z1200, Sigma-Aldrich) and multiwalled carbon nanotubes (MWCNTs, ≥95%, Nanocyl 3150) based composite was prepared through one-step pyrolysis (procedure P1), which consisted of holding the temperature at 900 °C for 2 h under N_2 atmosphere. A heating rate of 10 °C min^{-1} was used to reach the annealing temperature. In the work [IV, VI], the pyrolysis procedure P2 was used, which comprised subsequent annealing at 950 °C for 2 h under a N_2 atmosphere with a ramp rate of 5 °C min^{-1} [V] and 10 °C min^{-1} [VI].

6.1.1. Synthesis of Fe and Co doped materials

The following procedure was opted for the synthesis of metal-free and Fe/Co-doped catalyst materials [I]. Initially, 105 mg of ZIF-8 and 100 mg of MWCNTs were dispersed in 40 mL of methanol (MeOH) using ultrasonication (Branson 1510E-MTH; power output = 70 W, frequency = 40 kHz, Bransonic) for about 2 h and the resulting mixture was oven-dried at 60 °C overnight. The obtained powder mixture was then pyrolysed using procedure P1. The resulting blackish powder was named ZNT-900. The Fe_1Co_2 co-doped catalyst was prepared by dispersing 5.4 mg of iron(II) acetate ($Fe(OAc)_2$, 95%, Sigma-Aldrich), 10.3 mg of cobalt(II) acetate ($Co(OAc)_2$, 98%, Alfa Aesar), 100 mg of MWCNTs and 105 mg of ZIF-8 in 40 mL of MeOH. The solution mixture was sonicated for 2 h to obtain a homogeneous suspension. After oven-drying this mixture at 60 °C for overnight, it was pyrolysed again using P1. To prepare the Fe-doped catalyst, 8.2 mg of $Fe(OAc)_2$, 100 mg of MWCNTs and 105 mg of ZIF-8 were dissolved in 40 mL of MeOH. For Co-doped catalyst, 15.4 mg of $Co(OAc)_2$ was added to 100 mg of MWCNTs and 105 mg of ZIF-8 mixture via sonication. After drying in an oven at 60 ºC overnight, these mixtures were pyrolysed using P1. The resulting catalyst materials were designated as ZNT-900, Fe-ZNT-900, Co-ZNT-900, Fe_1Co_2-ZNT-900 (Fe:Co=1:2), and Fe_1Co_1-ZNT-900 (Fe:Co=1:1) [I]. The Fe-ZNT-900, Co-ZNT-900, Fe_1Co_2-ZNT-900 (Fe:Co=1:2) materials were used for article [II] with a slight modification in their nomenclature, and named as N-C@900, Fe-N-C@900 and FeCo-N-C@900, respectively.

6.1.2. Synthesis of Fe and Ce doped materials

The synthesis of Fe and Ce-based catalysts [III] was as follows: 7.8 mg of cerium nitrate hexahydrate ($Ce(NO_3)_3 \times 6H_2O$, Sigma-Aldrich, 99.9%) was added to a mixture containing 100 mg of ZIF-8 and MWCNTs prepared in MeOH. After sonication for about 2 h, the mixture was oven-dried at 60 °C overnight. Thereafter, it was pyrolysed using procedure P1 and the resulting catalyst was named

Ce@N-C. The Fe_1Ce_1@N-C catalysts were prepared by mixing 7.78 mg of $Fe(OAc)_2$, 7.8 mg of $Ce(NO_3)_3{\cdot}6H_2O$, 100 mg of ZIF-8 and MWCNTs in 30 mL of MeOH. This mixture was treated for about 2 h in an ultrasonication bath. After that, the mixture was dried and pyrolysed second time using P1. Similarly, by adjusting the Fe:Ce ratio, other variants of the FeCe bimetallic catalysts (Fe_1Ce_2@N-C, Fe_2Ce_1@N-C) were prepared using the same procedure [III].

6.2. Synthesis of FePc-derived catalyst materials

The following steps were used to design the hybrid Fe/Fe_4N@Fe-N-C material [IV]:

1. Initially, 280 mg of citric acid monohydrate ($C_6H_8O_7{\times}H_2O$, ≥99.8%, Fisher Scientific) was dissolved in 40 mL of ethanol. Subsequently, 8 g of melamine dissolved in ethanol was slowly added to the previous solution under continuous stirring. The resulting paste-like mixture was then dried in an oven overnight and pyrolysed using procedure P2. The resulting blackish powder was named as NC [IV].
2. 20 mg of pre-prepared NC catalyst was dispersed in 10 mL of MeOH and then 5 wt% iron phthalocyanine (FePc, Sigma Aldrich) was slowly added to this mixture. Subsequently, this mixture was sonicated and oven-dried overnight to evaporate ethanol. The resultant powder was collected and named as FePc/NC [IV].
3. 10 mg of FePc/NC catalyst was dispersed in 5 mL of 2-propanol by sonication. This catalyst suspension was deposited onto a silica boat, which was inverted and placed on top of another silica boat containing 10 g of melamine. This inverted dual-boat setup was then pyrolysed at 800 °C with a ramp rate of 5 °C min^{-1} for 2 h in N_2 atmosphere. After that, the material was scraped off from the top silica boat and named as Fe/Fe_4N@Fe-N-C [IV].

6.3. Synthesis of ZIF-8 and Mn-based catalyst materials

Typically, *n* mmol of ZIF-8 (*n* = 0.2, 0.5, 0.9, 1.8, 2.7) and 100 mg MWCNTs were dispersed in MeOH and treated in an ultrasonication bath for about 30 min. Thereafter, 22.3 mg of manganese acetate tetrahydrate ($Mn(OAc)_2{\times}4H_2O$, ≥99%, Sigma-Aldrich) was introduced to this mixture and treated in sonication for about 2 h until a homogeneous slurry is obtained. Following this, the mixture was oven-dried and pyrolysed using procedure P1. The resulting catalyst materials were referred as Mn/Zn-NC@CNT_x (x = 2, 5, 10, 20, 30), where x represents the molar ratio between Mn and ZIF-8 [V].

In the subsequent step, 50 mg of Mn/Zn-NC@CNT_10 catalyst was acid-washed with 1 M hydrochloric acid (HCl, 37%, Sigma-Aldrich) to remove residual Zn species and Mn-based oxide nanoparticles. After acid treatment, the catalyst was thoroughly washed with Milli-Q water (Type 1, 18.2 MΩ cm). This was then pyrolysed at 950 °C for 2 h in an inert atmosphere at a ramp rate of 5 °C min^{-1}. The resultant blackish powder was collected and named as Mn-N-C@CNT [V].

6.4. Synthesis of integrated MPc and ZIF-8-based bimetallic catalysts

The integrated MPc- and ZIF-8-derived bimetallic catalysts were prepared using the following synthetic pathway [VI]. Initially, 100 mg of ZIF-8 and MWCNTs were dispersed in MeOH using an ice bath sonication for 2 h. The obtained mixture was oven-dried and pyrolysed using procedure P1. The resulting blackish powder was collected and named as NC900. Afterwards, this was acid-washed with 1 M hydrochloric acid (HCl, 37%, Sigma-Aldrich) at 70–80 °C for 12 h. After thorough washing with Milli-Q water, the catalyst was dried at 60 °C and named NC900a. With a similar procedure, NC500a and NC700a catalysts were prepared, where 500 and 700 are the pyrolysis temperatures followed by acid washing (a). In the second step, 100 mg of NC900a, x wt% (1.5, 2.5) FePc and 1.5 wt% manganese phthalocyanine (MnPc, ≥99%, Sigma-Aldrich) in 40 mL of MeOH via ice bath sonication. After reaching a homogeneously dispersed mixture, it was oven-dried at 60 °C overnight. The resulting powder was then transferred to a silica pot and placed in a quartz tube for a second pyrolysis using procedure P2. The resulting blackish powder was named $Fe_{1.5}Mn_{1.5}$-NC900a. Following a similar synthesis procedure, $Fe_{1.5}Co_{1.5}$-NC900a and $Co_{1.5}Mn_{1.5}$-NC900a catalysts were prepared [VI].

6.5. Physico-chemical characterisation methods

A comprehensive set of physical characterisation methods was used to examine the structural morphology and chemical states of the prepared M-N-C materials.

X-ray diffraction (XRD) analysis was carried out using a Bruker D8 Advance diffractometer to determine the crystal structures of the catalyst materials [I-VI]. The diffractometer was equipped with a Ni-filtered Cu Kα radiation source and a LynxEye line detector. Scanning steps of 0.0183° were applied to record the diffraction patterns in 2θ range from 5° to 90° and a 525 s counting time per step. The full-profile analysis software Topas 6 (Bruker) was used to analyse the diffraction patterns.

The Micro-Raman spectroscopy was used to study the structural defects and graphitisation degree within the catalyst materials [I-VI]. Before measurements, the catalyst materials were dispersed in 2-propanol *via* sonication, then pipetted onto a clean Si wafer surface and oven-dried at 60 °C. Measurements were conducted using an inVia Renishaw spectrometer equipped with a 514.5 nm argon-ion laser and an Olympus confocal microscope (50× magnification objective). The Raman spectra were recorded in back-scattering geometry. To refine the data, the recorded Raman spectra were deconvoluted using a multiple-peak fitting procedure with Voigt functions. The baseline correction was applied to mitigate small fluorescence perturbations. The parameter W (full width at half-maximum (FWHM) of the D1 and G bands), I_{D1}/I_G (the ratio of the areas under the bands) and R2 = D1/(G + D1 + D2) (the ratio of the areas of indicated bands) were

extracted from these fits [I, II, III]. In a very defective carbon material, it is impossible to separate the G and D2 bands properly, as both are connected with a graphitic lattice. Therefore, I_{D1}/I_G+I_{D2} ratio is determined to [IV, V]. In contrast, for a highly-graphitised material, the I_D/I_G ratio can provide sufficient information to determine the structural order [VI].

The porosity parameters of the materials were determined by N_2 physisorption using a NOVAtouch LX2 (Quantachrome Instruments) [I-VI]. Before analysis, the samples were degassed under vacuum at 300 °C for 12 h. The specific surface area (S_{BET}) of the materials was calculated using the Brunauer-Emmett-Teller (BET) method over a P/P_0 range of 0.02–0.2. The total pore volume (V_{tot}) was calculated at a P/P_0 value of 0.97. The DFT-based specific surface area (S_{dft}), the volume of micropores (V_μ) and pore size distributions (PSD) were estimated from N_2 isotherms using a quenched solid density functional theory (QSDFT) equilibria model for slit-type [I, II, III, IV] or slit-syl [V, VI] type pores.

To gain insights into the bonding configurations and chemical states of the prepared M-N-C catalysts, the X-ray photoelectron spectroscopy (XPS) analysis was performed [I-VI]. Sample preparation includes catalyst dispersion in 2-propanol, followed by drop-casting onto the polished glassy carbon (GC) plates. All the measurements were performed under ultra-high vacuum conditions. The XPS measurements were conducted using an electron energy analyser SCIENTA SES 100 and Mg Kα X-ray radiation (1253.6 eV) [I-V] from the non-monochromatic twin anode X-ray tube (Thermo XR3E2). The survey scan was collected using the following parameters: energy range = 1200 to 0 eV, pass energy = 200 eV, step size = 0.5 eV, step duration 0.2 s and number of scans = 5. Being a surface-sensitive method (1–5 nm), XPS can provide compositional information by fitting the obtained core-level spectra. The high-resolution XPS spectra were thus recorded typically in the N1s and C1s regions for metal-free catalysts. While detailed XPS spectra in Fe2p [I-VI], Co2p [I, II, VI], Mn2p [V, VI], Ce3d [III], and Zn2p regions [III-VI] were obtained. The raw data were processed using the CasaXPS software (version 2.3.17) by eliminating X-ray satellites and fitting core-level peaks using the Gauss–Lorentz hybrid function (GL 70, Gauss 30 %, Lorentz 70 %). The background subtraction was performed using a blend of linear and Shirley-type models. For article [VI], the XPS survey spectra and Zn 2p spectra were measured using Al Kα radiation (1486.6 eV), for other spectra the Mg Kα radiation (1253.6 eV) was used. From the obtained peak areas, the atomic concentrations were calculated using built-in CasaXPS Scofield photoabsorption cross-sections and the electron effective attenuation lengths.

The catalyst surface morphology and elemental composition were examined using scanning electron microscopy (SEM) and scanning transmission electron microscopy (STEM). For the SEM analysis, the materials were suspended in 2-propanol (Millipore, Inc.), and the mixture was drop-cast onto silica substrates. The SEM images were captured at an accelerating voltage of 10 kV using a high-resolution scanning electron microscope (HR-SEM), the Helios NanoLab 600 (FEI Company) [I–VI]. The INCA Energy 350 EDX spectrometer (Oxford Instruments) attached to the microscope was used to quantify the elemental com-

position in weight% [I-VI]. Furthermore, STEM studies were conducted using a Titan Themis 200 (FEI) (S)TEM equipped with Cs-probe corrector at 200 kV to study surface morphology at the atomic scale [I-VI]. The samples were prepared by simply drop-casting the aliquot of catalyst ink (prepared in 2-propanol) onto lacey carbon film-coated copper TEM grids. Simultaneously, the SuperX EDX system (Bruker) connected to the same microscope provided energy-dispersive X-ray spectroscopy (EDX) elemental mapping. To investigate the bulk metal content in the catalyst materials, microwave plasma atomic emission spectroscopy (MP-AES) was employed for article [III].

6.6. Electrochemical characterisation

6.6.1. Catalyst inks and electrode preparation

The glassy carbon (GC) electrode was prepared by inserting GC disks (GC-20SS, Tokai Carbon Ltd., Japan) into the Teflon holder. The GC disk had a geometric surface area (A) of 0.2 cm^2. These were gently polished using 1 and 0.3 μm alumina slurries (Buehler, USA) until a mirror-like finish was achieved. After that, the GC disks were sequentially cleaned via sonication in Milli-Q water and 2-propanol for 5 min each [I–VI]. To prepare the catalyst ink, 4 mg of the catalyst powder was suspended in 1 mL of 2-propanol, followed by the addition of 5 μL of Nafion ionomer solution (5 wt%, Sigma-Aldrich). The mixture was sonicated for at least 90–120 min until a uniform dispersion was obtained. The catalyst ink aliquot (2 μL) was incrementally pipetted onto the polished GC surface and dried at 60 °C. This was done to achieve a final catalyst loading of 200 μg cm^{-2} [II–VI]. A lower catalyst loading of 100 μg cm^{-2} was used in article [I]. This was obtained by depositing a total of 5 μL catalyst ink onto the GC surface.

6.6.2. Electrochemical measurements in 0.1 M KOH and 0.1 M PBS electrolytes

The electrochemical ORR performance of the catalyst materials was evaluated by recording linear sweep voltammetry (LSV) and cyclic voltammetry (CV) curves using a rotating disk electrode (RDE) or a rotating ring-disk electrode (RRDE) methods. A customised round-bottom glass cell with a three-electrode setup was used for all electrochemical measurements. The experiments were controlled using a PGSTAT128N potentiostat (Metrohm Autolab, The Netherlands). The glassy carbon electrode (geometric surface area of 0.196 cm^2), the saturated calomel electrode (SCE) and the carbon rod were used as the working, reference and auxiliary electrodes, respectively. The reference electrode was connected via electrolyte bridge and the auxiliary electrode was separated by a glass frit. The cell was filled with 0.1 M KOH solution (purity ≥ 85%, Sigma-Aldrich) at pH=13 [I, V, VI]. During the RDE measurements, the electrode rotation rate (ω) was controlled using the EDI101 rotator and the CTV101 speed control unit (Radiometer). Before measurements, the electrolyte was purged with O_2 (99.999%,

Linde) for about 30 min. The *iR* correction was applied with Nova 2.1 software. The *iR*-corrected RDE polarisation curves were acquired at 310, 610, 960, 1900, 3100 and 4600 rpm between -1.2 and 0.0 V vs SCE in O_2-saturated 0.1 M KOH at a scan rate of 10 mV s^{-1}. Furthermore, the CV curves in O_2 and Ar (99.999%, Linde)-saturated 0.1 M KOH were recorded at a scan rate of 10 mV s^{-1} within the same potential window. The ORR performance is typically assessed based on the key parameters extracted from the polarisation curves. The potential at which the ORR commences is known as E_{onset}, which is usually determined at a current density of -0.1 mA cm^{-2}. The potential needed to achieve half of the diffusion-limited current density is known as $E_{1/2}$. All potential values (*vs* SCE) were converted with respect to the reversible hydrogen electrode (RHE) using the equation: $E_{RHE} = E_{SCE} + 0.241 + 0.059\times pH$. The Koutecky-Levich (K-L) plots constructed from the RDE polarisation data recorded at various electrode rotation rates in order to determine the electron transfer number (*n*) using the following equation [I-VI].

$$\frac{1}{j} = \frac{1}{j_k} + \frac{1}{j_d} = \frac{1}{j_k} - \frac{1}{0.62nFC_oD_o^{2/3}v^{-1/6}\omega^{1/2}} \tag{10}$$

where j, j_k, and j_d represent measured current density, kinetic current density and diffusion-limited current density, respectively. The number of electrons transferred per O_2 molecule is notated by n, F is the Faraday constant (96485 C mol^{-1}), D_O is the diffusion coefficient of O_2, v is the kinematic viscosity of the electrolyte solution, C_O is O_2 solubility in the bulk solution [226].

To gain further insights into the reaction pathway, the RRDE measurements were performed using a Pt-ring/GC disk electrode attached to the AFMSRX rotator and MSRX speed controller (Pine Research, USA) controlled by General Purpose Electrochemical System (GPES) software. This method enables the direct estimation of peroxide yield (%HO_2^-) and *n* during the ORR process [I, III–VI]. The Pt-ring was held at a constant potential of 1.55 V *vs* RHE to detect the peroxide formation. During ORR, the HO_2^- anions formed at the disk electrode migrate to the Pt ring encircling the GC disk electrode (0.164 cm^2), where they are oxidised back to O_2, generating a detectable ring current. Before each measurement, the Pt ring was electrochemically activated by scanning at least five potential cycles within the potential window 0.05–1.65 V *vs* RHE with a scan rate of 100 mV s^{-1}. Similarly, the GC disk was electrochemically activated by scanning at least 5 potential cycles at 100 mV s^{-1} between -0.2 and 1.0 V vs RHE. The following equations were used to estimate the RRDE parameters:

$$\%HO_2^- = \frac{200 \times \frac{I_r}{N}}{I_d + \frac{I_r}{N}} \tag{11}$$

$$n = \frac{4 \times I_d}{I_d + \frac{I_r}{N}} \tag{12}$$

where the disk and ring currents are denoted as I_d and I_r, respectively; N represents the ring collection efficiency (N), which was 0.25.

The M-N_x active sites are widely acknowledged as the primary centre for ORR electrocatalysis. While their existence and chemical nature can be investigated using the deconvolution of N1s core-level XPS spectra, the cyanide anions (CN^-) act as an effective probe for their electrochemical detection. These anions form stable, strong metal-cyanide complexes that prevent O_2 molecules from reaching the M-N_x sites. This was done by acquiring the RDE polarisation curves in O_2-saturated 0.1 M KOH electrolyte solution containing 10 mM NaCN. A drop in the key parameters i.e., $E_{1/2}$ or E_{onset} after NaCN addition provides definitive evidence of accessible, atomically dispersed M-N_x moieties. To determine the electrochemical stability of the catalyst materials, current-time (i-t) responses were measured at a constant potential of -0.1 V *vs* RHE for 13 h at 1900 rpm in O_2-saturated 0.1 M KOH electrolyte [II, III, IV, V]. Post-stability RDE [V] or RRDE [III, IV] polarisation curves were recorded at 1900 rpm in the range of 0.0–1.0 V vs RHE at a scan rate of 10 mV s^{-1}. In article [VI], accelerated durability tests were carried out by cycling 5000 potential scans between 0.4 and 1.0 V vs RHE at 200 mV s^{-1}. Following this, an RDE polarisation curve was obtained at 1900 rpm over 0.0–1.0 V vs RHE with a scan rate of 10 mV s^{-1}. If not stated otherwise, the commercial Pt/C catalyst (20% Pt on Vulcan XC-72, FC Catalyst) with a loading of 0.1 mg cm^{-2} (20 μg_{Pt} cm^{-2}) was used for comparison purposes.

In phosphate buffer saline (PBS) electrolyte (pH∼7), the electrochemical tests were conducted using a similar three-electrode configuration as described before. The preparation of 0.1 M PBS electrolyte involves dissolving 0.06 mol of disodium hydrogen phosphate (Na_2HPO_4, ≥99%, Fluka), 0.04 mol of potassium phosphate monobasic (KH_2PO_4, Merck) and 0.12 mol of sodium perchlorate monohydrate ($NaClO_4 \cdot H_2O$, ≥98%, Honeywell) in 1 L of Milli-Q water. The iR-corrected RDE polarisation curves were obtained at various electrode rotation rates (360, 610, 960, 1900, 3100 and 4600 rpm) [II, III] and for article [IV] at 400, 800, 1200, 1600, 2000 and 2400 rpm. The K-L equation (Eq. 10) was used with diffusion coefficient of O_2 (D_O) = 1.8×10^{-5} cm^2 s^{-1} to study the reaction kinetics and to determine the n value. The RRDE measurements were carried out to precisely examine the peroxide formation and n values using Eq. (11) and (12), respectively. The electrochemical conditioning of Pt ring electrode was done by scanning at least five potential cycles between 0.35–1.65 V *vs* RHE with scan rate of 100 mV s^{-1}. The *i-t* responses were recorded for 13 h at -0.1 V vs RHE [II, III]. The RDE polarisation curves were acquired at 1900 rpm in O_2-saturated 0.1 M PBS containing 10 mM NaCN to inspect the M-N_x centres [II, III, IV].

6.7. MFC assembly and operation

The MFC setup used in article [II] was constructed by joining two custom-built polycarbonate cylindrical containers (volume 25 mL each, inner diameter 3 cm) and securing them with a four-screw flange system (Figure 5a). These two compartments were separated by a PEM (Nafion™ 117, Sigma-Aldrich). The carbon felt (CF) electrode was cut from a CF sheet (thickness = 1.0 in., Thermo Scientific, 99%) and used as both anode and cathode, with a geometric surface area of 12.5 cm^2. Before use, the CF was treated in concentrated HNO_3 at room temperature to remove any impurities. Subsequently, it was thoroughly washed with Milli-Q water multiple times until the pH was neutral. The anolyte was prepared by mixing 10 mL of 0.05 M PBS (prepared by dissolving 0.31 g of NH_4Cl, 0.13 g of KCl, 2.69 g of $NaH_2PO_4 \times 2\ H_2O$, 4.33 g of Na_2HPO_4 in 1 L of Milli-Q water), 5 mL of trace elements. To support selective enrichment of electroactive microorganisms, 5 mL of sodium acetate solution was added to the anolyte. Under continuous N_2 purging, the anolyte was injected with a mixed culture obtained from the Tartu Wastewater Treatment Plant (Tartu Veevärk AS, Estonia). After that, the anode chamber was sparged with N_2 for 15–20 min to maintain anaerobic conditions. The initial open circuit voltage (OCV) of the MFC cell was recorded using Fluke 116 multimeter. The anolyte was frequently replaced (keeping 10% of the old anolyte) after each batch cycle (3-4 days) or when the OCV dropped to 50 mV to continue the enrichment process. The substrate oxidation efficiency was analysed by measuring the chemical oxygen demand (COD) of the anolyte, as described in Standard Methods for the Examination of Water and Wastewater [218]. This procedure was repeated for about 3-4 weeks until stable OCV and COD consumption rates were observed.

The cathode chamber consists of 0.1 M PBS electrolyte prepared using the same protocol as in section 6.6.2. The catalyst ink was prepared by dispersing 12 mg of catalyst powder in 3 mL of 2-propanol and 15 µL of 5 wt% Nafion™ ionomer solution. This solution was treated by sonication for 60-90 min or until a uniform suspension was visible. 0.625 mL of the ink was drop-casted onto the CF surface using a pipette until a catalyst loading of 0.2 mg cm^{-2} was obtained.

The MFC assembly was performed by sandwiching the anode chamber, PEM and the catalyst-equipped cathode chamber. The anode and cathode were placed at 2.5–3 cm and were connected to a titanium wire (1 mm in diameter, Alfa Aesar). The MFC polarisation tests were conducted by connecting an external resistance across the anode and cathode. The resistance load was sequentially lowered from the highest (100 kΩ) to the lowest (10 Ω) value, and the cell voltage (V) was frequently monitored with a Fluke 116 multimeter. The current (I) at each resistance (R) was determined using Ohm's Law ($V=I\times R$), and the power output was determined using the formula $P=V\times I$. The area-normalised current and power densities were obtained by dividing the current and power values by the cathode area. The slope (dE/dI) of the polarisation curve signifies the internal resistance (R_{int}) of the MFC cell. The MFC cells were then connected with the R_{int}, and the cell voltage and COD removal efficiency were measured after each batch cycle.

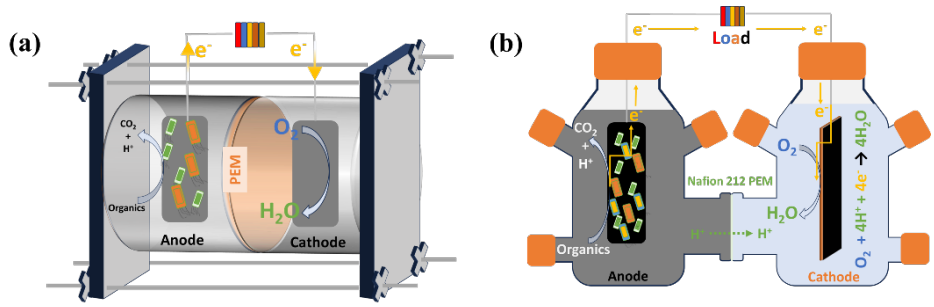

Figure 5. Schematic illustration of (a) Cylindrical-shaped dual-chamber MFC setup (volume = 25 mL) used in article [II] and (b) H-shaped dual-chamber MFC setup (volume = 500 mL) used for articles [III, IV].

To evaluate the MFC device's scalability, the anode and cathode working volumes were expanded to 500 mL using a custom-made H-shaped glass assembly (Figure 5b). In this configuration, both chambers were separated by a PEM (Nafion™ 212, Fuel Cell Store, USA) [III, IV]. A similar enrichment procedure was adopted as for the article [II]. While CF was used as the anode, the cathode was switched to carbon paper (CP, Toray, TGP-H-060) measuring 5 cm × 2.5 cm. For article [III], the electrocatalyst ink was prepared by dispersing 10 mg of catalyst in 5 mL of 2-propanol with 0.01 mL Nafion™ ionomer solution (Sigma-Aldrich, 5 wt%). About 0.8 mL of the uniformly dispersed catalyst ink was deposited to the CP external surface to obtain the active material loading of 200 µg cm^{-2}. For article [IV], different cathode catalyst loadings (0.2, 0.5 and 1.0 mg cm^{-2}) were used to evaluate the MFC performance. The resulting MFC devices were named as MFC-0.2, MFC-0.5 and MFC-1.0 equipped with the Fe/Fe_4N@Fe-N-C catalyst. The anolyte and catholyte were prepared using the same procedure as earlier [II]. The polarisation tests were conducted by varying external resistance from 90 kΩ to 10 Ω and area-normalised current and power density were determined. Before initiating the polarisation tests, the anolyte was frequently replenished after each batch cycle (4–5 days) and saturated with N_2 for 20–30 min. The catholyte was purged with O_2 to ensure sufficient electron acceptor availability.

6.8. MEA assembly and AEMFC operation

For article [I], cathode ink was prepared as follows: 12.5 mg of the catalyst powder (Fe_1Co_2-ZNT-900 and Fe_1Co_1-ZNT-900) was dispersed in 1.35 mL of MeOH, 0.390 mL of Milli-Q water and 0.130 mL of 3 w% ionomer solution. The ionomer solution was prepared by dissolving Aemion+ powder (AP2-INN8-00-X, Ionomr Innovations, Inc., Canada) in MeOH. Similarly, the anode ink was prepared by dispersing 6.67 mg of Pt-Ru/C (50:25:25, Alfa Aesar), 0.690 mL of MeOH, 0.196 mL of Milli-Q water and 0.049 mL of 3 wt% Aemion+ ionomer

solution. These were treated by sonication in ice water for about 90 min to achieve a homogeneously dispersed ink. These prepared catalyst inks were incrementally loaded onto the gas diffusion layers (GDL, Sigracet 39 BB) to achieve loadings of 0.4 $mg_{Pt\text{-}Ru}$ cm^{-2} for the anode and 2 mg cm^{-2} for the cathode. After that, the catalyst-coated gas-diffusion electrodes (GDE) and Aemion+®15 (AF2-HLF8-15-X, 15 µm, Ionomr Innovations, Canada) AEM were soaked in 3 M KOH solution for 24 and 96 h, respectively. This pre-treatment is essential to ensure sufficient ion-exchange during AEMFC operation. The KOH solution was replenished every 24 h. The MEA was prepared by sandwiching the KOH-soaked catalyst-coated electrodes, the AEM and silicone gaskets into a single-cell fixture (Fuel Cell Technologies Inc., USA) using a torque of 9 N m. The active surface area was 5 cm^2 and the AEMFC tests were performed using the Greenlight Fuel Cell Test Station (G40 Fuel Cell System, Hydrogenics, Canada). The cell was operated at a temperature of 65 ºC and was continuously fed with 65% humidified H_2 and O_2 at a flow rate of 1 normal litres per minute (NLPM). The backpressure was gradually increased to 200 kPa and held to perform the polarisation tests.

For article [V], the AEMFC tests were performed using the Greenlight Fuel Cell Test Station (G40 Fuel Cell System, Hydrogenics, Canada) fed with humidified H_2/O_2 gaseous reactants. The anode ink was prepared by co-dispersing 21.2 mg of PtRu/C (50:25:25, Alfa Aesar), 3230 µL of 2-propanol, 294 µL of Milli-Q water and 175 µL of a 5 wt% PiperION ionomer solution (Versogen). Similarly, the cathode ink was prepared by dispersing 25.4 mg of catalyst material (Mn-N-C@CNT, Mn/Zn-NC@CNT_10) in 3880 µL of 2-propanol, 353 µL of Milli-Q water and 208 µL of 5wt% PiperION ionomer solution (Versogen). These inks were sonicated in ice-cooled water for about 90–120 min or until a uniformly dispersed ink was visible. Thereafter, these inks were incrementally deposited onto the gas diffusion layer (GDL, Freudenberg Performance Materials SE& Co. KG, H23C8) using an airbrush (Harder & Steenbeck). The final catalyst loading at the anode and cathode was 0.9 $mg_{PtRu/C}$ cm^{-2} and 1.2 mg cm^{-2}, respectively. A higher Mn-N-C@CNT loading (1.5 mg cm^{-2}) was prepared to examine the effect of catalyst layer thickness and loading in power generation. The catalyst layer thicknesses for the anode and cathode electrodes were determined with a Mitutoyo ABS Digital thickness gauge (Item number: 547–526S). The thickness was measured at 5 different locations on GDEs before and after catalyst coating. The as-prepared electrodes and PiperION (20 µm, Fuel Cell Store, USA) AEM were soaked overnight in 1 M KOH solution. The MEA was constructed by sandwiching KOH-soaked catalyst-coated electrodes and AEM. The MEA and Teflon™ gaskets were fixed in a single-cell fixture (Fuel Cell Technologies Inc., USA) using a torque of 7 Nm to achieve about 25% compression of the MEA thickness. The active area of the electrode was 4.85 cm^2. The AEMFC tests were conducted at a constant cell temperature of 80 ºC, and the parameters such as backpressure (50–200 kPa) and gas flow rates (0.1–0.6 NLPM) were manually adjusted to keep the cell stable. For instance, the condition marked as 80-50-0.1/0.1-100/100 represents a cell temperature (80 °C),

backpressure (50 kbar), gas flow rates at anode/cathode (G_A=0.1 NLPM/G_C= 0.1 NLPM) and relative humidity at anode/cathode (%RH_A=100/%RH_C=100).

A similar procedure (as [V]) for MEA preparation and AEMFC operation was followed for article [VI]. However, a different anode catalyst; PtRu/C (40% Pt, 20% Ru on carbon black, HiSPEC™ 10000) was used with $Fe_{1.5}Mn_{1.5}$-NC900a, $Fe_{1.5}Co_{1.5}$-NC900a, and $Co_{1.5}Mn_{1.5}$-NC900a cathode catalysts. The anode and cathode catalyst loading of 0.9 $mg_{PtRu/C}$ cm^{-2} and 1.2 mg cm^{-2} was used to conduct the AEMFC tests. The MEA assembly, including the overnight 1 M KOH activation of the PiperION membrane and electrodes, thickness measurements using Mitutoyo ABS Digital thickness gauge, GDE compression and cell fixture parameters, followed the identical procedure established in a previous study [V].

7. RESULTS AND DISCUSSION

7.1. Electrocatalysis on Fe and Co-doped ZIF-8@CNTs composite catalysts

This section of the thesis deals with Fe- and Co-doped monometallic and bimetallic composite catalysts for AEMFC and MFC applications. The first part describes the ORR electrocatalytic activity of Fe, Co and Fe_xCo_y (x: y = 1:1, 1:2) catalysts in alkaline media. The Fe_xCo_y (x: y = 1:1, 1:2) catalysts were employed as cathode catalysts in AEMFCs [I]. The second part of this work investigates the ORR activity of these materials in neutral solution. Moreover, it addresses the applicability of Fe, Co, and Fe_1Co_2 catalysts at a dual-chamber MFC cathode [II]. The influence of the modified cathodes on the bioenergy generation performance and COD removal efficiency was evaluated.

7.1.1. Physicochemical characterisations of the catalysts

The crystal structure of the catalyst materials was examined using XRD, as presented in Figure 6a. For the metal-free ZNT-900 catalyst, the diffraction patterns showed two broad peaks at ~25.6° and 43.08°, corresponding to the (002) and (100) planes of graphitic carbon [177]. In addition, several small diffraction peaks were observed for the transition metal-doped ZNT-900 catalyst. These peaks correspond to metal nanoparticles (Fe or Co), alloy nanoparticles (FeCo) and metal oxides (Fe_3O_4). While this suggests that metal is agglomerated, the presence of atomically dispersed M-N_x sites cannot be ruled out. The structural defects and level of graphitisation evolved during pyrolysis were examined using Raman spectroscopy (Figure 6b). All catalysts exhibited two discernible peaks at ~1352 and ~1584 cm^{-1}, corresponding to the D and G bands, respectively. The D-to-G band intensity ratio (I_D/I_G) indicates the degree of defectiveness in the carbon structure. For each catalyst, this ratio was close to unity. Further deconvoluting these spectra into five Voigt-shaped bands (G, D1, D2, D3 and D4) provides an in-depth examination of the total structural imperfections within the graphitic crystal surface (D1), surface graphene layers (D2), amorphous carbon (D3) and the disordered graphitic lattice (D4). A higher I_{D1}/I_G value indicates greater structural disorder in bimetallic catalysts and a higher density of active sites, which are essential for efficient ORR electrocatalysis.

The specific surface area and pore architecture of the designed catalysts were examined using the BET method. The N_2 adsorption-desorption isotherms exhibit type I and III H3 hysteresis, a hallmark of micro- and mesoporous materials according to IUPAC classification (Figure 6c). Such a hierarchical porous carbon structure is advantageous for efficient diffusion of reactants to the active sites. The pore-size distribution for these materials is presented in Figure 6d and summarised in Table 1. The pristine ZNT-900 or N-C@900 catalyst had a higher proportion of micropores with a surface area of 189 $m^2 g^{-1}$.

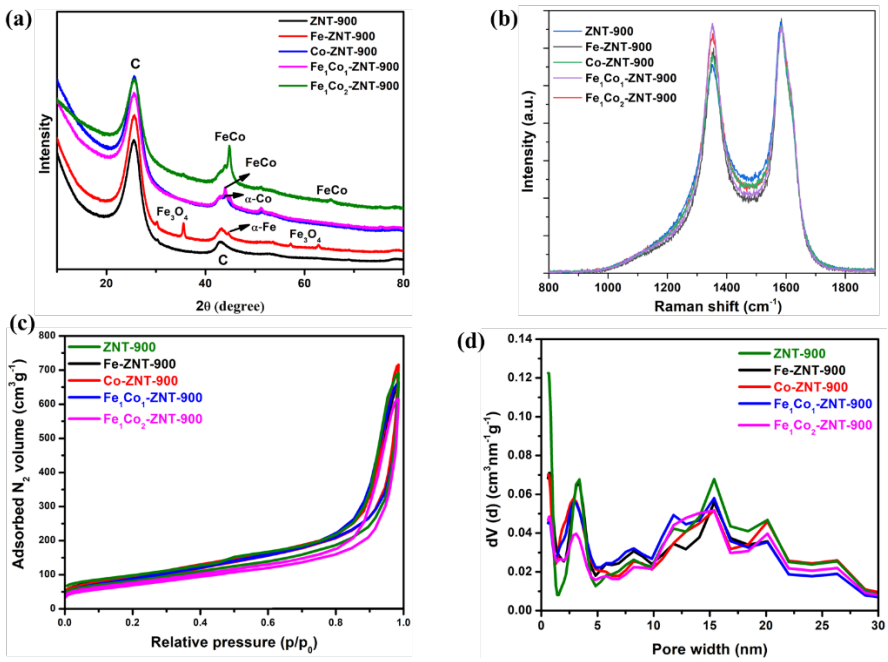

Figure 6. (a) XRD patterns, (b) Raman spectra, (c) N_2 adsorption-desorption isotherms and (d) pore size distribution for ZNT-900, Fe-ZNT-900, Co-ZNT-900, Fe_1Co_2-ZNT-900 and Fe_1Co_1-ZNT-900 catalysts [I, II].

This showed an effective Zn volatilisation at 900 ºC [205, 209]. However, the Fe- or Co-doped monometallic catalysts exhibited a similar total pore volume and micropore surface area. The incorporation of a dual metal slightly decreased the specific surface area (S_{BET}); the micropore surface area remained unchanged, whereas the mesopore surface area increased for the Fe_1Co_2-ZNT-900 or FeCo-N-C@900 catalyst. This suggests a complex structural transition and a distinct mechanism for anchoring the metal site during pyrolysis [205].

Table 1. BET surface area (S_{BET}), volume of micropores (V_{micro}), total pore volume (V_{tot}), DFT surface area for micropores and mesopores calculated for ZIF-8@CNT catalysts.

Catalyst material	S_{BET} ($m^2\ g^{-1}$)	V_{micro} ($cm^3\ g^{-1}$)	V_{tot} ($cm^3\ g^{-1}$)	Sa_μ ($m^2\ g^{-1}$)	Sa_m ($m^2\ g^{-1}$)
ZNT-900 [I] (N-C@900) [II]	290	0.07	0.65	189	172
Fe-ZNT-900 [I] (Fe-N-C@900) [II]	334	0.07	0.66	145	170
Co-ZNT-900	297	0.07	0.73	141	175
Fe_1Co_1-ZNT-900	247	0.05	0.61	106	147
Fe_1Co_2-ZNT-900 [I] (FeCo-N-C@900) [II]	312	0.06	0.66	109	181

The surface morphology of the catalyst materials was studied using SEM. As shown in Figure 7, each catalyst exhibits a structure resembling that of CNTs. The SEM images at higher magnifications revealed that the CNTs are randomly oriented in a three-dimensional network. Such a dense network of CNTs ensured high electrical conductivity and enhanced mass-transfer processes [183]. Clearly, the absence of ZIF-like morphology reflects the complete transformation of the parent ZIF-8 geometry to an NC framework. The elemental composition was determined by SEM-EDX and MP-AES analyses, as shown in Table 2. Both analyses revealed a similar metal content. It is worth noting that all the prepared catalysts exhibited a similar structure, suggesting that the specific transition-metal incorporation used did not significantly affect the catalyst structure. However, SEM is limited to lower magnifications; thus, STEM and STEM-EDX were used to provide an in-depth view of the catalyst's structure at the atomic scale. The bright-field (BF)-STEM images (Figure 8) for the bimetallic ZNT-900 catalysts show CNTs adorned with metal or FeCo alloy nanoparticles (Figure 8a). Both catalysts exhibit similar morphologies, with dense CNT networks that serve as conductive highways, improving electron transfer to the active sites. The STEM-EDX images shown in Figure 9 reveal uniform distributions of C, N, Fe, and Co.

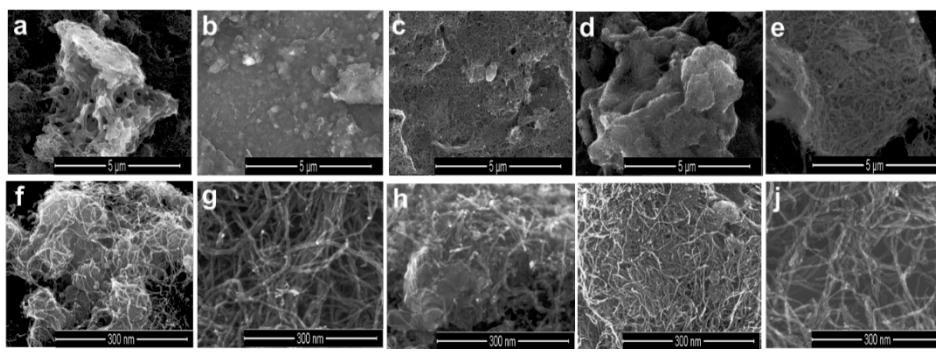

Figure 7. SEM images for (a, f) ZNT-900, (b, g) Fe-ZNT-900, (c, h) Co-ZNT-900, (d, i) Fe_1Co_1-ZNT-900 and (e, j) Fe_1Co_2-ZNT-900 catalysts at different resolutions.

Table 2. Bulk elemental composition (wt%) by SEM-EDX and MP-AES analysis.

Catalyst material	C	N	O	Fe (SEM)	Fe (MP-AES)	Co (SEM)	Co (MP-AES)
ZNT-900	90.42	6.45	1.96	-	-	-	-
Fe-ZNT-900	86.11	4.90	7.16	1.83	1.994	-	-
Co-ZNT-900	86.08	7.28	3.36	-	-	3.19	2.997
Fe_1Co_1-ZNT-900	89.16	3.17	4.46	2.70	3.561	2.86	3.016
Fe_1Co_2-ZNT-900	85.87	6.88	3.58	1.28	1.34	2.39	2.48

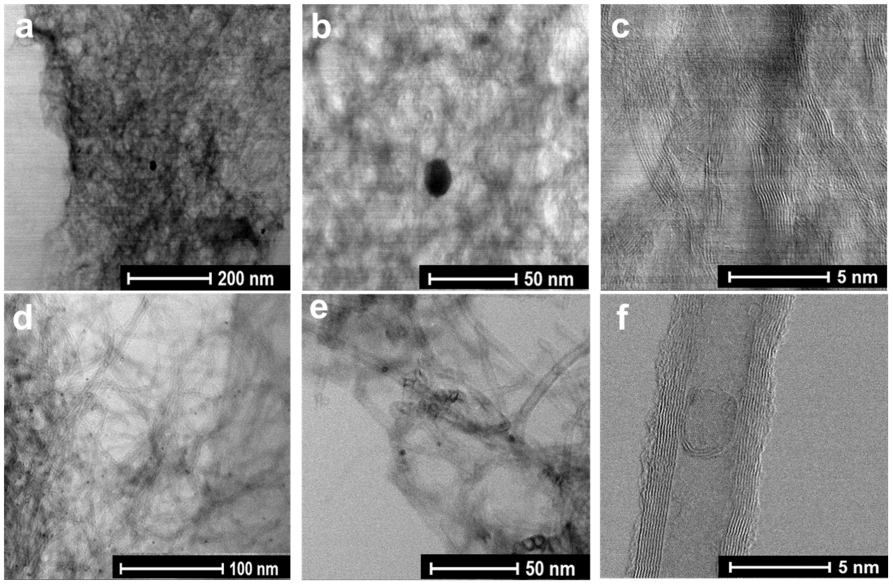

Figure 8. Bright field (BF)-STEM images obtained for (a–c) Fe_1Co_1-ZNT-900 and (d–f) Fe_1Co_2-ZNT-900 catalysts.

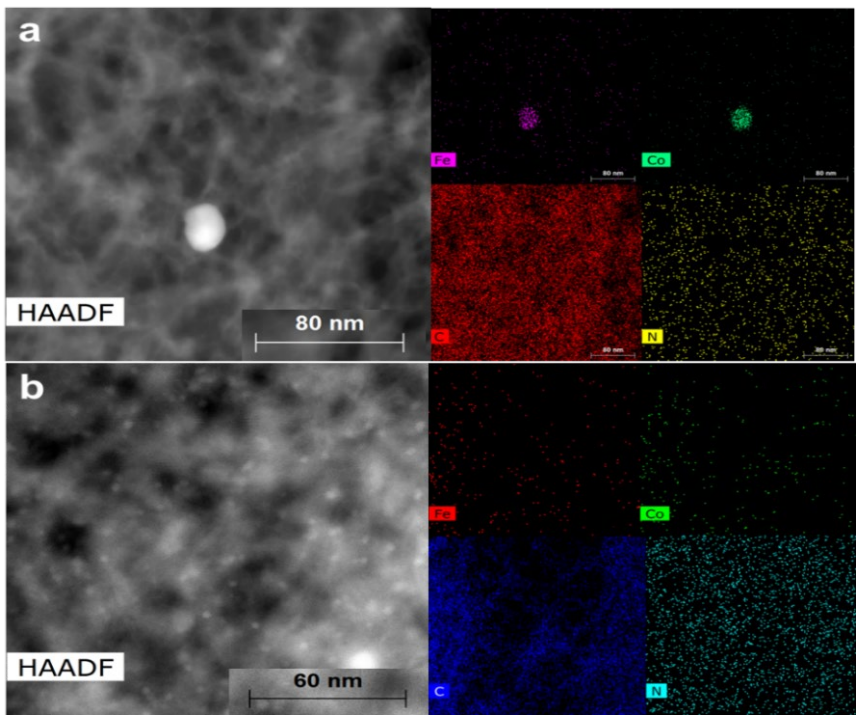

Figure 9. HAADF-STEM images for (a) Fe_1Co_1-ZNT-900 and (b) Fe_1Co_2-ZNT-900 catalysts with corresponding EDX elemental mapping representing C, N, Fe and Co.

XPS was used to determine the surface bonding configurations and chemical states of the designed catalysts. The surface elemental content obtained for all the catalysts is presented in Table 3. Clearly, each catalyst has a similar C content, while the N content was highest in the bimetallic catalysts. The presence of N creates a charge imbalance in the carbon framework due to its higher electronegativity than C, thereby favouring O_2 chemisorption [151]. Therefore, the detailed XPS spectra was recorded in the N1s region for all catalysts as presented in Figure 10. Notably, each catalyst comprises different N species, such as pyridinic-N, pyrrolic-N, graphitic-N, M-N_x, imines and bulk N-H. The relative content of pyridinic-N, pyrrolic-N, graphitic-N and M-N_x species is compared in Figure 10f. It is evident that the bimetallic catalysts possess a higher content of these N-species, especially the greater proportion of M-N_x centres. The presence of M-N_x species provides evidence of the atomically dispersed sites, which are considered highly active for ORR electrocatalysis [54].

The high-resolution Fe2p XPS spectra (see Fig. S6 in the article [I]) showed peaks at ~710.8 and ~724.3 eV, which are attributed to $Fe2p_{3/2}$ and $Fe2p_{1/2}$ spin-orbit coupling levels. Additionally, the deconvoluted peaks centred at ~710.8 and ~713.0 eV signify the majority of oxidised Fe^{2+} and Fe^{3+} species, respectively. Likewise, the detailed XPS spectra in the Co2p region showed two distinct, broader peaks at ~780.5 and ~796.0 eV, corresponding to $Co2p_{3/2}$ and $Co2p_{1/2}$, respectively. Furthermore, the deconvoluted peaks at ~783.0 and ~780.5 eV indicate the majority of oxidised Co^{2+}/Co^{3+} species.

Table 3. Surface elemental content (at%) measured using XPS.

Catalyst material	C	N	Fe	Co
ZNT-900	96.3	1.7	-	-
Fe-ZNT-900	95.8	1.1	0.1	-
Co-ZNT-900	95.0	2.0	-	0.5
Fe_1Co_2-ZNT-900	94.0	2.6	0.3	0.4
Fe_1Co_1-ZNT-900	94.4	2.5	0.2	0.6

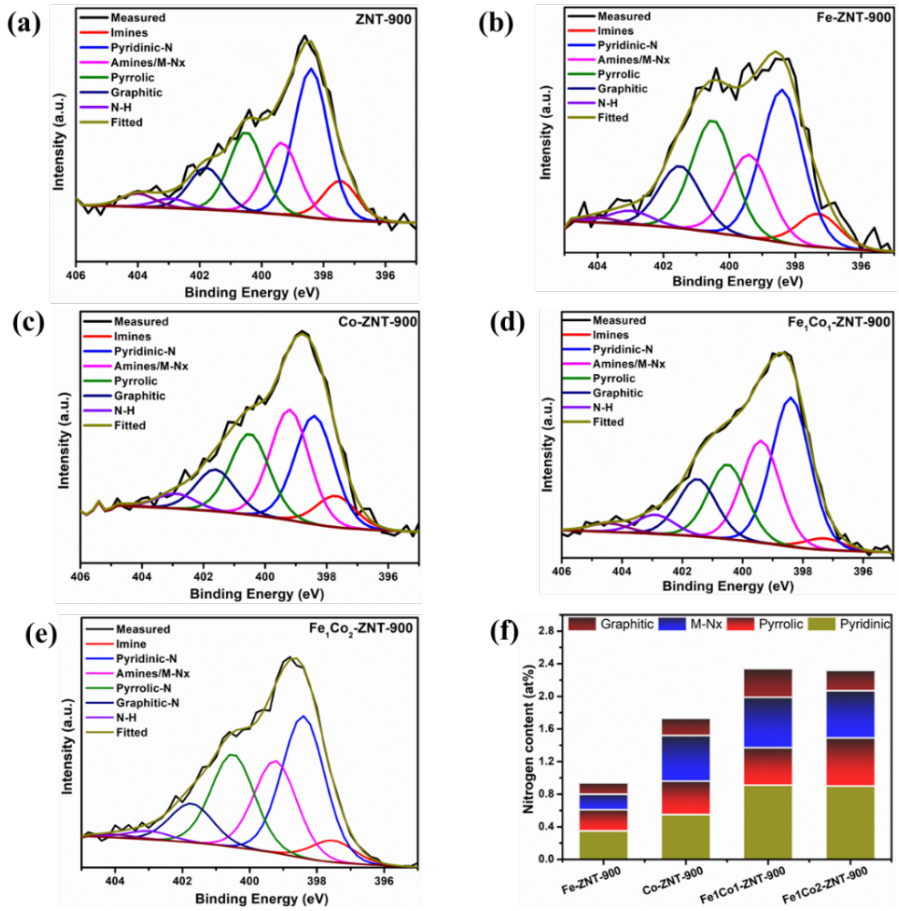

Figure 10. Detailed N1s XPS spectra for (a) ZNT-900, (b) Fe-ZNT-900, (c) Co-ZNT-900, (d) Fe_1Co_1-ZNT-900 and (e) Fe_1Co_2-ZNT-900 catalysts, and (f) comparison of the surface N content (pyridinic-N, pyrrolic-N, graphitic-N and M-N_x) across these catalysts.

7.1.2. Electrochemical performance of the catalyst materials

The ORR activity of the designed materials was evaluated using the RDE and RRDE methods in both alkaline and neutral solutions. In the first part, the electrochemical performance was investigated in 0.1 M KOH electrolyte [I]. The performance was compared based on $E_{1/2}$ and E_{onset} across all the materials. The metal-free ZNT-900 catalyst exhibited an $E_{1/2}$ and E_{onset} of 0.75 V and 0.87 V vs RHE, respectively (Figure 11a). Evidently, upon incorporation of transition metals, a significant positive shift was observed, attributable to their higher nitrogen content and the presence of M-N_x sites. Notably, both bimetallic catalysts reached the highest $E_{1/2}$ of 0.85 V vs RHE and an E_{onset} close to 1.0 V vs RHE, and these materials exhibit the fastest intrinsic kinetics. The hydrodynamic voltammograms were recorded at different electrode rotation rates as shown in

Figure 12. The K-L plots were constructed from these RDE polarisation curves to determine the *n* value. The deviation from linearity and parallelism in the K-L lines of ZNT-900 catalyst suggests a dominant two-electron ORR pathway. Clearly, the linear K-L lines for transition metal-doped catalysts suggest first-order reaction kinetics and a dominant $4e^-$ pathway.

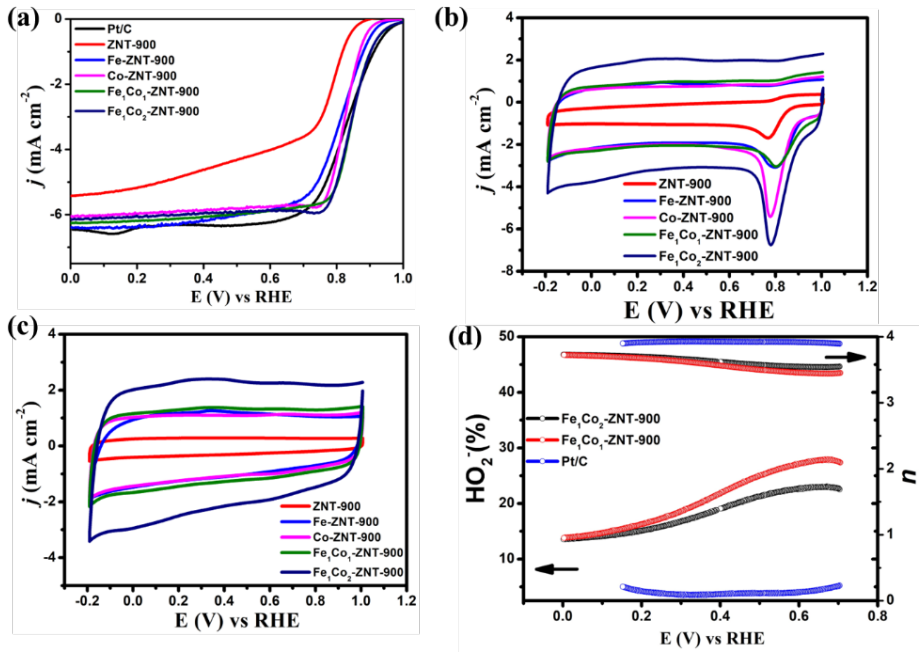

Figure 11. (a) RDE polarisation curves recorded in O_2-saturated 0.1 M KOH electrolyte at 1900 rpm with a scan rate of 10 mV s^{-1}, Cyclic voltammetry curves in (b) O_2-saturated and (c) Ar-saturated 0.1 M KOH electrolyte at 100 mV s^{-1} for all catalysts, (d) HO_2^- yield and *n* value across different potentials for bimetallic catalysts.

The CV curves recorded in O_2- and Ar-saturated 0.1 M KOH electrolyte are presented in Figure 11b and 11c, respectively. The CVs in Figure 11b showed a distinct sharp ORR peak for all materials, with Fe-ZNT-900, Co-ZNT-900 and Fe_1Co_2-ZNT-900 exhibiting a positive ORR peak potential near 0.80 V vs RHE. Furthermore, the higher capacitive currents observed for the Fe_1Co_2-ZNT-900 catalyst, as shown in Figure 11c, may reflect its highly porous morphology.

The RRDE analysis was performed to gain a precise insight into the reaction pathway, as it enables the detection of peroxide formed during the O_2 reduction process. The $\%HO_2^-$ and respective *n* values for bimetallic catalysts are presented in Figure 11d. Clearly, Fe_1Co_2-ZNT-900 catalyst showed a slightly lower HO_2^- yield than the Fe_1Co_1-ZNT-900 catalyst, with an average electron transfer number (n_{avg}) of 3.73, it delivered a predominantly $4e^-$ reduction pathway.

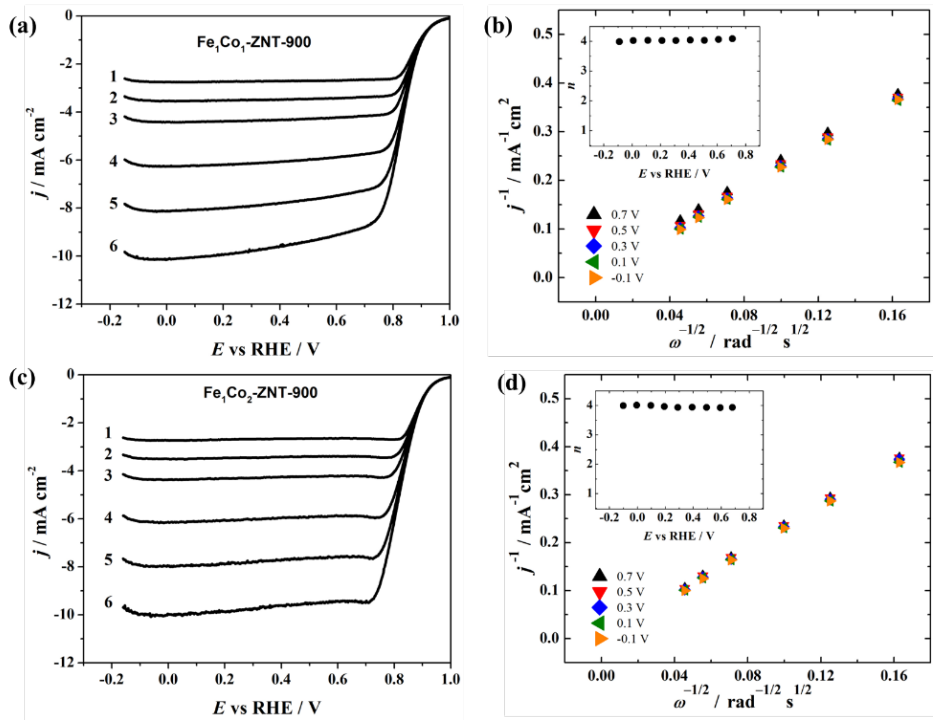

Figure 12. RDE voltammetry curves and K-L plots (insets to the K-L plots show the *n* value as a function of potential) for ORR on (a, b) Fe_1Co_1-ZNT-900, (c, d) Fe_1Co_2-ZNT-900 catalysts. [Scan rate: 10 mV s^{-1}. Rotation rate (ω): (*1*) 360, (*2*) 610, (*3*) 960, (*4*) 1900, (*5*) 3100 and (*6*) 4600 rpm].

Considering the outstanding ORR activity of the prepared materials in 0.1 M KOH electrolyte, the performance of ZNT-900, Fe-ZNT-900 and Fe_1Co_2-ZNT-900 catalysts was evaluated in 0.1 M PBS electrolyte (pH=7). These catalysts were designated as N-C@900, Fe-N-C@900 and FeCo-NC@900 for this part of the work (Figure 13) [II]. CV curves of these catalysts in O_2- and Ar-saturated 0.1 M PBS solution are presented in Figure 13a. The sharp reduction peak (E_p = 0.66 V) for the FeCo-NC@900 catalyst reflects high electrocatalytic activity towards the ORR in neutral media, attributed to the synergy of the FeCo dual-metal sites [155, 170]. Subsequently, the RDE polarisation curves at 1900 rpm showed that the FeCo-NC@900 catalyst exhibits superior ORR activity, with an $E_{1/2}$ of 0.71 V vs RHE, outperforming N-C@900 and Fe-N-C@900 catalysts under identical conditions (Figure 13). Moreover, a commercial Pt/C catalyst showed an $E_{1/2}$ of 0.82 V, which is 0.11 V more positive than the tested bimetallic catalyst.

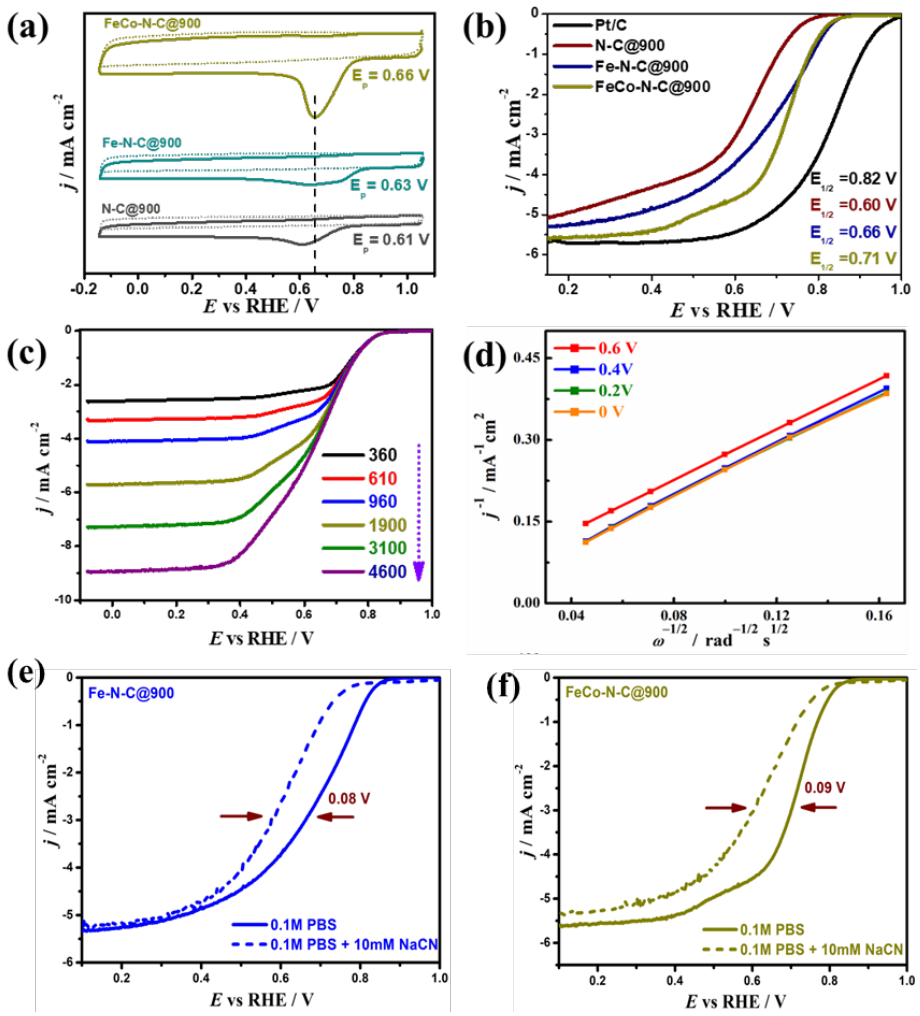

Figure 13. Comparison of the CV curves recorded in (a) O_2- and Ar-saturated 0.1 M PBS at a scan rate of 100 mV s^{-1}, (b) RDE polarization curves recorded in O_2 saturated 0.1 M PBS at 1900 rpm with a scan rate of 10 mV s^{-1}, (c) RDE polarisation curves at different electrode rotation rates and (d) the respective K-L plot for FeCo-N-C@900 catalyst. RDE polarisation curve at 1900 rpm in O_2-saturated 0.1 M PBS+10 mM NaCN electrolyte (scan rate=10 mV s^{-1}) for (e) Fe-N-C@900 and (f) FeCo-NC@900 catalysts.

The polarisation curves at different electrode rotation rates (ω) and the respective K-L plot for the FeCo-NC@900 catalyst are presented in Figures 13c and 13d, respectively. The diffusion-limited current densities (j_L) increased linearly with $\omega^{1/2}$, indicating thinning of the diffusion layer. Intriguingly, the bimetallic catalyst exhibited an *n* value of 3.7 across a broad potential range, reflecting a dominant $4e^-$ ORR pathway. To confirm the presence of M-N_x sites, the RDE polarisation curves were acquired at 1900 rpm in 0.1 M PBS containing 10 mM NaCN for the

Fe-N-C@900 (Figure 13e) and FeCo-NC@900 (Figure 13f) catalysts. Both catalysts showed a loss in the $E_{1/2}$ of about 80–90 mV. This prominent decline in ORR activity suggests that cyanide anions have coordinated the transition-metal sites within M-N_x centres, thereby obstructing the reactivity of O_2 molecules.

7.1.3. AEMFC and MFC performance with modified cathodes

Inspired by the excellent electrocatalytic ORR performance of these catalyst materials in both alkaline and neutral solutions, these were integrated as cathode modifications in AEMFC [I] and MFC [II] devices. The AEMFC tests were conducted with PtRu/C anode and catalyst-coated (Fe_1Co_1-ZNT-900, Fe_1Co_2-ZNT-900, Pt/C) cathodes. An open circuit voltage (OCV) of 1.0, 1.03 and 1.01 V was achieved with these materials, respectively. The polarisation and power density curves are presented in Figures 14a and 14b, respectively. Notably, the Fe_1Co_2-ZNT-900 catalyst achieved a maximum power density (P_{max}) of 0.171 W cm^{-2}, which was 26% greater than the Fe_1Co_1-ZNT-900 catalyst under similar conditions. Furthermore, the current density for Fe_1Co_2-ZNT-900 catalyst at 0.5 V ($j_{0.5}$) was close to that of the Pt/C catalyst. Compared with the reported works, the AEMFC performance was relatively lower in terms of P_{max}, primarily due to a thicker AEM (Aemion+ 15 μm) used in this work. This membrane has a lower ion exchange capacity than its thinner analogue (Aemion+ 10 μm)[227, 228]. Nevertheless, despite methodological distinctiveness in operating parameters such as backpressure, gas-flow rates, catalyst layer loading and thickness, and the MEA assembly, these catalysts achieved appreciable performance; however, further optimisations are required to boost AEMFC power densities. The summary comparison with the literature will be provided in the Section 7.5.3.

In the MFC device, the superior ORR activity of the FeCo-NC@900 catalyst yielded a remarkable P_{max} of 1556.9 mW m^{-2}, surpassing that of all other tested materials. During the initial two weeks of the enrichment period, the maximum OCV of 774 mV was observed. Anode performance continued to improve over time and the MFC achieved a stable OCV after 5 weeks. In addition to cathode performance, the rate of organic oxidation at the anode critically determines the overall cell performance. With the bare CF cathode, a COD removal efficiency of 72% was obtained, which for FeCo-NC@900 catalyst, increased to 87% when MFC was operated with an external resistance of 500 Ω. These results reflect that the anode and cathode performance are correlated. It should be noted that ZIF-8 was first implemented in a single-chamber MFC by Xue et al. [207]. However, far fewer studies have used ZIF-8-derived catalysts in a dual-chamber MFC device. This makes a comparison limited to the reported works. Moreover, due to differences in MFC configurations, electrode surface area-to-anode volume ratio (ESVAR), and PEM type, significant differences in the MFC performance can be observed [229]. The summary comparison with the literature will be provided in Section 7.3.3.

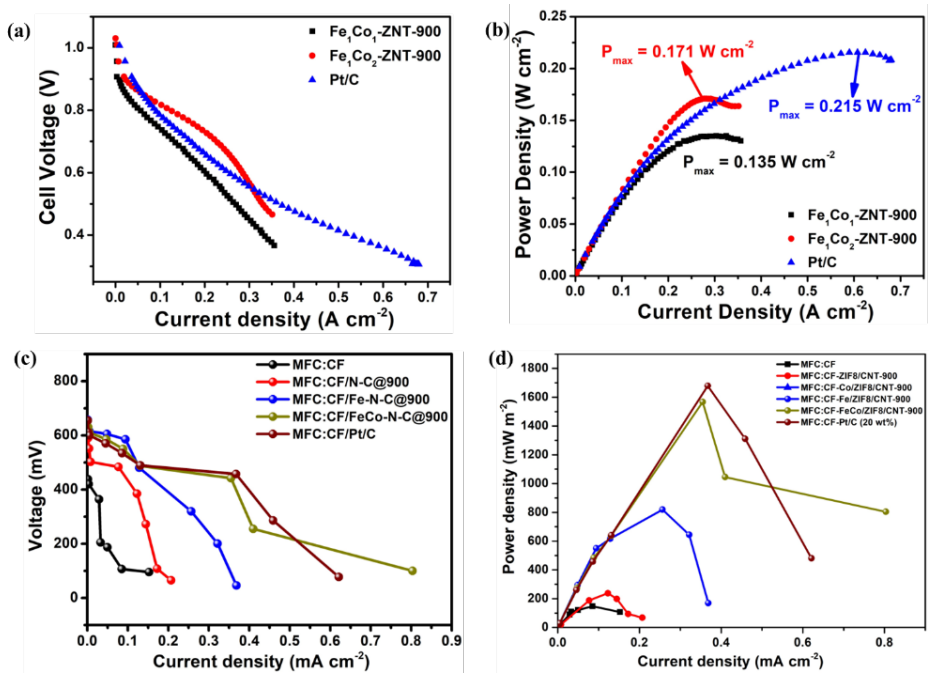

Figure 14. (a, b) AEMFC polarisation and power density curves for Pt/C and bimetallic catalysts [I], (c, d) MFC polarisation and power density curves with bare carbon felt (CF) cathode and catalyst-coated CF cathodes [II].

For instance, ESVAR plays a crucial role in dictating the performance of MFCs [229]. When the ESVAR values are between 0.375–0.750 cm^2 cm^{-3}, the P_{max} values can be five times higher than when ESVAR is ≤ 0.375 cm^2 cm^{-3}. This is corroborated by the ESVAR value (0.49 cm^2 cm^{-3}) of the MFC cell used in this work [II], where the bare CF cathode achieved a P_{max} of 144.6 mW m^{-2}. These findings are consistent with the reported studies [28]. Notably, after incorporating the transition metal catalyst-coated cathode, P_{max} increased significantly, owing to additional ORR-active sites, thereby enhancing reaction kinetics. Despite this, MFC longevity requires a comprehensive examination of all these operational parameters, and among them, catalyst feasibility is a significant challenge to the commercialisation of the MFC technology [19, 29]. Moreover, the high peroxide yield of FeCo-NC900a material poses a significant challenge for MFC operation.

7.2. Electrocatalysis on Fe and Ce-doped ZIF-8@CNT composite catalysts

As discussed in the previous section, Fe and Co-based bimetallic catalysts showed impressive ORR performance in both alkaline and neutral electrolytes. More importantly, when these were integrated into a real fuel cell device, they

significantly enhanced the cell performance. However, the high peroxide yield of the FeCo bimetallic catalyst (close to 20%), can be detrimental to the lifespan of the MFC device. Moreover, the continuous migration of H^+ towards the cathode leads to a localised acidic microenvironment within the catalyst structure, which can trigger the Fenton reaction with Fe-based catalysts, generating reactive oxygen species (ROS) e.g., $^{\bullet}OH$. Consequently, ROS can damage the fuel cell catalysts and membrane. Therefore, the incorporation of cerium (Ce) near Fe sites provides a robust defence mechanism as studied in the work [III]. Ce acts as a free-radical scavenger when placed in proximity to Fe-N_x moieties, thereby refining the electronic structure by generating oxygen vacancies [230, 231].

7.2.1. Physical characterisations of the catalyst materials

Initially, the XRD analysis was used to examine the crystallographic structure of the catalyst materials. As illustrated in Figure 15a, all catalysts exhibited two characteristic peaks at 25.4° and 42.9°, reflecting (002) and (100) graphitic carbon planes. In addition to this, there were other small diffraction peaks at ca. 30.3°, 44.5° and 65°, demonstrating the existence of CeO_2, metallic Fe and small traces of FeCe alloys. Micro-Raman spectroscopy was performed to investigate structural defects and the degree of graphitisation in the prepared catalysts (Figure 15b). Each catalyst showed two broader peaks, attributed to D (~1354 cm^{-1}) and G (1584 cm^{-1}) bands. The D band was further deconvoluted into five Voigt-shaped bands (G, D1, D2, D3, and D4) to provide additional information on the nature of defects formed within the catalysts, as shown for the Fe_1Ce_1@N-C catalyst in Figure 15c. The I_{D1}/I_G ratio was then determined for all catalysts to estimate the structural disorder. Notably, the greater value for Fe_1Ce_1@N-C (1.87) catalyst compared to Fe_1Ce_2@N-C (1.64) and Ce@N-C (1.55) catalysts suggests a higher order of structural defects in the first catalyst. This defective structure is advantageous for ORR electrocatalysis.

N_2 physisorption analysis was performed to assess the specific surface area and pore features of the prepared materials. Each catalyst exhibited type I and II isotherms, with H3 hysteresis, indicating a micro-mesoporous structure of the materials (Figure 15d) according to the IUPAC classification. Indeed, it also represents a smaller proportion of microporosity in these materials. The pore-size distribution is presented in the inset of Figure 15d. Notably, Table 4 showed that the Ce@N-C catalyst exhibits the highest S_{BET} and V_{tot} values. After the incorporation of Fe, a substantial drop in S_{BET} to about 300 $m^2\ g^{-1}$ and V_{tot} to 0.06 $cm^3\ g^{-1}$ indicates a partial occupation of micropores. While a higher S_{BET} suggests higher electrocatalytic activity, the delicate balance between micropores and mesopores ultimately dictates the electrolyte's access to the active sites. Too few micropores compromise active-site density, while excessive mesopores significantly increase charge-transfer resistance. The Ce@N-C and Fe_1Ce_2@N-C catalysts possess a majority of mesopores, which, under fuel cell conditions, improve mass-transfer processes but, due to their low active-site density, simultaneously dramatically reduce electrocatalytic processes.

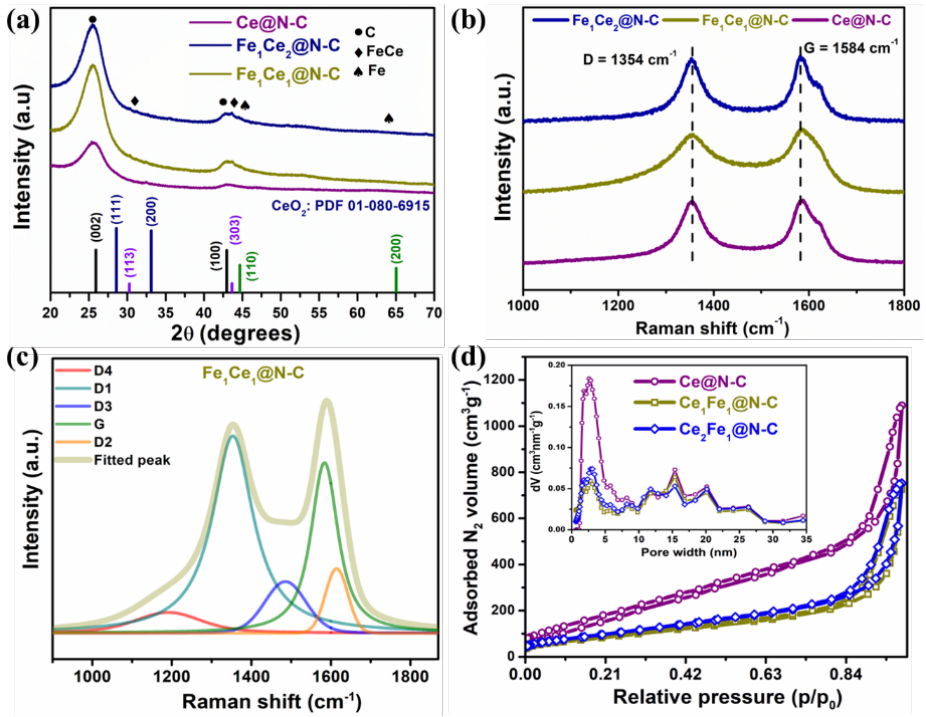

Figure 15. (a) X-ray diffraction patterns, (b) Micro-Raman spectrum showing D and G bands, (c) deconvoluted Raman spectra of Fe_1Ce_1@N-C catalyst, (d) N_2 physisorption isotherms with inset showing pore size-distribution for all catalysts.

Table 4. Specific surface area and porosity features of the prepared catalyst materials.

Catalyst material	S_{BET} ($m^2\ g^{-1}$)	V_μ ($cm^3\ g^{-1}$)	V_{tot} ($cm^3\ g^{-1}$)	Sa_μ ($m^2\ g^{-1}$)	Sa_m ($m^2\ g^{-1}$)
Ce@N-C	580	0.11	1.18	125	379
Fe_1Ce_1@N-C	301	0.06	0.71	92	183
Fe_1Ce_2@N-C	350	0.05	0.79	79	211

To examine the chemical states and surface bonding configurations, XPS analysis was performed on all the materials. As shown in Figure 16a, the XPS wide scan spectra revealed that all catalysts contain Ce, C, N and O, with Fe present only in the bimetallic catalysts as expected. The deconvoluted N1s core-level spectra of the catalysts are presented in Figure 16b. Each catalyst showed six distinct sub-peaks attributed to imines, pyridinic-N, pyrrolic-N, M-N_x, graphitic-N and bulk N-H. Furthermore, comparing the key N-species across all the materials demonstrated that the Fe_1Ce_1@N-C catalyst has a higher content of these N-species, particularly pyridinic-N and M-N_x sites (Figure 16c). This enhances electron transport within the carbon framework, thereby increasing ORR electrocatalytic activity. The detailed Fe2p XPS spectra (see Figure 2e in the article [III])

displayed two distinct, broader peaks centred at ~710.8 and ~724.4 eV, which were assigned to the $Fe2p_{3/2}$ and $Fe2p_{1/2}$ spin-orbit components. The chemical bonding configuration of Ce was examined using high-resolution XPS spectrum in the 3d region (see Figure 2f in the article [III]). The deconvoluted Ce3d spectra showed four different signals located at ~882.5 eV (u), ~886.2 eV (u′), ~890.7 eV (u″), and ~898.8 eV (u‴), that were assigned to $Ce3d_{5/2}$, and the peaks centred at ~900.9 eV (v), ~904.9 eV (v′), ~909.3 eV (v″), and ~917.7 eV (v‴) correspond to $Ce3d_{3/2}$, respectively. Most importantly, the peaks assigned as u′ and v′ indicate $3d^{10}4f^{1}$ electronic configuration of Ce^{3+}, whereas the other six peaks are attributed to Ce^{4+} exhibiting $3d^{10}4f^{0}$ electronic configuration.

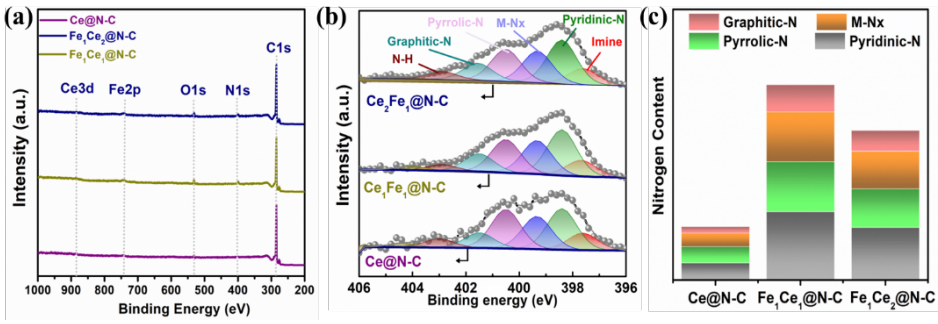

Figure 16. (a) XPS wide scan spectra, (b) comparative high-resolution N1s XPS spectra and (c) relative surface content of key nitrogen species across the prepared materials.

The SEM images were captured to investigate the surface morphology of the catalysts. As shown in Figure 17, all catalysts formed a randomly oriented, densely packed network of MWCNTs, ensuring high electrical conductivity throughout the carbon matrix. However, due to the limited magnification of the SEM method, STEM and STEM-EDX analyses were performed to achieve higher atomic-scale resolution (Figure 18). The HAADF-STEM image in Figure 18a shows CNTs interwoven with irregularly shaped carbonaceous fragments, forming an interconnected structure.

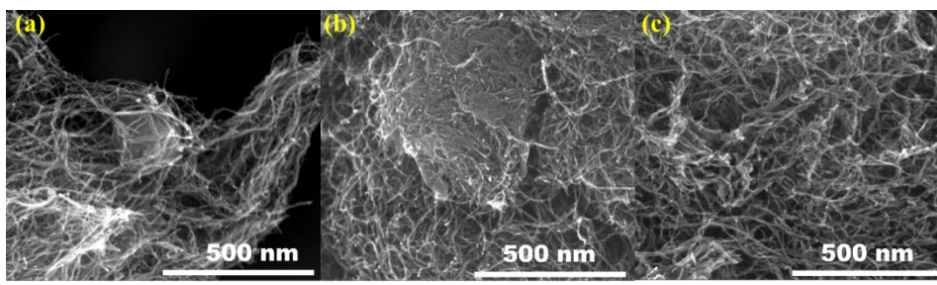

Figure 17. SEM images of (a) Ce@N-C, (b) Ce_1Fe_1@N-C and (c) Ce_2Fe_1@N-C catalysts.

The subsequent STEM image at 2 nm represents a homogeneous distribution of numerous bright spots, a signature of atomically dispersed M-N_x moieties. The EDX mapping (Figure 18d-f) confirms a uniform dispersion of C, N and Ce in Ce@N-C catalyst, while the elemental mapping in Figure 18 j-l shows uniformly dispersed C, N, O, Fe and Ce elements for Fe_1Ce_1@N-C catalyst. Moreover, the appearance of bright spots for Fe_1Ce_1@N-C catalyst shows that Fe and Ce are atomically dispersed within the carbon structure, facilitating electrocatalytic activity. The MP-AES analysis was conducted to determine the bulk metal content of Fe, Ce and Zn in all catalysts, as shown in Table 5. These results revealed that Fe incorporation favours the volatilisation of Zn, creating a more defect-rich structure. Previous studies suggest that Zn^{2+} sites can be substituted by Fe^{2+} during pyrolysis due to the similar local coordination environment and ionic radii [232]. Furthermore, the stabilisation constants of Fe^{2+} with 2-methylimidazole (2mIm) ligands make this substitution more favourable. This phenomenon is supported by the MP-AES findings, which show that the FeCe bimetallic material has approximately 83% lower Zn content.

Table 5. Bulk content of Fe, Ce, and Zn metals (wt%) determined by MP-AES analysis.

Element	Ce@N-C	Ce_1Fe_1@N-C	Ce_2Fe_1@N-C
Zn	1.072	0.119	0.013
Fe	0.038	1.653	1.560
Ce	0.838	1.643	2.507

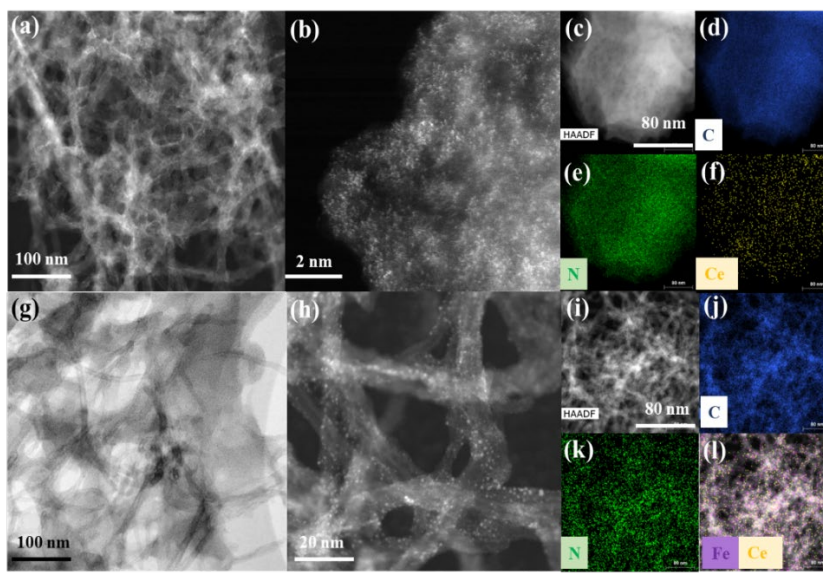

Figure 18. (a, b, c) HAADF-STEM images, (d-f) EDX mapping for Ce@N-C catalyst, (g) BF-STEM image, (h) HAADF-STEM image showing the bright spots and (j–l) the elemental mapping for Fe_1Ce_1@N–C catalyst.

7.2.2. Electrochemical performance of the catalysts

The ORR performance of the designed catalysts was evaluated using the RDE and RRDE techniques. Initially, the CVs were recorded in O_2- and Ar-saturated 0.1 M PBS (pH 7), as shown in Figure 19. For each catalyst, a distinct sharp reduction peak was observed, indicating pronounced electrocatalytic activity for ORR. Intriguingly, the most positive peak potential for Fe_1Ce_1@N-C material reflects its superior ORR activity. Furthermore, its higher capacitive currents in Ar-saturated CV indicate the characteristic of the double-layer charge-discharge process. The RDE polarisation curves at 1900 rpm were acquired to assess the catalysts performance. As shown in Figure 20a, Fe_1Ce_1@N-C material exhibited the highest $E_{1/2}$ of 0.76 V vs RHE, close to that of the commercial Pt/C catalyst ($E_{1/2}$ = 0.81 V). The ORR at the Ce@N-C catalyst commenced at 0.82 V, while a more positive E_{onset} was witnessed for the Fe_1Ce_1@N-C material (0.87 V). This is attributed to the higher N content of the bimetallic catalyst, especially the well-exposed M-N_x moieties, which are widely considered the primary active sites for ORR electrocatalysis. Intriguingly, this catalyst outperformed the FeCo-N-C@900 catalyst [II] by about 50 mV in the $E_{1/2}$, underscoring the advantage of Ce incorporation. To evaluate the reaction kinetics, the RDE polarisation curves were measured at different electrode rotation rates, as shown in Figure 20b. Subsequently, the K-L plot constructed from these polarisation curves showed good linearity and parallelism, reflecting the first-order reaction kinetics (Figure 20c). To gain further insight into the ORR pathway, the RRDE analysis was performed to estimate the peroxide yield and the number of electrons transferred during ORR (Figure 20d). Notably, the Fe_1Ce_1@N-C material yielded about 5% H_2O_2 yield, with n value approaching 3.9, which indicates a predominant $4e^-$ ORR pathway. More importantly, its performance matches the outcome of Pt/C catalyst ($\%H_2O_2 < 2\%$, $n > 3.9$), establishing a breakthrough activity in neutral solution. These findings suggest that Ce acted as a free-radical scavenger and promoted the electrocatalytic activity of the Fe-N_x centres. The unique electronic properties of Ce^{3+} tailor the catalytic environment of FeCe dual-metal sites [230, 231]. The lone pair on Ce exhibits a stronger coordination tendency with the neighbouring Fe atoms, inducing a local charge imbalance that promotes coordination vacancies for O_2 adsorption. The presence of these vacancies encourages the adsorption of O_2 molecule in a side-on or bridge orientation across the two metal sites, thereby exerting more strain on the O=O bond [231].

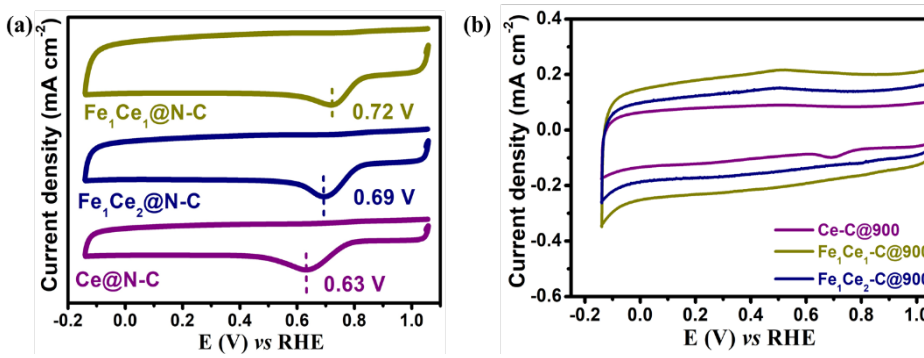

Figure 19. CV curves at a scan rate of 10 mV s^{-1} in (a) O_2- and (b) Ar-saturated 0.1 M PBS for all catalysts.

The electron transfer from the Ce 4f orbital to the Fe 3d orbitals optimises the Fe d-band centre, facilitating electron-transfer kinetics. Evidently, the hybridisation of Fe3d and Ce4f orbitals significantly reduces the band gap and enhances electron delocalisation in FeCe bimetallic materials. Consequently, this minimises charge-transfer resistance and facilitates ORR kinetics. These results provide strong evidence of how the coordination microenvironment of Fe influences the electronic structure and reaction kinetics by optimising the adsorption energetics of oxygen intermediates. In contrast, Co lacks the dynamic redox-shift capabilities and bonding flexibility of the 4f orbitals in Ce. Therefore, the rigid electronic structure of the FeCo bimetallic catalyst leads to stronger binding with the *OOH intermediate and poorer pathway selectivity than FeCe [125, 126, 231]. Besides the electrocatalytic activity of the catalyst materials, their electrochemical stability dictates their applicability in long-lasting energy conversion devices.

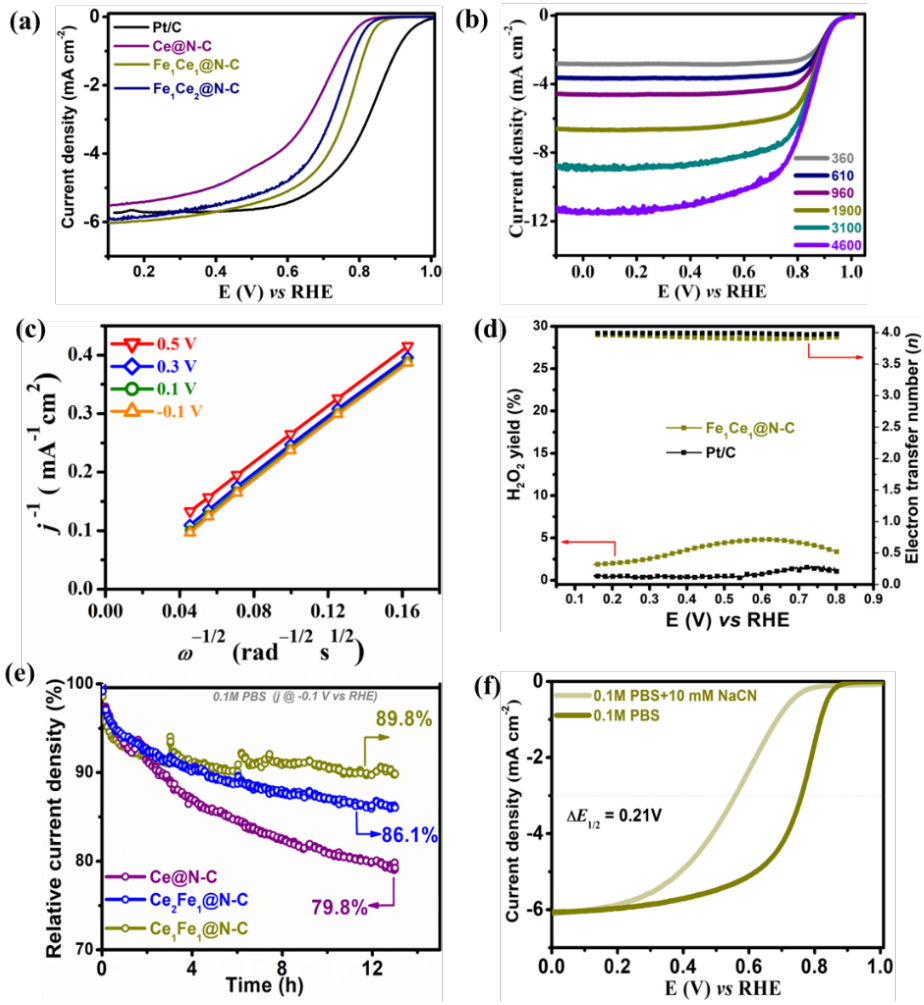

Figure 20. (a) RDE polarisation curves recorded in O_2-saturated 0.1 M PBS at 1900 rpm and 10 mV s^{-1}, (b) RDE polarisation curves at different electrode rotation rates and (c) respective K-L plot for Fe_1Ce_1@N-C catalyst, (d) H_2O_2 yield and *n* value as a function of potential for Fe_1Ce_1@N-C and Pt/C catalysts, (e) current-time responses recorded at -0.1 V *vs* RHE for all catalysts at 1900 rpm, (f) RDE polarisation curve at 1900 rpm before and after the addition of 10 mM NaCN to 0.1 M PBS.

To assess the stability of the Fe_1Ce_1@N-C catalyst, current-time responses were recorded at a constant potential of -0.1 V vs RHE at 1900 rpm for 13 h (Figure 20e). As shown in the stability test results, the Fe_1Ce_1@N-C catalyst retained about 90% of its initial current density, followed by Fe_1Ce_2@N-C and Ce@N-C. This indicates the robust structural integrity of the former catalyst. Furthermore, the cyanide poisoning tests were conducted by acquiring an RDE polarisation curve in 0.1 M PBS solution containing 10 mM NaCN at 1900 rpm (Figure 20f).

Evidently, the Fe_1Ce_1@N-C catalyst showed a significant loss in its ORR activity, demonstrated by a drop of over 200 mV in its $E_{1/2}$ value. This strong suppression provides conclusive evidence that the M-N_x sites were the main driver of the ORR process in FeCe dual-metal electrocatalyst.

7.2.3. Microbial Fuel Cell performance

As discussed in Section 4.2, the ORR kinetics play a central role in governing power performance and maintaining the functionality of anodic bacterial biofilm in MFC operation. The MFC with bare CP cathode (MFC-Con) achieved a steady-state OCV of 437.5 ± 10.6 mV after 2–3 weeks of operation, indicating an ongoing enrichment. The OCV continued to increase, attaining a steady state condition after 4–5 weeks of operation, demonstrating the enrichment of a mature EAB at the anode. Intriguingly, MFCs equipped with a Fe_1Ce_1@N-C-modified CP cathode exhibited an OCV of 0.882 V, attributable to faster intrinsic cathode reaction kinetics. To assess the MFC performance, polarisation and power density curves were recorded as the external resistance decreased from 90 kΩ to 10 Ω. The results obtained are presented in Figures 21a and b. The MFC-Fe_1Ce_1 achieved the highest P_{max} of 200 mW m^{-2}, followed by Pt/C, Ce@N-C and bare CP cathode under identical conditions. Interestingly, the Fe_1Ce_1@N-C catalyst outperformed the Pt/C catalyst under MFC conditions; however, the half-cell RDE tests showed the opposite (Figure 20a). This discrepancy arises from distinct MFC operating conditions, in which the dynamic interplay between the PEM and EAB at the anode collectively determines cathode performance. The ohmic region of the polarisation curves was linearly fitted to extract the R_{int}, and a similar resistor was connected across the anode and cathode to operate the MFC in closed-circuit mode. The operating cell voltage of MFC-Fe_1Ce_1 and MFC-Pt was 433.7 ± 21.8 mV and 379.4 ± 17.8 mV, against the external resistance of 450 and 500 Ω, respectively. As illustrated in Figure 21c, the MFC-Fe_1Ce_1 showed superior operational stability over a period of 600 hours compared to MFC-Pt.

Furthermore, MFC-Fe_1Ce_1 achieved a remarkable COD removal efficiency of 81.1 ± 7.3%, which for MFC-Pt was 76.8 ± 3.8% (Figure 21d). These findings provide compelling evidence that electrochemical oxidation kinetics at the anode are directly influenced by the ORR kinetics at the cathode. The excellent ORR electrocatalytic activity of the Fe_1Ce_1@N-C material facilitated proton and electron consumption, thereby improving the anodic metabolic oxidation rate and boosting the MFC bioenergy generation performance. However, compared to the MFC performance of the FeCo-N-C@900 catalyst [II], Fe_1Ce_1@N-C catalyst significantly underperformed in terms of P_{max} values. This can be ascribed to the large interelectrode distance, the suboptimal ESVAR value and the completely distinct MFC configurations. In this work, an H-shaped MFC cell with a working volume of 500 mL was used, which is 20 times bigger than the MFC cell used in article [II], where the diffusion of reactants is relatively faster due to a minimal distance of 2.5–3 cm between the electrodes. Therefore, their direct comparison is difficult.

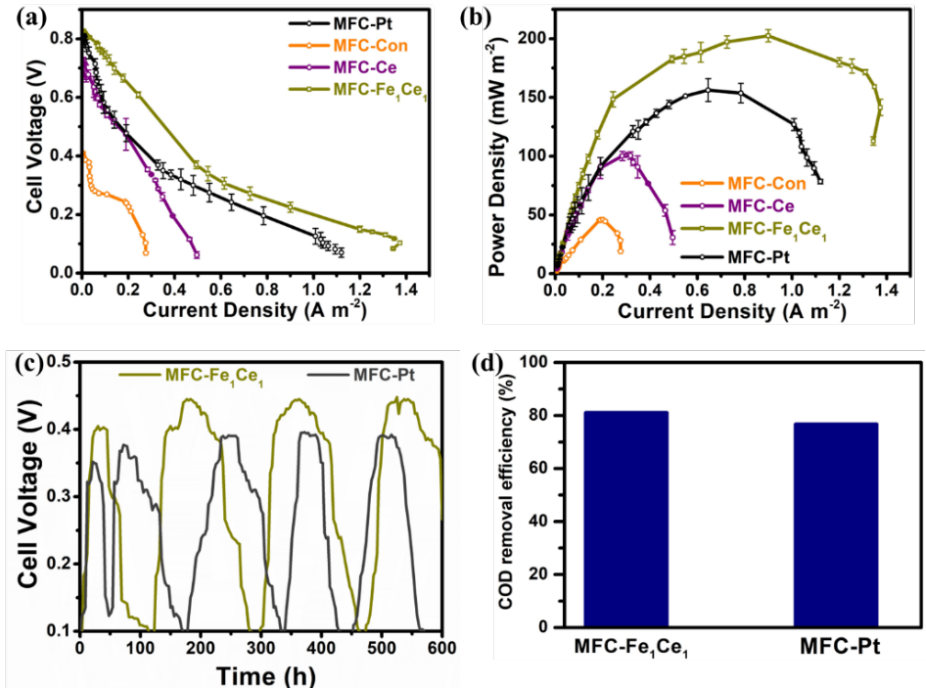

Figure 21. MFC (a) polarisation and (b) power density curves, (c) operational stability over a period of 600 h with Fe1Ce1@N-C and Pt/C cathode catalysts, and (d) respective COD removal efficiency.

These results demonstrate the challenges of scaling up MFC technology. Nevertheless, ORR performance remains the primary bottleneck for these devices, fuelling the ongoing scientific efforts to address these limitations.

7.3. Electrocatalysis on Fe-N_4 macrocycle-derived catalysts

As discussed so far, the designed FeCo [II] and FeCe [III] bimetallic catalysts have demonstrated attractive electrocatalytic ORR performance and enhanced MFC bioenergy generation and water treatment efficiency. However, these dual-metal sites often create a competitive electrocatalytic environment, suppressing the intrinsic activity of Fe-based active sites. Therefore, in this work [IV], we have developed a unique in-situ nitridation strategy to thermally transform FePc into a hybrid Fe- and Fe_4N-decorated Fe-N-C material. The high-temperature pyrolysis of a citric acid-melamine mixture yielded a nitrogen-doped carbon (NC) nanosheet-like structure that facilitated interaction with FePc via π-π stacking. The specific alignment of Fe_4N, phased in the vicinity of Fe-N_x moieties, promoted charge-transfer kinetics and optimised the adsorption energetics of oxygen intermediates, thereby boosting the ORR kinetics.

7.3.1. Physical characterisation of the catalysts

At first, the XRD analysis was performed to inspect the crystallographic structure of these materials. As shown in Figure 22a, the NC catalyst revealed two broader diffraction peaks centred at 25.4° and 43.1°, corresponding to (002) and (100) reflections of graphitic carbon. Subsequently, the FePc/NC material showed the characteristic peaks of molecular FePc at ~6.9° and ~15.5° (outlined in black), in addition to a diffraction peak at 43.1°, which reflects the (100) plane of graphitic carbon. Intriguingly, after the in-situ nitridation step, the impregnation of Fe/Fe_4N phases tuned the crystal structure of the resulting Fe/Fe_4N@Fe-N-C catalyst. The XRD pattern for this material showed peaks at 44.6° and 64°, reflecting the (110) and (200) planes of metallic α-Fe. Furthermore, the diffraction peaks at 40.8°, 47.5° and 69.4° are attributed to the cubic structure of Fe_4N nanoparticles. These embedded Fe/Fe_4N phases act as electronic promoters, lowering the charge-transfer resistance at the active sites [160].

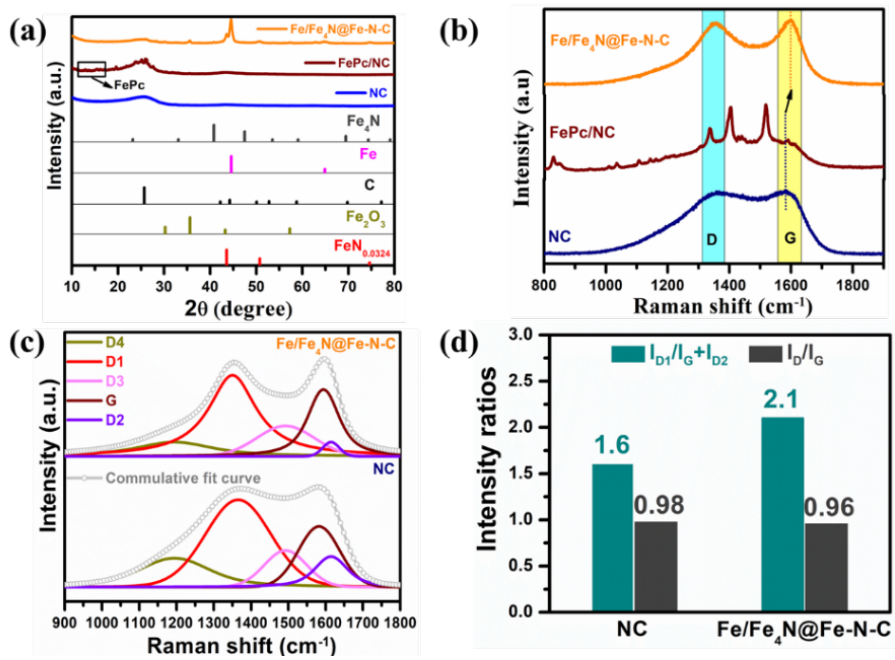

Figure 22. (a) X-ray diffraction patterns and (b) Micro-Raman spectra for all catalysts, (c) deconvoluted Raman spectra for Fe/Fe_4N@Fe-N-C catalyst, and (d) respective D and G band intensity ratios for each catalyst [IV].

The Raman spectroscopy analysed the surface defects and graphitisation levels in the prepared materials. The NC catalyst showed two distinct, broader peaks at ~1353 and ~1584 cm^{-1}, corresponding to the D and G bands, respectively. The FePc/NC material exhibited split D/G bands, indicating interactions between the FePc π-orbitals and the carbon framework (Figure 22b). Subsequently, the loss

of these raw FePc peaks in the Fe/Fe_4N@Fe-N-C catalyst suggests a complete transformation of Fe-N_4 macrocyclic compound into Fe-N-C architecture. The intensity ratio of the D and G bands (I_D/I_G) provided primary information regarding the defect-rich structure of the resultant hybrid catalyst. Moreover, the I_{D1}/I_G+I_{D2} ratio obtained from the deconvolved Raman spectra of this catalyst confirmed a high density of structural defects and graphitisation formed after the in-situ nitridation process (Figure 22c, d). Such a two-faced carbon structure is highly beneficial to ORR electrocatalysis.

To examine the specific surface area and pore size distribution characteristics, N_2 physisorption tests were performed on NC and the Fe/Fe_4N@Fe-N-C catalyst. The N_2 adsorption-desorption isotherms for these catalysts are presented in Figure 23a. Notably, the initial N_2 uptake at low relative pressure ($P/P_0 < 0.1$) and at higher relative pressure ($P/P_0 > 0.4$) confirms the existence of both micro-pores and mesopores, characteristic of a Type IV isotherm with an H3-type hyste-resis loop according to IUPAC classification. The pore-size distribution shown in Figure 23b revealed that the NC catalyst has a higher mesopore surface area, which was significantly compromised after the impregnation of Fe/Fe_4N phases. The quenched solid density functional theory (QSDFT) model analysis indicates that, while the total micropore volume (V_μ = 0.5 cm^3 g^{-1}) for both materials remains unchanged, the micropore surface area (Sa_μ) for Fe/Fe_4N@Fe-N-C shows a slight increase (Table 6). This additional microporosity can host to a higher number of M-N_x active sites.

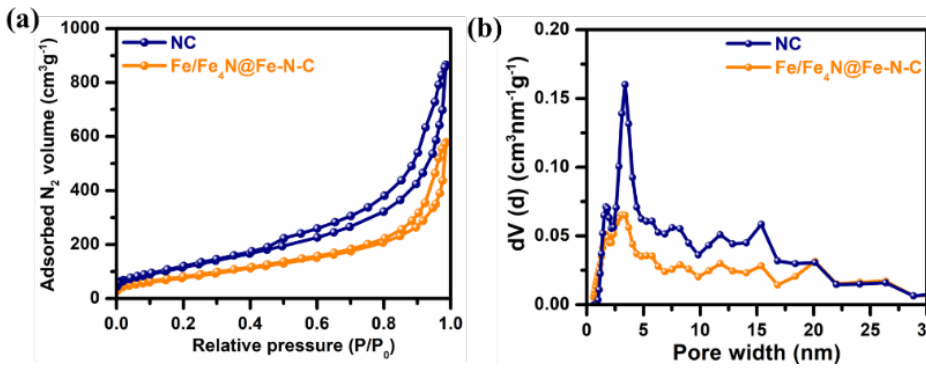

Figure 23. (a) N_2 physisorption isotherms and (b) PSD for NC and Fe/Fe_4N@Fe-N-C catalysts [IV].

Table 6. Specific surface area (S_{BET}), volume of micropores (V_μ), total pore volume (V_{tot}), and specific surface area of micropores (Sa_μ) and mesopores (Sa_m).

Catalyst material	S_{BET} (m^2 g^{-1})	V_μ (cm^3 g^{-1})	V_{tot} (cm^3 g^{-1})	Sa_μ (m^2 g^{-1})	Sa_m (m^2 g^{-1})
NC	416	0.05	0.99	65	299
Fe/Fe_4N@Fe-N-C	278	0.05	0.61	69	173

The XPS analysis was performed to shed light on the chemical states and bonding configuration within the prepared catalyst materials. The wide-scan spectrum in Figure 24a showed that each catalyst contained C, N and O, while FePc/NC and Fe/Fe_4N@Fe-N-C materials showed Fe in addition to these key elements. The comparative high-resolution C1s XPS spectra for the catalysts are presented in Figure 24b. Notably, the NC material showed six deconvoluted peaks, indicating the presence of sp^3- and sp^2-hybridised carbon, consistent with a disordered structure. Furthermore, after FePc incorporation, the progressive increase in sp^3 character indicates a substantial loss in overall structural periodicity.

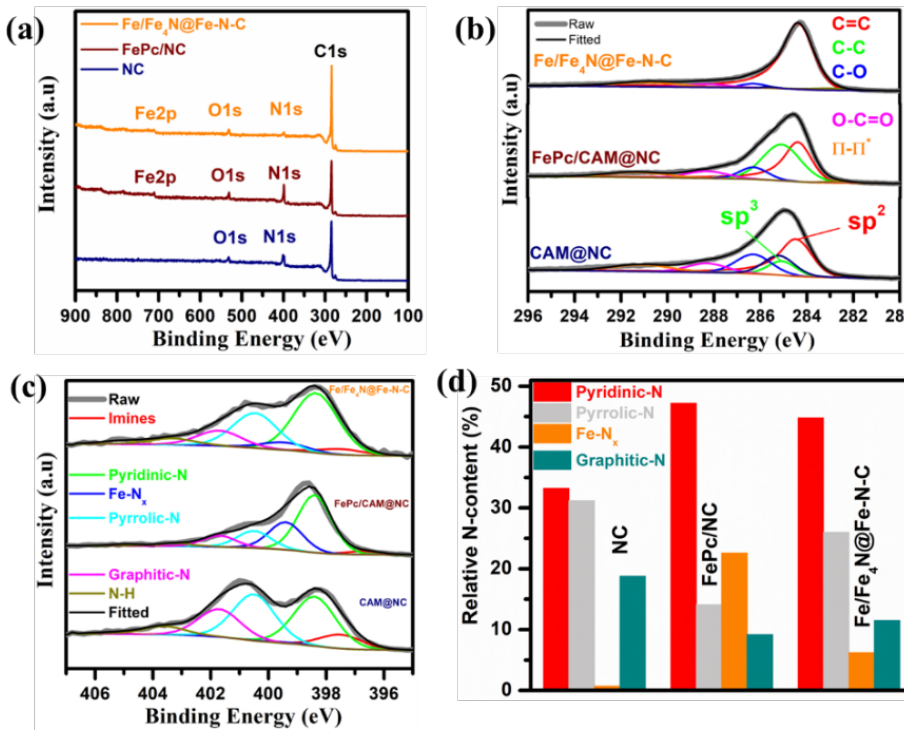

Figure 24. (a) XPS survey spectra, (b) detailed C1s XPS spectra, (c) detailed N1s XPS spectra and (d) relative N-content across all the catalyst materials [IV].

Interestingly, in the hybrid catalyst, the absence of sp^3 character is a signature of a highly graphitised carbon framework, resulting from the contributions of Fe/Fe_4N phases and the second pyrolysis. These results provide strong evidence that the proposed strategy has effectively altered the electronic structure of the Fe-N-C material. The deconvoluted N1s spectra displayed in Figure 24c showed key N-species, i.e. pyridinic-N, pyrrolic-N and graphitic-N for all catalysts, whilst a discernible peak for M-N_x sites was observed in Fe-containing materials. While all these N-centres are considered active for ORR electrocatalysis, M-N_x sites have attracted special attention due to the metal d-orbitals, which promote O_2 adsorption and its reduction via a direct $4e^-$ route. However, their specific role

is still a subject of debate. Notably, a shift in the binding energies of the N species for the hybrid catalyst indicates an altered electronic structure, possibly due to the incorporation of specific iron nitride species. Furthermore, the increase in graphitic-N content in the Fe/Fe4N@Fe-N-C material suggests enhanced electrical conductivity, which aligns well with the XRD and Raman analysis results. The detailed Fe2p XPS spectra for FePc/CAM@NC catalyst (see Figure 3f in the article [IV]) revealed a four-set of deconvoluted peaks, ascribed to $Fe2p_{3/2}$ and $Fe2p_{1/2}$ spin-orbital doublet at ~710.8 and ~724.2 eV, respectively. In addition, the ones at ~717.4 and ~731.8 eV correspond to the shake-up satellite peaks, suggesting that surface Fe exists in oxidised forms.

The surface morphology and elemental composition of the prepared materials were studied using SEM and EDX, respectively. The SEM images of FePc/NC catalyst show irregularly shaped aggregates with undefined surface boundaries (Figure 24a,b). This blocky morphology reduces reactant diffusion to the active sites and slows ORR kinetics at high current densities.

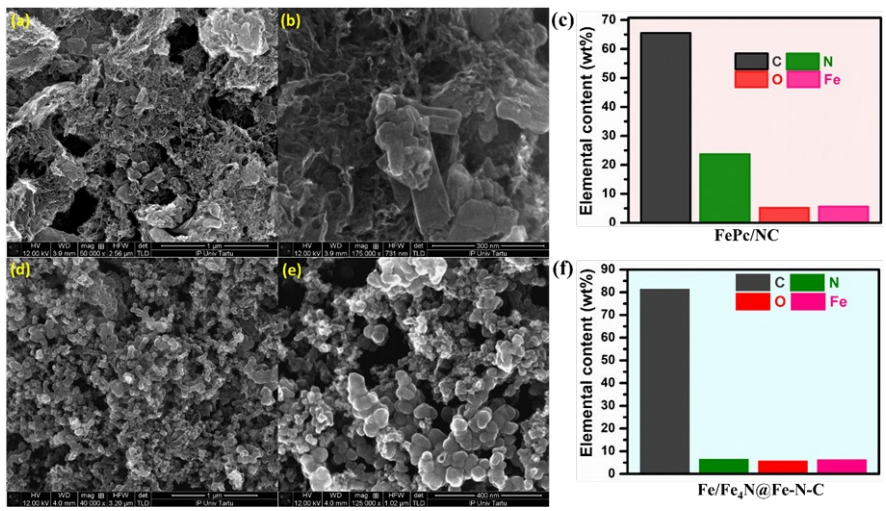

Figure 24. SEM images for (a, b) FePc/NC and (d, e) Fe/Fe_4N@Fe-N-C catalysts. The content of C, N, O, and Fe obtained from SEM-EDX analysis for (c) FePc/NC and (f) Fe/Fe_4N@Fe-N-C catalysts [IV].

In contrast, the Fe/Fe_4N@Fe-N-C material has a much finer, more homogeneous morphology, consisting of smaller spherical particles, offering a favourable architecture for superior mass-transport kinetics (Figure 24d, e). SEM-EDX was used to determine the bulk elemental composition of these materials, as shown in Figures 24c and 24f. Notably, the Fe/Fe_4N@Fe-N-C material consists of a relatively greater carbon content, whereas the Fe loading (~6 wt%) remained consistent amongst both materials.

Further insights into the catalyst's structure at atomic-scale resolution were obtained by STEM analysis, as shown in Figure 25. The BF-STEM image for

Fe/Fe_4N@Fe-N-C catalyst shows spherical-shaped particles, while the HAADF-STEM images (Figures 25b, c) identified these as (111) plane of Fe_4N nanoparticle encased in graphitic carbon layers, evidenced by the lattice fringes with a d-spacing of 0.21 nm. The Fast Fourier Transform (FFT) analysis shown in Figure 25d further confirms this structural alignment. The HAADF-STEM images at higher magnification (Figures 25e, f) highlight numerous bright spots (yellow circles) reflecting atomically dispersed Fe-N_x sites in addition to large Fe clusters (green). These Fe-N_x centres are highly active for ORR electrocatalysis, while the Fe_4N nanoparticles encapsulated within the protective graphitic carbon layers promote electrical conductivity. The EDX elemental mapping in Figure 25h-k shows evenly distributed C, N, O and Fe. Similarly, the STEM images of the FePc/NC material show the typical nanosheet structure derived from the carbonisation of citric acid and melamine, as shown in Figure 25l. In the subsequent HAADF-STEM image, these bright spots suggest the atomic dispersion of FePc. The EDX mapping for the image shown in Figure 25n is presented in Figures 25o–r, where all the elements are homogeneously dispersed.

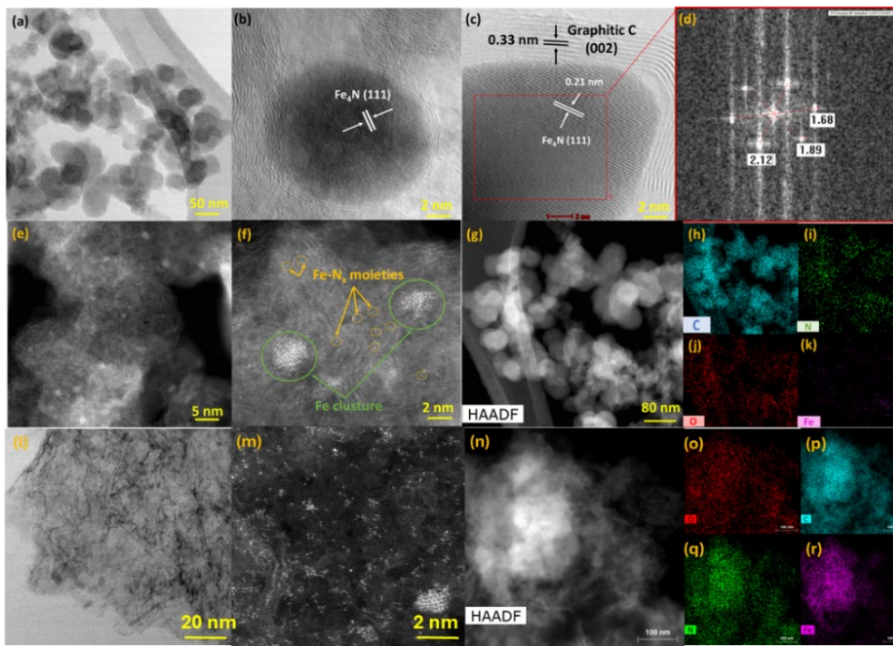

Figure 25. (a) Bright field (BF)-STEM image for Fe/Fe_4N@Fe-N-C catalyst, (b, c) Fe_4N nanoparticle encased in graphitic carbon layers, (d) FFT analysis, (e, f) HAADF-STEM image highlighting atomically dispersed Fe-N_x moieties (in yellow circles) and Fe clusters (in green circles), (g) HAADF-STEM image and, (h-k) its corresponding EDX mapping, (l) BF-STEM image showing the carbon nanosheet, (m) HAADF-STEM image at higher magnification showing a distribution of numerous bright spots, (n) HAADF-STEM image and (o-r) its respective EDX mapping for FePc/NC catalyst [IV].

7.3.2. Electrochemical performance of FePc-derived catalysts

The half-cell electrochemical tests with the prepared materials were performed in 0.1 M PBS solution. Initially, the RDE polarisation curves were acquired at 1600 rpm for each catalyst, as shown in Figure 26a. The NC materials exhibited the lowest $E_{1/2}$ of 0.49 V vs RHE, which significantly improved for FePc/NC material to 0.75 V vs RHE. This is attributed to the atomically dispersed and well-defined Fe-N_4 sites, which majorly contributed to this performance enhancement. Notably, the hybrid Fe/Fe_4N@Fe-N-C catalyst with an $E_{1/2}$ of 0.79 V vs RHE outperformed the other tested materials and reached close to the ORR activity of the commercial Pt/C catalyst ($E_{1/2}$ = 0.82 V). Furthermore, with an E_{onset} of 1.0 V, the hybrid catalyst demonstrated that the encapsulation of Fe/Fe_4N species significantly refined the material's structural and electronic properties. These findings are consistent with the outcomes of XPS and Raman spectroscopy analysis, which showed an improved graphitisation after the nitridation strategy. After that, the RDE polarisation curves were obtained at different electrode rotation rates (Figure 26b) and used to construct the K-L plots to study reaction kinetics (Figure 26c). The linearity and parallelism of these fitted K-L lines represent a predominant $4e^-$ ORR pathway.

Subsequently, the RRDE analysis was performed to determine the formation of peroxide and the *n* value during ORR. The ring currents for these materials are presented in Figure 26d. Notably, all catalysts exhibited some ring currents, indicating the formation of a detectable amount of H_2O_2 during the ORR process. The Fe/Fe_4N@Fe-N-C catalyst showed the lowest ring currents and a low H_2O_2 yield (< 2%), approaching that of Pt/C. Moreover, with an electron transfer number of 3.97, the Fe/Fe_4N@Fe-N-C catalyst enables a highly efficient $4e^-$ reduction pathway. These results strongly suggest that Fe/Fe_4N species modulate the electronic structure of the Fe d-band centre, thereby influencing the adsorption energetics of *OOH intermediate. Xiang et al. demonstrated that Fe_4N encapsulation within graphitic carbon layers can promote the hybridisation between the d-orbitals of Fe and p-orbitals of C and N. Using DFT calculations, they confirmed that this orbital overlap supports the initial adsorption and activation of the O_2 molecule [51]. Furthermore, the Gibbs free energy analysis indicated that the close alignment of Fe/Fe_4N with Fe-N_x centres aligns the energy levels toward the ideal value and enhances reaction kinetics [160, 233]. To assess the electrochemical stability of these materials, the current responses were recorded at a constant potential of -0.1 V vs RHE at 1600 rpm. As depicted in Figure 26f, the Fe/Fe_4N@Fe-N-C catalyst retained more than 81% of its initial current density after 15 h of continuous operation. This superior stability of the hybrid catalyst is attributable to the protected Fe_4N nanoparticles, which support electron-transfer kinetics. The post-stability SEM analysis confirmed the robust structural integrity of this catalyst.

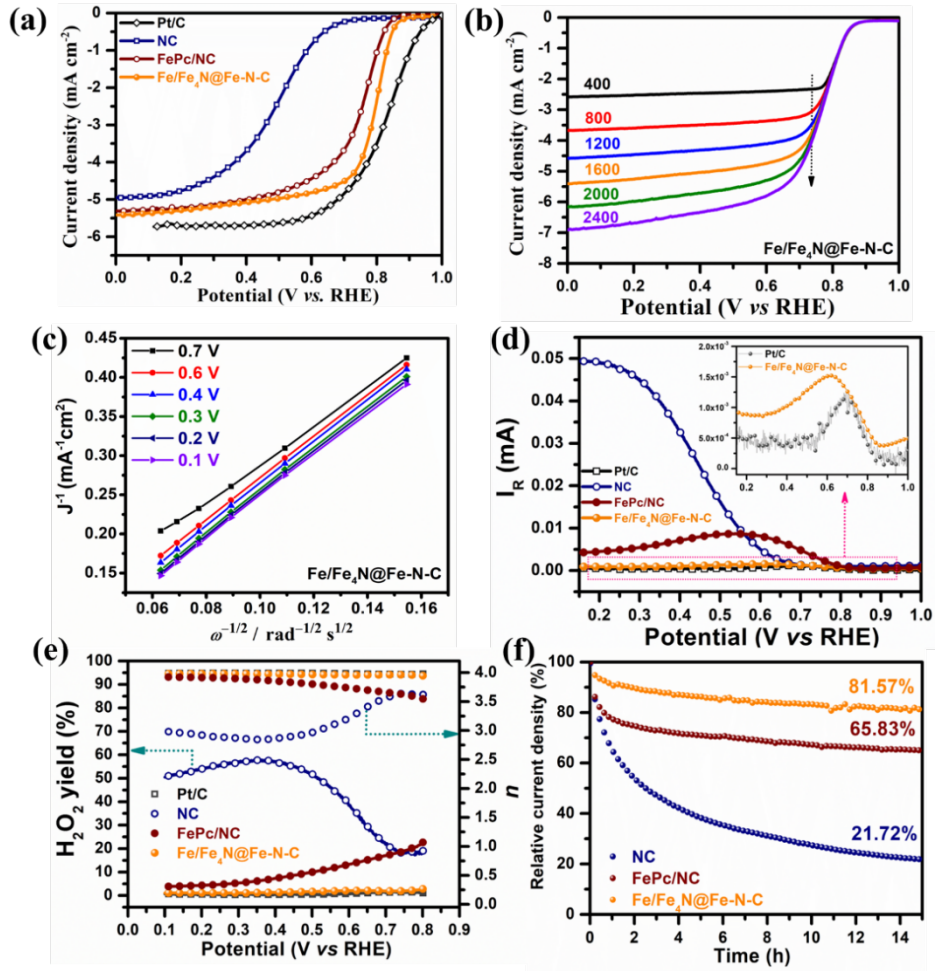

Figure 26. (a) RDE polarisation curve recorded in O_2-saturated 0.1 M PBS at 1600 rpm, (b) RDE polarisation curves at different electrode rotations rates and (c) corresponding K-L plot for Fe/Fe4N@Fe-N-C catalyst, (d) RRDE ring currents for all catalysts at 1600 rpm, (e) respective H_2O_2 yield and *n* value as a function of potential, (f) current-time responses collected at a potential of -0.1 V vs RHE at 1600 rpm for all catalysts [IV].

Furthermore, to confirm the role of Fe-N_x moieties, cyanide poisoning tests were performed in 0.1 M PBS solution containing 10 mM NaCN. The cyanide anions have a strong tendency to form an irreversible Fe-cyanide complex, restricting the reachability of O_2 molecules. The RDE polarisation curves shown in Figure 27a,b revealed a profound negative shift of about 0.37 V in the $E_{1/2}$ value for both catalysts after NaCN addition. This significant loss in the ORR activity across both materials provides compelling evidence that the Fe-N_x moieties were the dominant ORR-active centres. However, a slightly greater loss in the ORR activity of the Fe/Fe_4N@Fe-N-C catalyst indicates that it consists of a relatively

larger fraction of highly accessible Fe-N_x centres compared to FePc/NC catalyst. The SEM images in Figure 24 support these structural differences, where Fe/Fe_4N@Fe-N-C catalyst has a more open carbon structure that facilitates mass-transfer processes.

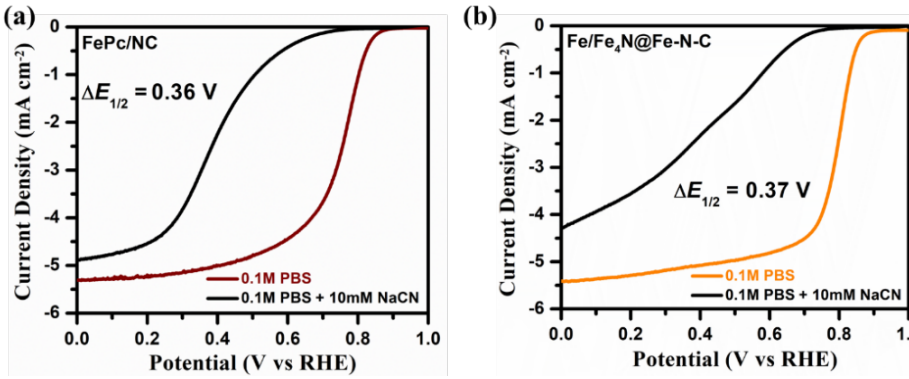

Figure 27. RDE polarisation curve at 1600 rpm before and after NaCN addition to 0.1 M PBS solution for (a) FePc/NC and (b) Fe/Fe_4N@Fe-N-C catalysts [IV].

These findings suggest that the in-situ nitridation strategy was highly effective in changing the electronic structure of the Fe-N-C material. Therefore, the resulting hybrid Fe/Fe_4N@Fe-N-C catalyst was selected for MFC application. Also, it should be noted that the Fe/Fe_4N@Fe-N-C catalyst exhibited the highest $E_{1/2}$ value of 0.79 V in 0.1 M PBS among all the catalysts studied in different articles within this PhD thesis, as other most promising catalysts in previous articles were Fe_1Ce_1@N-C ($E_{1/2}$ of 0.76 V) [III] and FeCo-N-C@900 ($E_{1/2}$ of 0.71 V) [II].

7.3.3. Microbial fuel cell performance

The MFC performance was evaluated with bare CP, Fe/Fe_4N@Fe-N-C and Pt/C-coated cathodes. The influence of the modified cathodes on the energy generation performance and wastewater treatment efficiency was systematically studied. The pre-acclimatised anodic biofilm [III] ensured non-limiting anode kinetics; therefore, the optimisation of cathode catalyst loading was investigated to reach the maximum MFC performance. The power density and polarisation curves of MFC equipped with different loadings of Fe/Fe_4N@Fe-N-C catalyst (0.2, 0.5 and 1.0 mg cm^{-2}) are presented in Figure 28b. Notably, the maximum power density (P_{max}) of MFC-0.2 was 152 mW m^{-2}, which significantly improved for MFC-0.5, reaching 277 mW m^{-2}. Intriguingly, at higher catalyst loadings, the MFC-1.0 showed a lower P_{max} of 205 mW m^{-2} under identical conditions. As illustrated in Figure 28a, at lower loadings, the low active-site density led to sluggish ORR kinetics, thereby reducing the power performance of MFC-0.2. In contrast, at the highest loadings, the active sites are deeply buried and inaccessible to reactants, resulting in poor ORR kinetics. However, at a loading of 0.5 mg cm^{-2}, the catalyst layer achieved an optimal balance between active site density and accessibility.

The MFC-0.5 performance was compared with MFC equipped with a bare CP cathode (MFC-Control) and a commercial Pt/C-coated cathode (MFC-Pt/C). As shown in Figure 28c, MFC-0.5 outperformed MFC-Pt/C by 77%, indicating faster reaction kinetics with the Fe/Fe_4N@Fe-N-C catalyst. It should be noted that overall MFC performance is governed by the dynamic interplay between the anode and cathode kinetics. Therefore, the COD removal efficiency of these MFCs was determined using the same method as used for the articles [II, III]. MFC-Control achieved a COD removal efficiency of 75%, indicating a mature EAB at the anode, with the uncoated cathode as the limiting factor. Apparently, the MFC-0.5 and MFC-Pt/C achieved COD removal of over 80%, clearly indicating that cathode kinetics directly affect the substrate oxidation rate. These results established a robust foundation for the development of Pt-free state-of-the-art catalysts for high-performance MFC devices.

The MFC performance discussed in articles [II, III, IV] shows consistent improvement in power generation, which is also consistent with the order of $E_{1/2}$ values from RDE studies of the M-N-C catalysts in these three investigations. Nevertheless, other factors, such as membrane biofouling, the thickness of anodic biofilm, interelectrode distance, etc., should be considered to establish a durable and scalable MFC technology [19, 127].

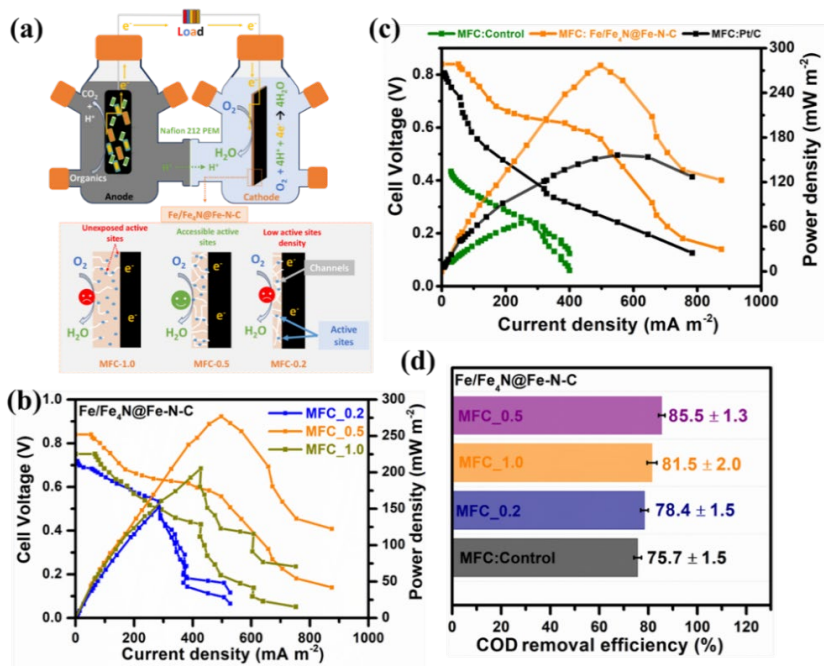

Figure 28. (a) Schematic illustration of the H-shaped dual chamber MFC setup, (b) polarisation and power density curves with Fe/Fe_4N@Fe-N-C cathode catalyst at different loadings, (c) polarisation and power density curves with optimised loading of Fe/Fe_4N@Fe-N-C cathode catalyst, uncoated cathode, and Pt/C cathode.

Table 7 summarises the M-N-C catalysts for MFC cathode applications prepared within this PhD thesis and relevant examples from the literature. A broad spectrum of monometallic and bimetallic catalysts has been designed and employed in MFC, influencing both energy generation and wastewater treatment efficiency. The COD is a measure of substrate (i.e., acetate) oxidation at the anode, indicating a well-functioning bacterial biofilm. Notably, the single chamber (SC) MFC achieved greater P_{max} values compared to the dual chamber (DC)-MFC. It should be noted that the diversity in electrode materials, catalyst loading, electrode surface area-to-anode volume ratio and distance between the anode and cathode plays a crucial role in high-performance MFCs [19, 29]. Typically, the SC-MFC uses an air-cathode and a shorter distance between the two electrodes, thereby reducing mass-transfer resistance. However, direct contact between the bacterial products and the catalyst layer raises durability concerns. In contrast, the DC-MFC setup alleviates this limitation and, with two distinct chambers, separates the anodic and cathodic electrochemical processes. Intriguingly, the use of DC-MFC with distinct shapes (such as classical H-shaped [III, IV], cubic, miniature-shaped, up-flow) in the studies summarised in Table 2, makes their inter-comparison difficult. Therefore, in addition to robust catalyst design, membrane fouling coupled with the aforementioned technical parameters, requires a thorough examination to evaluate the longevity of the MFC device.

Table 7. MFC performance of ZIF-8 and MPc-based catalysts prepared in this thesis in comparison with Pt-free cathode catalysts. The SC and DC represent single-chamber and dual-chamber MFC configurations, respectively.

Cathode catalyst	Cathode material	MFC type	P_{max} (mW m^{-2})	COD (%)	Ref.
FeCo-N-C@900	Carbon fiber	DC	1557	87.3	II
Fe_1Ce_1@N-C	Carbon paper	DC	200	81.1	III
Fe/Fe_4N@Fe-N-C	Carbon paper	DC	277	85.5	IV
Fe-BP(N)	Activated carbon	SC	2430*	-	[234]
Co-FePc/CDC	Activated carbon	DC	1500*	86	[235]
FePcMnO_x/MON	Carbon felt	SC	143	-	[219]
Fe-N/AC	Carbon cloth	DC	1092	-	[236]
FePc/CDC	Carbon paper	DC	82.6	88.4	[218]
FeAzPc-CNT	Carbon paper	SC	1540*	80	[237]
FePc/NGO	Carbon cloth	SC	280	-	[238]
C/FePc	Carbon cloth	SC	336.6	-	[239]
C-CoO_x-FePc	Carbon cloth	SC	654	-	[240]
a-MWCNT/FePc	Carbon cloth	SC	601	-	[241]
FePc/PID/CNTs	Carbon cloth	SC	800	-	[242]
Fe(A)-NC	Carbon cloth	SC	~2000	93.7	[243]
Cu-N/C@Cu-2	Carbon cloth	SC	~580	95.5	[244]
ZIF(0.5)-MFC	SS mesh	SC	2100	90.6	[207]
Fe@CNT@CuNC	Titanium mesh	SC	1600	-	[245]
Fe/Fe_3C@NiNC	Titanium mesh	SC	1600	-	[174]

7.4. Electrocatalysis on Mn-doped ZIF-8@CNT composite catalysts

This work [V] is encouraged by the findings of articles [I, II, III], which report that ZIF-8@CNT composite-derived bimetallic catalysts exhibit excellent porous morphology and electrocatalytic ORR activity. However, these materials underwent metal agglomeration, lowering the accessible M-N_x moieties. It is often assumed that increasing the loading of ZIF-8 will yield higher N content and, consequently, a higher density of M-N_x centres. However, this assumption is not fully accurate, as the ZIF-8 amount ultimately dictates the pore architecture of the resulting M-N-C material. Therefore, this part of the thesis investigated the key role of ZIF-8 loading on the resulting structural integrity and the anchoring capacity of Mn-N_x sites within the evolving NC framework. As stated in section 6.3., Mn/Zn-NC@CNT_x (x = 2, 5, 10, 20, 30) catalysts were designed to study the influence of ZIF-8 loading and Zn-retention. Subsequently, the acid-treatment and re-pyrolysis of the optimised Mn/Zn-NC@CNT_x catalyst eliminated the residual moieties and refined the electronic/textural features of the resulting Mn-N-C@CNT material.

7.4.1. Physical characterisation of the catalysts

XRD was used to investigate the crystal structure of the prepared materials. As shown in Figure 29a, the diffraction patterns of Mn/Zn-NC@CNT_10, Mn/Zn-NC@CNT_10@HCl and M-N-C@CNT catalysts displayed two broad peaks at around 26° and 43°, reflecting (002) and (100) planes of graphitic carbon. Interestingly, these diffraction patterns do not show the presence of any metallic Mn/Zn nanoparticles or their related compounds. This primarily suggests that Mn is atomically dispersed within the NC matrix, possibly as Mn-N_x sites. Raman spectroscopy analysis was performed to study defects and structural order in these materials. All catalysts showed the typical D and G band centred at 1352 and 1584 cm^{-1}, respectively. As illustrated in Figure 29b, Mn/Zn-NC@CNT_10 catalyst with an I_D/I_G ratio of 1.04 suggests a defect-rich carbon structure. Furthermore, the highest $I_{D1}/(I_G + I_{D2})$ ratio for this catalyst indicated an increased graphitisation (see Fig. S1, Table S1 in the article [V]).

The N_2 physisorption isotherms are presented in Figure 29c. Evidently, the resultant M-N-C@CNT catalyst exhibited the highest S_{BET} and V_{tot} amongst the tested materials (Table 8). Moreover, this material possessed a higher volume of micropores, reflecting a high density of active sites with superior accessibility. In contrast, the optimised Mn/Zn-NC@CNT_10 catalyst has relatively lower V_{tot} than the pristine Zn-NC material. This suggests that the residual Zn species have occupied the mesopores, thereby reducing the S_{BET}. Overall, it can be inferred that incorporating Mn into the ZIF-8-derived NC framework has profoundly refined the textural features. In particular, the significant enhancement in the pore architecture of Mn-N-C@CNT material supports the hypothesis of accelerated Zn volatilisation after the acid-treatment and re-pyrolysis step [205, 209]. Further-

more, such structural morphology is highly beneficial for ORR electrocatalysis in practical fuel cell conditions.

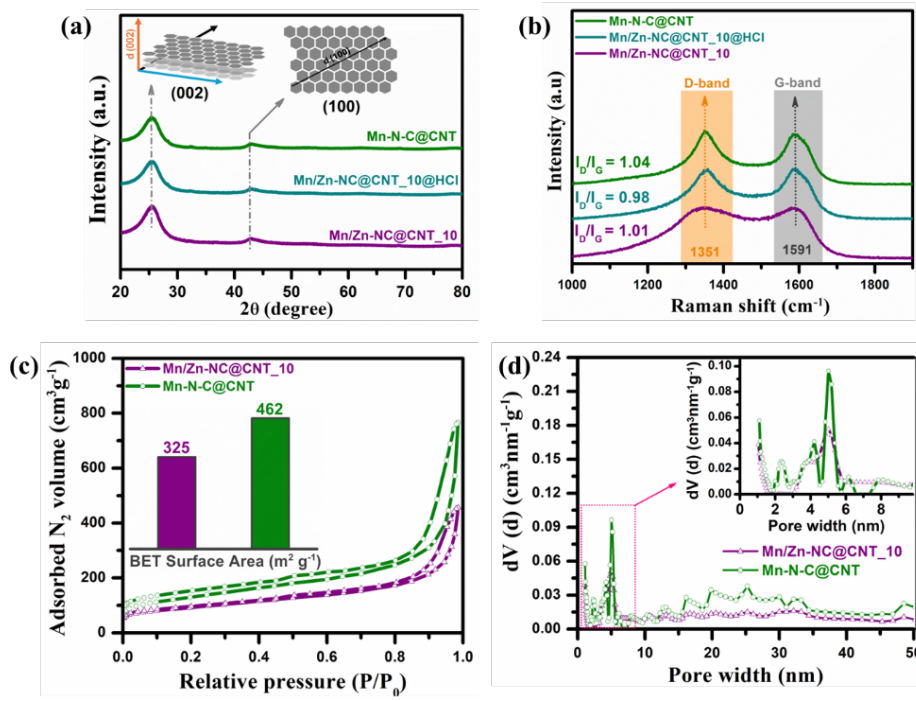

Figure 29. (a) XRD patterns, (b) Micro-Raman spectroscopy results, (c) N_2 adsorption-desorption isotherms and (d) pore size distribution analysis for the designed materials.

Table 8. Specific surface area, total pore volume and micropore volume for the catalyst materials.

Catalyst material	S_{BET} (m^2 g^{-1})	V_{tot} (cm^3 g^{-1})	V_{μ} (cm^3 g^{-1})
Zn-NC	317	0.7	0.01
Mn/Zn-C@CNT 10@HCl	325	0.49	0.07
Mn-N-C@CNT	462	0.78	0.11

XPS was utilised to scrutinise the chemical states and bonding configuration within the catalysts. As shown in Figure 30a, the wide-scan XPS spectra show the presence of C, N, O, Mn and Zn. Notably, the presence of distinct Zn peaks in the Zn-NC material indicates incomplete Zn volatilisation after the initial pyrolysis carried out at 900 °C. The progressive loss of this peak in Mn/Zn-NC@CNT_10 and Mn-N-C@CNT catalysts suggests a near-complete elimination of Zn from the carbon structure. Following this, the detailed XPS spectrum was recorded in the C1s and N1s regions, as shown in Figure 30b and 30c, respectively. The pristine Zn-NC material contained both sp^2 and sp^3 carbon, while the

Mn-containing material showed a complete absence of sp^3-C, a signature of enhanced graphitisation. Subsequently, the N1s spectra for Zn-NC material were fitted to six deconvoluted peaks corresponding to imines, pyridinic-N, Zn-N_x, pyrrolic-N, graphitic-N and bulk N-H. The distinct Zn-N_x peak reflects that Zn is thermally stabilised within the NC matrix during pyrolysis. Because of $3d^{10}$ electronic configuration of Zn^{2+}, the Zn-N_x sites are widely considered to be electrocatalytically inert. However, several studies have shown that these sites can catalyse ORR, preferably via a $2e^-$ pathway [210, 246]. Therefore, their removal is essential to divert the ORR to a $4e^-$ route. The one-step pyrolysis is unable to completely remove Zn; as evidenced by a Zn content of 0.61 at% in Mn/Zn-NC@CNT_10 catalyst. The Mn-N-C@CNT catalyst showed a drastic reduction in Zn content to 0.04 at%, indicating that the M-N_x peak originates from the Mn sites. Furthermore, this catalyst, despite having the lowest N content, has the highest relative concentration of M-N_x centres. The high-resolution Mn2p spectra (see Figure 3e in article [V]) showed well-resolved $Mn2p_{3/2}$ and $Mn2p_{1/2}$ peaks at ~641.68 and 653.38 eV, respectively, for both catalysts, with a spin-orbit splitting of ~11.7 eV. The deconvoluted XPS spectra revealed that both catalysts contain oxidised Mn species. The N_2 physisorption and XPS results together point to the high density and accessibility of the Mn-N_x active sites.

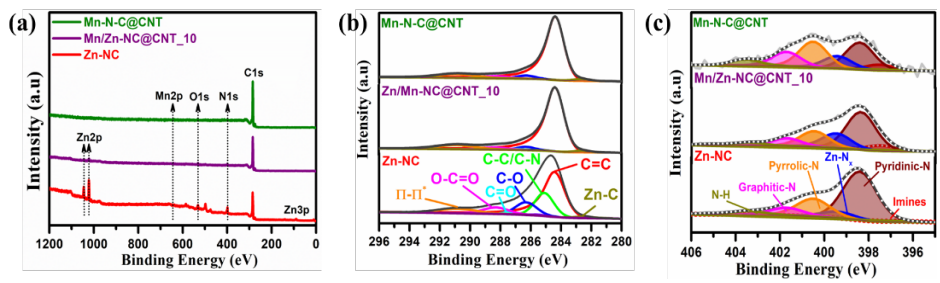

Figure 30. (a) XPS survey spectra, (b) detailed C1s XPS spectra and (c) detailed N1s XPS spectra for the catalyst materials.

SEM and EDX analyses were performed to examine the structural morphology and elemental composition of the materials, respectively. The SEM images for Zn-NC material in Figure 31 clearly show the typical rhombic dodecahedral morphology, a characteristic structure of pyrolysed ZIF-8. However, in the absence of a secondary carbon source, ZIF-8 particles aggregate and exhibit poor electrical conductivity. Such agglomerated morphology offers complex diffusion pathways. After incorporation of MWCNTs and Mn, the surfaces of these polyhedral-shaped particles become rougher, forming intricate bridges and connections across the porous network of the ZIF-derived carbon framework. In particular, the Mn-N-C@CNT catalyst exhibited a CNT-dominated network, alongside a partial retention of ZIF-like structure, suggesting the templating nature of ZIF-8. The resulting composite catalyst exhibits a highly porous morphology with exposed CNTs, enabling enhanced O_2 diffusion and providing

the framework with excellent mechanical strength. Moreover, these CNTs act as an electron transport chain during electrochemical reactions, which is especially advantageous for ORR electrocatalysis. The EDX analysis was used to determine the elemental composition of the catalysts, as listed in Table 9. Evidently, the progressive loss in Zn content from Zn-NC to Mn-N-C@CNT catalyst reflects the successful elimination of Zn species from the NC matrix. This is consistent with the XPS results in Table 8.

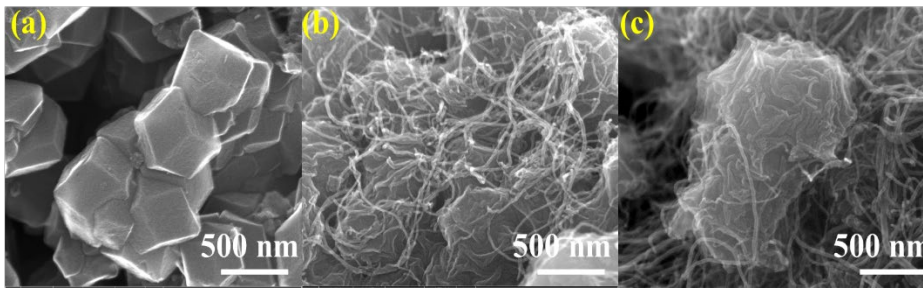

Figure 31. SEM images for (a) Zn-NC, (b) Mn/Zn-NC@CNT_10 and (c) Mn-N-C@CNT catalysts.

Table 9. Elemental composition (wt%) measured by SEM-EDX.

Catalyst material	C	N	O	Mn	Zn
Zn-NC	62.23	16.94	7.22	-	13.19
Mn/Zn-NC@CNT_10	77.33	9.97	7.46	2.53	2.45
Mn-N-C@CNT	87.59	6.59	4.02	1.01	0.58

Subsequently, STEM and STEM-EDX analyses were performed on these materials to gain further insights into the catalyst structure. Figure 32a presents the crystalline MnO_2 nanoparticles with a d-spacing of 0.25 nm. These nanoparticles can inhibit ORR activity by blocking reactant access to the active centres. However, these were not detected by XRD, probably due to their very low content. The next STEM image (Figure 32b) and its corresponding EDX mapping (Figure 32c-f) show the Mn-rich aggregates alongside a uniform dispersion of C, N, O, and Zn. Notably, the Mn-N-C@CNT catalyst does not contain such aggregate Mn/Zn species, indicating that they are effectively removed after the acid treatment step. The HAADF-STEM images shown in Figure 32g and 32h resemble the ZIF-like morphology embedded with pores, underscoring the Zn evaporation phenomenon. The EDX mapping performed in this region showed a uniform distribution of all elements. Intriguingly, the observed Zn signal in Figure 32l is mainly due to continuous X-ray radiation and the EDX spectrum of this area arises from non-zero background signals.

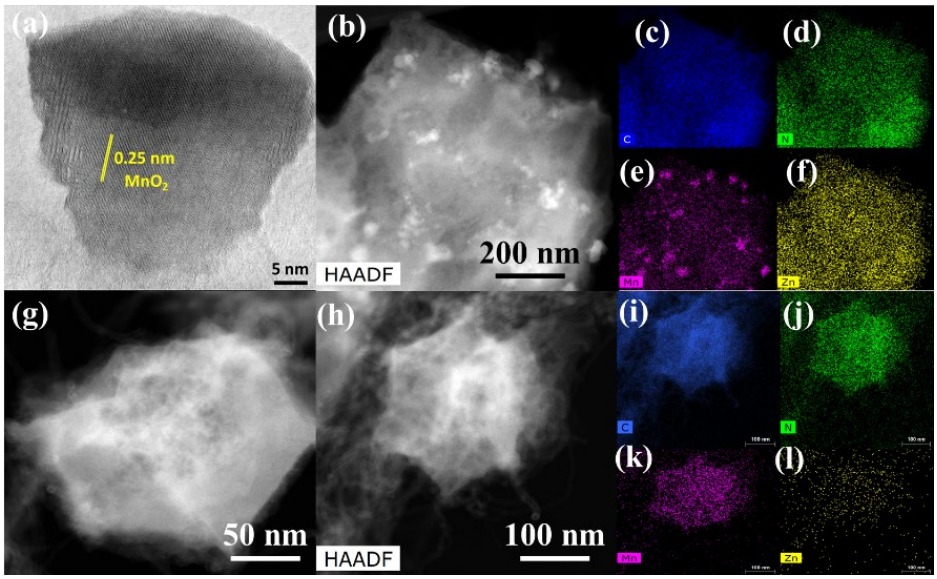

Figure 32. (a) BF-STEM image showing MnO_2 nanoparticle, (b) HAADF-STEM image and (c-f) corresponding EDX elemental mapping for Mn/Zn-NC@CNT_10 catalysts, (g, h) HAADF-STEM images and (i-l) EDX elemental mapping for M-N-C@CNT catalyst.

7.4.2. Electrochemical performance of Mn-N-C catalysts

Initially, the ORR activity of the Mn/Zn-NC@CNT_x catalysts was evaluated using the RDE and RRDE methods. At first, the CV curves were obtained in O_2- and Ar-saturated 0.1 M KOH at 10 mV s^{-1} for these catalysts (Figure 33a). The relatively sharper, more positive peak centred at 0.75 V vs RHE for the Mn/Zn-NC@CNT_10 catalyst reflects its superior ORR performance. The RDE polarisation curves shown in Figure 33b compare the ORR activity of these materials at 1900 rpm. Evidently, the $E_{1/2}$ increased with increasing ZIF-8 loading from Mn/Zn-NC@CNT_2 to Mn/Zn-NC@CNT_10, then decreased sharply upon further increasing the ZIF-8 loading. This trend suggests that at the lowest ZIF content, insufficient N content results in a low active site density and thus poor ORR activity, while with excessive ZIF-8 content, the high retention of residual Zn species decreased the electrocatalytic activity of Mn-N_x centres. Therefore, with optimal ZIF-8 content, the Mn/Zn-NC@CNT_10 catalyst exhibited the highest electrocatalytic activity under identical conditions. The K-L plot for this optimised material showed good linearity and parallelism (Figure 33c). Subsequently, the RRDE analysis was employed to determine the HO_2^- yield and the *n* value during the ORR process. As depicted in Figure 33d, the Mn/Zn-NC@CNT_2 catalyst with a HO_2^- yield of ~30–50% exhibits a considerable portion of $2e^-$ pathway (*n* approaching 3.2). The Mn/Zn-NC@CNT_5 catalyst showed a transition towards a dominant $4e^-$ ORR pathway, with the *n* value of approximately 3.4 and a moderate HO_2^- yield of about 25%. Intriguingly, a further

reduction in the HO_2^- yield to 22% for the Mn/Zn-NC@CNT_10 catalyst reflects its superior selectivity for a $4e^-$ ORR pathway.

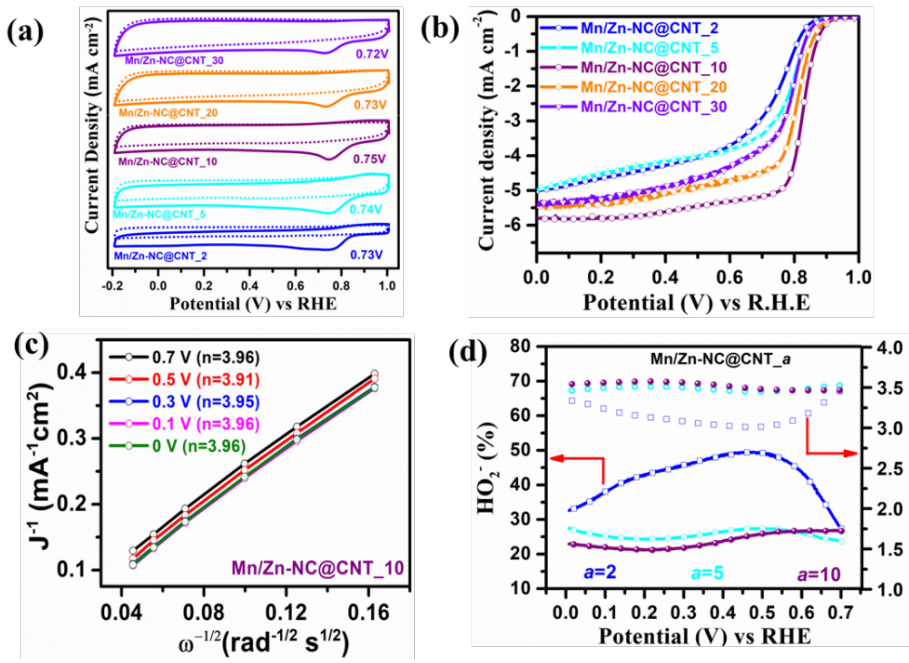

Figure 33. (a) CV curves in O_2- and Ar-saturated 0.1 M KOH at 10 mV s^{-1} for all Mn/Zn-NC@CNT_x catalysts, (b) RDE polarisation curves recorded in O_2-saturated 0.1 M KOH at 1900 rpm, (c) K-L plot for Mn/Zn-NC@CNT_10 catalyst, (d) HO_2^- yield and *n* value as a function of potential for Mn/Zn-NC@CNT_x (x = 2, 5, 10) catalysts.

Thereafter, this best-optimised Mn/Zn-NC@CNT_10 catalyst underwent an acid treatment, followed by a re-pyrolysis at 950 °C. The RDE polarisation curves in Figure 34a confirm that the resulting Mn-N-C@CNT catalyst with an $E_{1/2}$ of 0.85 V vs RHE outperformed both the commercial Pt/C and the Mn/Zn-NC@CNT_10 catalysts. Also, this $E_{1/2}$ value is equal to those for Fe_1Co_2-ZNT-900 and Fe_1Co_1-ZNT-900 catalysts reported in the article [I]. The outstanding ORR performance of Mn-N-C@CNT is rooted in its high relative N content, especially at the M-N_x sites, and in its excellent porous morphology, evidenced by N_2 physisorption analysis (Figure29c, d, Table 8). Moreover, with an E_{onset} value of 1.0 V vs RHE, this material demonstrates faster intrinsic reaction kinetics. The RDE polarisation curves at different electrode rotation rates indicate a progressive rise in the j_L. The K-L plot constructed from these polarisation curves deviates from linearity and violates the classical assumptions of the K-L equation. The RRDE measurements conducted with these materials showed that Zn-NC material produced about 50% HO_2^- yield and the *n* value was close to 3.0. This result suggests that a higher number of Zn-N_x sites promotes a dominant two-

electron ORR pathway, which also confirms previous literature reports [246]. Concurrently, it can be anticipated that the Zn-NC catalyst supports a $4e^-$ reduction pathway, likely originating from its abundant pyridinic-N sites, which, in principle, enhance the adsorption of oxygen intermediates ($^*OOH$) and ensure a direct ORR process. In contrast, the co-existing pyrrolic-N due to its delocalised lone pair has a lower tendency for initial O_2 adsorption and O=O bond cleavage, thereby weakening the adsorption strength of $^*OOH$ intermediate below the ideal value, thereby facilitating a $2e^-$ reduction. This becomes clearer when the HO_2^- yield for Mn-N-C@CNT material decreases to 17%, promoting a predominant $4e^-$ reduction. These results provide strong evidence that eliminating Zn-N_x sites is crucial for tuning the catalyst's electronic structure and selectivity for a $4e^-$ ORR pathway.

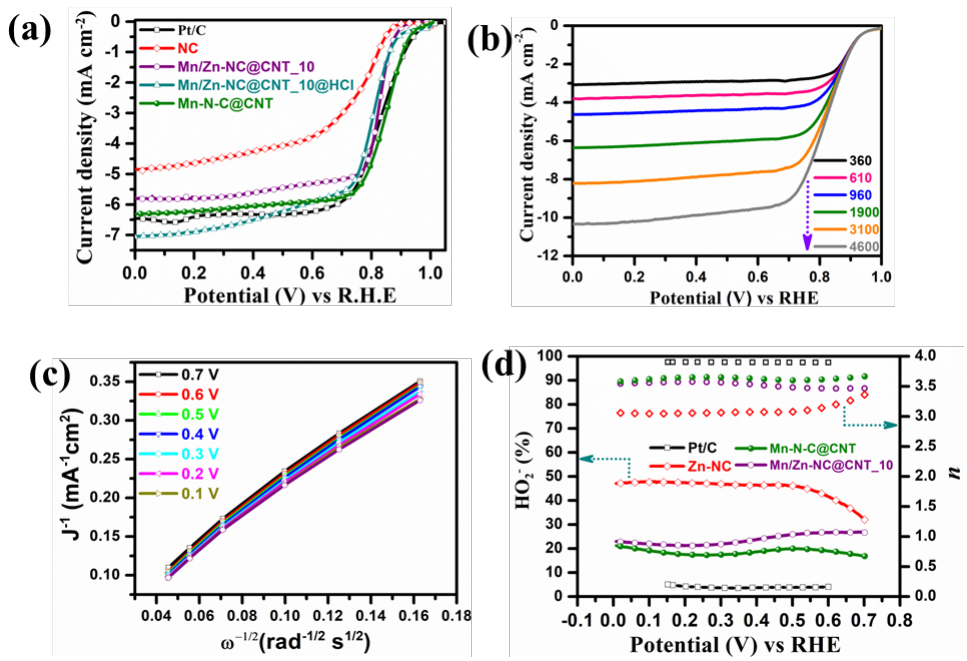

Figure 34. (a) RDE polarisation curves recorded in O_2-saturated 0.1 M KOH at 1900 rpm, (b) RDE polarisation curves at different electrode rotation rates, and (c) their respective K-L plot constructed for Mn-N-C@CNT catalyst, (d) HO_2^- yield and *n* value as a function of potential for all catalysts.

To assess the electrochemical stability of the Mn-N-C@CNT material, current-time responses were recorded at a constant potential of -0.1 V vs RHE for 15 h. Following this, an RDE polarisation curve was acquired to investigate any loss in the electrocatalytic activity. Evidently, after the stability tests, a loss of about 40 mV in the $E_{1/2}$ was observed, which suggests the catalyst is rather stable (see Figure 6i in article [V]). To investigate the catalytic role of these Zn-N_x sites, the cyanide poisoning tests were performed with Zn-NC catalysts, as shown in Figure

35a. The loss of 45 mV in the ORR activity clearly reflects the electrocatalytic contribution of Zn-N_x active centres, which have previously also been widely considered inert towards the ORR[211, 247]. Furthermore, the more pronounced loss in the ORR activity of the Mn-N-C@CNT material after NaCN addition indicates an accessible, high-density of Mn-N_x moieties (Figure 35b).

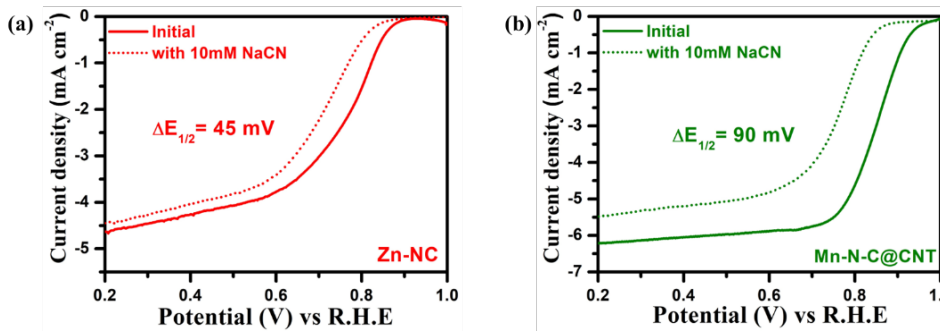

Figure 35. RDE polarisation curves in O_2-saturated 0.1 M KOH at 1900 rpm with and without the addition of 10 mM NaCN for (a) Zn-NC and (b) Mn-N-C@CNT catalysts.

7.4.3. AEMFC tests with Mn-N-C material

Single-cell AEMFC tests were performed with Pt/C, Mn/Zn-NC@CNT_10 and Mn-N-C@CNT cathode catalysts. The polarisation and power density curves for these materials are presented in Figure 36a. Notably, the Mn-N-C@CNT cathode achieved outstanding AEMFC performance, reaching a P_{max} of 975 mW cm^{-2}, and significantly outperforming the commercial Pt/C catalyst under identical conditions. A systematic optimisation of operational parameters, such as backpressure and gas flow rates, was performed before achieving this maximum AEMFC performance. This optimisation underscored the interplay between catalyst morphology and fuel cell performance. For instance, at a lower backpressure of 50 kPa, the AEMFC operated with Mn/Zn-NC@CNT_10 and Mn-N-C@CNT catalysts exhibited significant disparities in their P_{max} values, reflecting the direct impact of their distinct pore architecture on mass-transport.

Furthermore, the remarkable fuel cell performance of Mn-N-C@CNT catalyst is attributable to its tailored electronic structure. This was further evidenced by the total area-specific resistance (ASR_T) calculated from the slope of the linearly fitted ohmic region of the *J*-V curves (see Figure S14 in article [V]). The marginally lower resistance for Mn-N-C@CNT catalyst (0.16 Ω cm^2) in comparison to Mn/Zn-NC@CNT_10 (0.31 Ω cm^2) and Pt/C catalysts (0.32 Ω cm^2) suggests a superior intrinsic electrocatalytic activity and charge-transfer kinetics. The significantly higher current density and P_{max} at a cell voltage of 0.6 V showed that Mn-N-C@CNT catalyst represented a crucial trade-off between power, efficiency and durability at a practical level (Figure 36b). These results provide a conclusive argument that elimination of Zn-N_x sites is imperative to achieve a

more efficient reaction pathway for ORR, as demonstrated by the outstanding half-cell and AEMFC performance of Mn-N-C@CNT catalyst.

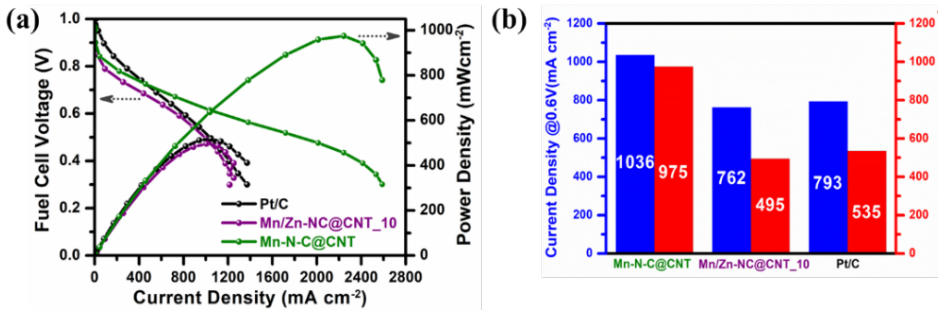

Figure 36. (a) AEMFC polarisation and power density curves with Pt/C, Mn/Zn-NC@CNT_10, and Mn-N-C@CNT cathode catalysts at 200 kPa, (b) current densities at a cell voltage of 0.6 V and maximum power densities of these cathode catalysts.

7.5. Electrocatalysis on MPc and ZIF-8@CNT derived bimetallic catalysts

As discussed in the previous study [V], the acid-based post-treatment strategy tuned the electronic/structural properties of the resulting catalyst. Benefiting from this post-treatment, the catalyst demonstrated impressive ORR electrocatalytic activity and remarkable AEMFC performance. However, this post-treatment led to a loss of the desired Mn sites, along with undesired Zn-N_x moieties, thereby diluting the resulting density of Mn-N_x centres. Therefore, the last part of this PhD thesis couples the structural benefits of MPc with the temperature-dependent structural evolution of ZIF-8@CNT-derived NC scaffolds. This study comprehensively evaluates the influence of acid-based pre-treatment on the resulting NC matrix and its anchoring capacity for bimetal phthalocyanines. Moreover, this work demonstrates that the initial pyrolysis temperature is crucial for determining the support material's porosity characteristics and electronic properties. The resulting catalysts were thoroughly examined for their ORR electrocatalytic activity and later their applicability in a practical AEMFC device.

7.5.1. Physical characterisations of the catalyst materials

XRD was used to investigate the crystal structures of the prepared catalysts. The comparative XRD patterns of pre-treated NC supports revealed that the ZIF500a catalyst retained the parent crystalline structure of ZIF-8 after pyrolysis (at 500 °C) and acid treatment. This result provides robust evidence that Zn-N_4 sites remain stable up to 500 °C, with negligible Zn loss. Eventually, two broader peaks appeared at 25.4° and 42.8°, corresponding to the (002) and (100) planes of graphitic carbon after pyrolysis at 700 °C. This suggests that the thermal decomposition of the ZIF-8 structure begins above 600 °C, consistent with previous

literature [209, 248]. The XRD patterns for NC900a, $Fe_{1.5}Mn_{1.5}$-NC900a, $Fe_{1.5}Co_{1.5}$-NC900a and $Co_{1.5}Mn_{1.5}$-NC900a catalysts are displayed in Figure 37a. All catalysts showed two broader peaks at 25° and 42°, which correspond to graphitic carbon. In addition, these bimetallic catalysts showed diffraction peaks attributed to FeCo alloys and Fe_2O_3 nanoparticles. Raman spectroscopy was used to examine the structural defects and the degree of graphitisation of the catalysts (Figure 37b). Each material exhibited two broad peaks: one at ~1355 cm^{-1}, corresponding to the D-band and the other at ~1581 cm^{-1}, corresponding to the G-band. Evidently, the bimetallic catalysts showed negligible deviations in their Raman spectra when compared to the NC900a support, suggesting a finely tuned carbon framework. Furthermore, the I_D/I_G ratio of <0.5 in these materials indicates a higher degree of graphitisation. Such morphology enables long-range structural order and electrical conductivity, necessary for efficient ORR electrocatalysis.

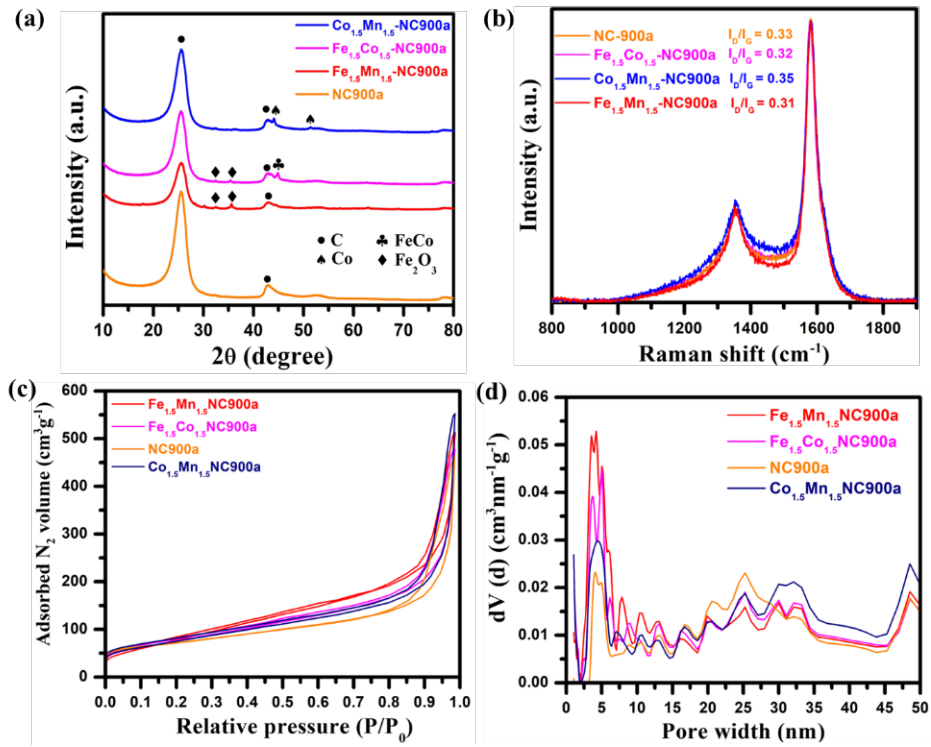

Figure 37. (a) XRD patterns, (b) Micro-Raman spectra, (c) N_2 physisorption isotherms and (d) corresponding pore size distribution for NC900a, FeMn-NC900a, FeCo-NC900a and CoMn-NC900a catalysts.

The porosity features and specific surface area for the prepared catalyst materials were determined using BET analysis. The N_2 physisorption isotherms presented in Figure 37c, revealed that each catalyst exhibited the characteristics of a Type

IV isotherm with H3 hysteresis loop, indicating the co-existence of micro- and mesopores. The S_{BET} was similar across all catalysts, while noticeable differences in their V_{μ} and V_{tot} values suggest that structural evolution is critically dependent on the combination of dual-metal sites (Table 10). Notably, the highest micropore volume of $Co_{1.5}Mn_{1.5}$-NC900a catalyst micropores suggests a relatively higher active site density, mainly the M-N_x centres.

Table 10. BET surface area (S_{BET}), total pore volume (V_{tot}) and micropore volume (V_{μ}) of catalysts.

Catalyst material	S_{BET} (m^2 g^{-1})	V_{tot} (cm^3 g^{-1})	V_{μ} (cm^3 g^{-1})
NC900a	251	0.42	0.05
$Fe_{1.5}Mn_{1.5}$NC900a	282	0.52	0.01
$Fe_{1.5}Co_{1.5}$NC900a	271	0.47	0.03
$Co_{1.5}Mn_{1.5}$NC900a	267	0.48	0.04

XPS analysis was used to examine the chemical states and surface bonding configurations of these bimetallic electrocatalysts. The wide-scan XPS spectra revealed the presence of C, N, O, Fe, Co, Mn and Zn in these materials. Notably, the NC900a catalyst displayed distinct sharp peaks at ~1021 and ~1045 eV, corresponding to $Zn2p_{3/2}$ and $Zn2p_{1/2}$, respectively. This strongly suggests an incomplete volatilisation of Zn from the evolving NC framework. However, the disappearance of the Zn peak from the survey scan of bimetallic catalysts clearly indicates its successful elimination. This is evident from the findings of article [V], where the acid-based post-treatment strategy effectively dissolved Zn sites. The detailed N1s XPS spectra for the NC900a material consist of seven deconvoluted peaks (Figure 38a). Among these, the distinct M-N_x peak is attributed to Zn-N_x sites. The detailed Zn2p spectra for this material further reinforce this conclusion (Figure 38b). The detailed N1s XPS spectra for the $Fe_{1.5}Co_{1.5}$-NC900a material revealed a similar set of seven deconvoluted peaks, assigned to imines, pyridinic-N, M-N_x, pyrrolic-N, graphitic-N, pyridinic-NO and bulk N-H (Figure 38c). The absence of Zn in this material provides strong evidence that the Fe/Co metal is coordinated to nitrogen sites to yield Fe/Co-N_x centres. Conversely, the N1s XPS spectra of $Fe_{1.5}Mn_{1.5}$-NC900a and $Co_{1.5}Mn_{1.5}$-NC900a materials do not display a distinct, clearly resolved peak assigned to M-N_x coordination. However, it does not suggest a complete loss of these centres; indeed, a closely overlapped signal of pyridinic-N and pyrrolic-N, that obscures the effective contribution of discernible M-N_x moieties [249]. Given the low surface concentration of these transition metals, these spectra inherently possess a low signal-to-noise ratio. Despite this, the definitive characteristic shake-up satellite peaks, featuring the metal oxidation states, remained clearly resolvable. Furthermore, the comparative Mn2p XPS spectra for $Co_{1.5}Mn_{1.5}$-NC900a and $Fe_{1.5}Mn_{1.5}$-NC900a catalysts presented in Figure 38d displayed well-resolved peaks at ~641 eV ($Mn2p_{3/2}$) and ~653 eV ($Mn2p_{1/2}$), with a spin-orbit splitting of ~11.5 eV. The comparative Fe2p

XPS spectra shown in Figure 38e displayed two broad characteristic peaks at ~709 and ~711 eV, suggesting that surface Fe exists in oxidised forms (Fe^{2+}/Fe^{3+}). Likewise, the comparison of high-resolution Co2p XPS spectra in Figure 38f reflects two distinct sharp peaks at ~781 and ~796 eV, corresponding to $Co2p_{3/2}$ and $Co2p_{1/2}$ spin-orbit doublets.

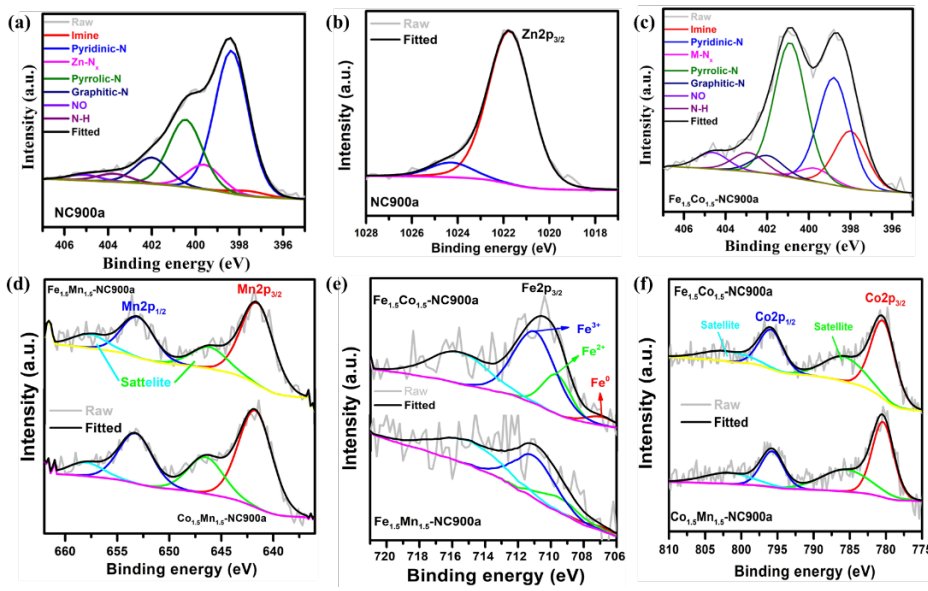

Figure 38. Detailed XPS spectra in (a) N1s and (b) Zn2p regions for NC900a catalyst, (c) detailed N1s XPS spectra for $Fe_{1.5}Co_{1.5}$-NC900a catalyst. Comparison of detailed (d) Mn2p XPS spectra for $Fe_{1.5}Mn_{1.5}$-NC900a and $Co_{1.5}Mn_{1.5}$-NC900a catalysts, (e) Fe2p XPS spectra for $Fe_{1.5}Co_{1.5}$-NC900a and $Fe_{1.5}Mn_{1.5}$-NC900a catalysts, (f) Co2p XPS spectra for $Fe_{1.5}Co_{1.5}$-NC900a and $Co_{1.5}Mn_{1.5}$-NC900a catalysts.

The SEM and EDX analyses were conducted to examine the morphology and the elemental composition of the bulk materials (Table 11, Figure 39). A similar morphology, comprising a densely packed tubular CNT network, was found for each bimetallic catalyst. Such interconnected CNT structures facilitate rapid electron and mass transfer processes. Notably, the ZIF500a material exhibited a distorted ZIF-like morphology, which diminished for NC700a and NC900a materials, indicating that the ZIF-8 structure has transformed into an NC matrix. Furthermore, the elemental mapping and respective bulk elemental content reflect that ZIF500a contains a higher proportion of Zn (13.2 wt%), which significantly decreased for NC700a (1.51 wt%) and NC900a (1.60 wt%) materials.

Table 11. Bulk elemental composition (wt%) obtained from SEM-EDX analysis.

Catalyst material	C	N	O	Fe	Co	Mn	Zn
NC900a	89.8	6.9	1.8	-	-	-	1.60
$Fe_{1.5}Mn_{1.5}$-NC900a	94.9	0.9	2.4	0.8	-	1.0	0.03
$Co_{1.5}Mn_{1.5}$-NC900a	92.4	3.7	2.5	-	0.7	0.7	0.03
$Fe_{1.5}Co_{1.5}$-NC900a	92.2	3.6	3.1	0.5	0.5	-	0.0

Interestingly, for $Co_{1.5}Mn_{1.5}$-NC900a, $Fe_{1.5}Co_{1.5}$-NC900a and $Fe_{1.5}Mn_{1.5}$-NC900a catalysts, the Zn content was close to 0.03 wt% as listed in Table 11. These results indicate that incorporating transition metals facilitates the volatilisation of Zn sites. This was also evidenced in previous work [III], where the addition of Fe favoured Zn elimination due to their similar ionic radii (see Section 7.2.1).

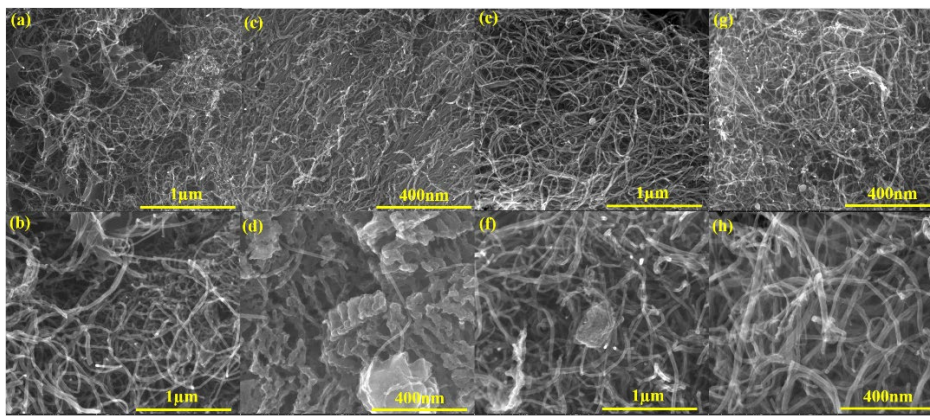

Figure 39. SEM images for (a, b) NC900a, (c, d) $Co_{1.5}Mn_{1.5}$-NC900a, (e, f) $Fe_{1.5}Co_{1.5}$-NC900a and (g, h) $Fe_{1.5}Mn_{1.5}$-NC900a catalysts.

SEM is often limited to lower magnifications and cannot provide an in-depth view of the evolved structural morphology, especially in a densely packed CNT network. Therefore, (S)TEM and EDX were employed to study the catalyst´s internal structure at the atomic scale and elemental mapping, respectively. The high-angle annular dark-field (HAADF) images for $Fe_{1.5}Co_{1.5}$-NC900a catalyst are shown in Figure 40. A distorted ZIF-alike structure is evident in Figure 40a, with a porous texture resulting from aggressive Zn volatilisation following dual pyrolysis. The images in Figure 40b and 40c show numerous bright spots that indicate the atomically dispersed M-N_x sites. Interestingly, the HAADF image in Figure 40d resembles the ZIF morphology, suggesting a highly porous, sponge-like structure with enlarged pores, attributed to enhanced Zn volatilisation [205]. Such a porous-dominated network is highly desirable to mitigate mass-transport limitations. Its corresponding EDX elemental mappings (Figures 40 e-j) further

confirm a uniform distribution of C, N, O, Fe, and Co, especially suggesting that Fe/Co is effectively coordinated as M-N_x sites within the carbon matrix without any visible aggregates. Furthermore, this elemental mapping indicates that Zn is almost eliminated after the two-step pyrolysis.

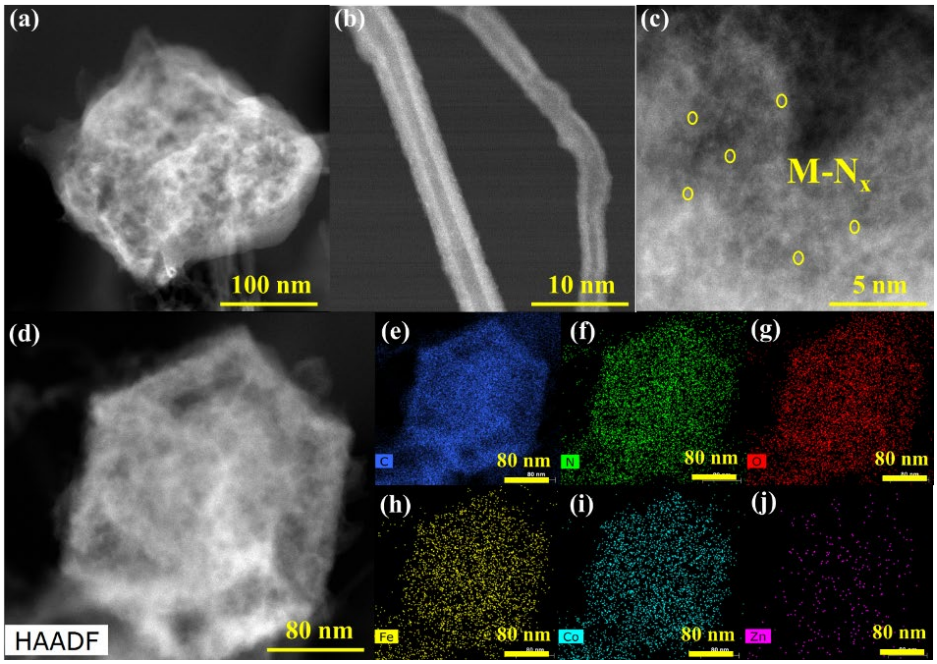

Figure 40. HAADF-STEM image (a) showing a distorted ZIF morphology, (b, c) STEM image showing with numerous bright spots representing atomically dispersed M-N_x moieties, (d) HAADF image resembling a ZIF-like morphology and (e-j) corresponding EDX elemental mapping for $Fe_{1.5}Co_{1.5}$-NC900a catalyst.

7.5.2. Electrochemical performance of the catalysts

The ORR performance of the NC900a and M_1M_2-NC900a electrocatalysts was examined using the RDE and RRDE methods. Amongst the prepared supports, NC900a showed superior ORR activity and therefore this was chosen for the anchoring of bimetal phthalocyanines. Initially, the RDE polarisation curves were acquired at 1900 rpm for all catalysts in O_2-saturated 0.1 M KOH (Figure 41a). Clearly, the $Fe_{1.5}Co_{1.5}$-NC900a material exhibited the $E_{1/2}$ and E_{onset} values of 0.88 and 1.0 V vs RHE, respectively. This was followed by $Fe_{1.5}Mn_{1.5}$-NC900a ($E_{1/2}$ = 0.87 V), $Co_{1.5}Mn_{1.5}$-NC900a ($E_{1/2}$ = 0.85 V) and commercial Pt/C catalyst ($E_{1/2}$ = 0.84 V) under identical conditions. Also, $Fe_{1.5}Co_{1.5}$-NC900a outperforms the Fe_1Co_1-ZNT-900 [I], Fe_1Co_2-ZNT-900 [I], and Mn-N-C@CNT [V] catalysts, which all exhibited the $E_{1/2}$ of 0.85 V in 0.1 M KOH. The superior electrocatalytic activity of $Fe_{1.5}Co_{1.5}$-NC900a suggests that the incorporation of Co optimises the adsorption of the *OH intermediate, which serves as the rate-limiting step with

single-atom Fe-N-C material [170]. Crucially, these dual-atom sites allow the side-on or bridge adsorption (Yeager type) of O_2 molecules. This specific attachment enables a dissociative ORR pathway, where the O=O bond might get cleaved immediately upon adsorption. For example, Park et al. used advanced in situ adsorption spectroscopy and DFT calculations to understand the adsorption energetics of oxygen intermediates on atomically engineered FeCo-based DAC [59]. They revealed that Fe-N_4 single-atom sites possess significantly stronger binding affinity to *OH intermediate (ΔG^*_{OH} = -0.57 eV) compared to FeCo dual-atom sites (ΔG^*_{OH} = -0.03 eV), which modulated this energy to a near-ideal value. This synergy shifted the d-band centre and reduced the population of antibonding states, effectively lowering the *OOH dissociation barrier. The Tafel plots constructed from the RDE polarisation curves are presented in Figure 41b. Evidently, all bimetallic catalysts exhibited a Tafel slope close to -60 mV dec^{-1}, suggesting that the first electron transfer is rapid, followed by a slow chemical rate-determining step. Thereafter, RDE polarisation curves at different rotation rates were obtained, as shown for the $Fe_{1.5}Co_{1.5}$-NC900a material in Figure 41c.

Subsequently, the K-L plots were constructed for $Fe_{1.5}Co_{1.5}$-NC900a. As shown in Figure 41d, the linearity of the K-L lines suggests first-order reaction kinetics and the *n* value remained constant (3.94–3.96) over the entire potential window. To gain further insights into the reaction pathway, RRDE analysis was performed to measure the HO_2^- yield and the *n* value. The RRDE polarisation curves for these materials are displayed in Figure 41e. Clearly, the $Fe_{1.5}Mn_{1.5}$-NC900a catalyst exhibits low HO_2^- yield (<10%) compared to the other two bimetallic catalysts (Figure 41f). Furthermore, with an *n* value close to 3.83, $Fe_{1.5}Mn_{1.5}$-NC900a catalyst predominantly promoted a $4e^-$ reduction pathway, indicating superior pathway selectivity compared to the other two bimetallic catalysts. This is attributable to Mn's dynamic redox activity across multiple oxidation states, which exerts a favourable adsorption free energy for *OH intermediate, leading to a $4e^-$ ORR pathway [250]. The electrochemical stability of the $Fe_{1.5}Mn_{1.5}$-NC900a catalyst was assessed by scanning 5000 potential cycles between 0.4 and 1.0 V vs RHE at 200 mV s^{-1}. Following this, an RDE polarisation curve at 1900 rpm was acquired, which is presented in Figure 42a. Clearly, a loss of about 30 mV in its $E_{1/2}$ suggests that this catalyst showed good stability. To inspect the role of M-N_x sites in the ORR electrocatalytic activity of the $Fe_{1.5}Mn_{1.5}$-NC900a catalyst, the RDE polarisation curve was acquired at 1900 rpm in 0.1 M KOH containing 10 mM NaCN (Figure 42b). Intriguingly, a significant loss of about 100 mV in the $E_{1/2}$ after NaCN addition provides strong evidence that these centres are the primary active sites. This finding resolved the apparent ambiguity visible in the N1s spectra of the $Fe_{1.5}Mn_{1.5}$-NC900a catalyst, where previously no distinct and clearly resolved peak assigned to M-N_x coordination was observed.

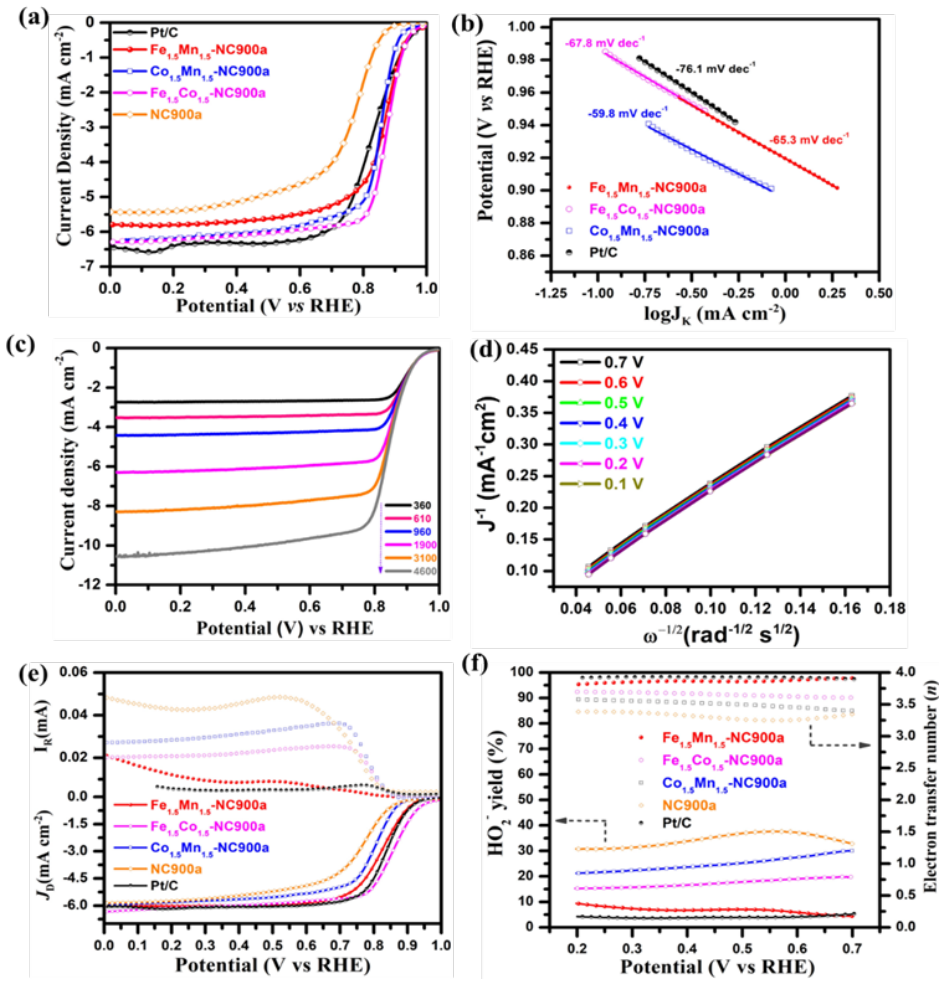

Figure 41. RDE polarisation curves recorded in O_2-saturated 0.1 M KOH electrolyte at 1900 rpm for NC900, $Fe_{1.5}Mn_{1.5}$-NC900a, $Fe_{1.5}Co_{1.5}$-NC900a, $Co_{1.5}Mn_{1.5}$-NC900a and Pt/C catalysts (v = 10 mVs^{-1}), (b) corresponding Tafel plots, (c) RDE polarisation curves at different electrode rotation rates and (d) respective K–L plot for $Fe_{1.5}Co_{1.5}$-NC900a catalyst, (e) RRDE polarisation curves at 1900 rpm in 0.1 M KOH electrolyte for NC900, $Fe_{1.5}Mn_{1.5}$-NC900a, $Fe_{1.5}Co_{1.5}$-NC900a, $Co_{1.5}Mn_{1.5}$-NC900a and Pt/C catalysts, and (f) their respective $\%HO_2^-$ and n values as a function of potential.

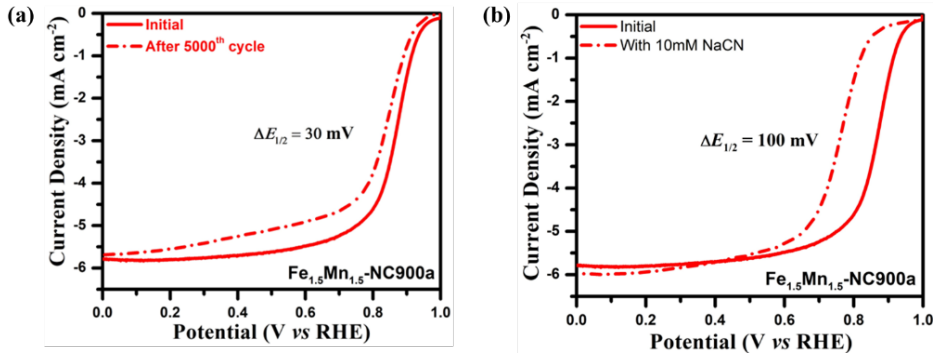

Figure 42. (a) RDE polarisation curve recorded with $Fe_{1.5}Mn_{1.5}$-NC900a catalyst before (solid) and after (dotted) 5000 potential cycles, (b) RDE polarisation curve at 1900 rpm before and after 10 mM NaCN addition to 0.1 M KOH solution.

7.5.3. AEMFC performance of the catalysts

The single-cell AEMFC tests were performed with M_1M_2-NC900a cathode catalysts, PtRu/C anode catalyst and PiperION AEM. A catalyst loading of 1.2 mg cm^{-2} was used at the cathode, whereas 0.9 mg cm^{-2} was used at the anode. The polarisation and power density curves for these materials were recorded at a cell temperature of 80 °C, whilst varying backpressures and gas flow rates were used to achieve the maximum AEMFC performance (Figure 43a, c). For instance, $Fe_{1.5}Co_{1.5}$-NC900a material with a catalyst layer thickness of 115 µm, achieved the maximum power density (P_{max}) of 1.02 W cm^{-2} with a backpressure of 200 kPa (anode/cathode) and gas flow rates of 0.6 NLPM (anode/cathode). Conversely, for the $Co_{1.5}Mn_{1.5}$-NC900a catalyst, with a backpressure of 175 kPa and a gas flow rate of 0.6 NLPM, the AEMFC reached its highest performance (P_{max} = 0.93 W cm^{-2}). However, $Fe_{1.5}Mn_{1.5}$-NC900a material utilised the lowest backpressure of 100 kPa and gas flow rates of 0.45 NLPM to gain the peak AEMFC performance (P_{max} = 0.78 W cm^{-2}). These differences in the operational parameters originated from their distinct porosity features, measured by N_2 physisorption studies. Evidently, the $Fe_{1.5}Mn_{1.5}$-NC900a catalyst, with very few micropores, exhibits a low active-site density. Furthermore, under zero backpressure conditions $Co_{1.5}Mn_{1.5}$-NC900a catalyst with a P_{max} of 0.52 W cm^{-2} showed superior performance than the other tested materials (Figure 43b, d).

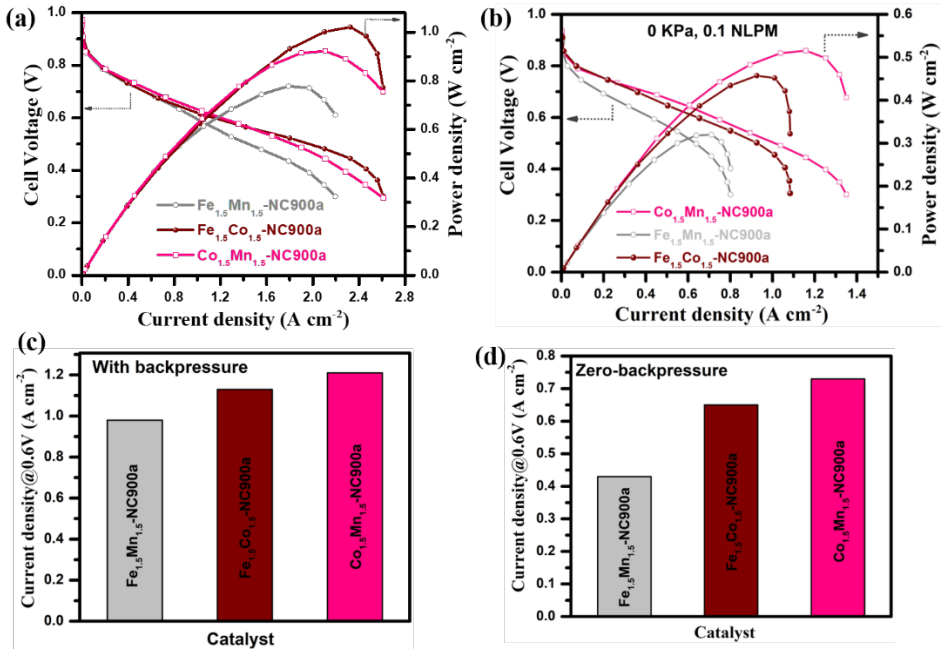

Figure 43. AEMFC power density and polarisation curve for $Fe_{1.5}Mn_{1.5}$-NC900a, $Fe_{1.5}Co_{1.5}$-NC900a and $Co_{1.5}Mn_{1.5}$-NC900a cathode catalysts (a) with backpressure, (b) without backpressure conditions. Current density at 0.6 V from *J-V* polarisation curves (c) with backpressure and (d) without backpressure conditions [Anode loading = 0.9 mg cm^{-2}, cathode loading = 1.2 mg cm^{-2}].

Moreover, the CoMn-based bimetallic catalyst showed the highest current densities under both backpressure and no backpressure conditions, reflecting its faster intrinsic reaction kinetics and pore features that facilitated mass- and charge-transfer processes. The prepared bimetallic catalyst outperformed most of the reported works summarised in Table 12 and established a breakthrough in the design of highly efficient non-noble catalyst materials for AEMFC application.

Table 12 summarises the comparison of AEMFC performance for the M-N-C catalysts prepared in this PhD thesis and relevant examples from the literature. Clearly, a wide range of Pt-free M-N-C cathode catalysts has been deployed in AEMFC, encompassing different AEMs and catalyst loadings. Therefore, these fundamental heterogeneities in methodology across the reported works limit a direct comparison based solely on P_{max} values. Furthermore, the parameters, i.e. backpressure, gas flow rates, cell operating temperature, and MEA structure, significantly influence the AEMFC performance and thus should be considered to draw a meaningful comparison. Still, the best performance for the Fe1.5Co1.5-NC900a cathode catalyst reported in article [IV] is currently among the best results worldwide for non-PGM bimetallic M-N-C catalysts applied in AEMFCs.

Table 12. AEMFC performance of ZIF-8@CNTs composite-based single and bimetallic M-N-C cathode catalysts prepared in this PhD thesis, compared against the Pt-free cathode catalysts documented in the literature.

Cathode catalyst	Cathode loading (mg cm^{-2})	Membrane	P_{max} (W cm^{-2})	Ref.
Fe_1Co_2-ZNT-900	2.0	Aemion+® 15 μm	0.17	I
Mn-N-C@CNT	1.2	PiperION	0.98	V
Mn/Zn-NC@CNT_10	1.2	PiperION	0.50	V
$Fe_{1.5}Mn_{1.5}$-NC900a	1.2	PiperION	0.78	VI
$Fe_{1.5}Co_{1.5}$-NC900a	1.2	PiperION	1.02	VI
$Co_{1.5}Mn_{1.5}$-NC900a	1.2	PiperION	0.93	VI
CoFe-NC-PPy	4.0	FAA-A-30	0.35	[251]
FeCoPc/C	0.30	LDPE	1.26	[252]
FeMn-N-MPC	2.0	HMT-PMBI	0.37	[181]
Mn–N–C	2.0	CCM	0.77	[161]
CoPc/KB	1.0	Functionalised ETFE	0.61	[217]
Fe-Mn-N-C	0.8	PAP-TP-85	1.32	[253]
FeCoN-MWCNT	0.7	FAA-3-05-rf	0.69	[254]
FeMnN-MWCNT	0.7	FAA-3-05-rf	0.58	[254]
MPF/Mn	1.0	$Aemion^+$ (10 μm)	0.30	[158]
SHUb-Fe/N-A	2.0	HMT-PMBI	0.23	[255]
CoMn-N-C-Ac-2-800	1.5-2.5	QAPPT	0.29	[256]
L FeMn	0.8	Functionalised HDPE	0.26	[257]
FeCoNC-MgOAc	0.96	Radiation-grafted LDPE	0.92	[258]
D-MN_4-CNF-IL-A	2.0	Aemion+™ (10 μm)	0.23	[259]
FeMn-N-MPC	2.0	HMT-PMBI	0.47	[181]
(FeMn-DA)-N-C	3.5	PAP-TP-85	1.06	[260]
α-Mn_2O_3/$Fe_{0.5}$-NH_3	1.2	ETFE	0.98	[261]
FeCoNC	0.6	HMT-PMBI	0.42	[262]
Fe-S-Phen/CNT	1.5	Monomer-impregnated	0.76	[263]
MC-CoFeN	0.8-0.85	PiperION	0.51	[264]
FeNSC2	2.0	$Aemion^+$ (10 μm)	0.16	[265]
FePc/C	-	Tokuyama A901	0.10	[266]
Fe-N-C/C	0.5-2.0	FAA-3	0.40	[267]
FeNiN-MWCNT	2.0	AF2-HLE8-10-X	0.41	[183]
CoFe/VC	2.4	LDPE	1.35	[268]
CoFe-N-CDC/CNT	0.75	ETFE	1.12	[178]

8. SUMMARY

The goal of this PhD thesis was to design ZIF-8-derived M-N-C catalysts for efficient ORR electrocatalysis in AEMFC and MFC devices. These materials exhibit impressive ORR activity in both neutral and alkaline media, making them a remarkable alternative to expensive Pt-based catalysts. All the prepared catalysts underwent comprehensive physical characterisation to gain insights into their nanostructures and active-site distribution. Furthermore, the RDE and RRDE methods were used to study their electrocatalytic performance and ORR pathway selectivity under different pH conditions. Lastly, the best-performing catalysts were integrated into AEMFC and MFC devices to evaluate their power generation performance. Therefore, this PhD thesis establishes a comprehensive foundation for the development of non-noble ORR catalysts with well-defined structure, controlled atomic dispersion of active sites and their accessibility, thereby addressing the significant drawbacks associated with M-N-C materials.

In the first part, Fe and Co-based bimetallic catalysts were designed using one-step pyrolysis methodology [I, II]. The resulting FeCo-N-C material exhibited a porous morphology with hierarchical porosity, facilitating mass transfer. Moreover, the use of MWCNTs offered electrical conductivity channels. Benefiting from this, the FeCo-based bimetallic catalyst showed impressive ORR activity, as evaluated by RDE and RRDE methods, in 0.1 M KOH and 0.1 M PBS solutions. With a peroxide yield of ca. 20%, the FeCo-N-C material exhibited excellent selectivity for a $4e^-$ reduction pathway. Furthermore, when applied in AEMFC and MFC devices, this material achieved P_{max} of 171 mW cm^{-2} and 1557 mW m^{-2}, respectively. This outstanding performance was attributed to the exposed atomically dispersed M-N_x active sites and high surface area. However, the high peroxide yield compromises the catalyst's true catalytic performance.

The second part of the thesis pivoted towards the incorporation of Ce, which, with its radical-scavenging ability, fine-tunes the electronic structure and drives the ORR via a predominant $4e^-$ reduction pathway [III]. This work used a one-step pyrolysis strategy, in which ZIF-8, MWCNTs and Fe/Ce salts were mixed and annealed at 900 °C in N_2 atmosphere. The physicochemical characterisation revealed that the incorporation of Fe favoured Zn volatilisation and evidenced their in-situ substitution. The enhanced structural defects after Ce addition reduced the charge-transfer resistance and increased the exposed active site density. The uniform distribution of M-N_x moieties was confirmed by STEM analysis. The resultant Fe_1Ce_1@N-C catalyst showed outstanding ORR activity in 0.1 M PBS, with an $E_{1/2}$ of 0.76 V vs RHE and excellent electrochemical stability. When applied in a dual-chamber MFC device, the Fe_1Ce_1@N-C catalyst achieved a P_{max} of 200 mW m^{-2}. Furthermore, the MFC-Fe_1Ce_1 demonstrated long-term operational stability (>600 h) under an external load of 450 Ω. The enhanced ORR kinetics improved wastewater treatment efficiency, with COD removal exceeding 85% [III].

In the next part of the thesis, a unique inverted pot dual-pyrolysis approach fine-tuned the electronic structure of the FePc-derived Fe-N-C material through an in situ nitridation mechanism, in which the hybrid Fe/Fe_4N species in proximity of Fe-N_x sites optimised the adsorption of oxygen intermediates [IV]. The resulting Fe/Fe_4N@Fe-N-C material exhibited a micropore-rich structure and a high density of exposed Fe-N_x sites. Moreover, these specific nitride species promoted graphitisation, enabling faster charge-transfer kinetics. In RDE tests, this material achieved an impressive $E_{1/2}$ of 0.79 V vs RHE, outperforming the Fe_1Ce_1@N-C [III] and FeCo-N-C@900 [II] catalysts. In MFC tests, a P_{max} of 277 mW m^{-2} and a COD removal efficiency of 85% were observed, providing compelling evidence for the altered catalyst structure induced by the nitridation approach.

In the fourth part of this thesis, Mn-doped ZIF-8@CNTs-derived catalysts were prepared using one-step pyrolysis at distinct initial ZIF-8-to-Mn molar ratios [V]. The resulting Mn/Zn-NC@CNT_10 catalyst exhibited the optimal porous morphology and the highest ORR activity in 0.1 M KOH. It was observed that the coexistence of residual Zn-N_x sites downshifted the electrocatalytic activity by decreasing the desired Mn-N_x population. Intriguingly, the subsequent acid-treatment and re-pyrolysis step substantially increased the surface area of the Mn-N-C@CNT catalyst and refined its electronic properties by eliminating the residual Zn species. Most importantly, the AEMFC performance significantly improved with Mn-N-C@CNT cathode catalyst, reaching a P_{max} of 975 W cm^{-2}, which outperformed the Pt/C cathode. The findings of this work demonstrated that eliminating Zn-N_x sites is crucial for refining ORR kinetics and pathway.

The last part is inspired by previous work [V] and explores the integration of MPc and ZIF-8 to address issues of active site density and metal aggregation [VI]. In this work, a dual-pyrolysis approach was adopted to prepare the final bimetallic M-N-C catalysts. In the initial pivotal step, the NC supports were designed from one-step pyrolysis of ZIF-8 and MWCNTs performed at different temperatures (500, 700, 900 °C). Following this, the acid-treatment step promoted graphitisation, improved ORR activity and eliminated most of the Zn-N_x sites. The structural/electronic properties of the optimised NC900a support were further improved through sequential anchoring of bimetal phthalocyanines, where $Fe_{1.5}Co_{1.5}$-NC900a material exhibited an outstanding ORR activity. In an AEMFC test, this cathode catalyst delivered a remarkable P_{max} of 1.02 W cm^{-2}.

The research reported in this PhD thesis provides valuable insights into the design of efficient Pt-free ORR catalysts for different fuel cell applications. The prime focus remained on resolving the key limitations of active-site density and site utilisation efficiency. Therefore, the prepared materials represent an advancement in the development of non-noble metal catalysts, making a valuable contribution to the field of oxygen reduction reaction electrocatalysis.

9. REFERENCES

[1] R. Vakulchuk, I. Overland, D. Scholten, Renewable energy and geopolitics: A review, Renew. Sustain. Energy Rev. 122 (2020) 109547. https://doi.org/10.1016/j.rser.2019.109547.

[2] H. Sethia, A. Priyam, Review on hydrogen fuel cells as an alternative fuel, Next Energy 9 (2025) 100460. https://doi.org/10.1016/j.nxener.2025.100460.

[3] N. Rajalakshmi, R. Balaji, S. Ramakrishnan, 14 – Recent developments in hydrogen fuel cells: Strengths and weaknesses, in: S. Dutta, C. Mustansar Hussain (Eds.), Sustainable Fuel Technologies Handbook, Academic Press, 2021, pp. 431–456. https://doi.org/10.1016/B978-0-12-822989-7.00015-9.

[4] C. Luo, H.L. Choo, H. Ahmad, P.N. Sivasankaran, Towards enhanced durability: A review of fuel cell electric vehicle development, Next Energy 9 (2025) 100399. https://doi.org/10.1016/j.nxener.2025.100399.

[5] M. Chandran, K. Palanisamy, D. Benson, S. Sundaram, A Review on Electric and Fuel Cell Vehicle Anatomy, Technology Evolution and Policy Drivers towards EVs and FCEVs Market Propagation, Chem. Rec. 22(2) (2022) e202100235. https://doi.org/10.1002/tcr.202100235.

[6] Y. Luo, Y. Wu, B. Li, T. Mo, Y. Li, S.-P. Feng, J. Qu, P.K. Chu, Development and application of fuel cells in the automobile industry, J. Energy Storage 42 (2021) 103124. https://doi.org/10.1016/j.est.2021.103124.

[7] A. Amarlou, R. M.A.Tehrani, Proton-Exchange Membrane Fuel Cells for Aviation: The Unresolved Challenges Behind Zero-Emission Flight, Fuel Cells 26(3) (2026) e70099. https://doi.org/10.1002/fuce.70099.

[8] Y. Xue, M. Alnajideen, R. Navaratne, Evolution of Proton Exchange Membrane Fuel Cell Technology for Aviation Applications: A Review, Energy Fuels 39(49) (2025) 22839–22887. https://doi.org/10.1021/acs.energyfuels.5c03463.

[9] Z. Wang, Z. Liu, L. Fan, Q. Du, K. Jiao, Application progress of small-scale proton exchange membrane fuel cell, Energy Rev. 2(2) (2023) 100017. https://doi.org/10.1016/j.enrev.2023.100017.

[10] T.A. Rafei, N.Y. Steiner, E. Pahon, D. Hissel, Polymer electrolyte membrane fuel cell for medium- and heavy-duty vehicles: An opportunity for commercialization, Energy Convers. Manag.: X 27 (2025) 101070. https://doi.org/10.1016/j.ecmx.2025.101070.

[11] T. Yoshida, K. Kojima, Toyota MIRAI Fuel Cell Vehicle and Progress Toward a Future Hydrogen Society, Electrochem. Soc. Interface 24(2) (2015) 45. https://doi.org/10.1149/2.F03152if.

[12] C. Vallejo-Cervantes, M. Espinoza-Andaluz, A. Iranzo, Technical review of commercial LT-PEMFC technologies: Performance, applications and challenges, Int. J. Hydrogen Energy 176 (2025) 151480.ˇ https://doi.org/10.1016/j.ijhydene.2025.151480.

[13] J. Biemolt, J.C. Douglin, R.K. Singh, E.S. Davydova, N. Yan, G. Rothenberg, D.R. Dekel, An Anion-Exchange Membrane Fuel Cell Containing Only Abundant and Affordable Materials, Energy Technol. 9(4) (2021) 2000909. https://doi.org/10.1002/ente.202000909.

[14] H. Lei, X. Yang, Z. Chen, D. Rawach, L. Du, Z. Liang, D.-S. Li, G. Zhang, A.C. Tavares, S. Sun, Multiscale Understanding of Anion Exchange Membrane Fuel Cells: Mechanisms, Electrocatalysts, Polymers, and Cell Management, Adv. Mater. 37(8) (2025) 2410106. https://doi.org/10.1002/adma.202410106.

[15] A. Mahmoodi Nasrabadi, A detailed survey of microbial fuel cells: Classifications, computational modeling, recent innovations, and emerging applications, Renew. Sustain. Energy Rev. 226 (2026) 116241. https://doi.org/10.1016/j.rser.2025.116241.
[16] M.C. Potter, Electrical effects accompanying the decomposition of organic compounds, Proceedings of the Royal Society of London. Series B, Containing Papers of a Biological Character 84(571) (1911) 260–276. https://doi.org/10.1098/rspb.1911.0073.
[17] H. Park Doo, J.G. Zeikus, Electricity Generation in Microbial Fuel Cells Using Neutral Red as an Electronophore, Appl. Environ. Microbiol. 66(4) (2000) 1292–1297. https://doi.org/10.1128/AEM.66.4.1292-1297.2000.
[18] U. Schröder, J. Nießen, F. Scholz, A Generation of Microbial Fuel Cells with Current Outputs Boosted by More Than One Order of Magnitude, Angew. Chem. Int. Ed. 42(25) (2003) 2880–2883. https://doi.org/10.1002/anie.200350918.
[19] T.C. Dakal, N. Singh, A. Kaur, P.K. Dhillon, J. Bhatankar, R. Meena, R.K. Sharma, B.R. Gadi, B.S. Sahu, A. Patel, B. Singh, K. Kumari, New horizons in microbial fuel cell technology: applications, challenges, and prospects, Biotechnol. Biofuels Bioprod. 18(1) (2025) 79. https://doi.org/10.1186/s13068-025-02649-y.
[20] C. Liu, L. Cheng, H. Jia, Application of microbial fuel cell-based biosensor in environmental monitoring – A critical review, Electroanalysis 36(10) (2024) e202400100. https://doi.org/10.1002/elan.202400100.
[21] J.-H. Baik, J.-H. Hwang, H. Ryu, V. Gomez-Alvarez, K.-T. Kim, W. Hyoung Lee, Microbial fuel cell (MFC)-based biosensor for real-time detection of heavy metals and BTEX contaminants in water, Biosens. Bioelectron. 305 (2026) 118675. https://doi.org/10.1016/j.bios.2026.118675.
[22] L.G. Olias, M. Di Lorenzo, Microbial fuel cells for in-field water quality monitoring, RSC Adv. 11(27) (2021) 16307–16317. https://doi.org/10.1039/D1RA01138C.
[23] L. Marelli, M. Trane, G. Barbero Vignola, C. Gastaldi, M. Guerreiro Miguel, L. Delgado Callico, S. Borchardt, L. Mancini, E. Sanye Mengual, T. Gourdon, M. Maroni, A. Georgakaki, I. Seigneur, R. M'barek, S. Acs, G. Listorti, Delivering the EU Green Deal – Progress towards targets, Publications Office of the European Union 2025. https://doi.org/doi/10.2760/3105205.
[24] A. Naha, R. Debroy, D. Sharma, M.P. Shah, S. Nath, Microbial fuel cell: A state-of-the-art and revolutionizing technology for efficient energy recovery, Clean. Circ. Bioeconomy 5 (2023) 100050. https://doi.org/10.1016/j.clcb.2023.100050.
[25] P.M.D. Serra, E.-S. A, Sourcing power with microbial fuel cells: A timeline, J. Power Sources 482 (2021) 228921. https://doi.org/10.1016/j.jpowsour.2020.228921.
[26] M.H. Do, H.H. Ngo, W.S. Guo, Y. Liu, S.W. Chang, D.D. Nguyen, L.D. Nghiem, B.J. Ni, Challenges in the application of microbial fuel cells to wastewater treatment and energy production: A mini review, Sci. Total Environ. 639 (2018) 910–920. https://doi.org/10.1016/j.scitotenv.2018.05.136.
[27] B. Kanani, A. Zahedi, F. Abtahi, S. Abedi, Exploring operational barriers in microbial fuel cells: Enhancing energy recovery from wastewater, Electrochem. Commun. 180 (2025) 108051. https://doi.org/10.1016/j.elecom.2025.108051.
[28] H. Rismani-Yazdi, S.M. Carver, A.D. Christy, O.H. Tuovinen, Cathodic limitations in microbial fuel cells: An overview, J. Power Sources 180(2) (2008) 683–694. https://doi.org/10.1016/j.jpowsour.2008.02.074.

[29] P. Dange, N. Savla, S. Pandit, R. Bobba, S. P. Jung, P.K. Gupta, M. Sahni, R. Prasad, A Comprehensive Review on Oxygen Reduction Reaction in Microbial Fuel Cells, J. Renew. Mater.10(3) (2021) 665–697. https://doi.org/10.32604/jrm.2022.015806.
[30] H. Yuan, Y. Hou, I.M. Abu-Reesh, J. Chen, Z. He, Oxygen reduction reaction catalysts used in microbial fuel cells for energy-efficient wastewater treatment: a review, Mater. Horiz. 3(5) (2016) 382–401. https://doi.org/10.1039/C6MH00093B.
[31] S. Babanova, C. Santoro, J. Jones, T. Phan, A. Serov, P. Atanassov, O. Bretschger, Practical demonstration of applicability and efficiency of platinum group metal-free based catalysts in microbial fuel cells for wastewater treatment, J. Power Sources 491 (2021) 229582. https://doi.org/10.1016/j.jpowsour.2021.229582.
[32] C. Santoro, A. Serov, K. Artyushkova, P. Atanassov, Platinum group metal-free oxygen reduction electrocatalysts used in neutral electrolytes for bioelectrochemical reactor applications, Curr. Opin. Electrochem. 23 (2020) 106–113. https://doi.org/10.1016/j.coelec.2020.06.003.
[33] S. Sahu, R. Kanwal, I. Ratnawat, A. Mir, I. Abrar, Hydrogen fuel cells: technical, economic, and policy pathways toward net-zero integration, Sustain. Energy Fuels 9(24) (2025) 6601–6630. https://doi.org/10.1039/D5SE01080B.
[34] B.Y.S. Lin, D.W. Kirk, S.J. Thorpe, Performance of alkaline fuel cells: A possible future energy system?, J. Power Sources 161(1) (2006) 474–483. https://doi.org/10.1016/j.jpowsour.2006.03.052.
[35] B. Rijo, C. Mateos-Pedrero, J.R. Copa Rey, A. Longo, P. Brito, C. Nobre, A review of solid oxide cell technologies for power, fuel, and reversible energy storage, Fuel 408 (2026) 137624. https://doi.org/10.1016/j.fuel.2025.137624.
[36] U. Shikhar, K. Hemmes, T. Woudstra, Exploring the Possibility of Using Molten Carbonate Fuel Cell for the Flexible Coproduction of Hydrogen and Power, Front. Energy Res. 9(2021).https://doi.org/10.3389/fenrg.2021.656490
[37] M. İnci, Future vision of hydrogen fuel cells: A statistical review and research on applications, socio-economic impacts and forecasting prospects, Sustain. Energy Technol. Assess. 53 (2022) 102739. https://doi.org/10.1016/j.seta.2022.102739.
[38] A. Comyns, Fuel Cells: An Overview Of Technology, Markets And Key Players, Mater. Technol. 19(3) (2004) 178–182. https://doi.org/10.1080/10667857.2004.11753082.
[39] U. Bedi, Recent advances in fuel cell design and modeling: A comprehensive review, Next Energy 11 (2026) 100517. https://doi.org/10.1016/j.nxener.2026.100517.
[40] V. Karol, P. Sharma, A. Singh, D. Goel, S. Kaur, Review of Energy Storage Devices: Fuel Cells, Hydrogen Storage Fuel Cells, Rechargeable Batteries, PV Solar Cells, Materials for Boosting Energy Storage. Volume 3: Advances in Sustainable Energy Technologies, American Chemical Society, 2024, pp. 1–15. https://doi.org/doi:10.1021/bk-2024-1488.ch001.
[41] J. Li, J. Cheng, Y. Zhang, Z. Chen, M. Nasr, M. Farghali, D.W. Rooney, P.-S. Yap, A.I. Osman, Advancements in Solid Oxide Fuel Cell Technology: Bridging Performance Gaps for Enhanced Environmental Sustainability, Adv. Energy Sustain. Res. 5(11) (2024) 2400132. https://doi.org/10.1002/aesr.202400132.
[42] A. Javed, P. Palafox Gonzalez, V. Thangadurai, A Critical Review of Electrolytes for Advanced Low- and High-Temperature Polymer Electrolyte Membrane Fuel Cells, ACS Appl. Mater. Interfaces 15(25) (2023) 29674–29699. https://doi.org/10.1021/acsami.3c02635.

[43] O. Fakhreddine, Y. Gharbia, J.F. Derakhshandeh, A.M. Amer, Challenges and Solutions of Hydrogen Fuel Cells in Transportation Systems: A Review and Prospects, World Electr. Veh. J., 14(6) (2023), 156. https://doi.org/10.3390/wevj14060156.
[44] J. Wang, C.-X. Zhao, J.-N. Liu, D. Ren, B.-Q. Li, J.-Q. Huang, Q. Zhang, Quantitative kinetic analysis on oxygen reduction reaction: A perspective, Nano Mater. Sci.3(3) (2021) 313–318. https://doi.org/10.1016/j.nanoms.2021.03.006.
[45] A. Staykov, H. Téllez, T. Akbay, J. Druce, T. Ishihara, J. Kilner, Oxygen Activation and Dissociation on Transition Metal Free Perovskite Surfaces, Chem. Mater. 27(24) (2015) 8273–8281. https://doi.org/10.1021/acs.chemmater.5b03263.
[46] Z. Wu, G. Yang, Q. Zhang, Z. Liu, F. Peng, Deciphering the high overpotential of the oxygen reduction reaction via comprehensively elucidating the open circuit potential, Energy Environ. Sci. 17(10) (2024) 3338–3346. https://doi.org/10.1039/D3EE04368A.
[47] Y. Tan, Z. Zhang, Z. Lei, L. Yu, W. Wu, Z. Wang, N. Cheng, Electronic modulation optimizes OH* intermediate adsorption on Co-Nx-C sites via coupling CoNi alloy in hollow carbon nanopolyhedron toward efficient reversible oxygen electrocatalysis, Appl. Catal. B: Environ. 304 (2022) 121006. https://doi.org/10.1016/j.apcatb.2021.121006.
[48] D.-G. Lee, S.H. Kim, J. Lee, S. Shin, S.H. Joo, Y. Lee, C. Park, Y. Kwon, S.K. Kwak, H.-K. Song, Double activation of oxygen intermediates of oxygen reduction reaction by dual inorganic/organic hybrid electrocatalysts, Nano Energy 86 (2021) 106048. https://doi.org/10.1016/j.nanoen.2021.106048.
[49] Y. Wang, D. Wang, Y. Li, A fundamental comprehension and recent progress in advanced Pt-based ORR nanocatalysts, SmartMat 2(1) (2021) 56–75. https://doi.org/10.1002/smm2.1023.
[50] G.P. Rangel, M.G. Domingos, J.C.B. Lopes, B. Neto, Sustainable green hydrogen production: Trading off costs and environmental impacts, Int. J. Hydrogen Energy 100 (2025) 994–1009. https://doi.org/10.1016/j.ijhydene.2024.12.330.
[51] A.A. Gewirth, J.A. Varnell, A.M. DiAscro, Nonprecious Metal Catalysts for Oxygen Reduction in Heterogeneous Aqueous Systems, Chem. Rev. 118(5) (2018) 2313–2339. https://doi.org/10.1021/acs.chemrev.7b00335.
[52] A. Sarapuu, E. Kibena-Põldsepp, M. Borghei, K. Tammeveski, Electrocatalysis of oxygen reduction on heteroatom-doped nanocarbons and transition metal–nitrogen–carbon catalysts for alkaline membrane fuel cells, J. Mater. Chem. A 6(3) (2018) 776–804. https://doi.org/10.1039/C7TA08690C.
[53] A. Sarapuu, J. Lilloja, S. Akula, J.H. Zagal, S. Specchia, K. Tammeveski, Recent Advances in Non-Precious Metal Single-Atom Electrocatalysts for Oxygen Reduction Reaction in Low-Temperature Polymer-Electrolyte Fuel Cells, ChemCatChem 15(22) (2023) e202300849. https://doi.org/10.1002/cctc.202300849.
[54] S. Aralekallu, V. Singh, M-N-C-based non-precious metal catalyst materials for electrocatalytic ORR applications, Fuel 404 (2026) 136163. https://doi.org/10.1016/j.fuel.2025.136163.
[55] Y. Duan, M. Chen, C. Wang, L. Gao, H. Luo, Y. Guan, Y. Zhou, J. Luo, R. Li, D. Wu, X. Tian, Z. Miao, Recent Advances in Fe-Free M–N–C Catalysts for Oxygen Reduction Reaction, ChemSusChem 18(15) (2025) e202500430. https://doi.org/10.1002/cssc.202500430.

[56] Y. He, G. Wu, PGM-Free Oxygen-Reduction Catalyst Development for Proton-Exchange Membrane Fuel Cells: Challenges, Solutions, and Promises, Acc. Mater. Res. 3(2) (2022) 224–236. https://doi.org/10.1021/accountsmr.1c00226.
[57] S. Hegde, R. Wörner, B. Shabani, Automotive PEM fuel cell catalyst layer degradation mechanisms and characterisation techniques, Part I: Carbon corrosion and binder degradation, Int. J. Hydrogen Energy 118 (2025) 268–299. https://doi.org/10.1016/j.ijhydene.2025.02.402.
[58] Y. Katayama, K. Yamauchi, K. Hayashi, T. Okanishi, H. Muroyama, T. Matsui, Y. Kikkawa, T. Negishi, S. Watanabe, T. Isomura, K. Eguchi, Anion-Exchange Membrane Fuel Cells with Improved CO2 Tolerance: Impact of Chemically Induced Bicarbonate Ion Consumption, ACS Appl. Mater. Interfaces 9(34) (2017) 28650–28658. https://doi.org/10.1021/acsami.7b09877.
[59] D.R. Dekel, Review of cell performance in anion exchange membrane fuel cells, J. Power Sources 375 (2018) 158–169. https://doi.org/10.1016/j.jpowsour.2017.07.117.
[60] K. Kumar, L. Dubau, F. Jaouen, F. Maillard, Review on the Degradation Mechanisms of Metal-N-C Catalysts for the Oxygen Reduction Reaction in Acid Electrolyte: Current Understanding and Mitigation Approaches, Chem. Rev. 123(15) (2023) 9265–9326. https://doi.org/10.1021/acs.chemrev.2c00685.
[61] N. Ramaswamy, S. Mukerjee, Influence of Inner- and Outer-Sphere Electron Transfer Mechanisms during Electrocatalysis of Oxygen Reduction in Alkaline Media, J. Phys. Chem. C 115(36) (2011) 18015–18026. https://doi.org/10.1021/jp204680p.
[62] J.L. Low, C. Roth, B. Paulus, Exploring the Inner- and Outer-Sphere Mechanistic Pathways of ORR on M–N–Cs with Pyrrolic MN4 Motifs, J. Phys. Chem. C 128(12) (2024) 5075–5083. https://doi.org/10.1021/acs.jpcc.4c00299.
[63] Y. Wang, B. Seo, B. Wang, N. Zamel, K. Jiao, X.C. Adroher, Fundamentals, materials, and machine learning of polymer electrolyte membrane fuel cell technology, Energy and AI 1 (2020) 100014. https://doi.org/10.1016/j.egyai.2020.100014.
[64] H. Nguyen, C. Klose, L. Metzler, S. Vierrath, M. Breitwieser, Fully Hydrocarbon Membrane Electrode Assemblies for Proton Exchange Membrane Fuel Cells and Electrolyzers: An Engineering Perspective, Adv. Energy Mater. 12(12) (2022) 2103559. https://doi.org/10.1002/aenm.202103559.
[65] B. Kienitz, Optimizing polymer electrolyte membrane thickness to maximize fuel cell vehicle range, Int. J. Hydrogen Energy 46(19) (2021) 11176–11182. https://doi.org/10.1016/j.ijhydene.2020.03.126.
[66] Q. Tang, B. Li, D. Yang, P. Ming, C. Zhang, Y. Wang, Review of hydrogen crossover through the polymer electrolyte membrane, Int. J. Hydrogen Energy 46(42) (2021) 22040–22061. https://doi.org/10.1016/j.ijhydene.2021.04.050.
[67] R. Gutru, Z. Turtayeva, F. Xu, G. Maranzana, B. Vigolo, A. Desforges, A comprehensive review on water management strategies and developments in anion exchange membrane fuel cells, Int. J. Hydrogen Energy 45(38) (2020) 19642–19663. https://doi.org/10.1016/j.ijhydene.2020.05.026.
[68] H.-S. Shiau, I.V. Zenyuk, A.Z. Weber, Elucidating Performance Limitations in Alkaline-Exchange- Membrane Fuel Cells, J. Electrochem. Soc. 164(11) (2017) E3583. https://doi.org/10.1149/2.0531711jes.
[69] P. von Tettau, P. Thiele, P. Mauermann, M. Wick, S. Tinz, S. Pischinger, Per- and polyfluoroalkyl substances in proton exchange membrane fuel cells — A review, J. Power Sources 630 (2025) 236104.

https://doi.org/10.1016/j.jpowsour.2024.236104.
[70] E.S. Napolitano, A. Rosati, A. Bezzon, I. Moretti, A. Suárez-Vega, F. Brusciotti, A. Meduri, Cleaner Chemistry for Clean Energy: PFAS-Free Materials in PEM Electrochemical Technologies, Sustain. Chem., 7 (2) (2026), 21. https://doi.org/10.3390/suschem7020021.
[71] M. Hren, M. Božič, D. Fakin, K.S. Kleinschek, S. Gorgieva, Alkaline membrane fuel cells: anion exchange membranes and fuels, Sustain. Energy Fuels 5(3) (2021) 604–637. https://doi.org/10.1039/D0SE01373K.
[72] V. Loise, C. Simari, Next-Generation Nafion Membranes: Synergistic Enhancement of Electrochemical Performance and Thermomechanical Stability with Sulfonated Siliceous Layered Material (sSLM), Polymers, 2025, p.1866. https://doi.org/10.3390/polym17131866.
[73] Y. Wang, J. Qiu, J. Peng, L. Xu, J. Li, M. Zhai, Study on the chemical stability of the anion exchange membrane of grafting dimethylaminoethyl methacrylate, J. Membr. Sci. 376(1) (2011) 70–77. https://doi.org/10.1016/j.memsci.2011.04.002.
[74] P. Fang, X. Zou, T. Zhou, Q. Zhang, J. Zhang, J. Pan, Z. Sun, F. Yan, Chemical stability of anion exchange membranes for alkaline fuel cells and water electrolysers: Experiment, multi-dimensional modeling and hybrid simulations, Chem. Eng. J. 492 (2024) 152144. https://doi.org/10.1016/j.cej.2024.152144.
[75] F. Xu, Y. Li, J. Ding, B. Lin, Current Challenges on the Alkaline Stability of Anion Exchange Membranes for Fuel Cells, ChemElectroChem 10(24) (2023) e202300445. https://doi.org/10.1002/celc.202300445.
[76] J. Zhang, X. Cao, Q. Lu, Y. Xiao, R. Yue, S. Guan, W. Guo, X. Yan, J. Wang, X. Wang, Z. Ren, L. Wang, Y. Yin, Ionomer Structure Engineering for Optimal Triple-Phase Boundaries in Anion Exchange Membrane Water Electrolysers, ACS Appl. Mater. Interfaces 18(13) (2026) 19773–19786. https://doi.org/10.1021/acsami.5c24607.
[77] H. Cao, J. Pan, H. Zhu, Z. Sun, B. Wang, J. Zhao, F. Yan, Interaction Regulation Between Ionomer Binder and Catalyst: Active Triple-Phase Boundary and High Performance Catalyst Layer for Anion Exchange Membrane Fuel Cells, Adv. Sci. 8(19) (2021) 2101744. https://doi.org/10.1002/advs.202101744.
[78] P.K. Gangadharan, V. Vijayakumar, S.A. Nediyirakkal, R.T. Fernandez, A.V. Siddharthan, S. Kurungot, In Situ Preparation of Ionomer as a Tool for Triple-Phase Boundary Enhancement in 3D Graphene Supported Pt Catalyst, Adv. Sustain. Syst. 5(1) (2021) 2000125. https://doi.org/10.1002/adsu.202000125.
[79] J. Liu, J. Mouallem, M. Ghadban, M. Secanell, Determination of anode and cathode overpotentials in AEMFCs using multiple edge-type reference electrodes: Experiments and simulations, Int. J. Hydrogen Energy 184 (2025) 151887. https://doi.org/10.1016/j.ijhydene.2025.151887.
[80] M. Fikry, Á. García-Padilla, J. Herranz, P. Khavlyuk, A. Eychmüller, T.J. Schmidt, A Comprehensive Analysis of the Overpotential Losses in Polymer Electrolyte Fuel Cells, ACS Catal. 14(3) (2024) 1903–1913. https://doi.org/10.1021/acscatal.3c04797.
[81] J.C. Douglin, K. Vijaya Sankar, A.L.G. Biancolli, E.I. Santiago, Y. Tsur, D.R. Dekel, Quantifying the Resistive Losses of the Catalytic Layers in Anion-Exchange Membrane Fuel Cells, ChemSusChem 16(24) (2023) e202301080. https://doi.org/10.1002/cssc.202301080.

[82] Y. Shang, L. Han, R. Ding, Y. Li, Q. Liang, Z. Guo, Enhancing PEMFC performance at high current density by incorporating PTFE emulsion into catalytic layer, J. Power Sources 623 (2024) 235462. https://doi.org/10.1016/j.jpowsour.2024.235462.
[83] W. Liu, V. Liso, T. Berning, High current density and low stoichiometry operation of a proton exchange membrane fuel cell with microchannels, J. Power Sources 658 (2025) 238236. https://doi.org/10.1016/j.jpowsour.2025.238236.
[84] Y. Xie, T. Zheng, J. Wang, W. Ding, A Critical Challenge for Anion Exchange Membrane Fuel Cells (AEMFCs): Insufficient Stability of Non-Precious Cathode Catalyst, Small (2026) e73564. https://doi.org/https://doi.org/10.1002/smll.73564.
[85] K. Yassin, D.R. Dekel, Grand challenges in anion exchange membrane energy applications, Front. Membr. Sci. Technol. 4 (2025).1691096. https://doi.org/10.3389/frmst.2025.1691096
[86] S.M. Zahan, A.A. Baranov, K. Yassin, J. Zhong, J.C. Douglin, S. Willdorf-Cohen, S. Bhowmick, J. Lilloja, K. Tammeveski, Y. Tsur, D.R. Dekel, Can Anion-Exchange Membrane Fuel Cells Operate with Ambient Air?, ACS Energy Lett. 11(2) (2026) 1688–1695. https://doi.org/10.1021/acsenergylett.5c03124.
[87] N. Ziv, W.E. Mustain, D.R. Dekel, The Effect of Ambient Carbon Dioxide on Anion-Exchange Membrane Fuel Cells, ChemSusChem 11(7) (2018) 1136–1150. https://doi.org/10.1002/cssc.201702330.
[88] N. Ziv, A.N. Mondal, T. Weissbach, S. Holdcroft, D.R. Dekel, Effect of CO2 on the properties of anion exchange membranes for fuel cell applications, J. Membr. Sci. 586 (2019) 140–150. https://doi.org/10.1016/j.memsci.2019.05.053.
[89] U. Krewer, C. Weinzierl, N. Ziv, D.R. Dekel, Impact of carbonation processes in anion exchange membrane fuel cells, Electrochim. Acta 263 (2018) 433–446. https://doi.org/10.1016/j.electacta.2017.12.093.
[90] X. Ma, X. Zhao, L. Fu, Y. Qiang, Q. Bai, Recent advances in modification strategies of anion exchange membranes for AEMFCs and AEMWEs, Int. J. Hydrogen Energy 214 (2026) 153748. https://doi.org/10.1016/j.ijhydene.2026.153748.
[91] B.E. Logan, B. Hamelers, R. Rozendal, U. Schröder, J. Keller, S. Freguia, P. Aelterman, W. Verstraete, K. Rabaey, Microbial Fuel Cells: Methodology and Technology, Environ. Sci. Technol. 40(17) (2006) 5181–5192. https://doi.org/10.1021/es0605016.
[92] C. Santoro, C. Arbizzani, B. Erable, I. Ieropoulos, Microbial fuel cells: From fundamentals to applications. A review, J. Power Sources 356 (2017) 225–244. https://doi.org/10.1016/j.jpowsour.2017.03.109.
[93] B. Thulasinathan, T. Jayabalan, N. Arumugam, M. Rasu Kulanthaisamy, W. Kim, P. Kumar, M. Govarthanan, A. Alagarsamy, Wastewater substrates in microbial fuel cell systems for carbon-neutral bioelectricity generation: An overview, Fuel 317 (2022) 123369. https://doi.org/10.1016/j.fuel.2022.123369.
[94] S. Thakur, R.K. Calay, M.Y. Mustafa, F.E. Eregno, R.R. Patil, Importance of substrate type and its constituents on overall performance of microbial fuel cells, Curr. Res. Biotechnol. 9 (2025) 100272. https://doi.org/10.1016/j.crbiot.2025.100272.
[95] G. Liu, M.D. Yates, S. Cheng, D.F. Call, D. Sun, B.E. Logan, Examination of microbial fuel cell start-up times with domestic wastewater and additional amendments, Bioresour. Technol. 102(15) (2011) 7301–7306. https://doi.org/10.1016/j.biortech.2011.04.087.

[96] G. Sun, A. Thygesen, A.S. Meyer, Acetate is a superior substrate for microbial fuel cell initiation preceding bioethanol effluent utilization, Appl. Microbiol. Biotechnol 99(11) (2015) 4905–4915. https://doi.org/10.1007/s00253-015-6513-5.
[97] K.-Y. Kim, R. Rossi, J.M. Regan, B.E. Logan, Enumeration of exoelectrogens in microbial fuel cell effluents fed acetate or wastewater substrates, Biochem. Eng. J. 165 (2021) 107816. https://doi.org/10.1016/j.bej.2020.107816.
[98] J. Lee, N.T. Phung, I.S. Chang, B.H. Kim, H.C. Sung, Use of acetate for enrichment of electrochemically active microorganisms and their 16S rDNA analyses, FEMS Microbiol. Lett. 223(2) (2003) 185–191. https://doi.org/10.1016/S0378-1097(03)00356-2.
[99] F. Feng, C.-H. Wu, F. Li, X. Wang, J. Zhu, R. Zhang, S.-C. Chen, Research on the integration of microbial fuel cells with conventional wastewater treatment technology: Advantages of anaerobic fermentation, Energy Convers. Manag.: X 23 (2024) 100680. https://doi.org/10.1016/j.ecmx.2024.100680.
[100] S.-S. Yu, J.-J. Chen, X.-Y. Liu, H.-Q. Yu, Interfacial Electron Transfer from the Outer Membrane Cytochrome OmcA to Graphene Oxide in a Microbial Fuel Cell: Spectral and Electrochemical Insights, ACS Energy Lett. 3(10) (2018) 2449–2456. https://doi.org/10.1021/acsenergylett.8b01299.
[101] S. Wang, H. Li, W. Han, Y. Feng, Review: Extracellular Electron Transfer Mechanisms and Enhancement Strategies of Electroactive Microorganisms in Bioelectrochemical Systems, ACS ES&T Water 6(1) (2026) 1–19. https://doi.org/10.1021/acsestwater.5c00865.
[102] Y. Hong, J.-D. Gu, Bacterial anaerobic respiration and electron transfer relevant to the biotransformation of pollutants, Int. Biodeterior. Biodegrad 63(8) (2009) 973–980. https://doi.org/10.1016/j.ibiod.2009.08.001.
[103] L.C. Staicu, J. Cosmidis, M. Mansor, C.M. Paquete, A. Kappler, Microbial respiration – a biomineral perspective, FEMS Microbiol. Ecol. 101(10) (2025) fiaf093. https://doi.org/10.1093/femsec/fiaf093.
[104] K. Mishra, M.M. Islam, U. Soni, V. Vinayak, Electron transfer mechanism in microbial fuel cells, Discov. Electrochem. 3(1) (2026) 33. https://doi.org/10.1007/s44373-026-00118-1.
[105] D. Ucar, Y. Zhang, I. Angelidaki, An Overview of Electron Acceptors in Microbial Fuel Cells, Front. Microbiol. 8 (2017). 00643. https://doi.org/10.3389/fmicb.2017.00643
[106] C.-S. He, Z.-X. Mu, H.-Y. Yang, Y.-Z. Wang, Y. Mu, H.-Q. Yu, Electron acceptors for energy generation in microbial fuel cells fed with wastewaters: A mini-review, Chemosphere 140 (2015) 12–17. https://doi.org/10.1016/j.chemosphere.2015.03.059.
[107] Y. Li, L. Liu, J. Lv, X. Wang, W. Cai, W. Shen, Recent advances in oxygen reduction reaction catalysis under neutral conditions, Chem. Commun. 61(77) (2025) 14814–14822. https://doi.org/10.1039/D5CC04010H.
[108] A. Tricase, M. Muhyuddin, B. Erable, P. Atanassov, D. Pant, C. Santoro, P. Bollella, Bio- and Electrocatalysts for Oxygen Reduction Reaction in Neutral Media: From Mechanisms to Practical Applications, J. Power Sources 646 (2025) 237267. https://doi.org/10.1016/j.jpowsour.2025.237267.
[109] F. Zhao, R.C.T. Slade, J.R. Varcoe, Techniques for the study and development of microbial fuel cells: an electrochemical perspective, Chem. Soc. Rev. 38(7) (2009) 1926–1939. https://doi.org/10.1039/B819866G.

[110] S. Li, L. Shi, Y. Guo, J. Wang, D. Liu, S. Zhao, Selective oxygen reduction reaction: mechanism understanding, catalyst design and practical application, Chem. Sci. 15(29) (2024) 11188–11228. https://doi.org/10.1039/D4SC02853H.
[111] T.-G. Vo, J. Gao, Y. Liu, Recent Development and Future Frontiers of Oxygen Reduction Reaction in Neutral Media and Seawater, Adv. Funct. Mater. 34(23) (2024) 2314282. https://doi.org/10.1002/adfm.202314282.
[112] J. Stacy, Y.N. Regmi, B. Leonard, M. Fan, The recent progress and future of oxygen reduction reaction catalysis: A review, Renew. Sustain. Energy Rev 69 (2017) 401–414. https://doi.org/10.1016/j.rser.2016.09.135.
[113] S. Bhaduri, M. Behera, From single-chamber to multi-anodic microbial fuel cells: A review, J. Environ. Manag. 355 (2024) 120465. https://doi.org/10.1016/j.jenvman.2024.120465.
[114] K. Lawson, R. Rossi, J.M. Regan, B.E. Logan, Impact of cathodic electron acceptor on microbial fuel cell internal resistance, Bioresour. Technol 316 (2020) 123919. https://doi.org/10.1016/j.biortech.2020.123919.
[115] O.O. Kolajo, C. Pandit, B.S. Thapa, S. Pandit, A.S. Mathuriya, P.K. Gupta, D.A. Jadhav, D. Lahiri, M. Nag, V.J. Upadhye, Impact of cathode biofouling in microbial fuel cells and mitigation techniques, Biocatal. Agric. Biotechnol 43 (2022) 102408. https://doi.org/10.1016/j.bcab.2022.102408.
[116] Y. Sun, H. Li, S. Guo, C. Li, Metal-based cathode catalysts for electrocatalytic ORR in microbial fuel cells: A review, Chin. Chem. Lett. 35(5) (2024) 109418. https://doi.org/10.1016/j.cclet.2023.109418.
[117] Z. Wang, C. Cao, Y. Zheng, S. Chen, F. Zhao, Abiotic Oxygen Reduction Reaction Catalysts Used in Microbial Fuel Cells, ChemElectroChem 1(11) (2014) 1813–1821. https://doi.org/10.1002/celc.201402093.
[118] E. Sonmez, B. Avci, N. Mohamed, H. Bermek, Investigation of performance losses in microbial fuel cells with low platinum loadings on air-cathodes, Eur. Chem. Biotechnol. J. (1) (2024) 11–26. https://doi.org/10.62063/ecb-14.
[119] T. Liu, Y. Wang, Y. Li, How pH Affects the Oxygen Reduction Reactivity of Fe–N–C Materials, ACS Catal. 13(3) (2023) 1717–1725. https://doi.org/10.1021/acscatal.2c05540.
[120] C. Santoro, A. Serov, R. Gokhale, S. Rojas-Carbonell, L. Stariha, J. Gordon, K. Artyushkova, P. Atanassov, A family of Fe-N-C oxygen reduction electrocatalysts for microbial fuel cell (MFC) application: Relationships between surface chemistry and performances, Appl. Catal. B: Environ. 205 (2017) 24–33. https://doi.org/10.1016/j.apcatb.2016.12.013.
[121] K. Zhao, Y. Shu, F. Li, G. Peng, Bimetallic catalysts as electrocatalytic cathode materials for the oxygen reduction reaction in microbial fuel cell: A review, Green Energy Environ. 8(4) (2023) 1043–1070. https://doi.org/10.1016/j.gee.2022.10.007.
[122] S. Liu, R. Wang, C. Ma, D. Yang, D. Li, Z. Lewandowski, Improvement of electrochemical performance via enhanced reactive oxygen species adsorption at ZnO–NiO@rGO carbon felt cathodes in photosynthetic algal microbial fuel cells, Chem. Eng. J.391 (2020) 123627. https://doi.org/10.1016/j.cej.2019.123627.
[123] J.T. Babauta, H.D. Nguyen, T.D. Harrington, R. Renslow, H. Beyenal, pH, redox potential and local biofilm potential microenvironments within Geobacter sulfurreducens biofilms and their roles in electron transfer, Biotechnol. Bioeng. 109(10) (2012) 2651–2662. https://doi.org/10.1002/bit.24538.

[124] N. Xu, C. Xiao, H. Yin, Y. Fan, Z. Ding, N. Sun, Q. Fu, A. Ding, Differential response of anode and cathode in dual chamber microbial electrochemical system for treatment of antibiotic and microplastic composite polluted wastewater, J. Clean. Prod. 535 (2025) 147133. https://doi.org/10.1016/j.jclepro.2025.147133.
[125] H. Zhang, Y. Wang, D. Song, L. Wang, Y. Zhang, Y. Wang, Cerium-Based Electrocatalysts for Oxygen Evolution/Reduction Reactions: Progress and Perspectives, Nanomaterials, 2023, p. 1921. https://doi.org/10.3390/nano13131921.
[126] M. Zhu, C. Zhao, X. Liu, X. Wang, F. Zhou, J. Wang, Y. Hu, Y. Zhao, T. Yao, L.-M. Yang, Y. Wu, Single Atomic Cerium Sites with a High Coordination Number for Efficient Oxygen Reduction in Proton-Exchange Membrane Fuel Cells, ACS Catal. 11(7) (2021) 3923–3929. https://doi.org/10.1021/acscatal.0c05503.
[127] D.A. Jadhav, S. Pandit, J.M. Sonawane, P.K. Gupta, R. Prasad, A.D. Chendake, Effect of membrane biofouling on the performance of microbial electrochemical cells and mitigation strategies, Bioresour. Technol. Rep. 15 (2021) 100822. https://doi.org/10.1016/j.biteb.2021.100822.
[128] M.I. Simeon, R. Freitag, Influence of electrode spacing and fed-batch operation on the maximum performance trend of a soil microbial fuel cell, Int. J. Hydrogen Energy 47(24) (2022) 12304–12316. https://doi.org/10.1016/j.ijhydene.2021.11.110.
[129] Y. Wang, J. Li, Z. Wei, Transition-metal-oxide-based catalysts for the oxygen reduction reaction, J. Mater. Chem. A 6(18) (2018) 8194–8209. https://doi.org/10.1039/C8TA01321G.
[130] T. Mageto, S. Bhoyate, A. Kumar, R.K. Gupta, Progress, challenges, and prospects with electrocatalyst (From transition metal oxides to dual-atom catalysts) for oxygen reduction reaction, Mol. Catal. 562 (2024) 114196. https://doi.org/10.1016/j.mcat.2024.114196.
[131] D. Mladenović, A. Mladenović, D.M.F. Santos, A.B. Yurtcan, Š. Miljanić, S. Mentus, B. Šljukić, Transition metal oxides for bifunctional ORR/OER electrocatalysis in unitized regenerative fuel cells, J. Electroanal. Chem. 946 (2023) 117709. https://doi.org/10.1016/j.jelechem.2023.117709.
[132] S. Piccinin, The band structure and optical absorption of hematite (α-Fe2O3): a first-principles GW-BSE study, Phys. Chem. Chem. Phys.21(6) (2019) 2957–2967. https://doi.org/10.1039/C8CP07132B.
[133] F. Cheng, T. Zhang, Y. Zhang, J. Du, X. Han, J. Chen, Enhancing Electrocatalytic Oxygen Reduction on MnO2 with Vacancies, Angew. Chem. Int. Ed 52(9) (2013) 2474–2477. https://doi.org/10.1002/anie.201208582.
[134] Y.-C. Zhang, S. Ullah, R. Zhang, L. Pan, X. Zhang, J.-J. Zou, Manipulating electronic delocalization of Mn3O4 by manganese defects for oxygen reduction reaction, Appl. Catal. B: Environ. 277 (2020) 119247. https://doi.org/10.1016/j.apcatb.2020.119247.
[135] S. Yuan, X. Duan, J. Liu, Y. Ye, F. Lv, T. Liu, Q. Wang, X. Zhang, Recent progress on transition metal oxides as advanced materials for energy conversion and storage, Energy Storage Mater. 42 (2021) 317–369. https://doi.org/10.1016/j.ensm.2021.07.007.
[136] R. Jana, C. Chowdhury, A. Datta, Deciphering the Role of Substitution in Transition-Metal Phosphorous Trisulfide (100) Surface: A Highly Efficient and Durable Pt-free ORR Electrocatalyst, ChemPhysChem 23(15) (2022) e202200013. https://doi.org/10.1002/cphc.202200013.

[137] Y. Liu, T.G. Kelly, J.G. Chen, W.E. Mustain, Metal Carbides as Alternative Electrocatalyst Supports, ACS Catal. 3(6) (2013) 1184–1194. https://doi.org/10.1021/cs4001249.
[138] K. Chen, X. Wang, C. Zhang, R. Xu, H. Wang, L. Chu, M. Huang, Three-phases Co/Co9S8/MnS heterostructures engineering for boosted ORR/OER activities in Zn–air batteries, Mater. Today Energy 30 (2022) 101150. https://doi.org/10.1016/j.mtener.2022.101150.
[139] D. Susac, L. Zhu, M. Teo, A. Sode, K.C. Wong, P.C. Wong, R.R. Parsons, D. Bizzotto, K.A.R. Mitchell, S.A. Campbell, Characterization of FeS2-Based Thin Films as Model Catalysts for the Oxygen Reduction Reaction, J. Phys. Chem. C 111(50) (2007) 18715–18723. https://doi.org/10.1021/jp073395i.
[140] K. Kisand, A. Sarapuu, J.C. Douglin, A. Kikas, M. Käärik, J. Kozlova, J. Aruväli, A. Treshchalov, J. Leis, V. Kisand, K. Kukli, D.R. Dekel, K. Tammeveski, Hierarchically Porous Fe−N−C Single-Atom Catalysts via Ionothermal Synthesis for Oxygen Reduction Reaction, ChemSusChem 18(2) (2025) e202401332. https://doi.org/10.1002/cssc.202401332.
[141] X. Li, D. Wang, S. Zha, Y. Chu, L. Pan, M. Wu, C. Liu, W. Wang, N. Mitsuzaki, Z. Chen, Active sites identification and engineering of M-N-C electrocatalysts toward oxygen reduction reaction, Int. J. Hydrogen Energy 51 (2024) 1110–1127. https://doi.org/10.1016/j.ijhydene.2023.07.161.
[142] V. Duraisamy, S.M.S. Kumar, Study of the Secondary Heteroatoms Doping on Nitrogen-Doped Carbon and Their Oxygen Reduction Reaction Performance Evaluation, ChemistrySelect 6(43) (2021) 11887–11899. https://doi.org/10.1002/slct.202103506.
[143] K. Preuss, A.M. Siwoniku, C.I. Bucur, M.-M. Titirici, The Influence of Heteroatom Dopants Nitrogen, Boron, Sulfur, and Phosphorus on Carbon Electrocatalysts for the Oxygen Reduction Reaction, ChemPlusChem 84(5) (2019) 457–464. https://doi.org/10.1002/cplu.201900083.
[144] S. Kaushal, J. Andrews, A review on the nitrogenated carbon materials and their electrochemical performance for energy storage applications, Int. J. Hydrogen Energy 100 (2025) 1231–1245. https://doi.org/10.1016/j.ijhydene.2024.12.202.
[145] R. Jasinski, A New Fuel Cell Cathode Catalyst, Nature 201(4925) (1964) 1212–1213. https://doi.org/10.1038/2011212a0.
[146] Y. Wei, D. Wang, S. Wang, J. Chou, X. Li, Y. Chen, X. Du, W. Wang, Z. Chen, Recent advances in stability of atomically dispersed metal-nitrogen-carbon catalysts for oxygen reduction reaction: from degradation mechanisms to enhancement strategies, Coord. Chem. Rev. 549 (2026) 217316. https://doi.org/10.1016/j.ccr.2025.217316.
[147] Y. Huang, Y. Chen, M. Xu, T. Asset, P. Tieu, A. Gili, D. Kulkarni, V. De Andrade, F. De Carlo, H.S. Barnard, A. Doran, D.Y. Parkinson, X. Pan, P. Atanassov, I.V. Zenyuk, Catalysts by pyrolysis: Direct observation of chemical and morphological transformations leading to transition metal-nitrogen-carbon materials, Mater. Today 47 (2021) 53–68. https://doi.org/10.1016/j.mattod.2021.02.006.
[148] P.G. Santori, F.D. Speck, J. Li, A. Zitolo, Q. Jia, S. Mukerjee, S. Cherevko, F. Jaouen, Effect of Pyrolysis Atmosphere and Electrolyte pH on the Oxygen Reduction Activity, Stability and Spectroscopic Signature of FeNx Moieties in Fe-N-C Catalysts, J. Electrochem. Soc. 166(7) (2019) F3311. https://doi.org/10.1149/2.0371907jes.

[149] Q. Lv, W. Si, J. He, L. Sun, C. Zhang, N. Wang, Z. Yang, X. Li, X. Wang, W. Deng, Y. Long, C. Huang, Y. Li, Selectively nitrogen-doped carbon materials as superior metal-free catalysts for oxygen reduction, Nat. Commun. 9(1) (2018) 3376. https://doi.org/10.1038/s41467-018-05878-y.
[150] H.N. Fernandez-Escamilla, J. Guerrero-Sanchez, E. Contreras, J.M. Ruiz-Marizcal, G. Alonso-Nunez, O.E. Contreras, R.M. Felix-Navarro, J.M. Romo-Herrera, N. Takeuchi, Understanding the Selectivity of the Oxygen Reduction Reaction at the Atomistic Level on Nitrogen-Doped Graphitic Carbon Materials, Adv. Energy Mater. 11(3) (2021) 2002459. https://doi.org/10.1002/aenm.202002459.
[151] D. Guo, R. Shibuya, C. Akiba, S. Saji, T. Kondo, J. Nakamura, Active sites of nitrogen-doped carbon materials for oxygen reduction reaction clarified using model catalysts, Science 351(6271) (2016) 361–365. https://doi.org/10.1126/science.aad0832.
[152] J. Yuan, X.-B. Yang, H.-F. Wang, Y. Cao, H. Wang, G. Yang, H. Yu, Pyridinic-N Dominates ORR Performance: Decoding Configuration-Sensitive Electrocatalysis of N-Doped Graphene Quantum Dots, ACS Catal. 15(21) (2025) 18112–18122. https://doi.org/10.1021/acscatal.5c04899.
[153] X. Hu, S. Chen, L. Chen, Y. Tian, S. Yao, Z. Lu, X. Zhang, Z. Zhou, What is the Real Origin of the Activity of Fe–N–C Electrocatalysts in the O2 Reduction Reaction? Critical Roles of Coordinating Pyrrolic N and Axially Adsorbing Species, J. Am. Chem. Soc. 144(39) (2022) 18144–18152. https://doi.org/10.1021/jacs.2c08743.
[154] S.K. Singh, K. Takeyasu, J. Nakamura, Active Sites and Mechanism of Oxygen Reduction Reaction Electrocatalysis on Nitrogen-Doped Carbon Materials, Adv. Mater. 31(13) (2019) 1804297. https://doi.org/10.1002/adma.201804297.
[155] Z. Jiang, X. Liu, X.-Z. Liu, S. Huang, Y. Liu, Z.-C. Yao, Y. Zhang, Q.-H. Zhang, L. Gu, L.-R. Zheng, L. Li, J. Zhang, Y. Fan, T. Tang, Z. Zhuang, J.-S. Hu, Interfacial assembly of binary atomic metal-Nx sites for high-performance energy devices, Nat. Commun. 14(1) (2023) 1822. https://doi.org/10.1038/s41467-023-37529-2.
[156] H. Xu, D. Wang, P. Yang, A. Liu, R. Li, Y. Li, L. Xiao, X. Ren, J. Zhang, M. An, Atomically dispersed M–N–C catalysts for the oxygen reduction reaction, J. Mater. Chem. A 8(44) (2020) 23187–23201. https://doi.org/10.1039/D0TA08732G.
[157] J. Xie, Z. Duan, Spin-Orientation-Dependent O2 Adsorption Mechanism in Fe Single-Atom Catalysts, J. Phys. Chem. C 128(49) (2024) 20819–20826. https://doi.org/10.1021/acs.jpcc.4c05219.
[158] S. Akula, M. Mooste, J. Kozlova, M. Käärik, A. Treshchalov, A. Kikas, V. Kisand, J. Aruväli, P. Paiste, A. Tamm, J. Leis, K. Tammeveski, Transition metal (Fe, Co, Mn, Cu) containing nitrogen-doped porous carbon as efficient oxygen reduction electrocatalysts for anion exchange membrane fuel cells, Chem. Eng. J. 458 (2023) 141468. https://doi.org/10.1016/j.cej.2023.141468.
[159] Z. Ahmed, V. Bagchi, Current trends and perspectives on emerging Fe-derived noble-metal-free oxygen electrocatalysts, New J. Chem. 45(47) (2021) 22012–22033. https://doi.org/10.1039/D1NJ05062A.
[160] X. Ao, W. Zhang, Z. Li, L. Lv, Y. Ruan, H.-H. Wu, W.-H. Chiang, C. Wang, M. Liu, X.C. Zeng, Unraveling the high-activity nature of Fe–N–C electrocatalysts

for the oxygen reduction reaction: the extraordinary synergy between Fe–N4 and Fe4N, J. Mater. Chem. A 7(19) (2019) 11792–11801. https://doi.org/10.1039/C9TA02338K.
[161] G. Chen, X. Qiu, S. Liu, Y. Cui, Y. Sun, Y. Zhang, Y. Liu, G. Liu, Y. Kim, W. Xing, H. Wang, M. Shao, Mn–N–C with High-Density Atomically Dispersed Mn Active Sites for the Oxygen Reduction Reaction, Angew. Chem. Int. Ed. 64(26) (2025) e202503934. https://doi.org/10.1002/anie.202503934.
[162] J. Rong, W. Chen, E. Gao, J. Wu, H. Ao, X. Zheng, Y. Zhang, Z. Li, M. Kim, Y. Yamauchi, C. Wang, Design of Atomically Dispersed CoN4 Sites and Co Clusters for Synergistically Enhanced Oxygen Reduction Electrocatalysis, Small 20(42) (2024) 2402323. https://doi.org/10.1002/smll.202402323.
[163] W. Zhang, J.-k. Pan, Y.-f. Yu, X.-j. Zhang, J.-h. Wang, W.-x. Chen, G.-l. Zhuang, Correlation of the spin state and catalytic property of M–N4 single-atom catalysts in oxygen reduction reactions, Phys. Chem. Chem. Phys. 25(16) (2023) 11673–11683. https://doi.org/10.1039/D3CP00010A.
[164] Y. Tian, M. Li, Z. Wu, Q. Sun, D. Yuan, B. Johannessen, L. Xu, Y. Wang, Y. Dou, H. Zhao, S. Zhang, Edge-hosted Atomic Co−N4 Sites on Hierarchical Porous Carbon for Highly Selective Two-electron Oxygen Reduction Reaction, Angew. Chem. Int. Ed. 61(51) (2022) e202213296. https://doi.org/10.1002/anie.202213296.
[165] S. Chen, T. Luo, X. Li, K. Chen, J. Fu, K. Liu, C. Cai, Q. Wang, H. Li, Y. Chen, C. Ma, L. Zhu, Y.-R. Lu, T.-S. Chan, M. Zhu, E. Cortés, M. Liu, Identification of the Highly Active Co–N4 Coordination Motif for Selective Oxygen Reduction to Hydrogen Peroxide, J. Am. Chem. Soc. 144(32) (2022) 14505–14516. https://doi.org/10.1021/jacs.2c01194.
[166] A. Kumar, N. Goyal, S. Mathur, I.A. Bakhtiyarovich, Y. Zhao, M. Khalid, M. Ubaidullah, A.M. Al-Enizi, Advances in coordination engineering of M-N-C single atom catalysts for superior oxygen reduction performance, Coord. Chem. Rev. 549 (2026) 217244. https://doi.org/10.1016/j.ccr.2025.217244.
[167] Z. Yang, Q. Wu, H. Zhang, C. Hu, X. Bao, P. Yuan, Strategic Engineering of Axially Coordinated Ligands in Fe–N–C Catalysts for Enhanced Oxygen Reduction Electrocatalysis, ChemSusChem 18(15) (2025) e202500855. https://doi.org/10.1002/cssc.202500855.
[168] C. Brea, G. Hu, Dual-Atom Catalysts for the Oxygen Reduction Reaction: Unraveling Atomic Structures under Reaction Conditions, J. Am. Chem. Soc. 147(22) (2025) 19210–19216. https://doi.org/10.1021/jacs.5c04776.
[169] Y. Zeng, X. Wang, W. Qi, C. Liu, L. Lu, M. Xiao, K. Li, F. Xiao, M. Shao, W. Xing, J. Zhu, Aligned d-orbital energy level of dual-atom sites catalysts for oxygen reduction reaction in anion exchange membrane fuel cells, Nat. Commun. 16(1) (2025) 8111. https://doi.org/10.1038/s41467-025-63322-4.
[170] B.J. Park, Y. Choi, K.-J. Noh, J. Shin, K. Cho, S. Han, W. Kim, J.K. Kim, I. Nam, J.W. Han, Dissociative oxygen reduction on FeCo dual-atom catalysts for enhanced Zn–air battery performance, Appl. Catal. B: Environ. 387 (2026) 126508. https://doi.org/10.1016/j.apcatb.2026.126508.
[171] X. Tang, Y. Zhang, S. Tang, D. Lützenkirchen-Hecht, K. Yuan, Y. Chen, Structural and Chemical Origin of Dual-Atom Sites for Enhanced Oxygen Electroreduction, ACS Catal. 14(17) (2024) 13065–13080. https://doi.org/10.1021/acscatal.4c03068.

[172] Y. Wang, L. Cao, Y. Li, H.-P. Liang, Low-Cost Synthesis of Atomically Dispersed Fe–Mn Dual-Site Single-Atom Catalysts for Oxygen Reduction in Zn–Air Batteries, ACS Appl. Energy Mater. 8(22) (2025) 16621–16629. https://doi.org/10.1021/acsaem.5c02407.
[173] M. Zhang, J. Gao, W. Hong, X. Wang, Q. Tian, Z. An, L. Wang, H. Yao, Y. Liu, X. Zhao, H. Qiu, Bimetallic Mn and Co encased within bamboo-like N-doped carbon nanotubes as efficient oxygen reduction reaction electrocatalysts, J. Colloid Interface Sci. 537 (2019) 238–246. https://doi.org/10.1016/j.jcis.2018.11.022.
[174] X. Wang, X. Lin, J. Zhou, Y. Jiang, Y. Wang, Fe/Fe3C nanoparticles encapsulated in ZIF-8-derived carbon nanotubes as a cathode oxygen reduction catalyst for microbial fuel cells, Nanoscale 17(45) (2025) 26403–26410. https://doi.org/10.1039/D5NR03967C.
[175] M. Arif, A. Mahsud, T. Muhmood, F.L. Deepak, Design, synthesis, and electronic structure modulation of ORR electrocatalysts, J. Environ. Chem. Eng. 12(5) (2024) 113417. https://doi.org/10.1016/j.jece.2024.113417.
[176] W. Chen, Y. Qin, C. Heng, S. Wang, M. Ge, Y. Li, X. Wan, X. Li, J. Shui, Y. Su, D. Su, Degradation of FeNC Electrocatalysts for Acidic and Alkaline Oxygen Reduction, J. Am. Chem. Soc. 147(39) (2025) 35730–35741. https://doi.org/10.1021/jacs.5c11985.
[177] Y. Kumar, E. Kibena-Põldsepp, S. Akula, J. Kozlova, A. Kikas, J. Aruväli, V. Kisand, K. Kukli, K. Tammeveski, The effect of additional nitrogen source on iron phthalocyanine-based nanocarbon catalysts for oxygen reduction reaction in acidic media, Electrochem. Commun. 157 (2023) 107623. https://doi.org/10.1016/j.elecom.2023.107623.
[178] J. Lilloja, E. Kibena-Põldsepp, A. Sarapuu, J.C. Douglin, M. Käärik, J. Kozlova, P. Paiste, A. Kikas, J. Aruväli, J. Leis, V. Sammelselg, D.R. Dekel, K. Tammeveski, Transition-Metal- and Nitrogen-Doped Carbide-Derived Carbon/Carbon Nanotube Composites as Cathode Catalysts for Anion-Exchange Membrane Fuel Cells, ACS Catal. 11(4) (2021) 1920–1931. https://doi.org/10.1021/acscatal.0c03511.
[179] M. Kim, J.M. Yoo, C.-Y. Ahn, J.-H. Jang, Y.J. Son, H. Shin, J. Kang, Y.S. Kang, S.J. Yoo, K.-S. Lee, Y.-E. Sung, Rational Generation of Fe−Nx Active Sites in Fe−N−C Electrocatalysts Facilitated by Fe−N Coordinated Precursors for the Oxygen Reduction Reaction, ChemCatChem 11(24) (2019) 5982–5988. https://doi.org/10.1002/cctc.201901242.
[180] F.O. Ibrahim, K. Kisand, J.C. Douglin, A. Sarapuu, A. Kikas, M. Käärik, J. Kozlova, J. Aruväli, A. Treshchalov, J. Leis, V. Kisand, K. Kukli, K. Yassin, D.R. Dekel, K. Tammeveski, Ionothermal synthesis of mesoporous FeNC electrocatalysts for high-performance anion-exchange membrane fuel cells, Chem. Eng. J. 510 (2025) 161560. https://doi.org/10.1016/j.cej.2025.161560.
[181] J. Lilloja, E. Kibena-Põldsepp, A. Sarapuu, M. Käärik, J. Kozlova, P. Paiste, A. Kikas, A. Treshchalov, J. Leis, A. Tamm, V. Kisand, S. Holdcroft, K. Tammeveski, Transition metal and nitrogen-doped mesoporous carbons as cathode catalysts for anion-exchange membrane fuel cells, Appl. Catal. B: Environ. 306 (2022) 121113. https://doi.org/10.1016/j.apcatb.2022.121113.
[182] X. Wang, W. Li, Z. Chen, M. Waje, Y. Yan, Durability investigation of carbon nanotube as catalyst support for proton exchange membrane fuel cell, J. Power Sources 158(1) (2006) 154–159. https://doi.org/10.1016/j.jpowsour.2005.09.039.

[183] Y. Kumar, E. Kibena-Põldsepp, M. Mooste, J. Kozlova, A. Kikas, J. Aruväli, M. Käärik, V. Kisand, J. Leis, A. Tamm, S. Holdcroft, J.H. Zagal, K. Tammeveski, Iron and Nickel Phthalocyanine-Modified Nanocarbon Materials as Cathode Catalysts for Anion-Exchange Membrane Fuel Cells and Zinc-Air Batteries, ChemElectroChem 9(20) (2022) e202200717. https://doi.org/10.1002/celc.202200717.
[184] Y. Ma, H. Wang, S. Ji, J. Goh, H. Feng, R. Wang, Highly active Vulcan carbon composite for oxygen reduction reaction in alkaline medium, Electrochim. Acta 133 (2014) 391–398. https://doi.org/10.1016/j.electacta.2014.04.080.
[185] I. Ritacco, G. Santoriello, G. Gatta, M. Farnesi Camellone, L. Caporaso, Advances in ORR Catalysis Promoted by Graphene-Supported Low-Cost Metal Clusters: A DFT Study, ACS Appl. Mater. Interfaces 17(27) (2025) 39708–39718. https://doi.org/10.1021/acsami.5c08441.
[186] K. Gong, F. Du, Z. Xia, M. Durstock, L. Dai, Nitrogen-Doped Carbon Nanotube Arrays with High Electrocatalytic Activity for Oxygen Reduction, Science 323(5915) (2009) 760–764. https://doi.org/10.1126/science.1168049.
[187] S.A. Adeoye, P.B. Amama, Catalytic applications of carbon nanotubes in energy and environmental remediation: multifunctional roles and design strategy, Nanoscale 18(17) (2026) 8953–8990. https://doi.org/10.1039/D5NR05306D.
[188] F. Jaouen, M. Lefèvre, J.-P. Dodelet, M. Cai, Heat-Treated Fe/N/C Catalysts for O2 Electroreduction: Are Active Sites Hosted in Micropores?, J. Phys. Chem. B 110(11) (2006) 5553–5558. https://doi.org/10.1021/jp057135h.
[189] S. Kim, M. Her, Y. Kim, C.-Y. Ahn, S. Park, Y.-H. Cho, Y.-E. Sung, The impact of the catalyst layer structure on the performance of anion exchange membrane fuel cell, Electrochim. Acta 400 (2021) 139439. https://doi.org/10.1016/j.electacta.2021.139439.
[190] M.M. Hossen, M.S. Hasan, M.R.I. Sardar, J.b. Haider, Mottakin, K. Tammeveski, P. Atanassov, State-of-the-art and developmental trends in platinum group metal-free cathode catalyst for anion exchange membrane fuel cell (AEMFC), Appl. Catal. B: Environ. 325 (2023) 121733. https://doi.org/10.1016/j.apcatb.2022.121733.
[191] M. Ma, L. Shen, Z. Zhao, P. Guo, J. Liu, B. Xu, Z. Zhang, Y. Zhang, L. Zhao, Z. Wang, Activation methods and underlying performance boosting mechanisms within fuel cell catalyst layer, eScience 4(6) (2024) 100254. https://doi.org/10.1016/j.esci.2024.100254.
[192] X. Xu, C. Xu, J. Liu, R. Jin, X. Luo, C. Shu, H. Chen, C. Guo, L. Xu, Y. Si, The synergistic effect of “soft-hard template” to in situ regulate mass transfer and defective sites of doped-carbon nanostructures for catalysis of oxygen reduction, J. Alloys Compd. 939 (2023) 168782. https://doi.org/10.1016/j.jallcom.2023.168782.
[193] J. Lilloja, M. Mooste, E. Kibena-Põldsepp, A. Sarapuu, A. Kikas, V. Kisand, M. Käärik, J. Kozlova, A. Treshchalov, P. Paiste, J. Aruväli, J. Leis, A. Tamm, S. Holdcroft, K. Tammeveski, Cobalt-, iron- and nitrogen-containing ordered mesoporous carbon-based catalysts for anion-exchange membrane fuel cell cathode, Electrochim. Acta 439 (2023) 141676. https://doi.org/10.1016/j.electacta.2022.141676.
[194] Y. Mun, M.J. Kim, S.-A. Park, E. Lee, Y. Ye, S. Lee, Y.-T. Kim, S. Kim, O.-H. Kim, Y.-H. Cho, Y.-E. Sung, J. Lee, Soft-template synthesis of mesoporous non-

precious metal catalyst with Fe-Nx/C active sites for oxygen reduction reaction in fuel cells, Appl. Catal. B: Environ. 222 (2018) 191–199. https://doi.org/10.1016/j.apcatb.2017.10.015.
[195] Z. Ye, C. Chen, Y. Su, J. Feng, Y. Yin, Templating Methods for Materials Fabrication Across Scales, Chem. Rev. 126(2) (2026) 717–798. https://doi.org/10.1021/acs.chemrev.5c00709.
[196] B. Yan, J. Zheng, F. Wang, L. Zhao, Q. Zhang, W. Xu, S. He, Review on porous carbon materials engineered by ZnO templates: Design, synthesis and capacitance performance, Mater. Des. 201 (2021) 109518. https://doi.org/10.1016/j.matdes.2021.109518.
[197] S. Zhu, N. Zhao, J. Li, X. Deng, J. Sha, C. He, Hard-template synthesis of three-dimensional interconnected carbon networks: Rational design, hybridization and energy-related applications, Nano Today 29 (2019) 100796. https://doi.org/10.1016/j.nantod.2019.100796.
[198] Y. Gong, Z. Wei, J. Wang, P. Zhang, H. Li, Y. Wang, Design and Fabrication of Hierarchically Porous Carbon with a Template-free Method, Sci. Rep. 4(1) (2014) 6349. https://doi.org/10.1038/srep06349.
[199] Y. Xie, D. Kocaefe, C. Chen, Y. Kocaefe, Review of Research on Template Methods in Preparation of Nanomaterials, J. Nanomater. 2016(1) (2016) 2302595. https://doi.org/10.1155/2016/2302595.
[200] J.-C. Li, Y. Meng, R. Ma, H. Hu, S. Zhao, Y. Zhu, P.-X. Hou, C. Liu, Ionothermal-Transformation Strategy to Synthesize Hierarchically Tubular Porous Single-Iron-Atom Catalysts for High-Performance Zinc–Air Batteries, ACS Appl. Mater. Interfaces 13(49) (2021) 58576–58584. https://doi.org/10.1021/acsami.1c16915.
[201] L. Chai, R. Li, Y. Sun, K. Zhou, J. Pan, MOF-derived Carbon-Based Materials for Energy-Related Applications, Adv. Mater. 37(8) (2025) 2413658. https://doi.org/https://doi.org/10.1002/adma.202413658.
[202] Y. Song, C. Yu, D. Ma, K. Liu, Recent progress on ZIF-8 based MOF derivatives for electrocatalysis, Coord. Chem. Rev. 499 (2024) 215492. https://doi.org/10.1016/j.ccr.2023.215492.
[203] K.S. Park, Z. Ni, A.P. Côté, J.Y. Choi, R. Huang, F.J. Uribe-Romo, H.K. Chae, M. O'Keeffe, O.M. Yaghi, Exceptional chemical and thermal stability of zeolitic imidazolate frameworks, Proc. Natl. Acad. Sci. U.S.A. 103(27) (2006) 10186–10191. https://doi.org/10.1073/pnas.0602439103.
[204] C.S. Cereceda, Y. Du, Effect of synthesis parameters on ZIF-8 morphology: Insights from experimental and statistical integrated analysis, Microporous Mesoporous Mater. 390 (2025) 113588. https://doi.org/10.1016/j.micromeso.2025.113588.
[205] S.R. Venna, J.B. Jasinski, M.A. Carreon, Structural Evolution of Zeolitic Imidazolate Framework-8, J. Am. Chem. Soc. 132(51) (2010) 18030–18033. https://doi.org/10.1021/ja109268m.
[206] H.-x. Zhong, J. Wang, Y.-w. Zhang, W.-l. Xu, W. Xing, D. Xu, Y.-f. Zhang, X.-b. Zhang, ZIF-8 Derived Graphene-Based Nitrogen-Doped Porous Carbon Sheets as Highly Efficient and Durable Oxygen Reduction Electrocatalysts, Angew. Chem. Int. Ed. 53(51) (2014) 14235–14239. https://doi.org/10.1002/anie.201408990.
[207] W. Xue, Q. Zhou, F. Li, B.S. Ondon, Zeolitic imidazolate framework-8 (ZIF-8) as robust catalyst for oxygen reduction reaction in microbial fuel cells, J. Power Sources 423 (2019) 9–17. https://doi.org/10.1016/j.jpowsour.2019.03.017.

[208] D. Zhao, Z. Qiu, C. Lin, Challenges and performance optimization strategies of carbon-based transition metal single-atom catalysts derived from ZIF-8 for oxygen reduction reaction: Active site regulation, 3D structural engineering, and inter-facial function design, J. Environ. Chem. Eng. 13(6) (2025) 119305. https://doi.org/10.1016/j.jece.2025.119305.
[209] Q. Wang, T. Ina, W.-T. Chen, L. Shang, F. Sun, S. Wei, D. Sun-Waterhouse, S.G. Telfer, T. Zhang, G.I.N. Waterhouse, Evolution of Zn(II) single atom catalyst sites during the pyrolysis-induced transformation of ZIF-8 to N-doped carbons, Sci. Bull. 65(20) (2020) 1743–1751. https://doi.org/10.1016/j.scib.2020.06.020.
[210] R. Chen, W. Liu, Z. Sang, J. Jia, Z. Li, J. Nie, Q. Jiang, Z. Mao, B. Guo, Q. Wang, F. Hou, L. Yin, D.a. Yang, J. Liang, Identification of the highly active Zn-N4 sites with pyrrole/pyridine-N synergistic coordination by dz2+s-band center for electro-catalytic H2O2 production, J. Energy Chem. 98 (2024) 105–113. https://doi.org/10.1016/j.jechem.2024.06.021.
[211] F. Li, Y. Bu, G.-F. Han, H.-J. Noh, S.-J. Kim, I. Ahmad, Y. Lu, P. Zhang, H.Y. Jeong, Z. Fu, Q. Zhong, J.-B. Baek, Identifying the structure of Zn-N2 active sites and structural activation, Nat. Commun. 10(1) (2019) 2623. https://doi.org/10.1038/s41467-019-10622-1.
[212] Y.-F. Xia, B. Liu, P. Guo, F.-D. Tu, L.-X. Shen, M. Ma, Y.-K. Dai, J. Liu, B. Xu, Y.-L. Zhang, L. Zhao, Y. Wang, Z.-B. Wang, Residual ZnNx moieties in ZIF-8 derived catalysts: Protective and synergistic effects for oxygen reduction, J. Catal. 429 (2024) 115296. https://doi.org/10.1016/j.jcat.2024.115296.
[213] Z. Ahmed, K. Muñoz-Becerra, S. Akula, J.H. Zagal, K. Tammeveski, Recent progress on MN4 macrocycle-derived oxygen reduction reaction electrocatalysts for polymer electrolyte fuel cell applications, Chem. Commun. 62(30) (2026) 7680–7697. https://doi.org/10.1039/D5CC07438J.
[214] J.H. Zagal, F. Javier Recio, C.A. Gutierrez, C. Zuñiga, M.A. Páez, C.A. Caro, Towards a unified way of comparing the electrocatalytic activity MN4 macro-cyclic metal catalysts for O2 reduction on the basis of the reversible potential of the reaction, Electrochem. Commun. 41 (2014) 24–26. https://doi.org/10.1016/j.elecom.2014.01.009.
[215] J.H. Zagal, M.T.M. Koper, Reactivity Descriptors for the Activity of Molecular MN4 Catalysts for the Oxygen Reduction Reaction, Angew. Chem. Int. Ed. 55(47) (2016) 14510–14521. https://doi.org/10.1002/anie.201604311.
[216] K. Tammeveski, J.H. Zagal, Electrocatalytic oxygen reduction on transition metal macrocyclic complexes for anion exchange membrane fuel cell application, Curr. Opin. Electrochem. 9 (2018) 207–213. https://doi.org/10.1016/j.coelec.2018.04.001.
[217] Z. Chen, S.M. Zahan, D.R. Dekel, Metal-Phthalocyanine-Based Advanced Cata-lysts for the Oxygen Reduction Reaction in Anion-Exchange Membrane Fuel Cells, ACS Catal. 16(2) (2026) 992–1001. https://doi.org/10.1021/acscatal.5c05772.
[218] G.D. Bhowmick, E. Kibena-Põldsepp, L. Matisen, M. Merisalu, M. Kook, M. Käärik, J. Leis, V. Sammelselg, M.M. Ghangrekar, K. Tammeveski, Multi-walled carbon nanotube and carbide-derived carbon supported metal phthalocyanines as cathode catalysts for microbial fuel cell applications, Sustain. Energy Fuels 3(12) (2019) 3525–3537. https://doi.org/10.1039/C9SE00574A.

[219] R. Burkitt, T.R. Whiffen, E.H. Yu, Iron phthalocyanine and MnOx composite catalysts for microbial fuel cell applications, Appl. Catal. B: Environ. 181 (2016) 279–288. https://doi.org/10.1016/j.apcatb.2015.07.010.
[220] R. Cao, R. Thapa, H. Kim, X. Xu, M. Gyu Kim, Q. Li, N. Park, M. Liu, J. Cho, Promotion of oxygen reduction by a bio-inspired tethered iron phthalocyanine carbon nanotube-based catalyst, Nat. Commun. 4(1) (2013) 2076. https://doi.org/10.1038/ncomms3076.
[221] K. Chen, K. Liu, P. An, H. Li, Y. Lin, J. Hu, C. Jia, J. Fu, H. Li, H. Liu, Z. Lin, W. Li, J. Li, Y.-R. Lu, T.-S. Chan, N. Zhang, M. Liu, Iron phthalocyanine with coordination induced electronic localization to boost oxygen reduction reaction, Nat. Commun. 11(1) (2020) 4173. https://doi.org/10.1038/s41467-020-18062-y.
[222] S. Wang, K. Meng, L. Qin, Y. Wu, Y. Wei, J. Rong, Y. Sui, X. Yu, Y. Yang, High-throughput screening of transition metal phthalocyanine electrocatalysts for oxygen reduction reactions, Int. J. Hydrogen Energy 88 (2024) 850–857. https://doi.org/10.1016/j.ijhydene.2024.09.201.
[223] H. Yang, G. Luo, Atomistic Insights into the Degradation of Metal Phthalocyanine Catalysts during Oxygen Reduction Reaction, ACS Appl. Mater. Interfaces 17(42) (2025) 58333–58345. https://doi.org/10.1021/acsami.5c17314.
[224] S. Tian, S. Wu, J. Yang, J. Li, C. Liu, J. Shi, X. Xiang, L. Wang, Y. Sun, Q. Yang, Star-shaped ZIF-derived carbon-based electrocatalysts with FeNX active sites for enhanced oxygen reduction reaction in high-performance zinc-air batteries, J. Electroanal. Chem. 980 (2025) 118991. https://doi.org/10.1016/j.jelechem.2025.118991.
[225] A. Nugroho, A. Wahyudhi, H.S. Oktaviano, R. Yudianti, A. Hardiansyah, F. Destyorini, Y. Irmawati, Effect of Iron Loading on Controlling Fe/N−C Electrocatalyst Structure for Oxygen Reduction Reaction, ChemistrySelect 7(45) (2022) e202202042. https://doi.org/10.1002/slct.202202042.
[226] A.J. Bard, L.R. Faulkner, Electrochemical Methods: Fundamentals and Applications, 2nd ed., New York: Wiley, 2001.
[227] D.R. Dekel, I.G. Rasin, M. Page, S. Brandon, Steady state and transient simulation of anion exchange membrane fuel cells, J. Power Sources 375 (2018) 191–204. https://doi.org/10.1016/j.jpowsour.2017.07.012.
[228] B. Shanahan, B. Britton, A. Belletti, S. Vierrath, M. Breitwieser, Performance and stability comparison of Aemion™ and Aemion+™ membranes for vanadium redox flow batteries, RSC Adv. 11(22) (2021) 13077–13084. https://doi.org/10.1039/D1RA01079D.
[229] M.A. Chowdhury, N. Hossain, S.R. Islam, M.J. Hossain, D. Chowdhury, S. Ahmed, M.M. Rana, H. Aoyon, Enhancement of microbial fuel cell performance using pure magnesium anode, Energy Rep. 9 (2023) 1621–1636. https://doi.org/10.1016/j.egyr.2022.12.053.
[230] S.G. Peera, C. Liu, P.S. Prasada Reddy, S.K. Das, A.K. Sahu, M.R. Siddiqui, I.J. Ramala Sarkar, S. Kumar, A. Bhatnagar, Enhanced oxygen reduction reaction with rare-earth metal-based Ce-N-C catalyst, Int. J. Hydrogen Energy (2024). https://doi.org/10.1016/j.ijhydene.2024.09.106.
[231] F.-D. Tu, Z.-Y. Wu, P. Guo, L.-X. Shen, Z.-Y. Zhang, Y.-K. Dai, M. Ma, J. Liu, B. Xu, Y.-L. Zhang, L. Zhao, Z.-B. Wang, Fe-N-C catalysts decorated with oxygen vacancies-rich CeOx to increase oxygen reduction performance for Zn-air batteries, J. Colloid Interface Sci. 637 (2023) 10–19. https://doi.org/10.1016/j.jcis.2023.01.057.

[232] J. Tian, A. Morozan, M.T. Sougrati, M. Lefèvre, R. Chenitz, J.-P. Dodelet, D. Jones, F. Jaouen, Optimized Synthesis of Fe/N/C Cathode Catalysts for PEM Fuel Cells: A Matter of Iron–Ligand Coordination Strength, Angew. Chem. Int. Ed. 52(27) (2013) 6867–6870. https://doi.org/10.1002/anie.201303025.
[233] C.-X. Xu, J.-J. Zhang, H.-R. Dou, Y.-Z. Li, D.-M. Li, Y.-J. Zhang, B. Liu, P. Inbaraj, P.-P. Huo, Fe4N particles embedded in nitrogen-doped electrospun carbon nanofibers as efficient ORR catalysts for zinc-air battery, Rare Met. 44(5) (2025) 3156–3169. https://doi.org/10.1007/s12598-024-03167-w.
[234] C. Santoro, R. Gokhale, B. Mecheri, A. D'Epifanio, S. Licoccia, A. Serov, K. Artyushkova, P. Atanassov, Design of Iron(II) Phthalocyanine-Derived Oxygen Reduction Electrocatalysts for High-Power-Density Microbial Fuel Cells, ChemSusChem 10(16) (2017) 3243–3251. https://doi.org/10.1002/cssc.201700851.
[235] M.T. Noori, N. Verma, Cobalt – Iron phthalocyanine supported on carbide – Derived carbon as an excellent oxygen reduction reaction catalyst for microbial fuel cells, Electrochim. Acta 298 (2019) 70–79. https://doi.org/10.1016/j.electacta.2018.12.056.
[236] Y. Liu, Y.-S. Fan, Z.-M. Liu, Pyrolysis of iron phthalocyanine on activated carbon as highly efficient non-noble metal oxygen reduction catalyst in microbial fuel cells, Chem. Eng. J. 361 (2019) 416–427. https://doi.org/10.1016/j.cej.2018.12.105.
[237] E.O. Nyangau, H. Abe, Y. Nakayasu, M. Umetsu, M. Watanabe, C. Tada, Iron azaphthalocyanine electrocatalysts for enhancing oxygen reduction reactions under neutral conditions and power density in microbial fuel cells, Bioresour. Technol. Rep. 23 (2023) 101565. https://doi.org/10.1016/j.biteb.2023.101565.
[238] B. Mecheri, V.C.A. Ficca, M.A. Costa de Oliveira, A. D'Epifanio, E. Placidi, F. Arciprete, S. Licoccia, Facile synthesis of graphene-phthalocyanine composites as oxygen reduction electrocatalysts in microbial fuel cells, Appl. Catal. B: Environ. 237 (2018) 699–707. https://doi.org/10.1016/j.apcatb.2018.06.031.
[239] Y. Yuan, J. Ahmed, S. Kim, Polyaniline/carbon black composite-supported iron phthalocyanine as an oxygen reduction catalyst for microbial fuel cells, J. Power Sources 196(3) (2011) 1103–1106. https://doi.org/10.1016/j.jpowsour.2010.08.112.
[240] J. Ahmed, Y. Yuan, L. Zhou, S. Kim, Carbon supported cobalt oxide nano-particles–iron phthalocyanine as alternative cathode catalyst for oxygen reduction in microbial fuel cells, J. Power Sources 208 (2012) 170–175. https://doi.org/10.1016/j.jpowsour.2012.02.005.
[241] Y. Yuan, B. Zhao, Y. Jeon, S. Zhong, S. Zhou, S. Kim, Iron phthalocyanine supported on amino-functionalized multi-walled carbon nanotube as an alternative cathodic oxygen catalyst in microbial fuel cells, Bioresour. Technol. 102(10) (2011) 5849–5854. https://doi.org/10.1016/j.biortech.2011.02.115.
[242] M.-T. Nguyen, B. Mecheri, A. Iannaci, A. D'Epifanio, S. Licoccia, Iron/ Polyindole-based Electrocatalysts to Enhance Oxygen Reduction in Microbial Fuel Cells, Electrochim. Acta 190 (2016) 388–395. https://doi.org/10.1016/j.electacta.2015.12.105.
[243] Z. Shen, B. Tan, Y. Liu, Q. Wang, T. Zhang, L. Wang, Synthesis of Fe-NC catalysts derived from ZIF-8 encapsulating different Fe sources: Oxygen reduction activity and application in air-cathode microbial fuel cell, J. Power Sources 660 (2025) 238545. https://doi.org/10.1016/j.jpowsour.2025.238545.

[244] B.-L. Lai, H.-X. Wei, Z.-N. Luo, T. Zheng, Y.-H. Lin, Z.-Q. Liu, N. Li, ZIF-8-derived Cu, N co-doped carbon as a bifunctional cathode catalyst for enhanced performance of microbial fuel cell, Sci. Total Environ. 856 (2023) 159083. https://doi.org/10.1016/j.scitotenv.2022.159083.
[245] K. Cheng, Z. Liu, D. Jiang, M. Song, Y. Wang, Jellyfish bio-inspired Fe@CNT@CuNC derived from ZIF-8 for cathodic oxygen reduction, Nano Res. 17(4) (2024) 2352–2359. https://doi.org/10.1007/s12274-023-6064-5.
[246] P. Xia, T. He, Y. Sun, X. Duan, X. Chen, Z.-S. Zhu, C. Wang, Y. Liu, Q. He, Z. Ye, Defective-Engineered ZnO Encapsulated in N-Doped Carbon for Sustainable 2e– ORR: Interfacial Zn–N Bond Regulated Oxygen Reduction Pathways, ACS Catal. 14(17) (2024) 12917–12927. https://doi.org/10.1021/acscatal.4c02587.
[247] G. Wei, Y. Li, X. Liu, J. Huang, M. Liu, D. Luan, S. Gao, X.W. Lou, Single-Atom Zinc Sites with Synergetic Multiple Coordination Shells for Electrochemical H2O2 Production, Angew. Chem. Int. Ed. 62(47) (2023) e202313914. https://doi.org/10.1002/anie.202313914.
[248] S. Gadipelli, W. Travis, W. Zhou, Z. Guo, A thermally derived and optimized structure from ZIF-8 with giant enhancement in CO2 uptake, Energy Environ. Sci. 7(7) (2014) 2232–2238. https://doi.org/10.1039/C4EE01009D.
[249] M. Mooste, R. Kumar, S. Juvanen, J. Kozlova, A. Kikas, A. Treshchalov, M. Käärik, J. Aruväli, J. Leis, V. Kisand, K. Kukli, D. Schonvogel, P. Wagner, M. Wilhelm, K. Tammeveski, K.A. Friedrich, Binary Transition Metal and Nitrogen Functionalised Silicon Oxycarbide Electrocatalysts for Zn–Air Battery Air Electrode Application, Int. J. Energy Res. 1 (2025) 4252866. https://doi.org/10.1155/er/4252866.
[250] K.A. Stoerzinger, M. Risch, B. Han, Y. Shao-Horn, Recent Insights into Manganese Oxides in Catalyzing Oxygen Reduction Kinetics, ACS Catal. 5(10) (2015) 6021–6031. https://doi.org/10.1021/acscatal.5b01444.
[251] Q.H. Nguyen, V.D.C. Tinh, S. Oh, T.M. Pham, T.N. Tu, D. Kim, J. Han, K. Im, J. Kim, Metal-organic framework-polymer complex-derived single-atomic oxygen reduction catalyst for anion exchange membrane fuel cells, Chem. Eng. J. 481 (2024) 148508. https://doi.org/10.1016/j.cej.2023.148508.
[252] L. Wang, M. Bellini, H.A. Miller, J.R. Varcoe, A high conductivity ultrathin anion-exchange membrane with 500+ h alkali stability for use in alkaline membrane fuel cells that can achieve 2 W cm−2 at 80 °C, J. Mater. Chem. A 6(31) (2018) 15404–15412. https://doi.org/10.1039/C8TA04783A.
[253] S. Huang, Z. Qiao, P. Sun, K. Qiao, K. Pei, L. Yang, H. Xu, S. Wang, Y. Huang, Y. Yan, D. Cao, The strain induced synergistic catalysis of FeN4 and MnN3 dual-site catalysts for oxygen reduction in proton- /anion- exchange membrane fuel cells, Appl. Catal. B: Environ. 317 (2022) 121770. https://doi.org/10.1016/j.apcatb.2022.121770.
[254] Y. Kumar, E. Kibena-Põldsepp, J. Kozlova, M. Rähn, A. Treshchalov, A. Kikas, V. Kisand, J. Aruväli, A. Tamm, J.C. Douglin, S.J. Folkman, I. Gelmetti, F.A. Garcés-Pineda, J.R. Galán-Mascarós, D.R. Dekel, K. Tammeveski, Bifunctional Oxygen Electrocatalysis on Mixed Metal Phthalocyanine-Modified Carbon Nanotubes Prepared via Pyrolysis, ACS Appl. Mater. Interfaces 13(35) (2021) 41507–41516. https://doi.org/10.1021/acsami.1c06737.
[255] M. Mooste, T. Tkesheliadze, J. Kozlova, A. Kikas, V. Kisand, A. Treshchalov, A. Tamm, J. Aruväli, J.H. Zagal, A.M. Kannan, K. Tammeveski, Transition metal

phthalocyanine-modified shungite-based cathode catalysts for alkaline membrane fuel cell, Int. J. Hydrogen Energy 46(5) (2021) 4365–4377. https://doi.org/10.1016/j.ijhydene.2020.10.231.
[256] W. Luo, L. Cao, M. Hou, Y. Zhou, Z. Ren, J. Geng, Z. Shao, MOF-Based Co and Mn Embedded in Nitrogen-Doped Microporous Carbon as an Efficient Catalyst for Oxygen Reduction Reaction in Anion Exchange Membrane Fuel Cell, Int. J. Energy Res. 2023(1) (2023) 9148994. https://doi.org/10.1155/2023/9148994.
[257] M. Muhyuddin, A. Friedman, F. Poli, E. Petri, H. Honig, F. Basile, A. Fasolini, R. Lorenzi, E. Berretti, M. Bellini, A. Lavacchi, L. Elbaz, C. Santoro, F. Soavi, Lignin-derived bimetallic platinum group metal-free oxygen reduction reaction electrocatalysts for acid and alkaline fuel cells, J. Power Sources 556 (2023) 232416. https://doi.org/10.1016/j.jpowsour.2022.232416.
[258] K. Kisand, A. Sarapuu, J.C. Douglin, A. Kikas, A. Treshchalov, M. Käärik, H.-M. Piirsoo, P. Paiste, J. Aruväli, J. Leis, V. Kisand, A. Tamm, D.R. Dekel, K. Tammeveski, Templated Nitrogen-, Iron-, and Cobalt-Doped Mesoporous Nanocarbon Derived from an Alkylresorcinol Mixture for Anion-Exchange Membrane Fuel Cell Application, ACS Catal. 12(22) (2022) 14050–14061. https://doi.org/10.1021/acscatal.2c03683.
[259] K. Muuli, A. Sokka, M. Mooste, J. Lilloja, V. Gudkova, M. Käärik, M. Otsus, A. Kikas, V. Kisand, A. Tamm, J. Leis, A. Krumme, S. Holdcroft, J.H. Zagal, K. Tammeveski, Iron and cobalt phthalocyanine embedded electrospun carbon nanofiber-based catalysts for anion exchange membrane fuel cell cathode, J. Catal. 422 (2023) 117–130. https://doi.org/10.1016/j.jcat.2023.04.008.
[260] L. Zhang, Y. Dong, L. Li, Y. Shi, Y. Zhang, L. Wei, C.-L. Dong, Z. Lin, J. Su, Concurrently Boosting Activity and Stability of Oxygen Reduction Reaction Catalysts via Judiciously Crafting Fe–Mn Dual Atoms for Fuel Cells, Nanomicro Lett. 17(1) (2024) 88. https://doi.org/10.1007/s40820-024-01580-5.
[261] P.G. Santori, F.D. Speck, S. Cherevko, H.A. Firouzjaie, X. Peng, W.E. Mustain, F. Jaouen, High Performance FeNC and Mn-oxide/FeNC Layers for AEMFC Cathodes, J. Electrochem. Soc. 167(13) (2020) 134505. https://doi.org/10.1149/1945-7111/abb7e0.
[262] K. Kisand, A. Sarapuu, D. Danilian, A. Kikas, V. Kisand, M. Rähn, A. Treshchalov, M. Käärik, M. Merisalu, P. Paiste, J. Aruväli, J. Leis, V. Sammelselg, S. Holdcroft, K. Tammeveski, Transition metal-containing nitrogen-doped nanocarbon catalysts derived from 5-methylresorcinol for anion exchange membrane fuel cell application, J. Colloid Interface Sci. 584 (2021) 263–274. https://doi.org/10.1016/j.jcis.2020.09.114.
[263] J. Woo, S.Y. Yang, Y.J. Sa, W.-Y. Choi, M.-H. Lee, H.-W. Lee, T.J. Shin, T.-Y. Kim, S.H. Joo, Promoting Oxygen Reduction Reaction Activity of Fe–N/C Electrocatalysts by Silica-Coating-Mediated Synthesis for Anion-Exchange Membrane Fuel Cells, Chem. Mater. 30(19) (2018) 6684–6701. https://doi.org/10.1021/acs.chemmater.8b02117.
[264] J.K. Piir, J. Lilloja, M. Käärik, J. Kozlova, A. Kikas, A. Treshchalov, J. Aruväli, V. Kisand, J. Leis, K. Kukli, K. Tammeveski, Mesoporous carbon materials doped with Co, Fe and nitrogen as oxygen reduction reaction electrocatalysts for anion-exchange membrane fuel cell, Electrochim. Acta 527 (2025) 146226. https://doi.org/10.1016/j.electacta.2025.146226.
[265] I. Palm, R. Sibul, E. Kibena-Põldsepp, M. Mooste, J. Lilloja, M. Käärik, J. Kozlova, A. Kikas, A. Treshchalov, J. Leis, V. Kisand, A. Tamm, N. Bibent, F.

Jaouen, S. Holdcroft, K. Tammeveski, ZIF-8 derived iron-, sulphur-, and nitrogen-doped catalysts for anion-exchange membrane fuel cell application, Renew. Energy 228 (2024) 120613. https://doi.org/10.1016/j.renene.2024.120613.
[266] J. Guo, H. He, D. Chu, R. Chen, OH−-Binding Effects on Metallophthalocyanine Catalysts for O2 Reduction Reaction in Anion Exchange Membrane Fuel Cells, Electrocatalysis 3(3) (2012) 252–264. https://doi.org/10.1007/s12678-012-0106-1.
[267] S.S. Chougule, A.A. Jeffery, D. Kim, M. Kim, Y. Kim, K. Ko, J. Min, K. Davletbaev, A.A. Chavan, H. Park, Y. Lee, S. Jang, N. Jung, Rational engineering of iron phthalocyanine-derived single atom catalysts for anion exchange membrane fuel cells, J. Am. Ceram. Soc. 108(10) (2025) e20557. https://doi.org/10.1111/jace.20557.
[268] X. Peng, V. Kashyap, B. Ng, S. Kurungot, L. Wang, J.R. Varcoe, W.E. Mustain, High-Performing PGM-Free AEMFC Cathodes from Carbon-Supported Cobalt Ferrite Nanoparticles, Catalysts, 2019, p. 264. https://doi.org/10.3390/catal9030264.

10. SUMMARY IN ESTONIAN

ZIF-8 põhised M-N-C elektrokatalüsaatorid hapniku redutseerumisreaktsiooniks AEMFC ja MFC seadmetes

Doktoritöö eesmärk oli valmistada ZIF-8 põhised siirdemetall-lämmastik-süsinik (M-N-C) tüüpi katalüsaatorid hapniku redutseerumisreaktsiooni (ORR) elektrokatalüüsiks anioonivahetusmembraaniga kütuseelemendi (AEMFC) ja mikroobse kütuseelemendi (MFC) katoodidele. Need materjalid näitasid kõrget ORRi elektrokatalüütilist aktiivsust nii neutraalses kui ka aluselises keskkonnas ning osutusid paljulubavaks alternatiiviks kallitele Pt-põhistele katalüsaatoritele. Kõik valmistatud materjalid läbisid põhjaliku füüsikalise karakteriseerimise, et hinnata nende struktuuri ja aktiivtsentrite jaotusest. Töös kasutati pöörleva ketaselektroodi (RDE) ja pöörleva rõngas-ketaselektroodi (RRDE) meetodeid, et uurida nende materjalide elektrokatalüütilist aktiivsust ja ORRi reaktsiooniteed. Lõpuks integreeriti parimad katalüsaatorid AEMFC ja MFC seadmetesse, et hinnata nende energiatootmise võimekust. Käesolev doktoritöö loob tervikliku aluse aktiivsete M-N-C elektrokatalüsaatorite väljatöötaamiseks, keskendudes aktiivtsentrite soodsale jaotusele ja hapniku ligipääsetavusele nendele tsentritele.

Töö esimeses osas valmistati Fe ja Co sisaldusega katalüsaatorid pürolüüsi teel [I, II]. Saadud FeCo-N-C katalüsaatormaterjalid olid hierarhilise poorsusega, mis soodustas hapniku massiülekannet. Süsiniknanotorude (MWCNT) lisamine parandas materjalide elektrijuhtivust. Sünteesitud FeCo-põhised katalüsaatorid näitasid RDE ja RRDE testides head ORRi aktiivsust nii 0,1 M KOH kui ka 0,1 M PBS lahustes. Vesinikperoksiidi saagis 20% RRDE testis osutas FeCo-N-C materjali suuremale selektiivsusele $4e^-$ reaktsioonitee osas. Lisaks saavutati selle katalüsaatori rakendamisel katoodina AEMFC ja MFC seadmetes maksimaalse võimsustiheduse (P_{max}) väärtuseks vastavalt 171 mW cm^{-2} ja 1557 mW m^{-2}. Selline silmapaistev jõudlus omistati O_2 molekulidele hästi ligipääsetavatele ning atomaarselt dispergeeritud M-N_x aktiivtsentritele ja materjali suurele eripinnale.

Doktoritöö teine osa keskendus Ce lisamisele katalüsaatoritele, et optimeerida materjali elektronstruktuuri, millel on hapnikkusisaldavate radikaalide püüdmise võime ja mis katalüüsib hapniku redutseerumist valdavalt $4e^-$ reaktsioonitee kaudu [III]. Selles töös kasutati katalüsaatormaterjalide valmistamiseks ZIF-8, MWCNT ja Fe/Ce soolade segu kõrgtemperatuurset pürolüüsi. Füüsikalis-keemilise iseloomustamine näitas, et Fe lisamine soodustas Zn lendumist. Ce lisamise tõttu vähenes laenguülekande takistus ja suurenes O_2 molekulidele ligipääsetavate aktiivtsentrite tihedus. M-N_x tsentrite ühtlast jaotust kinnitas skaneeriva läbistuselektronmikroskoopia analüüs. Sünteesitud Fe_1Ce_1@N-C katalüsaatoril oli suurepärane ORRi aktiivsus 0,1 M PBS lahuses, kus saadi $E_{1/2}$ väärtuseks 0,76 V vs RHE. Kahekambrilise MFC katoodina rakendamisel saavutas Fe_1Ce_1@N-C katalüsaator P_{max} väärtuseks 200 mW m^{-2}. Valmistatud katalüsaator kiirendas ORRi kineetikat, mistõttu parandas ka reovee puhastamise efektiivsust, sest keemilise hapnikutarbe (COD) eemaldamine ületas 85% [III].

Väitekirja järgmises osas valmistati kahe pürolüüsilaevukese ainulaadse kooskasutamisel ja kaheetapilise pürolüüsimeetodi abil FePc põhjal saadud Fe-N-C materjalid *in situ* nitrideerimise abil. Saadud materjalis Fe-N_x tsentrite läheduses olevad hübriidsed Fe/Fe_4N funktsionaalrühmad optimeerisid hapniku redutseerumise vaheühendite adsorptsiooni [IV]. Saadud Fe/Fe_4N@Fe-N-C materjali iseloomustas mikropoorne struktuur ja ligipääsetavate Fe-N_x tsentrite suur tihedus. Lisaks soodustas moodustunud nitriid grafitiseerumist, võimaldades kiiremat laenguülekande kineetikat. RDE testides saavutas see katalüsaator muljetavaldava $E_{1/2}$ väärtuse 0,79 V, edestades varasemaid Fe_1Ce_1@N-C [III] ja FeCo-N-C@900 [II] katalüsaatoreid. MFC testis saadi P_{max} väärtuseks 277 mW m^{-2} ja COD eemaldamise efektiivsuseks 85%, mis kinnitab, et nitriidimismeetodil soodsamaks muudetud katalüsaatori struktuurist parandab ORRi kineetikat.

Doktoritöö neljandas osas valmistati Mn-dopeeritud ZIF-8@CNT põhised katalüsaatorid pürolüüsi abil erinevate ZIF-8 ja Mn molaarsuhetega [V]. Sellisel viisil valmistatud Mn/Zn-NC@CNT_10 katalüsaatoril oli optimaalne poorsus ja kõrgeim ORRi aktiivsus 0,1 M KOH lahuses. Täheldati Zn-N_x tsentrite esinemist, mis vähendas elektrokatalüütiliselt aktiivsete ja eelistatud Mn-N_x tsentrite mõju. Järgnev happetöötlus ja teistkordne pürolüüs suurendasid oluliselt Mn-N-C@CNT katalüsaatori eripinda ja kõrvaldasid järelejäänud Zn sisalduse. Veelgi olulisem, et Mn-N-C@CNT katoodkatalüsaatoriga paranes AEMFC jõudlus märgatavalt, saavutades P_{max} väärtuseks 975 mW cm^{-2}, mis oli kõrgem kui Pt/C katoodil. Selle töö tulemused näitasid, et Zn-N_x tsentrite kõrvaldamine on ORRi kineetika ja reaktsioonitee optimeerimiseks ülioluline. Väitekirja viimane osa on inspireeritud varasemast tööst [V] ja selles uuritakse MPc ja ZIF-8 integreerimist materjali, et lahendada aktiivtsentrite tiheduse ja metalli aglomeratsiooniga seotud probleeme [VI]. Selles töös kasutati kahte siirdemetalli sisaldavate M-N-C katalüsaatorite valmistamiseks kahekordset pürolüüsi. Kõigepealt valmistati süsinikskelett ZIF-8 ja MWCNT segu pürolüüsi teel, mis viidi läbi erinevatel temperatuuridel (500, 700, 900 °C). Seejärel tehti happetöötlus, mis kõrvaldas suurema osa Zn jäägist ning parandas ORRi aktiivsust. Optimeeritud NC900a süsinikskeleti struktuurilisi ja elektroonseid omadusi parandati veelgi kahe metalloftalotsüaniini lisamisega, misjärel $Fe_{1.5}Co_{1.5}$-NC900a materjal näitas silmapaistvaimat ORRi aktiivsust 0,1 M KOH lahuses. AEMFC katoodil saadi selle katoodkatalüsaatoriga erakordselt kõrge P_{max} väärtus 1,02 W cm^{-2}.

Kokkuvõttes annab see doktoritöö suure panuse aktiivsete Pt-vabade ORRi katalüsaatorite arendamisse eri tüüpi kütuseelementide (AEMFC ja MFC) katoodide jaoks. Töös keskenduti aktiivtsentrite tiheduse ja ligipääsetavuse optimeerimisele, et parandada katalüsaatorite elektrokatalüütilist aktiivsust. Saadud tulemused näitavad märkimisväärset arengut mitteväärismetallidel põhinevate katalüsaatorite väljatöötamisel ning toetavad selle teadusvaldkonna edasist arengut.

11. ACKNOWLEDGEMENTS

My deepest gratitude to my supervisors, Dr. Marek Mooste, Dr. Ivar Zekker, and Professor Kaido Tammeveski, for their valuable guidance and support throughout my PhD journey. My special thanks to Professor Kaido Tammeveski for giving me the opportunity to work in his workgroup. His patience, motivation, enthusiasm, and profound knowledge have been invaluable in contributing to the quality of this work.

I would like to extend my gratitude to all the members of our working group. I am very thankful to all my co-authors for their valuable contributions in the publications, with special recognition to Jaan Aruväli (for XRD), Dr Alexey Treshchalov (for Raman spectroscopy), Professor Arvo Kikas (for XPS), Dr Jekaterina Kozlova (for STEM-EDX), Markus Otsus and Markus Kõiv for SEM measurements. Furthermore, I would like to thank Professor José H. Zagal from the University of Santiago de Chile.

My sincere appreciation to my friends Dr. Zubair Ahmed, Faysal Al-Mamun, Ashish and Ankit for their unwavering support and motivation. A special note of gratitude goes to Dr. Geeta Arya, whose unwavering support during challenging times gave me immense strength and resilience. Last, but not least, I want to extend my heartfelt thanks to the most beloved people in my life, my parents and my sister Anjali, for their constant love and encouragement in every situation. I would especially like to thank my father, Mr Rampal, and my mother, Ms Sushma, for their constant support and belief in me during distressing situations.

Finally, I sincerely thank the Estonian Research Council (grants PRG723, PRG2569 and KOHTO12), the European Regional Development Fund (TK141, “Advanced materials and high-technology devices for energy recuperation systems”) and the Estonian Ministry of Education and Research (TK210, “Centre of Excellence in Sustainable Green Hydrogen and Energy Technologies”) for the financial support to fulfil this thesis work.

PUBLICATIONS

CURRICULUM VITAE

Name: Rohit Kumar
Date of birth: January 12, 1996
Citizenship: Indian
Current position: Junior Research Fellow
Phone: +372 5632 2341
E-mail: rohit.kumar@ut.ee

Education:

2022–…	PhD student, University of Tartu
2013–2019	BS-MS dual degree, Indian Institute of Science Education and Research (IISER), Mohali, India

Major scientific publications:

1. **R. Kumar**, M. Mooste, Z. Ahmed, S. Akula, I. Zekker, M. Marandi, M. Käärik, J. Leis, A. Kikas, A. Treshchalov, M. Otsus, J. Aruväli, V. Kisand, A. Tamm, K. Tammeveski, Highly active ZIF-8@CNT composite catalysts as cathode materials for anion exchange membrane fuel cells, *Industrial Chemistry & Materials* 1(4) (2023) 526-541.
2. **R. Kumar**, M. Mooste, Z. Ahmed, I. Zekker, M. Marandi, M. Käärik, J. Leis, A. Kikas, A. Treshchalov, M. Otsus, J. Aruväli, V. Kisand, A. Tamm, K. Tammeveski, Catalyzing oxygen reduction by morphologically engineered ZIF-derived carbon composite catalysts in dual-chamber microbial fuel cells, *Journal of Environmental Chemical Engineering* 12 (2) (2024) 112242.
3. **R. Kumar**, M. Mooste, I. Zekker, M. Käärik, J. Leis, A. Kikas, A. Treshchalov, J. Kozlova, M. Otsus, J. Aruväli, V. Kisand, K. Kukli, K. Tammeveski, Tailoring highly efficient ZIF-derived Fe_xCe_y@N–C composite catalysts for oxygen reduction reaction in H-shape microbial fuel cells, *International Journal of Hydrogen Energy* 98 (2025) 793-806.
4. **R. Kumar**, M. Mooste, I. Zekker, J. Kozlova, M. Otsus, M. Käärik, J. Aruväli, A. Kikas, A. Treshchalov, J. Leis, V. Kisand, K. Kukli, K. Tammeveski, Hybrid Fe/Fe_4N and Fe-N_x decorated Fe-N-C material for efficient oxygen reduction reaction electrocatalysis in microbial fuel cells, *Journal of Alloys and Compounds* 1060 (2026) 187251.
5. **R. Kumar**, M. Mooste, I. Zekker, J. Kozlova, M. Käärik, M. Otsus, A. Treshchalov, J. Aruväli, J. Leis, A. Kikas, V. Kisand, K. Kukli, K. Tammeveski, Mn-N-C material with high-density and accessible Mn-N_x sites emerging as an efficient oxygen reduction reaction electrocatalyst for AEMFCs, *Journal of Power Sources* 667 (2026) 239191.

Other scientific publications:

1. Mooste, M., **Kumar, R.**, Juvanen, S., Kozlova, J., Kikas, A., Treshchalov, A., Käärik, M., Aruväli, J., Leis, J., Kisand, V., Kukli, K., Schonvogel, D., Wagner, P., Wilhelm, M., Tammeveski, K., Friedrich, K.A. Binary transition metal and nitrogen functionalised silicon oxycarbide electrocatalysts for Zn–air battery air electrode application. *International Journal of Energy Research*, 2025 (1), (2025) 4252866.

2. **Kumar, R.**, Rauwel, P., Kriipsalu, M., Wragg, D., Rauwel, E. Nanocobalt based (Co@Co(OH)2) sand nanocomposite applied to manganese extraction from contaminated water. *Journal of Environmental Chemical Engineering*, 11(3), (2023) 109818.
3. Muuli, K., **Kumar, R.**, Mooste, M., Gudkova, V., Treshchalov, A., Piirsoo, H.-M.; Kikas, A., Aruväli, J., Kisand, V., Tamm, A., Krumme, A., Moni, P., Wilhelm, M., Tammeveski, K. Iron, cobalt, and nickel phthalocyanines tri-doped electrospun carbon nanofibre-based catalyst for rechargeable zinc-air battery air electrode. *Materials*, 16 (13), (2023) 4626.
4. **Kumar, R.**, Yadav, S., Patil, Sunil A. Bioanode-Assisted Removal of Hg^{2+} at the Cathode of Microbial Fuel Cells. *Journal of Hazardous Toxic and Radioactive Waste*, 24 (4), (2020) 04020034.

ELULOOKIRJELDUS

Nimi: Rohit Kumar
Sünniaeg: 12. jaanuar1996
Kodakondsus: India
Praegune töökoht: nooremteadur
Telefon: +372 5632 2341
E-post: rohit.kumar@ut.ee

Haridus:

2022–…	Tartu Ülikool, doktorant (keemia)
2013–2019	Teadushariduse ja Uuringute India Instituut, Mohali (India) bakalaureuse- ja magistrikraad

Publikatsioonide loetelu:

1. **R. Kumar**, M. Mooste, Z. Ahmed, S. Akula, I. Zekker, M. Marandi, M. Käärik, J. Leis, A. Kikas, A. Treshchalov, M. Otsus, J. Aruväli, V. Kisand, A. Tamm, K. Tammeveski, Highly active ZIF-8@CNT composite catalysts as cathode materials for anion exchange membrane fuel cells, *Industrial Chemistry & Materials* 1(4) (2023) 526-541.
2. **R. Kumar**, M. Mooste, Z. Ahmed, I. Zekker, M. Marandi, M. Käärik, J. Leis, A. Kikas, A. Treshchalov, M. Otsus, J. Aruväli, V. Kisand, A. Tamm, K. Tammeveski, Catalyzing oxygen reduction by morphologically engineered ZIF-derived carbon composite catalysts in dual-chamber microbial fuel cells, *Journal of Environmental Chemical Engineering* 12 (2) (2024) 112242.
3. **R. Kumar**, M. Mooste, I. Zekker, M. Käärik, J. Leis, A. Kikas, A. Treshchalov, J. Kozlova, M. Otsus, J. Aruväli, V. Kisand, K. Kukli, K. Tammeveski, Tailoring highly efficient ZIF-derived Fe_xCe_y@N–C composite catalysts for oxygen reduction reaction in H-shape microbial fuel cells, *International Journal of Hydrogen Energy* 98 (2025) 793-806.
4. **R. Kumar**, M. Mooste, I. Zekker, J. Kozlova, M. Otsus, M. Käärik, J. Aruväli, A. Kikas, A. Treshchalov, J. Leis, V. Kisand, K. Kukli, K. Tammeveski, Hybrid Fe/Fe_4N and Fe-N_x decorated Fe-N-C material for efficient oxygen reduction reaction electrocatalysis in microbial fuel cells, *Journal of Alloys and Compounds* 1060 (2026) 187251.
5. **R. Kumar**, M. Mooste, I. Zekker, J. Kozlova, M. Käärik, M. Otsus, A. Treshchalov, J. Aruväli, J. Leis, A. Kikas, V. Kisand, K. Kukli, K. Tammeveski, Mn-N-C material with high-density and accessible Mn-N_x sites emerging as an efficient oxygen reduction reaction electrocatalyst for AEMFCs, *Journal of Power Sources* 667 (2026) 239191.

Muud teaduspublikatsioonid:

1. Mooste, M., **Kumar, R.**, Juvanen, S., Kozlova, J., Kikas, A., Treshchalov, A., Käärik, M., Aruväli, J., Leis, J., Kisand, V., Kukli, K., Schonvogel, D., Wagner, P., Wilhelm, M., Tammeveski, K., Friedrich, K.A. Binary transition metal and nitrogen functionalised silicon oxycarbide electrocatalysts for Zn–air battery air electrode application. *International Journal of Energy Research*, 2025 (1), (2025) 4252866.

2. **Kumar, R.**, Rauwel, P., Kriipsalu, M., Wragg, D., Rauwel, E. Nanocobalt based (Co@Co(OH)2) sand nanocomposite applied to manganese extraction from contaminated water. *Journal of Environmental Chemical Engineering*, 11(3), (2023) 109818.
3. Muuli, K., **Kumar, R.**, Mooste, M., Gudkova, V., Treshchalov, A., Piirsoo, H.-M.; Kikas, A., Aruväli, J., Kisand, V., Tamm, A., Krumme, A., Moni, P., Wilhelm, M., Tammeveski, K. Iron, cobalt, and nickel phthalocyanines tri-doped electrospun carbon nanofibre-based catalyst for rechargeable zinc-air battery air electrode. *Materials*, 16 (13), (2023) 4626.
4. **Kumar, R.**, Yadav, S., Patil, Sunil A. Bioanode-Assisted Removal of Hg^{2+} at the Cathode of Microbial Fuel Cells. *Journal of Hazardous Toxic and Radioactive Waste*, 24 (4), (2020) 04020034.

DISSERTATIONES CHIMICAE UNIVERSITATIS TARTUENSIS

1. **Toomas Tamm.** Quantum-chemical simulation of solvent effects. Tartu, 1993, 110 p.
2. **Peeter Burk.** Theoretical study of gas-phase acid-base equilibria. Tartu, 1994, 96 p.
3. **Victor Lobanov.** Quantitative structure-property relationships in large descriptor spaces. Tartu, 1995, 135 p.
4. **Vahur Mäemets.** The ^{17}O and ^{1}H nuclear magnetic resonance study of H_2O in individual solvents and its charged clusters in aqueous solutions of electrolytes. Tartu, 1997, 140 p.
5. **Andrus Metsala.** Microcanonical rate constant in nonequilibrium distribution of vibrational energy and in restricted intramolecular vibrational energy redistribution on the basis of slater's theory of unimolecular reactions. Tartu, 1997, 150 p.
6. **Uko Maran.** Quantum-mechanical study of potential energy surfaces in different environments. Tartu, 1997, 137 p.
7. **Alar Jänes.** Adsorption of organic compounds on antimony, bismuth and cadmium electrodes. Tartu, 1998, 219 p.
8. **Kaido Tammeveski.** Oxygen electroreduction on thin platinum films and the electrochemical detection of superoxide anion. Tartu, 1998, 139 p.
9. **Ivo Leito.** Studies of Brønsted acid-base equilibria in water and non-aqueous media. Tartu, 1998, 101 p.
10. **Jaan Leis.** Conformational dynamics and equilibria in amides. Tartu, 1998, 131 p.
11. **Toonika Rinken.** The modelling of amperometric biosensors based on oxidoreductases. Tartu, 2000, 108 p.
12. **Dmitri Panov.** Partially solvated Grignard reagents. Tartu, 2000, 64 p.
13. **Kaja Orupõld.** Treatment and analysis of phenolic wastewater with microorganisms. Tartu, 2000, 123 p.
14. **Jüri Ivask.** Ion Chromatographic determination of major anions and cations in polar ice core. Tartu, 2000, 85 p.
15. **Lauri Vares.** Stereoselective Synthesis of Tetrahydrofuran and Tetrahydropyran Derivatives by Use of Asymmetric Horner-Wadsworth-Emmons and Ring Closure Reactions. Tartu, 2000, 184 p.
16. **Martin Lepiku.** Kinetic aspects of dopamine D_2 receptor interactions with specific ligands. Tartu, 2000, 81 p.
17. **Katrin Sak.** Some aspects of ligand specificity of P2Y receptors. Tartu, 2000, 106 p.
18. **Vello Pällin.** The role of solvation in the formation of iotsitch complexes. Tartu, 2001, 95 p.
19. **Katrin Kollist.** Interactions between polycyclic aromatic compounds and humic substances. Tartu, 2001, 93 p.

20. **Ivar Koppel.** Quantum chemical study of acidity of strong and superstrong Brønsted acids. Tartu, 2001, 104 p.
21. **Viljar Pihl.** The study of the substituent and solvent effects on the acidity of OH and CH acids. Tartu, 2001, 132 p.
22. **Natalia Palm.** Specification of the minimum, sufficient and significant set of descriptors for general description of solvent effects. Tartu, 2001, 134 p.
23. **Sulev Sild.** QSPR/QSAR approaches for complex molecular systems. Tartu, 2001, 134 p.
24. **Ruslan Petrukhin.** Industrial applications of the quantitative structure-property relationships. Tartu, 2001, 162 p.
25. **Boris V. Rogovoy.** Synthesis of (benzotriazolyl)carboximidamides and their application in relations with *N*- and *S*-nucleophyles. Tartu, 2002, 84 p.
26. **Koit Herodes.** Solvent effects on UV-vis absorption spectra of some solvatochromic substances in binary solvent mixtures: the preferential solvation model. Tartu, 2002, 102 p.
27. **Anti Perkson.** Synthesis and characterisation of nanostructured carbon. Tartu, 2002, 152 p.
28. **Ivari Kaljurand.** Self-consistent acidity scales of neutral and cationic Brønsted acids in acetonitrile and tetrahydrofuran. Tartu, 2003, 108 p.
29. **Karmen Lust.** Adsorption of anions on bismuth single crystal electrodes. Tartu, 2003, 128 p.
30. **Mare Piirsalu.** Substituent, temperature and solvent effects on the alkaline hydrolysis of substituted phenyl and alkyl esters of benzoic acid. Tartu, 2003, 156 p.
31. **Meeri Sassian.** Reactions of partially solvated Grignard reagents. Tartu, 2003, 78 p.
32. **Tarmo Tamm.** Quantum chemical modelling of polypyrrole. Tartu, 2003. 100 p.
33. **Erik Teinemaa.** The environmental fate of the particulate matter and organic pollutants from an oil shale power plant. Tartu, 2003. 102 p.
34. **Jaana Tammiku-Taul.** Quantum chemical study of the properties of Grignard reagents. Tartu, 2003. 120 p.
35. **Andre Lomaka.** Biomedical applications of predictive computational chemistry. Tartu, 2003. 132 p.
36. **Kostyantyn Kirichenko.** Benzotriazole – Mediated Carbon–Carbon Bond Formation. Tartu, 2003. 132 p.
37. **Gunnar Nurk.** Adsorption kinetics of some organic compounds on bismuth single crystal electrodes. Tartu, 2003, 170 p.
38. **Mati Arulepp.** Electrochemical characteristics of porous carbon materials and electrical double layer capacitors. Tartu, 2003, 196 p.
39. **Dan Cornel Fara.** QSPR modeling of complexation and distribution of organic compounds. Tartu, 2004, 126 p.
40. **Riina Mahlapuu.** Signalling of galanin and amyloid precursor protein through adenylate cyclase. Tartu, 2004, 124 p.

41. **Mihkel Kerikmäe.** Some luminescent materials for dosimetric applications and physical research. Tartu, 2004, 143 p.
42. **Jaanus Kruusma.** Determination of some important trace metal ions in human blood. Tartu, 2004, 115 p.
43. **Urmas Johanson.** Investigations of the electrochemical properties of polypyrrole modified electrodes. Tartu, 2004, 91 p.
44. **Kaido Sillar.** Computational study of the acid sites in zeolite ZSM-5. Tartu, 2004, 80 p.
45. **Aldo Oras.** Kinetic aspects of dATPαS interaction with $P2Y_1$ receptor. Tartu, 2004, 75 p.
46. **Erik Mölder.** Measurement of the oxygen mass transfer through the air-water interface. Tartu, 2005, 73 p.
47. **Thomas Thomberg.** The kinetics of electroreduction of peroxodisulfate anion on cadmium (0001) single crystal electrode. Tartu, 2005, 95 p.
48. **Olavi Loog.** Aspects of condensations of carbonyl compounds and their imine analogues. Tartu, 2005, 83 p.
49. **Siim Salmar.** Effect of ultrasound on ester hydrolysis in aqueous ethanol. Tartu, 2006, 73 p.
50. **Ain Uustare.** Modulation of signal transduction of heptahelical receptors by other receptors and G proteins. Tartu, 2006, 121 p.
51. **Sergei Yurchenko.** Determination of some carcinogenic contaminants in food. Tartu, 2006, 143 p.
52. **Kaido Tämm.** QSPR modeling of some properties of organic compounds. Tartu, 2006, 67 p.
53. **Olga Tšubrik.** New methods in the synthesis of multisubstituted hydrazines. Tartu. 2006, 183 p.
54. **Lilli Sooväli.** Spectrophotometric measurements and their uncertainty in chemical analysis and dissociation constant measurements. Tartu, 2006, 125 p.
55. **Eve Koort.** Uncertainty estimation of potentiometrically measured ph and pK_a values. Tartu, 2006, 139 p.
56. **Sergei Kopanchuk.** Regulation of ligand binding to melanocortin receptor subtypes. Tartu, 2006, 119 p.
57. **Silvar Kallip.** Surface structure of some bismuth and antimony single crystal electrodes. Tartu, 2006, 107 p.
58. **Kristjan Saal.** Surface silanization and its application in biomolecule coupling. Tartu, 2006, 77 p.
59. **Tanel Tätte.** High viscosity $Sn(OBu)_4$ oligomeric concentrates and their applications in technology. Tartu, 2006, 91 p.
60. **Dimitar Atanasov Dobchev**. Robust QSAR methods for the prediction of properties from molecular structure. Tartu, 2006, 118 p.
61. **Hannes Hagu**. Impact of ultrasound on hydrophobic interactions in solutions. Tartu, 2007, 81 p.
62. **Rutha Jäger.** Electroreduction of peroxodisulfate anion on bismuth electrodes. Tartu, 2007, 142 p.

63. **Kaido Viht.** Immobilizable bisubstrate-analogue inhibitors of basophilic protein kinases: development and application in biosensors. Tartu, 2007, 88 p.
64. **Eva-Ingrid Rõõm.** Acid-base equilibria in nonpolar media. Tartu, 2007, 156 p.
65. **Sven Tamp.** DFT study of the cesium cation containing complexes relevant to the cesium cation binding by the humic acids. Tartu, 2007, 102 p.
66. **Jaak Nerut.** Electroreduction of hexacyanoferrate(III) anion on Cadmium (0001) single crystal electrode. Tartu, 2007, 180 p.
67. **Lauri Jalukse.** Measurement uncertainty estimation in amperometric dissolved oxygen concentration measurement. Tartu, 2007, 112 p.
68. **Aime Lust.** Charge state of dopants and ordered clusters formation in CaF_2:Mn and CaF_2:Eu luminophors. Tartu, 2007, 100 p.
69. **Iiris Kahn**. Quantitative Structure-Activity Relationships of environmentally relevant properties. Tartu, 2007, 98 p.
70. **Mari Reinik.** Nitrates, nitrites, N-nitrosamines and polycyclic aromatic hydrocarbons in food: analytical methods, occurrence and dietary intake. Tartu, 2007, 172 p.
71. **Heili Kasuk.** Thermodynamic parameters and adsorption kinetics of organic compounds forming the compact adsorption layer at Bi single crystal electrodes. Tartu, 2007, 212 p.
72. **Erki Enkvist.** Synthesis of adenosine-peptide conjugates for biological applications. Tartu, 2007, 114 p.
73. **Svetoslav Hristov Slavov**. Biomedical applications of the QSAR approach. Tartu, 2007, 146 p.
74. **Eneli Härk.** Electroreduction of complex cations on electrochemically polished Bi(*hkl*) single crystal electrodes. Tartu, 2008, 158 p.
75. **Priit Möller.** Electrochemical characteristics of some cathodes for medium temperature solid oxide fuel cells, synthesized by solid state reaction technique. Tartu, 2008, 90 p.
76. **Signe Viggor.** Impact of biochemical parameters of genetically different pseudomonads at the degradation of phenolic compounds. Tartu, 2008, 122 p.
77. **Ave Sarapuu.** Electrochemical reduction of oxygen on quinone-modified carbon electrodes and on thin films of platinum and gold. Tartu, 2008, 134 p.
78. **Agnes Kütt.** Studies of acid-base equilibria in non-aqueous media. Tartu, 2008, 198 p.
79. **Rouvim Kadis.** Evaluation of measurement uncertainty in analytical chemistry: related concepts and some points of misinterpretation. Tartu, 2008, 118 p.
80. **Valter Reedo.** Elaboration of IVB group metal oxide structures and their possible applications. Tartu, 2008, 98 p.
81. **Aleksei Kuznetsov.** Allosteric effects in reactions catalyzed by the cAMP-dependent protein kinase catalytic subunit. Tartu, 2009, 133 p.

82. **Aleksei Bredihhin.** Use of mono- and polyanions in the synthesis of multisubstituted hydrazine derivatives. Tartu, 2009, 105 p.
83. **Anu Ploom.** Quantitative structure-reactivity analysis in organosilicon chemistry. Tartu, 2009, 99 p.
84. **Argo Vonk.** Determination of adenosine A_{2A}- and dopamine D_1 receptor-specific modulation of adenylate cyclase activity in rat striatum. Tartu, 2009, 129 p.
85. **Indrek Kivi.** Synthesis and electrochemical characterization of porous cathode materials for intermediate temperature solid oxide fuel cells. Tartu, 2009, 177 p.
86. **Jaanus Eskusson.** Synthesis and characterisation of diamond-like carbon thin films prepared by pulsed laser deposition method. Tartu, 2009, 117 p.
87. **Marko Lätt.** Carbide derived microporous carbon and electrical double layer capacitors. Tartu, 2009, 107 p.
88. **Vladimir Stepanov.** Slow conformational changes in dopamine transporter interaction with its ligands. Tartu, 2009, 103 p.
89. **Aleksander Trummal.** Computational Study of Structural and Solvent Effects on Acidities of Some Brønsted Acids. Tartu, 2009, 103 p.
90. **Eerold Vellemäe.** Applications of mischmetal in organic synthesis. Tartu, 2009, 93 p.
91. **Sven Parkel.** Ligand binding to 5-HT_{1A} receptors and its regulation by Mg^{2+} and Mn^{2+}. Tartu, 2010, 99 p.
92. **Signe Vahur.** Expanding the possibilities of ATR-FT-IR spectroscopy in determination of inorganic pigments. Tartu, 2010, 184 p.
93. **Tavo Romann**. Preparation and surface modification of bismuth thin film, porous, and microelectrodes. Tartu, 2010, 155 p.
94. **Nadežda Aleksejeva.** Electrocatalytic reduction of oxygen on carbon nanotube-based nanocomposite materials. Tartu, 2010, 147 p.
95. **Marko Kullapere.** Electrochemical properties of glassy carbon, nickel and gold electrodes modified with aryl groups. Tartu, 2010, 233 p.
96. **Liis Siinor.** Adsorption kinetics of ions at Bi single crystal planes from aqueous electrolyte solutions and room-temperature ionic liquids. Tartu, 2010, 101 p.
97. **Angela Vaasa.** Development of fluorescence-based kinetic and binding assays for characterization of protein kinases and their inhibitors. Tartu 2010, 101 p.
98. **Indrek Tulp.** Multivariate analysis of chemical and biological properties. Tartu 2010, 105 p.
99. **Aare Selberg.** Evaluation of environmental quality in Northern Estonia by the analysis of leachate. Tartu 2010, 117 p.
100. **Darja Lavõgina.** Development of protein kinase inhibitors based on adenosine analogue-oligoarginine conjugates. Tartu 2010, 248 p.
101. **Laura Herm.** Biochemistry of dopamine D_2 receptors and its association with motivated behaviour. Tartu 2010, 156 p.

102. **Terje Raudsepp.** Influence of dopant anions on the electrochemical properties of polypyrrole films. Tartu 2010, 112 p.
103. **Margus Marandi.** Electroformation of Polypyrrole Films: *In-situ* AFM and STM Study. Tartu 2011, 116 p.
104. **Kairi Kivirand.** Diamine oxidase-based biosensors: construction and working principles. Tartu, 2011, 140 p.
105. **Anneli Kruve.** Matrix effects in liquid-chromatography electrospray mass-spectrometry. Tartu, 2011, 156 p.
106. **Gary Urb.** Assessment of environmental impact of oil shale fly ash from PF and CFB combustion. Tartu, 2011, 108 p.
107. **Nikita Oskolkov.** A novel strategy for peptide-mediated cellular delivery and induction of endosomal escape. Tartu, 2011, 106 p.
108. **Dana Martin.** The QSPR/QSAR approach for the prediction of properties of fullerene derivatives. Tartu, 2011, 98 p.
109. **Säde Viirlaid.** Novel glutathione analogues and their antioxidant activity. Tartu, 2011, 106 p.
110. **Ülis Sõukand.** Simultaneous adsorption of Cd^{2+}, Ni^{2+}, and Pb^{2+} on peat. Tartu, 2011, 124 p.
111. **Lauri Lipping.** The acidity of strong and superstrong Brønsted acids, an outreach for the "limits of growth": a quantum chemical study. Tartu, 2011, 124 p.
112. **Heisi Kurig.** Electrical double-layer capacitors based on ionic liquids as electrolytes. Tartu, 2011, 146 p.
113. **Marje Kasari.** Bisubstrate luminescent probes, optical sensors and affinity adsorbents for measurement of active protein kinases in biological samples. Tartu, 2012, 126 p.
114. **Kalev Takkis.** Virtual screening of chemical databases for bioactive molecules. Tartu, 2012, 122 p.
115. **Ksenija Kisseljova**. Synthesis of aza-β^3-amino acid containing peptides and kinetic study of their phosphorylation by protein kinase A. Tartu, 2012, 104 p.
116. **Riin Rebane.** Advanced method development strategy for derivatization LC/ESI/MS. Tartu, 2012, 184 p.
117. **Vladislav Ivaništšev.** Double layer structure and adsorption kinetics of ions at metal electrodes in room temperature ionic liquids. Tartu, 2012, 128 p.
118. **Irja Helm.** High accuracy gravimetric Winkler method for determination of dissolved oxygen. Tartu, 2012, 139 p.
119. **Karin Kipper.** Fluoroalcohols as Components of LC-ESI-MS Eluents: Usage and Applications. Tartu, 2012, 164 p.
120. **Arno Ratas.** Energy storage and transfer in dosimetric luminescent materials. Tartu, 2012, 163 p.
121. **Reet Reinart-Okugbeni**. Assay systems for characterisation of subtype-selective binding and functional activity of ligands on dopamine receptors. Tartu, 2012, 159 p.

122. **Lauri Sikk.** Computational study of the Sonogashira cross-coupling reaction. Tartu, 2012, 81 p.
123. **Karita Raudkivi.** Neurochemical studies on inter-individual differences in affect-related behaviour of the laboratory rat. Tartu, 2012, 161 p.
124. **Indrek Saar.** Design of GalR2 subtype specific ligands: their role in depression-like behavior and feeding regulation. Tartu, 2013, 126 p.
125. **Ann Laheäär.** Electrochemical characterization of alkali metal salt based non-aqueous electrolytes for supercapacitors. Tartu, 2013, 127 p.
126. **Kerli Tõnurist.** Influence of electrospun separator materials properties on electrochemical performance of electrical double-layer capacitors. Tartu, 2013, 147 p.
127. **Kaija Põhako-Esko.** Novel organic and inorganic ionogels: preparation and characterization. Tartu, 2013, 124 p.
128. **Ivar Kruusenberg.** Electroreduction of oxygen on carbon nanomaterial-based catalysts. Tartu, 2013, 191 p.
129. **Sander Piiskop.** Kinetic effects of ultrasound in aqueous acetonitrile solutions. Tartu, 2013, 95 p.
130. **Ilona Faustova**. Regulatory role of L-type pyruvate kinase N-terminal domain. Tartu, 2013, 109 p.
131. **Kadi Tamm.** Synthesis and characterization of the micro-mesoporous anode materials and testing of the medium temperature solid oxide fuel cell single cells. Tartu, 2013, 138 p.
132. **Iva Bozhidarova Stoyanova-Slavova.** Validation of QSAR/QSPR for regulatory purposes. Tartu, 2013, 109 p.
133. **Vitali Grozovski**. Adsorption of organic molecules at single crystal electrodes studied by *in situ* STM method. Tartu, 2014, 146 p.
134. **Santa Veikšina**. Development of assay systems for characterisation of ligand binding properties to melanocortin 4 receptors. Tartu, 2014, 151 p.
135. **Jüri Liiv.** PVDF (polyvinylidene difluoride) as material for active element of twisting-ball displays. Tartu, 2014, 111 p.
136. **Kersti Vaarmets.** Electrochemical and physical characterization of pristine and activated molybdenum carbide-derived carbon electrodes for the oxygen electroreduction reaction. Tartu, 2014, 131 p.
137. **Lauri Tõntson**. Regulation of G-protein subtypes by receptors, guanine nucleotides and Mn^{2+}. Tartu, 2014, 105 p.
138. **Aiko Adamson.** Properties of amine-boranes and phosphorus analogues in the gas phase. Tartu, 2014, 78 p.
139. **Elo Kibena**. Electrochemical grafting of glassy carbon, gold, highly oriented pyrolytic graphite and chemical vapour deposition-grown graphene electrodes by diazonium reduction method. Tartu, 2014, 184 p.
140. **Teemu Näykki.** Novel Tools for Water Quality Monitoring – From Field to Laboratory. Tartu, 2014, 202 p.
141. **Karl Kaupmees.** Acidity and basicity in non-aqueous media: importance of solvent properties and purity. Tartu, 2014, 128 p.

142. **Oleg Lebedev**. Hydrazine polyanions: different strategies in the synthesis of heterocycles. Tartu, 2015, 118 p.
143. **Geven Piir.** Environmental risk assessment of chemicals using QSAR methods. Tartu, 2015, 123 p.
144. **Olga Mazina.** Development and application of the biosensor assay for measurements of cyclic adenosine monophosphate in studies of G protein-coupled receptor signalinga. Tartu, 2015, 116 p.
145. **Sandip Ashokrao Kadam.** Anion receptors: synthesis and accurate binding measurements. Tartu, 2015, 116 p.
146. **Indrek Tallo.** Synthesis and characterization of new micro-mesoporous carbide derived carbon materials for high energy and power density electrical double layer capacitors. Tartu, 2015, 148 p.
147. **Heiki Erikson.** Electrochemical reduction of oxygen on nanostructured palladium and gold catalysts. Tartu, 2015, 204 p.
148. **Erik Anderson.** *In situ* Scanning Tunnelling Microscopy studies of the interfacial structure between Bi(111) electrode and a room temperature ionic liquid. Tartu, 2015, 118 p.
149. **Girinath G. Pillai.** Computational Modelling of Diverse Chemical, Biochemical and Biomedical Properties. Tartu, 2015, 140 p.
150. **Piret Pikma.** Interfacial structure and adsorption of organic compounds at Cd(0001) and Sb(111) electrodes from ionic liquid and aqueous electrolytes: an *in situ* STM study. Tartu, 2015, 126 p.
151. **Ganesh babu Manoharan.** Combining chemical and genetic approaches for photoluminescence assays of protein kinases. Tartu, 2016, 126 p.
152. **Carolin Siimenson**. Electrochemical characterization of halide ion adsorption from liquid mixtures at Bi(111) and pyrolytic graphite electrode surface. Tartu, 2016, 110 p.
153. **Asko Laaniste.** Comparison and optimisation of novel mass spectrometry ionisation sources. Tartu, 2016, 156 p.
154. **Hanno Evard.** Estimating limit of detection for mass spectrometric analysis methods. Tartu, 2016, 224 p.
155. **Kadri Ligi.** Characterization and application of protein kinase-responsive organic probes with triplet-singlet energy transfer. Tartu, 2016, 122 p.
156. **Margarita Kagan.** Biosensing penicillins' residues in milk flows. Tartu, 2016, 130 p.
157. **Marie Kriisa.** Development of protein kinase-responsive photoluminescent probes and cellular regulators of protein phosphorylation. Tartu, 2016, 106 p.
158. **Mihkel Vestli.** Ultrasonic spray pyrolysis deposited electrolyte layers for intermediate temperature solid oxide fuel cells. Tartu, 2016, 156 p.
159. **Silver Sepp**. Influence of porosity of the carbide-derived carbon on the properties of the composite electrocatalysts and characteristics of polymer electrolyte fuel cells. Tartu, 2016, 137 p.
160. **Kristjan Haav**. Quantitative relative equilibrium constant measurements in supramolecular chemistry. Tartu, 2017, 158 p.

161. **Anu Teearu**. Development of MALDI-FT-ICR-MS methodology for the analysis of resinous materials. Tartu, 2017, 205 p.
162. **Taavi Ivan**. Bifunctional inhibitors and photoluminescent probes for studies on protein complexes. Tartu, 2017, 140 p.
163. **Maarja-Liisa Oldekop**. Characterization of amino acid derivatization reagents for LC-MS analysis. Tartu, 2017, 147 p.
164. **Kristel Jukk**. Electrochemical reduction of oxygen on platinum- and palladium-based nanocatalysts. Tartu, 2017, 250 p.
165. **Siim Kukk**. Kinetic aspects of interaction between dopamine transporter and *N*-substituted nortropane derivatives. Tartu, 2017, 107 p.
166. **Birgit Viira**. Design and modelling in early drug development in targeting HIV-1 reverse transcriptase and Malaria. Tartu, 2017, 172 p.
167. **Rait Kivi**. Allostery in cAMP dependent protein kinase catalytic subunit. Tartu, 2017, 115 p.
168. **Agnes Heering**. Experimental realization and applications of the unified acidity scale. Tartu, 2017, 123 p.
169. **Delia Juronen**. Biosensing system for the rapid multiplex detection of mastitis-causing pathogens in milk. Tartu, 2018, 85 p.
170. **Hedi Rahnel.** ARC-inhibitors: from reliable biochemical assays to regulators of physiology of cells. Tartu, 2018, 176 p.
171. **Anton Ruzanov.** Computational investigation of the electrical double layer at metal–aqueous solution and metal–ionic liquid interfaces. Tartu, 2018, 129 p.
172. **Katrin Kestav.** Crystal Structure-Guided Development of Bisubstrate-Analogue Inhibitors of Mitotic Protein Kinase Haspin. Tartu, 2018, 166 p.
173. **Mihkel Ilisson.** Synthesis of novel heterocyclic hydrazine derivatives and their conjugates. Tartu, 2018, 101 p.
174. **Anni Allikalt.** Development of assay systems for studying ligand binding to dopamine receptors. Tartu, 2018, 160 p.
175. **Ove Oll.** Electrical double layer structure and energy storage characteristics of ionic liquid based capacitors. Tartu, 2018, 187 p.
176. **Rasmus Palm.** Carbon materials for energy storage applications. Tartu, 2018, 114 p.
177. **Jörgen Metsik.** Preparation and stability of poly(3,4-ethylenedioxythiophene) thin films for transparent electrode applications. Tartu, 2018, 111 p.
178. **Sofja Tšepelevitš.** Experimental studies and modeling of solute-solvent interactions. Tartu, 2018, 109 p.
179. **Märt Lõkov.** Basicity of some nitrogen, phosphorus and carbon bases in acetonitrile. Tartu, 2018, 104 p.
180. **Anton Mastitski**. Preparation of α-aza-amino acid precursors and related compounds by novel methods of reductive one-pot alkylation and direct alkylation. Tartu, 2018, 155 p.
181. **Jürgen Vahter**. Development of bisubstrate inhibitors for protein kinase CK2. Tartu, 2019, 186 p.

182. **Piia Liigand.** Expanding and improving methodology and applications of ionization efficiency measurements. Tartu, 2019, 189 p.
183. **Sigrid Selberg.** Synthesis and properties of lipophilic phosphazene-based indicator molecules. Tartu, 2019, 74 p.
184. **Jaanus Liigand.** Standard substance free quantification for LC/ESI/MS analysis based on the predicted ionization efficiencies. Tartu, 2019, 254 p.
185. **Marek Mooste.** Surface and electrochemical characterisation of aryl film and nanocomposite material modified carbon and metal-based electrodes. Tartu, 2019, 304 p.
186. **Mare Oja.** Experimental investigation and modelling of pH profiles for effective membrane permeability of drug substances. Tartu, 2019, 306 p.
187. **Sajid Hussain.** Electrochemical reduction of oxygen on supported Pt catalysts. Tartu, 2019, 220 p.
188. **Ronald Väli.** Glucose-derived hard carbon electrode materials for sodium-ion batteries. Tartu, 2019, 180 p.
189. **Ester Tee.** Analysis and development of selective synthesis methods of hierarchical micro- and mesoporous carbons. Tartu, 2019, 210 p.
190. **Martin Maide.** Influence of the microstructure and chemical composition of the fuel electrode on the electrochemical performance of reversible solid oxide fuel cell. Tartu, 2020, 144 p.
191. **Edith Viirlaid.** Biosensing Pesticides in Water Samples. Tartu, 2020, 102 p.
192. **Maike Käärik.** Nanoporous carbon: the controlled nanostructure, and structure-property relationships. Tartu, 2020, 162 p.
193. **Artur Gornischeff.** Study of ionization efficiencies for derivatized compounds in LC/ESI/MS and their application for targeted analysis. Tartu, 2020, 124 p.
194. **Reet Link.** Ligand binding, allosteric modulation and constitutive activity of melanocortin-4 receptors. Tartu, 2020, 108 p.
195. **Pilleriin Peets.** Development of instrumental methods for the analysis of textile fibres and dyes. Tartu, 2020, 150 p.
196. **Larisa Ivanova.** Design of active compounds against neurodegenerative diseases. Tartu, 2020, 152 p.
197. **Meelis Härmas.** Impact of activated carbon microstructure and porosity on electrochemical performance of electrical double-layer capacitors. Tartu, 2020, 122 p.
198. **Ruta Hecht.** Novel Eluent Additives for LC-MS Based Bioanalytical Methods. Tartu, 2020, 202 p.
199. **Max Hecht.** Advances in the Development of a Point-of-Care Mass Spectrometer Test. Tartu, 2020, 168 p.
200. **Ida Rahu.** Bromine formation in inorganic bromide/nitrate mixtures and its application for oxidative aromatic bromination. Tartu, 2020, 116 p.
201. **Sander Ratso**. Electrocatalysis of oxygen reduction on non-precious metal catalysts. Tartu, 2020, 371 p.
202. **Astrid Darnell.** Computational design of anion receptors and evaluation of host-guest binding. Tartu, 2021, 150 p.

203. **Ove Korjus.** The development of ceramic fuel electrode for solid oxide cells. Tartu, 2021, 150 p.
204. **Merit Oss.** Ionization efficiency in electrospray ionization source and its relations to compounds' physico-chemical properties. Tartu, 2021, 124 p.
205. **Madis Lüsi**. Electroreduction of oxygen on nanostructured palladium catalysts. Tartu, 2021, 180 p.
206. **Eliise Tammekivi.** Derivatization and quantitative gas-chromatographic analysis of oils. Tartu, 2021, 122 p.
207. **Simona Selberg.** Development of Small-Molecule Regulators of Epi-transcriptomic Processes. Tartu, 2021, 122 p.
208. **Olivier Etebe Nonga.** Inhibitors and photoluminescent probes for in vitro studies on protein kinases PKA and PIM. Tartu, 2021, 189 p.
209. **Riinu Härmas.** The structure and H2 diffusion in porous carbide-derived carbon particles. Tartu, 2022, 123 p.
210. **Maarja Paalo.** Synthesis and characterization of novel carbon electrodes for high power density electrochemical capacitors. Tartu, 2022, 144 p.
211. **Jinfeng Zhao.** Electrochemical characteristics of Bi(hkl) and micro-meso-porous carbon electrodes in ionic liquid based electrolytes. Tartu, 2022, 134 p.
212. **Alar Heinsaar.** Investigation of oxygen electrode materials for high-temperature solid oxide cells in natural conditions. Tartu, 2022, 120 p.
213. **Jaana Lilloja.** Transition metal and nitrogen doped nanocarbon cathode catalysts for anion exchange membrane fuel cells. Tartu, 2022, 202 p.
214. **Maris-Johanna Tahk.** Novel fluorescence-based methods for illuminating transmembrane signal transduction by G-protein coupled receptors. Tartu, 2022, 200 p.
215. **Eerik Jõgi.** Development and Applications of E. coli Immunosensor. Tartu, 2022, 103 p.
216. **Alo Rüütel.** Design principles of synthetic molecular receptors for anion-selective electrodes. Tartu, 2022, 109 p.
217. **Tanel Sõrmus.** Development of stimuli-responsive and covalent bisubstrate inhibitors of protein kinases. Tartu, 2022, 148 p.
218. **Oleg Artemchuk.** Autotrophic nitrogen removal processes for nutrient removal from sidestream and mainstream wastewater. Tartu, 2022, 115 p.
219. **Andre Leesment.** Quantitative studies of Brønsted acidity in biphasic systems and gas-phase. Tartu, 2023, 83 p.
220. **Meeli Arujõe-Sado.** Structural effects in aza-peptide bond formation reaction. Tartu, 2023, 83 p.
221. **Jonas Mart Linge.** Electrochemical reduction of oxygen on silver-based catalysts. Tartu, 2023, 269 p.
222. **Tõnis Laasfeld.** Integrating Image Analysis and Quantitative Modeling for a Holistic View of GPCR Ligand Binding Dynamics. Tartu, 2023, 226 p.
223. **Ernesto de Jesus Zapata Flores.** Derivatization Reagents used in negative mode electrospray LC-MS. Tartu, 2023, 107 p.

224. **Patrick Teppor.** Obtaining platinum-free oxygen reduction catalysts through biomass valorization: a case study of peat. Tartu, 2023, 161 p.
225. **Peeter Valk.** Methanol Oxidation on Platinum-Rare-Earth Metal Oxide Activated Catalysts. Tartu, 2023, 162 p.
226. **Shidong Chen.** Unravelling prehistoric plant exploitation in eastern Baltic: organic residue analysis of plant-based materials by multi-method approach. Tartu, 2023, 245 p.
227. **Yogesh Kumar.** M-N_4 macrocycle-based catalysts for electrocatalysis of oxygen reduction and oxygen evolution. Tartu, 2023, 224 p.
228. **Kerli Martin.** Recognition of carboxylates by synthetic receptors – from structure-affinity studies to solid-contact anion-selective electrode prototyping. Tartu, 2024, 130 p.
229. **Huy Quí Vinh Nguyen.** Development of Carbon Supported Pt–CeO_2 Catalysts for Proton Exchange Membrane Fuel Cells. Tartu, 2024, 198 p.
230. **Heigo Ers**. Adsorption and Structuring Processes at Single Crystal Electrode – Ionic Liquid Interface – Insights from Simulations and *in situ* Studies. Tartu, 2024, 137 p.
231. **Ritums Cepitis.** Modelling Structural and Geometrical Effects in Carbon Dioxide and Oxygen Electrocatalysis. Tartu, 2024, 99 p.
232. **Kaarel Kisand.** Resorcinol-derived carbon-based catalysts for polymer electrolyte fuel cell cathodes. Tartu, 2024, 205 p.
233. **Akmal Kosimov**. Template-assisted Mechanosynthesis (TAMS) for the production of bifunctional transition metal-based catalysts. Tartu, 2024, 123 p.
234. **Larissa Silva Macieli.** Derivatization-targeted LC-MS analysis of compounds containing amino group. Tartu, 2024, 157 p.
235. **Silvester Jürjo.** Separation of rare earth elements from Estonian phosphorite ore using liquid extraction followed by electrochemical reduction. Tartu, 2024, 99 p.
236. **Jan-Michael C. Cayme.** Organic-inorganic interactions in experimental and archaeological ceramics. Tartu, 2025, 156 p.
237. **Miriam Koppel.** The diffusion of H2 adsorbed in carbide-derived carbons: a quasi-elastic neutron scattering study. Tartu, 2025, 138 p.
238. **Kenneth Tuul.** Evaluating lithium-ion pouch cells and hydrogen storage materials under extreme conditions using advanced techniques. Tartu, 2025, 188 p.
239. **Marta-Lisette Pikma.** Exploring the basicity of phosphanes and related compounds. Tartu, 2025, 100 p.
240. **Indrek Saar.** Development of novel on-site chemical analysis tests – from alternative materials and technologies to functional prototypes. Tartu, 2025, 214 p.
241. **Gulnara Yusibova.** TAL MOF-Derived M-N-C Electrocatalysts for Oxygen Reduction and Evolution Reactions. Tartu, 2025, 120 p.

242. **Karl Marti Toots.** Cheminformatics Approaches for Analyzing and Modeling the Gas-Ionic Liquid Distribution of Organic Solutes. Tartu, 2025, 249 p.
243. **Freddy Kukk.** Electrochemical Characterization of Structurally and Chemically Modified Solid Oxide Cells Operated in Electrolysis Mode. Tartu, 2026, 142 p.
244. **Shrikant Shivaji Pawade.** Metrological Aspects of Sampling and Water/ Moisture Determination on the Example of Lignin. Tartu, 2026, 146 p.
245. **Raegan Danielle Chambers.** Electrocatalysis of oxygen reduction on Pt nanoparticles deposited on novel support materials. Tartu, 2026, 172 p.
246. **John Paulo Aquino Samin.** Unified pH in aqueous-organic solvent mixtures and low-polarity solvents. Tartu, 2026, 132 p.
247. **Silver Juvanen.** Non-precious metal catalysts based on biomass-derived carbon for electrocatalytic applications. Tartu, 2026, 200 p.